The mechanism of Leak-Before-Break fracture and its application in Engineering Critical Assessment

A thesis submitted for the degree of
Doctor of Philosophy

By

Renaud Bourga

Department of Mechanical, Aerospace and Civil Engineering
Brunel University London, Uxbridge
United Kingdom

March 2017

Abstract

This thesis investigated the different aspects and mechanisms of leak-before-break (LBB) assessment. The main objective was to improve the understanding of the transition between surface and through wall defects. While existing procedures generally idealise the through-wall crack into a rectangular shape, in reality a crack propagates with a shape depending on the loading. Comparison between the related solutions from established procedures have been undertaken. The apparent variation depending on the solutions used in the assessment has been highlighted. Two different methodologies have been employed to investigate the transition of flaw: (i) non-ideal through-wall and (ii) surface-breaking flaw propagation. The first approach consists of numerical models of non-idealised flaws in order to assess the effect on LBB parameters. For the second approach, experiments have been first carried out to visualise the shape of defect growths. To further study surface-breaking flaws, both experimental and numerical studies were performed. Fatigue tests on deeply notched plates with two crack aspect ratios were carried out. Strain evolutions on the back surface were recorded along the axes parallel and perpendicular to the crack. Numerical models have been prepared to investigate a larger scope. Behaviour of growing surface-breaking defects was examined. Based on the work conducted in this research, the major findings can be summarised as follows:

- The existing solutions to carry out a LBB assessment using available procedures were reviewed and discussed. For axial flaws, SIF solutions were found similar and in good agreement with FEA values. Reference stress solutions showed significant difference between BS 7910 and API 579-1/ASME FFS-1. When compared to experimental data, API's solutions were able to distinguish between leak and break cases.
- Flaw geometry assumption for through-wall crack yet to become idealised did not always reflect the actual behaviour, especially for COA calculation. In this case, FEA can be used as a good predictive tool for LBB to estimate margins when assessing leak rate.
- The experiment using metallic specimens showed that high stress/strain on back surface would provide a good estimate of the crack propagation as it approached break-through. This offers a more accurate monitoring mechanism. Strain-mapping devices such as gauges could be used.

Acknowledgements

Writing these acknowledgements marks the end of my adventure at TWI / Brunel University London as a student.

I would like to express my gratitude to my Supervisor, Dr Bin Wang for his precious guidance and help.

Next, I would like to thank Dr Yin Jin Janin for her excellent supervision, valuable guidance throughout this research and for going through several drafts of my thesis! Her support before being my industrial supervisor, during her maternity leave and up to the end has been a source of comfort and inspiration and has made this research possible.

I would like to thank Dr Simon Smith for the really valuable discussions, for sharing me his knowledge and answering my questions on FEA in general and experiment. His support was greatly appreciated.

Furthermore, I would like to thank everyone that I had the pleasure to share the office with for their continuous support during the period of my PhD studies. It was a great time and I learned a lot from all of you. Thank you very much.

Lastly, and most importantly, I would like to thank my family for its continuous and unconditional support.

Contents

Symbols list

Symbol	Name	Unit
a	Crack depth (surface crack) / Half crack length (through-wall crack)	mm
c	Half crack length (surface crack)	mm
C	Fatigue parameter	—
D_i	Internal diameter	mm
D_m	Mean diameter	mm
D_o	External diameter	mm
E	Young modulus	MPa
E	Weld efficiency factor	—
J	Rice's J-Integral	$MPa.\sqrt{m}$
K_I, K_{II}, K_{III}	Stress Intensity Factor mode I, II and III	$MPa.\sqrt{m}$
K_r	Fracture ratio	—
L_r	Load ratio	—
N	Number of cycles (Fatigue)	Cycles
P	Pressure	MPa
P_b	Primary bending stress	MPa
P_m	Primary membrane stress	MPa
R_i	Internal radius	mm
R_m	Mean radius	mm
R_o	External radius	mm
S	Allowable stress	MPa
SF	Safety Factor	—
t	Thickness	mm
W	Width	mm
w	Strain energy density	—
δ	Crack Tip Opening Displacement	mm
Δ	Stress Intensity Factor range	$MPa.\sqrt{m}$
ν	Poisson ratio	—
σ_f	Flow stress	MPa
σ_{ref}	Reference stress	MPa
σ_{uts}	Ultimate Tensile Stress	MPa
σ_{ys}	Yield Stress	MPa

Abbreviations

Symbol	Name
CFP	Crack Face Pressure
CMOD	Crack Mouth Opening Displacement
COA	Crack Opening Area
CSA	Cross Section Area
CTOD	Crack Tip Opening Displacement
ECA	Engineering Critical Assessment
EPFM	Elastic Plastic Fracture Mechanics
FAD	Failure Assessment Diagram
FEA	Finite Element Analysis
FFS	Fitness For Service
LBB	Leak-Before-Break
LEFM	Linear Elastic Fracture Mechanics
RS	Reference Stress
SF	Safety Factor
SG	Strain Gauge
SIF	Stress Intensity Factor
UTS	Ultimate Tensile Stress
YS	Yield Stress

Chapter 1

Introduction

Contents

1.1 Background

Different industries (i.e. oil and gas, nuclear, process, etc) commonly use pressurised components for static or circulating fluids. It may be an isolated component or a complex system consisting of a number of different engineered structures. With an ever increasing demand in energy coupled with potential economical restraint, these structures tend to be used up to their maximum capacity. For this reason, increasingly demanding operating conditions and extended service life are sought for pressurised components.

A good example is the oil and gas sector. Resources are becoming more and more difficult to extract. They need to be transported and processed as quickly as possible. Rising demands have pushed suppliers to extract resources from deeper source and often require extensive refinement process/treatments. Thus, more intensive operations are required with structures working under harsher conditions.

Numerous countries, such as USA or France, began constructing their nuclear power plants (NPPs) in 1960's - 1970's. These countries are now planning for large-scale refurbishment programs to extend their operations for another 20-30 years. This has increased the need to assess the structural integrity of these components beyond their initial design life. Life extension is used to bridge the gap between ageing and new plants. Extending the operating life of existing NPPs will help to reduce the short term need for new generating capacity without new capital costs. However, these extensions must take place with careful safety analysis and monitoring of equipment of ageing concerns. Ageing in NPPs must, therefore, be efficiently assessed to ensure the availability of design functions throughout the extended service life. It is crucial to demonstrate that adequate safety margins (i.e. integrity and functional capability) remain in excess of minimum safety requirements.

Fracture mechanics-based structural integrity assessments, most commonly referred to as either Engineering Critical Assessments (ECAs) or Fitness-For-Service (FFS) assessments, are not a new concept. Established since the 1960s, they have found more widespread acceptance over the years. The nuclear and offshore oil and gas industries were the main drivers behind the development of them. BS 7910 [1], a British Standard focusing on the assessment of brittle fracture and fatigue, offers three levels of assessment for fracture, based on the failure assessment diagram (FAD) concept.

Structural integrity assessments can be used at the design stage to: (i) estimate the maximum flaw size that will not grow to an intolerable size during the life of the component, or (ii) assess defects that have grown after some time in service. Such task requires information about defect tolerance, which itself relies on the availability of representative and reliable experimental data. For structures operating in inert environments, primary

material properties that are needed for this type of assessment are tensile properties, fracture toughness and fatigue crack growth rate (FCGR).

A typical requirement for average component would be to stipulate the maximum allowable flaw size lasting two design service lives (DSL), or twice the expected life of the component. However, in the case of pressure vessels, a further requirement is added that the body must be able to leak for 0.5 DSL before failure, giving the maintenance team sufficient time to notice the leak and replace the part. Satisfying this leak before break (LBB) requirement means placing a through-wall flaw in any location receiving a damage tolerance inspection and ensuring that a crack with a depth equal to the wall thickness of the pressure vessel and a length of twice the wall thickness will survive for the required number of cycles. LBB concept essentially demonstrates through fracture mechanics analysis there is negligible chance of any catastrophic break without giving earlier indication of leakage.

One area where there is still significant uncertainty is the behaviour of deep flaws and their transition from part-penetrating to through thickness. It is known that there can be substantial uncertainty in calculating leak rates from crack opening area, and often safety factors are used to account for this. The work described in this thesis serves the purpose to try to reduce this uncertainty. The methods of assessing these flaws (with a more accurate crack shape) is crucial and the main motivation for this research.

1.2 Research hypothesis

Traditional crack evaluation uses conservative methods to predict maximum loading that a flawed component can sustain. When performing an analysis, it is appropriate to use the current standards and assume an idealized flaw shape of either constant depth (i.e through-wall) or semi-elliptical. However, when cracks grow from surface to through-wall, their shapes are more complex than the ideal models assume. These cracks can grow as very long surface cracks before breaking through the surface and complex irregular shape. Deterministic LBB assessments often consider an already through-wall cracked component. This configuration is often assumed to be ideal as the solutions available have been derived for these geometries. However, the existing procedures do not assess components with active degradation mechanisms such as fatigue, while some have been granted for LBB such as nuclear piping systems affected by Primary Water Stress Corrosion Cracking (PWSCC). An understanding of the effect of crack shape hypothesis can help reducing safety margins applied and saving significant resources by not having to develop complex FE models. This research determines the actual shape of flaws breaking through the wall and compares their behaviour in terms of leak and break to the predictions assuming an "ideal" through-wall flaw.

1.3 Aims and objectives

The overall purpose of this research project is to improve fracture assessment methods for leak-before-break procedures available in BS 7910 (2013) or API 579-1/ASME FFS-1 (2007) for non-nuclear industries. Through this research it is intended that the safety and integrity assessment of pressurised components could be improved and it would help to optimise operations. This aim is achieved in this thesis by performing the following:

- Review available integrity assessment / leak-before-break procedures available;
- Determine the best available solutions up to date to carry out a full assessment;
- Provide guidance on performing LBB calculations and improved and/or revised expression for surface breaking or existing through-thickness flaws in pressurised components;
- Give an increased knowledge of the behaviour of cracked components during LBB transition.

1.4 Outline of thesis

This thesis is divided into eight chapters including this introductory chapter.

Chapter 2 focuses on literature review. Different types of defects that can be present in metallic structures, especially pressurised components are reviewed and discussed (Section 2.1). Conventional and leak-related non-destructive testing (NDT) methods are discussed in order to determine how FFS input parameters are obtained (Section 2.2). These existing defects (i.e. cracks), once detected and characterised, are assessed using fracture mechanics (Section 2.3). The assessment of the criticality of a defect is performed using fitness-for-service procedures (Section 2.4). The basis of Fitness-For-Service and associated advantages are reviewed. Since leak-before-break concept is mainly applicable for pressurised components, a review of related solutions and design codes is discussed in Section 2.5.

Chapter 3 focuses on the literature review on Leak-Before-Break. Its underlying basic principles are discussed (Section 3.2) and existing procedures are reviewed (Section 3.3). Application in industries is discussed (Section 3.4). Parameters specific to this concept (i.e. Crack Opening Area (COA)) are evaluated (Section 3.5). Review of work carried out in the last 30 years and scope for future work is provided in section 3.6.

Chapter 4 focuses on the analysis of current LBB solutions from procedures. As this concept can be applied at either design or in-service stage, both design codes and FFS procedures have been reviewed. A short discussion on the effect of pressure vessel design codes on the required minimum thickness is given in Section 4.2. Leak-Before-Break

assessment can be divided into two separated analyses, namely crack stability and leakage analysis. These two analyses require calculations of different parameters. The solutions for Crack Opening Area models (Section 4.3), Failure Assessment Diagram (Section 4.4.2), Stress Intensity Factors (Section 4.4.3) and Reference Stress (Section 4.4.4) solutions have been examined. Existing solutions are compared to each other. When possible, they are compared against experimental data from literature.

Chapter 5 presents the numerical work carried out on through-thickness defects. Both plate and cylindrical component geometries have been evaluated. The main objective of this chapter is to investigate the flaw geometrical parameters and validate current FE work with benchmark cases (Section 5.2). Different modelling strategies have been employed and the validation of existing solution is included. Finite element work undertaken to assess the effect of crack idealisation in cylinders is provided in section 5.3. Investigation on stress intensity factor and crack opening area for 'short' and 'long' crack has also been accounted for in this chapter. The effect of crack face pressure on existing solutions is also discussed.

Chapter 6 presents the experimental work undertaken. Effort to assess crack shape evolution when a crack propagates through wall is given in section 6.2. As a qualitative approach, plates made of Perspex have been studied. Four geometries have been considered (2 widths / 2 thicknesses). This experiment provides an insight of the transformation of a surface crack of 80% through-thickness when it is subject to fatigue loading (i.e. break-through). Using the experience gained from Perspex experiments, tests have been reproduced with metallic specimens (Section 6.3). Two different notch geometries have been considered to include 'short' and 'long' c racks. Stress/strain field evolution on the back surface of a surface cracked plate has been investigated. A set of strain gauges on the back surface recorded the strain evolution during the transition from surface to through thickness crack. Further discussion was made on the fracture surface from specimens.

Chapter 7 covers the numerical work undertaken to examine the transition from surface-breaking to through-thickness crack. Experimental work validation from the static tests was done in section 7.3. The evolution of stresses on the axis of the crack and the axis perpendicular to the crack were assessed (Section 7.4). Investigation of the stress field on the back surface of a surface-cracked plate is done for crack depth ranging from 20% to 95% thickness. Models were prepared in order to increase the range of observations from experiments.

The final conclusions, summary of the findings and highlights of future research topics related to this research is presented in Chapter 8. Two appendices are provided to include the complementary files from experiment (App.A) and a compendium of solutions compared in Chapter 4 (App.B)

1.5 Contribution to new knowledge

The main contributions from this work are:

- Comparison of the different LBB available procedures and highlight of the shortcomings when they are applied to non-nuclear industries. Solutions for SIF, RS and COA from literature for different parameters are discussed. The best available solutions are highlighted when compared to experimental data;
- Validation of existing solutions with FE models of plates and cylinders containing through-thickness defects for a wide range of geometries. The effect of crack shape idealisation in cylinders with axial through-wall defect using numerical model results (both 'short' and 'long' cracks inclusive) was investigated;
- Analysis of stress/strain field on the back surface of a plate during the crack growth to provide a better understanding of crack transition from surface to through-thickness. Experimental observation on shape evolution from deep surface-breaking crack to through thickness crack in Perspex and metallic specimens;
- Draft improved LBB procedure for BS 7910 Annex F based on research findings.

1.6 List of publications

- R. Bourga, P. Moore, Y.-J. Janin, B.Wang, and J. Sharples. Leak-before-break: Global perspectives and procedures. International Journal of Pressure Vessels and Piping, 129-130:43-49, 2015.

- R. Bourga, P. Moore, Y.-J. Janin, B.Wang. Comparison of BS 7910:2013 and API 579-1 / ASME FFS-1 solutions with regards to Leak-Before-Break. In Proceedings of the ASME 2016 Pressure Vessels & Piping Conference, Vancouver, 17-21 July 2016. Paper No.PVP2016-63876

- R. Bourga, P. Moore, Y.-J. Janin, B.Wang. The effect of crack shape idealisation on Leak-Before-Break assessment. In Proceedings of the ASME 2016 Pressure Vessels & Piping Conference, Vancouver, 17-21 July 2016. Paper No.PVP2016-63877

- R. Bourga, Y.-J. Janin, B.Wang. Transition from part-penetrating to through thickness cracks: experimental and numerical study. International Journal of Pressure Vessels and Piping (Submitted on 02/04/2017)

Chapter 2

Literature Review

Contents

2.1 Typical defects in pressurised equipment

Any metallic structure can contain defects that are introduced during the manufacture of the material, during the fabrication of the piece (i.e. defects of machining or welding) or in service. Pipes and pressure vessels are examples of such structures. They are widely used for fluid transport or storage in various environments. However, they are also safety-critical structural elements of which the risk of a malfunction cannot be accepted. In the case of pipes, their increased diameters and operating pressures increase the risk of fracture initiated from defects. The presence of a defect coupled with the effect of the loading (i.e. internal pressure) can cause a localized fracture inducing leakage or in the worst case a general fracture or explosion. Defects can be divided into three general categories: manufacturing defects, service induced defects or defects caused by external forces.

2.1.1 Fabrication induced defects

Numerous defects can be introduced in components during fabrication, especially welding [2]. There are many different welding processes, thus different types of defect can be introduced depending on the methods and the materials. Physical discontinuities around a weld bead may also alter the local stress distribution and metallurgical differences between the parent metal and weld metal affect the mechanical and chemical properties of the weld joint. Thermal gradients from fusion welding give rise to a range of microstructures and properties that varies from the parent material through the heat-affected zone (HAZ) associated with the weld. The different types of possible discontinuity may be categorized as:

- **Porosity**: More commonly in the form of spherical defects, some gas inclusions may have elongated forms (wormholes).
- **Inclusions**: These are external solid particles that may be introduced during the welding, casting and rolling processes.
- **Lack of fusion or incomplete root penetration**: Lack of complete melting and fusing between the molten weld bead and other parts of the joint. The atom-to-atom bond is incomplete reducing the effective contact area carrying the load.
- **Cracks**: Although many cracking mechanisms exist for many different materials, the most common types of cracks in steel welds are hydrogen cracks, sometimes called cold cracks. This common mechanism can form cracks in several different orientations and locations; transverse in high strength weld metal, longitudinal along the HAZ or weld root, or crater cracks at the end of a weld run . Figure 2.1 presents a view of different locations and orientations of cracks which can occur in a weld.

After fabrication, welds are inspected to ensure that no unacceptable defects remain in the welds. This is usually done 24 or 48 hours after welding, since hydrogen cracks can occur up to several hours after cooling. This work considers the subsequent degradation that occurs in-service in piping and pressure vessels, whether or not that occurs as a leak or as a consequence of catastrophic failure.

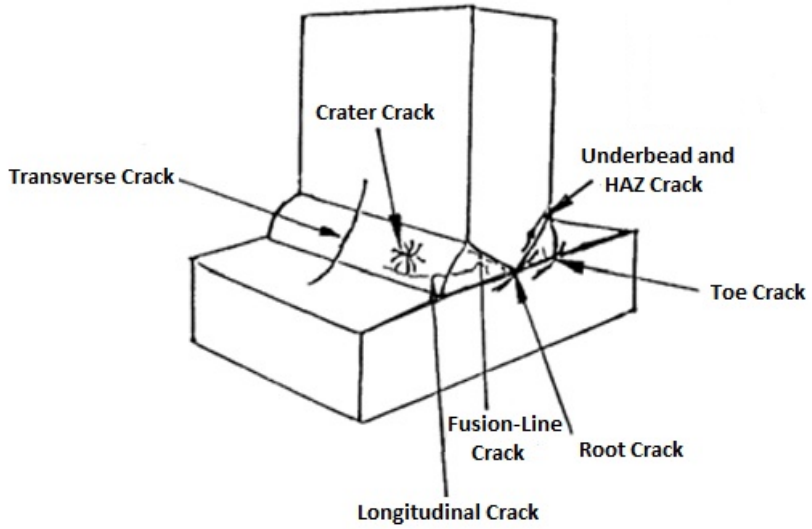

Figure 2.1: Different types of cracks located in and around a welded T-joint [2]

2.1.2 Environmentally induced defects

Defects can develop in components depending on the operating conditions, such as the loads imposed (static or cyclic), service temperatures, locations of components, etc. Three types of environmentally induced defects are discussed here: corrosion, fatigue and fluid-related defects. These defects have been widely observed in pressurised components.

2.1.2.1 Corrosion

Corrosion is the degradation of a metal and its properties because of a reaction with the surrounding environment. It is a significant factor in the failure and damage of metals, including pressurized components [3]. Due to the large amount of metals and applications, many factors contribute to the corrosion process [4]. The nature of corrosion products, the rate of corrosion and the mechanism can vary widely depending on the environment [5]. The full complexities of corrosion engineering (general corrosion, galvanic corrosion, erosion corrosion, fatigue corrosion, pitting corrosion and stress corrosion cracking (SCC)) are beyond the scope of this thesis but the last two are of the most significance to the risk of leak and/or break in pressure equipment [6]:

- Pitting corrosion is localized and can result in small holes on the surface of a metal. The metal loss is negligible compared to the total mass of metal of the component but it can be rapid. Nevertheless, equipment failure by perforation, particularly where a large number of pits occur in a localised region is the usual outcome of pitting corrosion.
- Stress Corrosion cracking (SCC) is a localized phenomenon and occurs mostly when residual stress remains high [6]. When high stresses are applied to metals in a corrosive environment, cracking can be accelerated in the form of SCC. A way to reduce this effect by redistributing the load and reducing the residual tensile stress is post-weld heat treatments [7]. In industrial plants, SCC is responsible for a third of all damage due to corrosion [6]. The average age to encounter a first SCC incident in gas transmission pipelines has been evaluated after 20-25 years of service life [4].

2.1.2.2 Damage related to the fluid

The interaction between the fluid in movement and the structure can lead to damage mechanisms. This failure-related phenomenon depends on the operating conditions and the fluid conveyed. Two phenomenon will be discussed here:

- Erosion is an undesired removal of material due to the action of the fluid on the component-wall. In service, the friction due to the contact between the fluid in movement and the static component wall may lead to an erosion of the wall, also known as wall-thinning. Another aspect may be noted when a leak occurs. Erosion of the area surrounding the leak site also increases the crack opening area.
- Water hammer is a phenomenon that takes place when a sudden change in flow velocity occurs resulting in a sudden increase in load and possible negative pressure in a very short time. It may lead to other degradation mechanisms such as fatigue.

2.1.2.3 Fatigue

Another mechanism that can lead to failure of pressurized components is fatigue. When components are subjected to repeated changes in their loading conditions, fatigue cracks will initiate at locations of stress concentration, often weld toes. These cracks progressively propagate over many thousands of load cycles until they can cause failure at stresses below the material's yield strength with no sign of plastic deformation. The number of cycles leading to fracture at a given stress is generally referred to as fatigue strength. This phenomenon begins generally from a crack that continues to grow as a result of the stress fluctuations to its critical length. Fatigue is greatly influenced by the type of alloy, and the magnitude and frequency of loading cycles. Different models have been developed to assess fatigue based on fracture mechanics, from the simplest, such as the well-known

Paris' law (Eq.2.1):

$$\frac{da}{dN} = C \times (\Delta K)^m \tag{2.1}$$

to the most complex such as the NASGRO equation (Eq.2.2) which incorporates the effects of fatigue crack closure:

$$\frac{da}{dN} = C \times \left(\frac{1-F}{1-R}\right)^n \times \frac{\left(1-\frac{\Delta K_{th}}{\Delta K}\right)^p}{\left(1-\frac{K_{max}}{K_{Ic}}\right)^q} \tag{2.2}$$

In these models, the crack increment, a, per cycle N, is expressed as a function of the stress intensity factor range ΔK.

2.1.3 Third-party caused defects

Third-party caused defects may be unforeseeable in the general design and operation of equipment, but may need to be assessed after the event for their impact on structural integrity. During installation or maintenance, components may be subjected to an external mechanical impact. Two mechanical defects are summarized here: dents and gouges depending on whether there is material removal or not.

- Dents are a permanent plastic deformation due to an impact. In case of pressurized components, a dent is a change of the curvature in the wall without changing wall-thickness. Dents are distinguished as plain or kinked depending if there is a change in wall thickness or not [8]. It causes local concentration of stress and strain and a local reduction of the pipe diameter.
- A gouge or scratch is a superficial surface damage due to contact with a foreign object causing material removal. The dimensions of a scratch are defined so that the length is greater than the width. Figure 2.2 presents an illustration of a combination of a dent and a gouge, which can be resulting from an external impact.

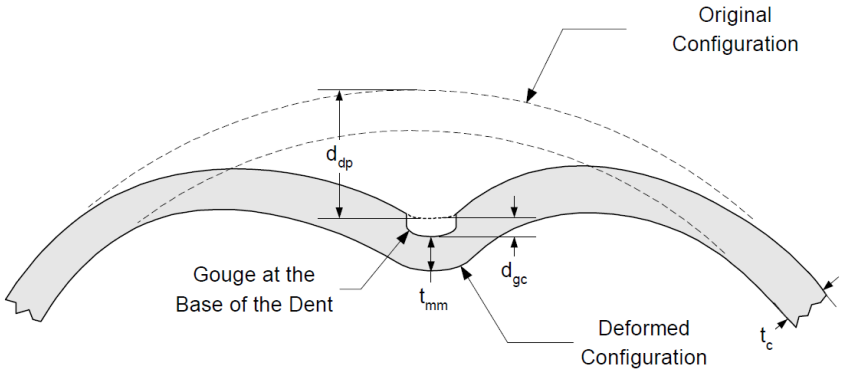

Figure 2.2: Illustration of a dent and gouge combination [9]

2.2 Non-Destructive Testing (NDT)

Non-Destructive Testing (NDT) is the inspection of materials without causing any subsequent damage to the material. In contrast, destructive testing (involving the extraction of test specimens for mechanical or metallurgical testing) usually makes testing more costly and is also inappropriate in many circumstances once a component is in service. Discontinuities as surface or internal (embedded) defects, discussed in Section 2.1, have to be evaluated to ensure product integrity and reliability. During manufacturing, NDT methods are applied to ensure the quality of materials and joining processes before the component is used. In-service, NDT inspections are planned at regular intervals during service to ensure that the components still exhibit the integrity necessary to be safe. In order to make a Leak-Before-Break case, NDT techniques have an important application to detect defects as early as possible and characterize their geometries. No single method will satisfy all requirements of sensitive flaw detection and accurate geometry measurement), each of the NDT methods has advantages and disadvantages when compared to other methods. Figure 2.3 provides some guidance on the selection of NDT methods for common flaw detection and measurement applications [10], [11].

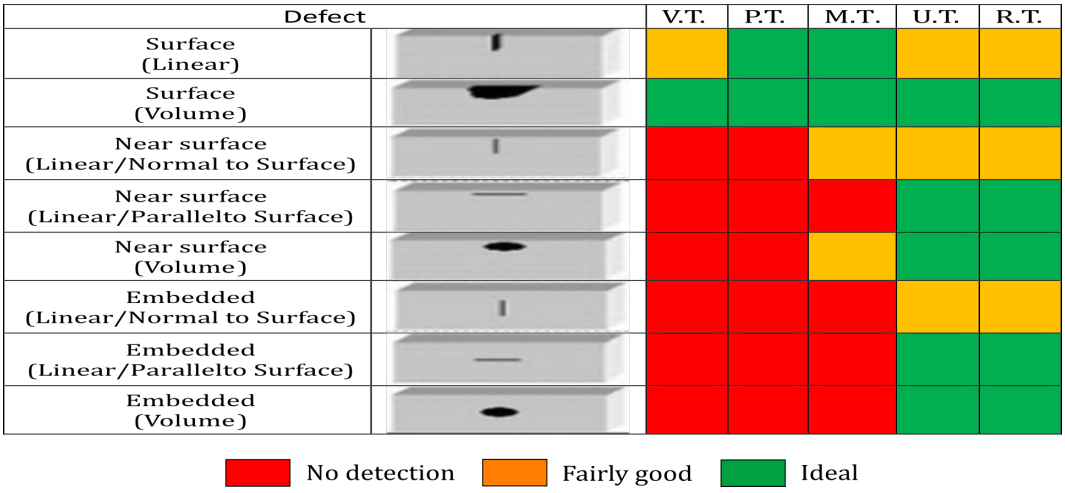

Figure 2.3: Comparison of NDT methods available for different defect type [10],[11]

Having in mind that Leak-Before-Break procedures are of interest here and will be discussed in detail, both penetrating and through-wall defects will be evaluated. The first part focuses on partially-penetrating defects. Methods to detect and size both surface, sub-surface or embedded defects are reviewed. These methods are generally known as conventional NDT methods. The leak testing method for through-wall defects is a collection of different methods which can be considered more as proof testing or performance testing, although they are non-destructive in their application. These methods, specific to particular industries using pressurized components, are generally less commonly known as NDT techniques.

2.2.1 Conventional NDT (Surface/Embedded defects)

According to pressure vessel design codes such as BS PD 5500 [12], Radiographic Testing (RT) / Ultrasonic Testing (UT) should be used for examination of embedded flaws and Penetrant Testing (PT) / Magnetic Particle Testing (MT) for surface breaking flaws. Numerous standards exist for each NDT method. Relevant ASME and BS standards are given in the title of each part. Further guidance can also be found in Section V of ASME Boiler and Pressure Vessel Code [13]. However, before applying one of these NDT techniques, the first approach is to simply look at the component and visually examine the locations of concern for evidence of damage.

- **Visual Testing (VT)**: VT is done to check the surface condition (for evidence of corrosion products, weld appearance and fusion, coating condition etc), the shape of the component (and the presence of dents or gouges) or evidence of leakage. Only surface-breaking defects can be detected (and access to the surface is required) and sizing the crack geometry is not easy.
- **Penetrant Testing (PT) ([13]-6, [14], [15])**: PT can be used for the detection of discontinuities that are open to the surface such as cracks, seams, laminations, through leaks or lack of fusion in non-porous materials. However the surfaces tested must be free of all contaminants (dirt, oil, grease, paint, rust, etc.). This is a good alternative method to the VT for large components
- **Magnetic Particle Testing (MT) ([13]-7, [16], [17])**: MT can be used to locate surface and near-surface discontinuities in ferromagnetic materials. Surface and subsurface flaws approximate size and shape can be detected rapidly on large surface areas of complex parts. Surface preparation is less critical than it is in PT. The orientation and strength of magnetic field is critical, a proper alignment of magnetic field and defect is necessary. Large currents are needed for very large parts.
- **Ultrasonic Testing (UT) ([13]-4/5, [18], [19])**: Ultrasonic testing has a high accuracy to position and size embedded as well as surface defects. It has a higher penetrating power than RT which allows examination of extremely thick sections (up to about 7 meters of steel) and its fast response permits rapid and automatic inspection. Moreover, access to only one surface of the specimen is needed. However, the geometry of the part being tested, the defect orientation or material properties affects the detectability (i.e. materials having coarse grain microstructure such as austenitic stainless steel can be difficult to inspect).
- **Radiographic Testing (RT)([13]-2, [20])**: Radiographic testing is used for the detection of surface breaking and embedded flaws in many different materials. Surface preparation may be necessary to avoid confusion with discontinuities. Moreover, planar defects and the depth of defect cannot be detected easily.

2.2.2 Leak Testing (Through-wall defects)

Leak testing methods group together a number of conventional and unconventional NDT techniques to detect, locate and size leaks. A leak is generally due to an unintended crack, hole or porosity in an enveloping wall which must contain fluids or gases. A section about leak testing is present in most pressure vessel codes as quality control step in terms of hydrostatic or pneumatic pressure test where the pressure vessel is pressurized above its design pressure in order to assure that there is no leak. Many modern designs are based on the "leak before break" principle, in which critical thickness and other dimensions are selected so that a cracked vessel will leak before the crack grows to catastrophic proportions. In these applications, the ability to detect the leak at a very early stage is therefore important. Numerous methods are available in the field of leak testing. However, due to the huge range of methods for the determination of the leakage rate, it is often not easy to select the right method. Some standards give advices for the selection of the appropriate leak testing technique and for calibration (i.e ASTM E432 [21] and BS EN 1779 [22]). Figure 2.4 reviews some of these methods with their sensitivity. Some general guidance are given in Section V of ASME Boiler and Pressure Vessel Code [13] Article 10. The surfaces to be tested have to be as clean as possible in order to avoid leaks clogging. Pressure gauges range shall be not less than 1/2 or more than 4 times the maximum pressure. All openings have to be sealed and components to be tested shall not be pressurized at more than 25% of the maximum design pressure if no other indications are specified. As seen previously, visual examination is a basic non-destructive test to detect surface defects. It can also be used for leaks detection. Prior to employing a sensitive leak testing method, a preliminary test to detect and eliminate potential large leaks may be useful to perform in order to avoid missing small leaks.

Sensitivity range (mbar.l/s)	10^{0}	10^{-1}	10^{-2}	10^{-3}	10^{-4}	10^{-5}	10^{-6}	10^{-7}	10^{-8}	10^{-9}
Pressure decay										
Ultrasonic										
Acoustic Emission										
Bubble test										
Dye penetrant										
Thermal conductivity										
Halogen detector										
He sniffer										
Radioisotope										
Mass spectrometer										

Figure 2.4: Sensitivity ranges of various leak detection methods [23] [24]

- **Liquid penetrants and chemical tracers ([13]-6, [2])**: Although this test is time consuming, it requires no significant equipment and no pressure differential is necessary. It is easy to apply and the results are visual. However, access to both sides of the envelope is necessary and it may require extensive cleaning before and after the test. It cannot be applied while the component is in operation.
- **Ultrasonic leak testing ([13]-10, [25])**: Ultrasonic gas leak detector are used to detect the ultrasonic energy produced by the flow of a gas leaking through a pressure boundary. Mainly used for outdoor environments where weather conditions can easily dissipate the escaping gas before allowing it to reach more conventional gas leak detectors. This simple, fast and non-contacting method is useful for locating and estimating the size of pressurized gas leaks in service. However, due to the low sensitivity of this technique, it should not be utilized for the acceptance testing of vessels that will contain lethal or hazardous substances [13], [25]. Sensitive to other environmental noises, it is qualified as a semi-quantitative method used to detect and locate leaks. It may be used as a pre-test or monitoring technique before other more time consuming and sensitive leak test methods are employed.
- **Acoustic Emission (AE) leak testing ([13]-12/13, [26], [27], [28], [29])**: Acoustic emission leak detection detects high frequency sound waves travelling within the wall thickness of the component. Using this method it is possible to detect, locate, and characterize AE sources to evaluate their significance relative to integrity. It is the most used method in the water industry to locate leaks. AE testing is considered to be more sensitive than ultrasonic leak testing, but does require access to the component surface.
- **Testing by means of pressure ([13]-10, [30])**: Another common method is the observation of pressure change that can reveal leakage of a pressurized component.The test object is initially pressurized to establish a reference pressure. After a stabilizing period for temperature and moisture equalization (not less than 1h [30]), the pressure is monitored again. As this method tends to detect only large leaks, this procedure is generally used as a preliminary leak test and is often combined with another leak detection method such as bubble testing or tracer gas detection to detect and locate smaller leaks. The limit of sensitivity for pressure decay test is in the range of 10^{-1} to $10^{-3} mbar.l/s$.
- **Bubble testing ([13]-10, [31], [32])**: Bubble testing for leak location is one of the most widely used tests because of it is quick, simple and has relatively low cost to perform [2]. Immersion and liquid application are possible, however liquid application is the most useful on large components on which the immersion technique is impractical. The sensitivity of the method is dependent on the pressure differential, the gas used to create the differential, and the liquid used for testing. Unless otherwise specified, the test gas is air; but, inert gases may be used.

This provides immediate indications of the existence and location of large leaks (10^{-2} to $10^{-4} mbar.l/s$). Smaller leaks may be found with longer inspection times (up to $10^{-5} mbar.l/s$). A quantitative measure is not possible with this method but it can be used as pretest for the hydrostatic test.

- **Tracer gas method ([13]-10, [33], [34], [35], [36], [37])**:Tracer gas methods describe a group of test methods used to detect and measure a tracer gas flowing through a leak. It is one of the most efficient test methods because of its high sensitivity [13]. The basic principle is to create a tracer gas pressure differential across the pressure boundary and detect it on the low pressure side due to its physical or chemical properties [37]. Two methods are generally described: Halogen Diode Detection and Helium Mass Spectrometer Test. However, halogen detection methods are losing their appeal as a tracer gas, due to environmental issues. An important factor for any tracer gas detector is the background concentration in air. Helium, being present in only small amounts (5 ppm) in the ambient air is preferred for different reasons. Firstly, it penetrates small leaks rapidly. The only smaller molecule is hydrogen, which is not inert. Helium is also non-toxic and relatively inexpensive to produce. Typically a helium leak detector will be used to measure leaks in the range of 10^{-6} to $10^{-13} mbar.l/s$. A basic limitation to this method is therefore that a large leak will saturate the detection. A pre-test method can be employed to weed out the gross leaks.
- **Radiotracer testing ([38], [39])**: Radiotracers provide a powerful alternative to other leak detection techniques. It uses the principle of detecting radioactive material introduced from one side of the pressure boundary. They are the most sensitive tools available and they can be used in-service, providing information in the shortest possible time. Only very small concentrations of radioactive isotope can provide an extremely detectable level of measurable radiation. The emission of radiation is a specific property of the radioisotope and is not affected by interference from other materials in the system. Thus radiotracers have strong resistance against severe process conditions. As the characteristics of the radiation differs from one radioisotope to another, multiple radiotracers may be employed and measured simultaneously if needed to locate the leaks. The amounts of radiotracer used are virtually insignificant. For this reason, when injected, they do not disturb the fluid dynamics inside the vessel under investigation and do not interfere with product quality. The radiotracer technique is very sensitive and enables the measurement of leak flows up to $10^{-10} mbar.l/s$.

2.3 Fracture mechanics tools

As mentioned in Section 2.1, any structures can contain defects introduced during different stages of the component's life. These defects must be taken into account because they affect the reliability of the structure. Once detected and characterised (Section 2.2), defects criticality must be assessed. Fracture mechanics is a field of solid mechanics that analyses the mechanical behaviour of cracked bodies taking into account the stress and strain fields in the area of a crack. Its objective is to characterize the crack behaviour with measurable parameters (i.e. stress field, flaw size or material toughness) and can be applied to a large range of scale, from the atomistic level to the full structure. Fracture mechanics is used to evaluate the strength of a structure or component in the presence of a defect. Historically, the first major development in modern fracture mechanics was initiated by Inglis [40] in 1913. He published a stress analysis for an elliptical hole in an infinite linear elastic plate. The next decades brought developments in the establishment of methods to measure fracture toughness in laboratory specimens from wide plate test to smaller standard notched specimens [41].

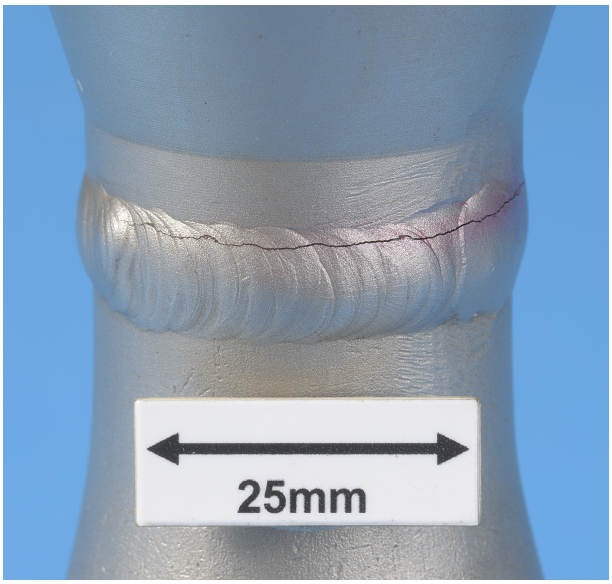

Figure 2.5: Illustration of a circumferential crack in a weld (TWI Ltd)

2.3.1 Crack behaviours

In fracture mechanics, two main modes of rupture are considered: brittle or ductile. During crack propagation, new free surfaces are generated with a specific surface energy. Not all available energy provided by the external load is used for the generation of new crack surfaces. It is also transformed into other energies, like kinetic energy or dissipative heat in the plastic zone at the crack tip. When a large part of this energy is used for crack growth and little energy is absorbed in other ways, the fracture is said to be brittle.

Here, the component fails unstably and no measurement of the fracture resistance beyond initiation is possible. When a lot of energy is transformed into other energies, mainly due to dissipative mechanisms, the fracture is said to be ductile. The plastic deformation dominates at the crack-tip, and the material fracture resistance increases as the crack grows. A crack can be defined as a plane defect that separates a solid locally. The displacement field is then discontinuous across this surface and three vector components of this discontinuity form the three possible crack surface displacements to allow a crack to propagate, known as Mode I, Mode II and Mode III (See Figure 2.6):

- **Mode I (Opening mode)**: The crack tip is subjected to a tensile stress normal to the crack plane. Crack faces separate at the crack front and the displacements of the crack surfaces are normal to the crack plane.
- **Mode II (In-plane shear mode)**: The crack tip is subjected to a shear stress parallel to the plane of the crack and perpendicular to the crack front. Crack faces slide relative to each other so that the displacements of the crack surfaces are in the crack plane and normal to the crack front.
- **Mode III (out-of plane shear mode)**: The crack tip is subjected to a shear stress parallel to the plane of the crack and parallel to the crack front. Crack faces move relative to each other so that the displacements of the crack surfaces are in the crack plane and parallel to the crack front.

The superimposition of these three modes is sufficient to describe the most general case of a loaded cracked body (mixed mode). However, most of developments have been proposed for mode I, this being the usual mode for isotropic materials brittle fracture.

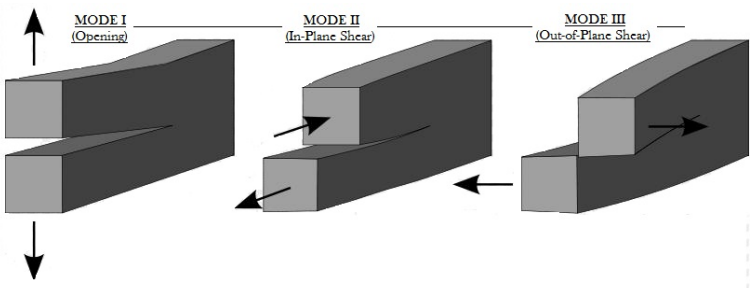

Figure 2.6: Illustration of the three modes of crack opening

Most formulae in fracture mechanics are derived considering these modes by assuming either plane stress or plane strain conditions as defined below. However, mixed-modes analyses is limited. In the case of a thick body, the plastic zone size depends on the position of the crack tip through the thickness (Figure 2.7). There is a progressive decrease in the size of the plastic zone when moving from the outer surface, where the plane stress conditions are dominant, to within the field, where plane strain conditions are dominant.

- **Plane Stress Condition**: In a thin body, the stress through the thickness (σ_{zz}) is assumed to be equal to zero ($\sigma_{zz} = 0$) because it cannot change significantly due to the thin section.
- **Plane Strain Condition**: In a thick body, the material is constrained through the thickness and strain in this direction is equal to zero ($\epsilon_{zz} = 0$) and $\sigma_{zz} = \nu \times (\sigma_{xx} + \sigma_{yy})$.

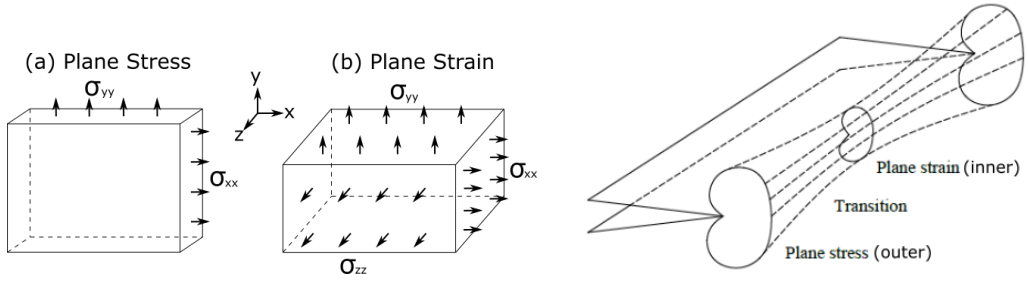

Figure 2.7: Illustration of the plane stress / plane strain conditions

For a century, a considerable amount of work has been done to study crack propagation under different loading conditions (constant and variable) and environments. Most of these studies were conducted to develop efficient characterizing parameters. One of them is fracture toughness which represents the material's resistance to fracture. In general, fracture toughness of a standard fatigue pre-cracked specimen depends on temperature, environment, loading rate, the composition of the material and its microstructure, together with geometric, thickness and constraint effects. Crack stability assessment methods have been developed in three different frameworks: Linear Elastic Fracture Mechanics (LEFM), Elastic-Plastic Fracture Mechanics (EPFM) and Limit Analysis (LA) [42]:

- **LEFM methods** are restricted to small-scale yielding configurations (i.e., geometry, loading...) for brittle materials without significant ductility or plastic zone.
- **EPFM methods** do not have these limitations but require FE techniques which are expensive and time consuming to perform to obtain correct and precise evaluations.
- **Limit analysis methods** are effective only for deeply cracked structures for which initiation and maximum load are close to each other.

In simple terms, fracture occurs when the crack driving force exceeds the material resistance to fracture. A description is given in the following subsections. The fracture toughness which can be established from a single specimen [41] in terms of any or all of the four parameters below:

- Energy release rate, G
- Stress Intensity Factor, K
- Crack Tip Opening Displacement, δ
- J-Integral, J

2.3.2 Energy release rate, G (Energy-based)

Based on the work of Griffith [43] on brittle materials in 1920s, energy release rate criterion is based on the idea is that when a crack initiates or extends, it releases energy and crack growth occurs when this energy is greater than the energy necessary to create the surface relative to this extension. Using Inglis' stress analysis [40], Griffith showed that the change of energy, U, due to a through-thickness crack in an infinitely plate equals to:

$$U_{cracked} - U_{uncracked} = \frac{-2\pi a^2\sigma^2}{E} + \frac{\pi a^2\sigma^2}{E} + 4a\gamma_s \tag{2.3}$$

where a is the crack half-length, σ the remote tensile stress, E the Young's modulus and γ_s is the surface energy of the material. Minimizing the energy in relation to the crack length gives:

$$\frac{\partial}{\partial a}\left(-\frac{\pi a^2\sigma^2}{E} + 4a\gamma_s\right) = 0 \tag{2.4}$$

That leads to σ_f, the failure stress, given as:

$$\sigma_f = \sqrt{\frac{2E\gamma_s}{\pi a}} \tag{2.5}$$

This equation is significant because it relates the size of the imperfection to the tensile strength of the material and predicts that small defects are less damaging than large ones. Irwin [44] generalized Griffith's energy approach (Eq.2.5) for ductile materials. He added plastic deformation energy γ_p to the surface energy introduced by Griffith. He concluded that rupture thus occurs for a critical stress defined by:

$$\sigma_f = \sqrt{\frac{E(\gamma_s + \gamma_p)}{b_0}} \tag{2.6}$$

He also proposed the energy release rate, based on Griffith's work, defined by the variation of the potential energy Π stored in the structure when increasing the free surface of the corresponding extension of the crack:

$$G = lim\frac{\Delta\Pi}{\Delta A} = -\frac{\partial\Pi}{\partial A} \tag{2.7}$$

where Π is the potential energy obtained by the subtraction of energy provided by external forces and the internal strain energy and A the crack area. Using the energy required to advance per unit of length by the crack, known as crack growth resistance R and the energy release rate G, the crack propagation can be defined. The so-called R-Curve is a rising curve, nearly independent of the initial crack [41], that describes that the plastic zone growth as the crack extends. The propagation may be stable or unstable, depending on

how parameters vary with crack size. It can be noted that R-curve is geometry dependent and decreases with an increasing thickness. The conditions for stable crack growth can be expressed as follows:

$$\begin{cases} G = R, \frac{dG}{da} \leq \frac{dR}{da} & \text{for stable crack growth} \\ \frac{dG}{da} > \frac{dR}{da} & \text{for unstable crack growth} \end{cases} \tag{2.8}$$

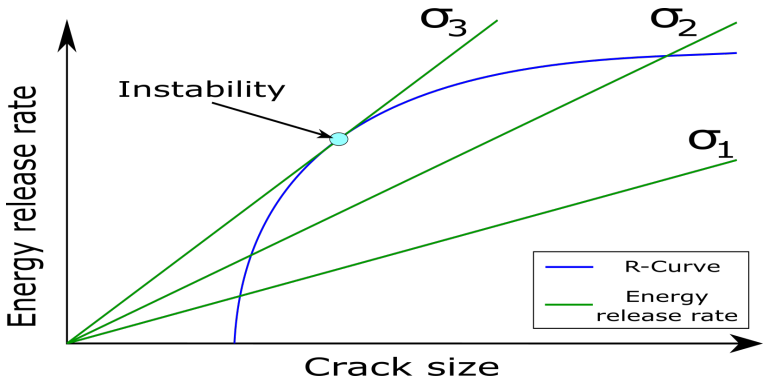

Figure 2.8: Schematic driving force vs. rising R curve

2.3.3 Stress Intensity Factor, K (Stress-based)

The stress intensity factor, K, defines the magnitude of the local stresses around the crack tip depending on loading, crack size, crack shape, and geometric boundaries. Assuming isotropic linear elastic material behaviour, some authors [45] showed that the stress field in a cracked body exhibit a $\frac{1}{\sqrt{r}}$ singularity at the crack-tip. Employing polar coordinates (r, θ) centered at the crack tip, stresses can be expressed as:

$$\sigma_{ij} = \frac{k}{\sqrt{r}} \times f_{ij}(\theta) + \sum_{m=0}^{\infty} A_m \times r^{\frac{m}{2}} \times g_{ij}^{m}(\theta) \tag{2.9}$$

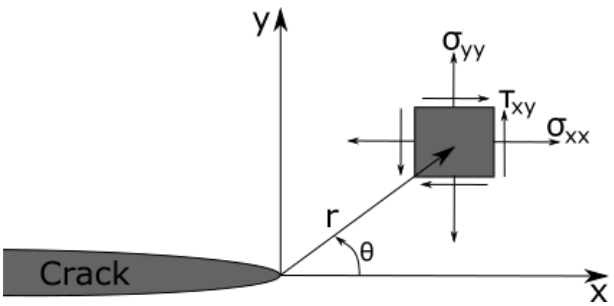

Figure 2.9: Stresses at an arbitrary distance (in terms of distance and angle) from the crack-tip under linear elastic assumptions [45]

Irwin [44] showed that it was convenient at this point to replace k by the stress intensity factor K, where $K = k \times \sqrt{2\pi}$. The $\frac{1}{\sqrt{r}}$ singularity being dominant, this led to:

$$\begin{cases} \lim_{r\to 0} \sigma_{ij}^{I} = \frac{K_I}{\sqrt{2\pi r}} \times f_{ij}^{I}(\theta) \\ \lim_{r\to 0} \sigma_{ij}^{II} = \frac{K_{II}}{\sqrt{2\pi r}} \times f_{ij}^{II}(\theta) \\ \lim_{r\to 0} \sigma_{ij}^{III} = \frac{K_{III}}{\sqrt{2\pi r}} \times f_{ij}^{III}(\theta) \end{cases} \tag{2.10}$$

He defined the stress intensity factor, K, a single parameter which characterises the stress field near the crack-tip. It is a stress-based measure proportional to the square root of the crack size, multiplied by a function Y which depends on both the geometry and the loading mode. A more general form of K is given as:

$$K = \sigma Y \sqrt{\pi a} \tag{2.11}$$

where σ is the remote stress applied to the component, a, the crack length and Y a geometrical correction factor. Many solutions for stress intensity factor have been developed for various geometries and loading to assess the Y factor and can be found in many handbooks. When the stresses at crack-tip reach a critical material value, known as K_{mat} the materials' generic fracture toughness, the crack will grow. Note that K_{Ic} is often used for brittle fracture. Irwin [44] also introduced a simple relationship between K and the elastic energy release rate G. The contributions to G from the three modes are additive because energy release rate is a scalar quantity and can be written as:

$$G = \frac{K_I^2}{E'} + \frac{K_{II}^2}{E'} + \frac{K_{III}^2}{2\mu} \tag{2.12}$$

where $E' = E$ for plane stress and $E' = \frac{E}{1-\nu^2}$ for plane strain. It is important to note that if "the three modes K" contribute to G, they are not additive to calculate the total SIF ($K_{tot} \neq K_I + K_{II} + K_{III}$). But it is possible to add different sources of stress in the same mode to obtain the total SIF ($K_{tot} = K_I^a + K_I^b + K_I^c + ...$)according to the principle of superposition [45]. However, most fracture mechanics analyses are based on K solutions for crack opening Mode I loading (K_I). So the previous relation is generally limited to:

$$G = \frac{K_I^2}{E'} \tag{2.13}$$

Fracture occurs when the driving force K_I (which is load and geometry dependent) reaches its critical intensity K_{Ic} (which is material, temperature and rate of loading dependent), the plane strain fracture toughness which represents the material resistance to fracture, expressed as:

$$K_I \geq K_{Ic} \tag{2.14}$$

However as r (defined in Figure 2.9) approaches zero, the stress at the crack-tip tends to infinity because of the singularity at r = 0. As infinite stresses cannot exist physically, the elastic solution must be modified to take some crack tip plasticity into account. This plastic zone formed permits a relaxation of stresses near the crack-tip. Westergaard [46] developed a first-order estimation of the size of the plastic zone on the axis of the crack where the presence of a plastic zone is assumed small compared to the length of the crack and yielding occurring when $\sigma = \sigma_{ys}$ the yield strength of the material. It leads to a first order estimate of the plastic zone size for perfectly elastic materials and is presented as follows:

$$\begin{cases} r_y = \frac{1}{2\pi} \times \left(\frac{K_I}{\sigma_{ys}}\right)^2 \text{for plane stress} \\ r_y = \frac{1}{2\pi} \times \left(\frac{K_I}{\sigma_{ys}}\right)^2 \times (1 - 2\nu^2) \text{for plane strain} \end{cases} \tag{2.15}$$

When yielding occurs, stresses must redistribute at the crack-tip in order to reach equilibrium. The plastic zone must increase in size in order to accommodate these forces. Irwin [47] developed the second order approximation for the confined plastic zone based on the redistribution of stresses around the crack tip. A simple force balance leads to a second-order estimate of the plastic zone size r_p:

$$\sigma_{ys} r_p = \int_0^{r_y} \sigma dr = \int_0^{r_y} \frac{K_I}{\sqrt{2\pi r}} dr \tag{2.16}$$

Integrating and solving this leads to:

$$\begin{cases} r_p = \frac{1}{\pi} \times \left(\frac{K_I}{\sigma_{ys}}\right)^2 \text{for plane stress} \\ r_p = \frac{1}{3\pi} \times \left(\frac{K_I}{\sigma_{ys}}\right)^2 \text{for plane strain} \end{cases} \tag{2.17}$$

This plastic effect, applicable only to low levels of loading when there is no generalized plasticity, is shown on Figure 2.10, coloured area (*) representing loads that must be redistributed, resulting in a larger plastic zone.

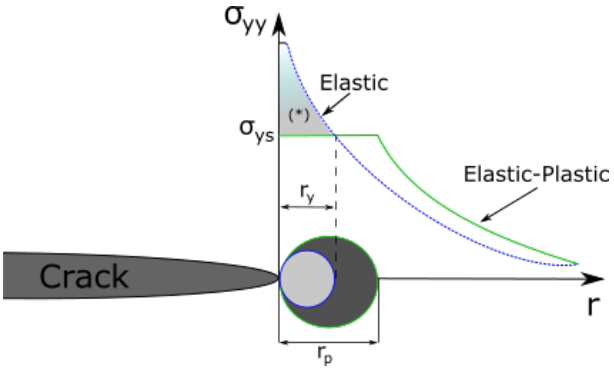

Figure 2.10: Irwin's plastic zone correction for the stresses at the tip of a crack [45]

A similar result was obtained by Dugdale [48] (Irwin's solution was $\frac{1}{\pi} = 0.318$ and Dugdale instead used $\frac{\pi}{8} = 0.392$) who developed another model known as strip yield model:

$$\rho = \frac{\pi}{8} \times \left(\frac{K_I}{\sigma_{ys}}\right)^2 \tag{2.18}$$

An important restriction to the use of LEFM (K) is that plastic zone size at the crack tip must be small relative to the crack length as well as the geometrical dimensions of the specimen or part. Otherwise, a plasticity correction is required for the stress intensity factor, K, or elastic-plastic fracture mechanics may be needed.

2.3.4 J-Integral (Energy-based)

An alternative fracture parameter, developed by Rice is called 'J' and characterizes the energy required to propagate a crack based on an integral around the crack tip. The J-Integral calculation is applicable to elastic or elastic-plastic material treated by a deformation theory of plasticity [49] and is related to the previous work of Griffith [43]. A general definition of the J-Integral can be expressed as the rate of decrease of potential energy with respect to crack area:

$$J = -\frac{d\Pi}{dA} \tag{2.19}$$

where Π is the potential energy obtained by the subtraction of energy provided by external forces and the internal strain energy and A the crack area. In case of a linear-elastic material and small scale yielding, J is assumed to be equal to G:

$$J = G = \frac{K_I^2}{E'} \tag{2.20}$$

The mathematical definition of the J-Integral proposed in 1968 by Rice [50], is calculated on a closed curve Γ surrounding the crack tip. A physical interpretation on a contour Γ, which represent any curve surrounding the crack-tip, is that the J-Integral is equal to the rate of decrease of the potential energy stored in the field surrounded by Γ when the crack grows. It describes the crack face-opening work when a flaw grows in a linear or non-linear material. The original familiar form of the J-Integral is:

$$J = \int_\Gamma \left(w dy - T_i \frac{\partial u_i}{\partial x}\right) ds \tag{2.21}$$

where u_i are displacement vector components, T_i traction vector components are defined by $T_i = \sigma_{ij}.n_j$, w the strain-energy density defined by $w = \int_0^\epsilon \sigma_{ij} d\epsilon_{ij}$ and ds and y are defined in Figure 2.11.

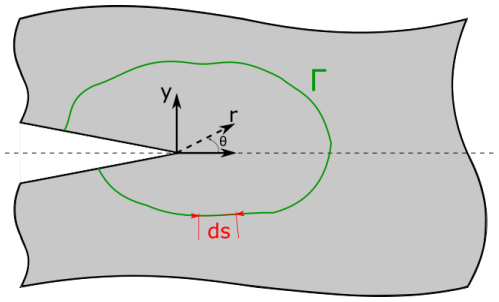

Figure 2.11: Representation of parameters in J-Integral (Adapted from [41])

An important aspect to highlight is the path-independence of J-Integral for linear elasticity [50]. This property remains true for elastic-plastic behaviour if the loading increases monotonically without unloading. J always increases with an increase of the crack length under constant load conditions, suggesting that no crack arrest is possible. As a result, the integration path can be taken through regions where the elastic-plastic state is determined with sufficient accuracy and possible sources of numerical inaccuracy (due to the possible singular state in the region surrounding the crack tip) can be avoided. Rice [50] also showed that the J-integral may be interpreted as the energy release rate on a nonlinear elastic body containing a crack per unit fracture surface area. The elastic energy release rate is defined as the rate of change in potential energy with the crack area whereas much of the strain energy absorbed by an elastic-plastic material is not recovered when the crack grows. Therefore, rather than defining the energy released from the body when crack grows, the following equation, expressed in displacement control condition, relates J to the difference in energy absorbed during load:

$$J = -\left(\frac{dU}{Bda}\right)_{\Delta} \tag{2.22}$$

where U is the strain energy, a, the crack length, B the thickness and Δ the associated load-point displacement, kept constant during partial differentiation. An alternate form has been developed by Rice [51] to evaluate the J-Integral directly from the load-displacement curve from a single specimen. This approach is relatively easy to apply in an experimental procedure and does not require multiple specimen tests. It allows J to be related the total load applied (P) or the associated load-point displacement (Δ):

$$J = -\frac{1}{B}\int_0^P \left(\frac{\partial \Delta}{\partial a}\right)_P dP = -\frac{1}{B}\int_0^{\Delta} \left(\frac{\partial P}{\partial a}\right)_{\Delta} d\Delta \tag{2.23}$$

A more general relationship for estimating the J-integral was proposed by Sumpter and Turner [52] as a sum of elastic and plastic components:

$$J = \frac{\eta_{el} A_{el}}{Bb} + \frac{\eta_{pl} A_{pl}}{Bb} \tag{2.24}$$

where B is the thickness, $b = (W - a)$ the ligament length, A_{el} and A_{pl} the elastic and plastic area under the load–displacement curve and η_{el} and η_{pl} two geometry factors dependent on a/W but independent of material properties.

2.3.5 Crack-Tip Opening Displacement (CTOD) (Strain-based)

Crack-tip opening displacement (CTOD) proposed by Wells [53] in 1963 is used to quantify fracture toughness. It represents the physical opening of the crack faces to characterize the fracture toughness. In the first instance, it was approximated for a centre-cracked plate as:

$$\delta = \frac{4}{\pi} \frac{K_I^2}{E\sigma_{ys}} \tag{2.25}$$

Two definitions of CTOD can be found in the literature: (i) the opening displacement of the original crack tip calculated from the crack mouth opening displacement (CMOD) and (ii) the displacement at the intersection of a 90° vertex with the crack edges when it comes from numerical modelling (Figure 2.12).

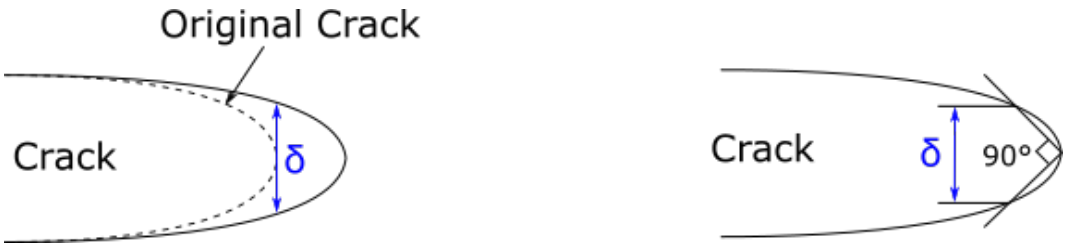

Figure 2.12: Two different definition for Crack Tip Opening Displacement (CTOD) (Adapted from [54])

Rice and Rosengren [55] showed that a general relationship can be made between J and CTOD :

$$J = m \times \sigma_{ys} \times \delta \tag{2.26}$$

where m is an empirical plastic constraint factor set as 1 for plane stress conditions and varying from 1 to 2 for actual stress states. Under linear elastic conditions ($\sigma \ll \sigma_{ys}$), fracture toughness parameters can therefore be linearly related so that they are equivalent as fracture characterizing parameters:

$$G = J = \frac{K_I^2}{E'} = m \times \sigma_{ys} \times \delta \tag{2.27}$$

CTOD is a strain-based criterion separated into two components: elastic and plastic. While the elastic part of CTOD is obtained from the stress intensity factor, K considering LEFM, the plastic component is derived from the crack mouth opening displacement

which is measured with the help of a clip gauge (See Figure 2.13). A general estimate of CTOD was proposed by Hellman and Schwalbe [56] as:

$$\delta = \frac{K_I^2(1-\nu^2)}{m\sigma_{ys}E} + \frac{[r_p(W-a)+\Delta a]V_{pl}}{[r_p(W-a)+a+Z]} \tag{2.28}$$

where a is the crack length, Δa the crack extension, Z the distance of knife edges from the front face of specimen, V_{pl} the plastic component of the crack mouth opening displacement and r_p a plastic rotation factor.

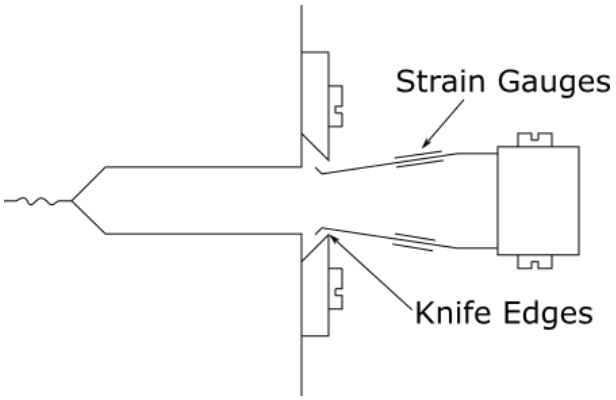

Figure 2.13: CTOD measurement using clip-gauge (Adapted from [54])

CTOD is a single parameter which also accounts for the crack-tip plasticity. From a practical point of view, CTOD is easier to conceptualise and measure compared to the similar techniques like J-integral, being a fracture parameter which has more physical meaning. However, the concept of CTOD is harder to expand the for large deformation conditions and it is easier to calculate J-integral in case of a design process using finite element modelling (FEM) techniques

2.4 Fitness-for-Service and Engineering Critical Assessment

Conventional design and fabrication codes/standards aim to ensure that the structure is safe and fabrication quality is high, assuming the components to be defect-free. Specific codes exist for a range of different engineering structures, from pipelines and bridges to pressure vessels and nuclear equipment. However, engineering structures may contain defects and mechanical properties can change over time depending on the type of the component and operating conditions [10]. Even when the components are manufactured with due care they may still contain or develop defects. As a result, many items of operating equipment may not still satisfy the original requirements after some years in

service. These defects can occur during manufacture of metal components and during service life, with different origins and are governed by various growth mechanisms as discussed in Section 2.1 (e.g. corrosion, pores, flaws, cracks or welding defects). In cases where safety is a primary issue (such as aircraft, pipelines, pressure vessels, etc.), the failure of a single part due to the presence of a defect can threaten human lives and can result in severe economic or environmental consequences. The structural importance of such defects needs to be assessed to prevent component failure during its service life. If a defect is found, an assessment is required in accordance with a recognised and codified procedure. This will determine if it should be removed, can be repaired, or whether the component has to be replaced. Conversely, some defects may be harmless and do not lead to failure during the lifetime of the component. The cost implication of replacement or repair of such defects is a financial loss and could even lead to the introduction of more significant defects. In this case, defects can be left in the component to continue its use. Five major failure modes, namely fracture, fatigue, creep, plastic collapse and corrosion have been identified as the most common phenomena in engineering structures [57]. A procedure for the Fitness-For-Service (FFS) assessment based on the principles of fracture mechanics are used to evaluate planar defects consistently through an Engineering Critical Assessment (ECA), and make rational decisions about the remaining life, whether to repair, replace a component or reduce operating conditions. For this reason, different FFS methods have been developed to cover each of these failure mechanisms.

2.4.1 Definitions

Fitness-For-Service procedure is defined [58] as a quantitative engineering analysis process incorporating calculations and assessments, which are performed to assess the structural integrity of an in-service item of a plant, containing defects or has the potential to develop defects. An item is considered to be fit for the intended service, if it can be clearly demonstrated (with acceptable safety margin) that the conditions to cause failure will not be reached within a predetermined time period or lifetime. In practice, the use of FFS procedures involves performing an Engineering Critical Assessment (ECA) of a component containing a defect to assure its structural integrity during the intended service-life or until the next planned inspection period. Generally speaking, FFS assessment methods allow the users to determine whether the structural components are safe and suitable for operating conditions, to make informed decisions in the operation (repair, reclassification, alteration or removal) to assess the remaining life of the equipment, set up inspection at regular intervals, reduce downtime and extend life time. FFS assessments are also used as a preventive measure to demonstrate the tolerance and existing safety margins for a postulated defect.

2.4.2 Assessment procedures available and application

A large survey was conducted among FFS-users in 2003 which provided an insight into FFS assessment methods available [57]. FFS procedures are applicable to most metallic structures including pressure vessels, pipelines, offshore rigs, storage tanks, ships, bridges and other structural components. Some common types of defects assessed using FFS evaluations are uniform/localized or pitting corrosion, blisters, laminations, creep, gouges/dents, cracks, fatigue or fire damages. A number of industrial sectors have established FFS standards in place for the assessment of flaws found in-service depending on the field of application (e.g. nuclear industry, oil and gas, etc.). Some of the widely used standards are:

- BS 7910 - Guide to methods for assessing the acceptability of flaws in metallic structures [1]
- FITNET - FITness-for-service NETwork [59]
- API 579-1/ASME FFS-1 - Fitness for Service [9]
- R6 - Assessment of the integrity of structures containing defects [60]

FFS assessment methods are used in different ways to assess the reliability of components. There are typically four distinct ways of using FFS assessments. In terms of design, FFS assessments can be used to determine material properties requirements or stress levels that would be suitable for the design. A defect is postulated to assess the critical condition of the new component based on NDT detection limit. It can assist in material selection, design and decision to select the appropriate NDT technique (Section 2.2). Secondly, in terms of fabrication, FFS analyses can be used to determine flaw acceptance criteria and provide guidance on the fabrication route to assure the quality of component. In-service, FFS can be used to assess the structural integrity of components when defects are detected. Criticality of defects and remaining lifetime of the component can be assessed. Thirdly, FFS can also help in deciding the repair/replacement strategy of the component, for example a reduction of the operating loads may be required in order for the component to remain in-service. It can also be used to support cases for life extension or change of service. Finally, FFS methods can also be used to investigate and clarify the root cause of failures and evolution of defects and thus avoiding similar failures in the future.

2.4.3 Input data and assessment

Traditional design codes and standards generally concentrate only on two main sets of parameters: the applied stresses and material properties, assuming a certain level of fabrication quality. However, the integrity of a structure depends on a combination of factors taking into account the actual condition (i.e. presence of defects or flaws). This is illustrated with the FFS triangle in Figure 2.14. Therefore, a typical FFS assessment requires interdisciplinary inputs for the components in-service [9]. Defects have to be identified (type, location, size, etc.) and information about operating conditions, component geometries and material properties have to be known. The quality of these inputs data has a significant effect on the value of the FFS analysis results.

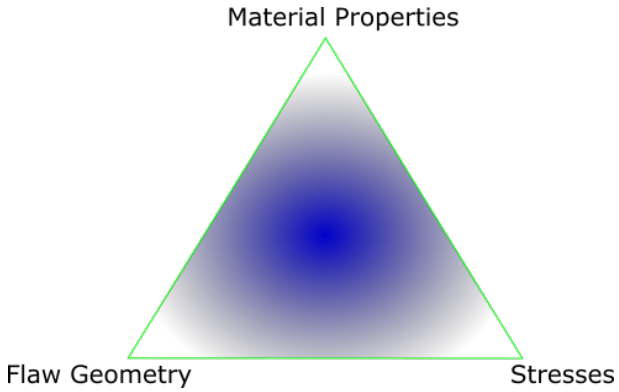

Figure 2.14: Illustration of the three factors affecting structural integrity

The following guidance is given in BS 7910 (Annexe H) [1] to report FFS assessment:

1. Provide analysis details, including the Option or Level of analysis carried out
2. Input data
   (a) Loading/operating conditions: loads (normal, transient, fault,...), temperature, environment, etc
   (b) Material properties: material spec., stress-strain data, fracture toughness, source and validity of all data, etc
   (c) Defect characterisation: type, location, orientation, shape, allowance for sizing errors, etc
   (d) Defect growth: allowance for defect extension (i.e fatigue, tearing, creep, stress corrosion), growth laws employed, etc
   (e) Plastic limit load and stress intensity factor solution employed: from published solutions or finite element analysis.

3. Results

4. Sensitivity analysis

The framework described permits to have an overview of a classical assessment procedure. Note that depending on the defects and mechanisms under investigation, additional steps may be required. In every case, care has to be taken with the input data and justification made at each step. Sensitivity analysis are undertaken to assess the effect of possible uncertainty on final results.

2.5 Pressure vessel design

Pressure vessels are widely used, both in everyday life as well as in industry, for storage and transportation of liquids or gases. They can be found in a wide range of applications from a fire extinguisher to a reactor pressure vessel (RPV) in the nuclear industry or as components of aerospace and marine vehicles. Most common are cylindrical, hence hoop(circumferential) or axial (longitudinal) stresses, and spherical (circumferential/meridional). Depending on the ratio of the wall-thickness to diameter, pressure vessels are classified in terms of design as thin- or thick-walled pressure vessels. Thin-wall theory is developed from strength of materials solutions which yields the state of stress as an average over the pressure vessel wall thickness whereas thick-wall theory is developed from the theory of elasticity which yields the state of stress as a continuous function of radius over the pressure vessel wall thickness [61]. For thin-walled pressure vessels, the wall thickness is assumed to be small compared to other dimensions. According to theory, for a wall thickness (t) and radius (R), a pressure vessels is assumed as thin-walled if $R/t > 20$. In practice, a less conservative rule is typically used and a pressure vessel is assumed to be thin-walled if $R/t > 10$ and thick-walled if $R/t < 10$. In terms of thin-wall theory, it is assumed that the hoop and longitudinal stresses are constant across the wall thickness, and the radial stress, being small in comparison with the hoop and longitudinal stresses, is negligible. This is an approximation since it will vary from zero at the outside surface to a value equal to the internal pressure at the inside surface. Note that depending on the curvature, they might also be considered to have the same behaviour as flat plates.

2.5.1 Stresses in cylindrical components

For a cylinder subjected to internal pressure, the coordinate system is cylindrical with axial, circumferential and radial direction as shown in Figure 2.15. The cylinder is defined by its inside radius (R_i), outside radius (R_o), thickness (t) and length (L). When subjected to an internal pressure (P_i), stresses develop in the cylinder. Each element of pipe is subjected to the following stresses:

- Circumferential stress (or hoop stress σ_h)
- Axial stress (or longitudinal stress σ_l)
- Radial Stress (σ_r)

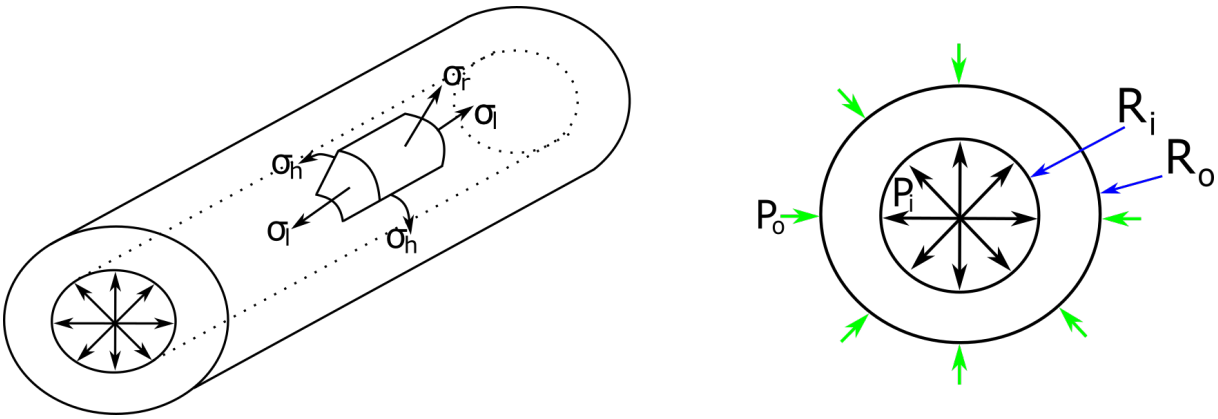

Figure 2.15: Geometry and stresses in a cylinder

The following expressions are meant for internal pressure. If the external pressure is higher, the solutions should be applied with caution because other failure modes such as instability due to wall buckling may come into play. Thin-walled cylinders are calculated by Barlow's formula and thick-walled cylinder with Lame's formula.

2.5.1.1 Stress in Circumferential Direction - Hoop Stress

Circumferential or hoop stress (σ_h) acts around the circumference of a cylinder. It is assumed to be uniform across the wall thickness. Very high hoop stress may split the pipe into two halves across any plane, including the diameter and axis of the pipe. The hoop stress at a given point in the cylinder wall can be expressed as:

- **Thin-walled cylinder**

$$\sigma_h = \frac{P_i R_i}{t} \tag{2.29}$$

- **Thick-walled cylinder**

$$\sigma_h = \frac{P_i R_i^2 - P_o R_o^2}{R_o^2 - R_i^2} - \frac{R_i^2 R_o^2 (P_o - P_i)}{r^2 \left(R_o^2 - R_i^2\right)} \tag{2.30}$$

2.5.1.2 Stress in Axial Direction – Longitudinal stress

Longitudinal stress (σ_l) is parallel to the longitudinal direction of the cylinder. It is only valid when at a distance far away from end caps where bending, non-linearities and stress concentrations are not significant. The stress in axial direction at a given point in the cylinder wall can be expressed as:

- **Thin-walled cylinder**

$$\sigma_l = \frac{P_i R_i}{2t} \tag{2.31}$$

- **Thick-walled cylinder**

$$\sigma_l = \frac{P_i R_i^2 - P_o R_o^2}{R_o^2 - R_i^2} \tag{2.32}$$

2.5.1.3 Stress in Radial Direction

Radial stress (σ_r) acts in directions coplanar with but perpendicular to the symmetry axis. In most pipe design, the radial component of normal stresses (σ_r) is negligible compared to the other two components (σ_h and σ_l). For a thick-walled pipe it may be taken equal and opposite to the gauge pressure on the inside surface, and zero on the outside surface. The stress in radial direction at a point in the cylinder wall can be expressed as:

- **Thin-walled cylinder**

$$\sigma_r = p \text{ (Generally } \sigma_r = 0 \text{ by definition)} \tag{2.33}$$

- **Thick-walled cylinder**

$$\sigma_r = \frac{P_i R_i^2 - P_o R_o^2}{R_o^2 - R_i^2} + \frac{R_i^2 R_o^2 (P_o - P_i)}{r^2 \left(R_o^2 - R_i^2\right)} \tag{2.34}$$

2.5.1.4 Discussion

The relationships presented earlier are sufficiently accurate to design cylindrical pressure components if no defect is present. But presence of defects such as presented in Section 2.1 can affect component integrity. In pressure vessels codes, various shapes are detailed including cap ends. For a comparable radius, wall thickness and internal pressure, a spherical pressure vessel is the optimum geometry with its maximum normal stress in is one half as large as that in a cylindrical one.

In a cylindrical shaped vessel, the internal pressure is resisted only by the hoop stress in “arch action” whereas in the spherical vessel, the double curvature means that all stress

directions around the pressure point contribute to resisting the pressure. However, cylindrical geometry may be more convenient to fabricate and transport. Moreover cylinder and the ends would in general expand by different level. If thick plates are used instead of relatively flexible hemispherical ends, juncture stresses would increase considerably. For this reason, the ends of cylindrical pressure vessels must be designed carefully, and flat ends should be avoided if possible.

2.5.2 Pressure vessel codes

Pressure vessels design methods can be divided into two basic categories regardless of which code is used: the Design by Rule (DBR) method and the Design by Analysis (DBA) method. In the first one, overall dimensions and loads are known and the wall-thickness is calculated in consequence. In the latter, the vessel geometry and dimensions are known and allowable loads are evaluated. The structural analysis is divided into elastic analysis and inelastic or plastic analysis depending on anticipated material behaviour. Differences between the material behaviours will be explained with reference to the stress-strain diagram. Various pressure vessels codes exist, depending on industrial regulations and laws. Amongst the most known and used there are:

- USA - ASME Section VIII-Boiler & Pressure Vessel Code (Division 1, Division 2) [62]
- EU - EN 13445 - Harmonised European code for unfired pressure vessels [63]
- UK - PD 5500 - Specification for unfired pressure vessels [12]

These codes can be applied to all pressure equipment except such pressure equipment that are critical to nuclear safety which should be designed and manufactured in accordance with specific codes not detailed here. Two main approaches are used for the design of pressure vessels. In Europe, pressure vessels have to be designed and built according to the Pressure Equipment Directive (PED), whereas the ASME Boiler & Pressure Vessel Code [62] prevails in North America. The philosophy is different between the two. Some aspects are detailed here. While PED is a European legal requirement applied for all European Union Member States, the ASME BPVC is “only” a construction standard even if it is mandatory in USA and Canada. In PED, Essential Safety Requirements have to be met. The recommendation is to follow harmonized standards (EN-13445, EN-13480, etc.) to reach PED’s requirements but other codes can be used including ASME, providing conformance with the PED can be demonstrated. Welding procedures and NDT require recognized third-party certification to meet the PED’s requirements whereas in ASME code it is approved by the manufacturer himself. Moreover the qualification of welders is valid without time limit to ASME IX whereas the welder’s certificate to EN 287-1) is only valid for 2 years. There are also differences on acceptable materials between PED

and ASME. Some authorized materials are listed in ASME Section II can also be used in harmonized standards for the PED. The British pressure vessel code, PD 5500 [12] , can be used under the PED to design and manufacture a pressure vessel. Another aspect that can differ is the safety factors to apply on material properties. Table 2.1 summarizes values of safety factors used to obtain the allowable stress for a general case. Note that different safety factors can be found in relation to the material used in the design or the application.

Table 2.1: General safety factors used in pressure vessel codes

Codes	**Value of safety factor n** (UTS/n)	**Value of safety factor n** (YS/n)
ASME Section VIII Div.1	3.5	1.5
ASME Section VIII Div.2	2.4	1.5
EN 13445-3	2.4	1.5
PD 5500	2.35	1.5

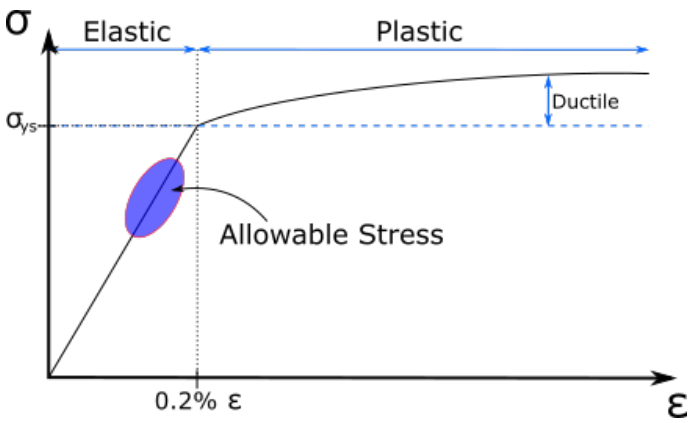

Figure 2.16: Allowable stress based on the material stress-strain curve behaviour

A study comparing the costs of pressure vessels designed using the EN 13445-3 [63] and ASME Boiler & Pressure Vessel (Section VIII) [62] codes has been carried out under a European Commission contract [64]. Nine examples of widely used pressure vessels were considered, including a gas storage tank, hydrogen reactor, stirring vessel, autoclave, water separator, air cooler header and three different types of heat exchangers. Overall it was demonstrated that EN 13445-3 offers an economically competitive design for unfired pressure vessels. Material costs are frequently greater when using the ASME code. However, savings attributable to lower material costs with EN 13445-3 are partly offset by additional costs of weld testing and NDT when compared with ASME requirements.

2.6 Summary

This literature study has covered different aspects of the subject. It has been shown that metallic components are unlikely to be defect-free. A wide range of defects can be present at different stages of their life (Section 2.1). These defects that can be introduced during fabrication or in-service due to the operating conditions might be harmful and are often covered by design codes safety margins.

Advances in knowledge of material behaviour and Non-Destructive Testing (NDT) technologies permit these defects to be predicted and detected, and can help reduce the number of defects that may occur at the different stages (Section 2.2). A better knowledge about material behaviour permits a better material selection depending on the application. Improved NDT technologies and wide use enables improvements in a component's safety. Note that as a result of methods or equipment's accuracy, they are accompanied by some uncertainty of measurement which have to be taken into account. An understanding of suitable NDT techniques is important to help evaluate the final shape and dimensions of defects. They are particularly important in a leak-before-break assessment that requires a certain monitoring of a detected defect. Both part-penetrating and through-wall defects might be assessed via conventional NDT or leak testing.

Numerous techniques are available in terms of leak detection. Conventional leak testing methods such as hydrostatic testing, visual inspection or bubble testing are only qualitative (which means they are of limited use to provide input for a LBB assessment) and offer limited leak detection capability. In terms of in-service monitoring, hydrostatic testing and visual inspection have limited practical potential. Relying on visual inspection requires large leaks in order for the change to be noticeable, and it may be hours or days before the leak is discovered. However, visual detection is widely used to detect leaks in long pipelines. These tests are used on a go/no-go basis to assure that no large leaks are present. Liquid penetrant testing permits qualitative detection and location of leaks without application of a pressure boundary however access to both sides is necessary and the measurement of flow rates is not practical. Tracer gases (or radiotracers) and Acoustic Emissions methods on another hand permit testing of the component in the same conditions as in service, or directly in-service monitoring. The former permits detection of very small leaks however, the precise detection can be difficult. The latter gives better results in identifying the location of the leak but the sensitivity range is limited and will depend on the material and fluid properties. Common practice is to use a combination of the different methods to reach the final objective of leak detection, identification of the location, and measurement of defect size and leak rate. Due to the range of sensitivity, some methods are used as pre-test to assure that no large leaks exist, more sensitive studies being carried out afterwards.

To assess these detected defects, fracture mechanics solutions have been developed (Section 2.3). Depending on the materials under investigation or assumptions made, solutions are generally divided into linear elastic (LEFM) or elastic-plastic (EPFM). Different parameters have been defined to characterise the stress field at proximity of the defects to assess their criticality. These parameters provide a link between the local crack tip response (Stress/Strain) to the global conditions (Loads, material properties, geometry). Many solutions have been derived for different cases and can be found in standards or handbook.

For unstable crack propagation to occur, the crack driving force must exceed the resistance of the material to crack growth. Fracture toughness is a critical input parameter for fracture mechanics based fitness-for-service assessments. For example some standards as BS 7910 [1] recommend to use the lowest value measured from three small-scale specimens. It can sometimes be estimated from the literature or materials properties databases but it is preferable to base this input on experimental measurement for the particular material and condition being assessed. It is important when establishing appropriate fracture toughness data that the service conditions to which the component is subject to are adequately considered including the dimensions of the crack, the section thickness, temperature, strain rate and environment.

Moreover, for particular cases, solutions can be derived using finite element analysis. Fitness-For-Service (FFS) assessments based on the principles of fracture mechanics are used to evaluate the defects consistently through an Engineering Critical Assessment (ECA) (Section 2.4). This permits to make rational decisions about the remaining life, whether to repair, replace a component or reduce operating conditions. As the concept of leak-before-break is mainly employed for pressurised components, a brief review of pressure vessel design codes is discussed in section 2.5. Depending on the design code employed, the requirement in terms of materials or geometrical dimensions might differs. This has to be taken into account while applying FFS assessment.

Chapter 3

Leak-Before-Break concept

Contents

3.1 Background

Structural integrity of components containing fluids is critical for economic, environmental and safety issues. Any risk of catastrophic failure, in either a brittle or ductile manner, is not acceptable across the majority of industries. Consequently, many efforts have been invested in the structural integrity aspect to improve the assessment methodologies of pressure containing equipment. One of the ways to aid the decision whether or not to live with the defect is through the demonstration of Leak-Before-Break (LBB). LBB is a well-established practice in the nuclear industry around the world, albeit as a defence-in-depth argument or to justify the elimination of pipe whip restraints, but it also finds applicability in other industries. The principle of Leak-Before-Break (LBB) is that a flaw in a structure will become sufficiently large to grow through the thickness of the material wall, and allow leakage of the fluid contained within the pipe or pressure vessel. The safety principle is to ensure the leak rate is sufficiently large to ensure the flaw is detected (and can then be repaired) before the flaw becomes sufficiently large to cause catastrophic global fracture of the structure. A review of the available procedures, their associated limitations and the research carried out in the last thirty years is presented below. Application of this concept within non-nuclear industries is also discussed.

Since 1950, numerous investigations have been performed to assess the mechanical and structural behaviour of pressurized components, such as loading capacity and failure behaviour of piping. One of the first few cases associated with LBB was presented by Irwin [65] in the 1960s. According to his work, leakage was predicted to occur due to an axial flaw if the defect length was less than twice the thickness of the pressure vessel. In that case, crack driving forces in the radial direction exceed those in the axial direction resulting in a through-wall crack which could exist up to a significant size without any risks of pipe burst. After that, most research on LBB has been carried out for nuclear applications. Historically, an instantaneous double-ended guillotine break (DEGB) of the largest heat transport pipe was used as the design basis in nuclear power plant, assuming that the pipe would break in a brittle manner [66]. This led to the installation of numerous pipe-whip restraints to hold ruptured pipes in place. However this criterion was restrictive [67], due to the risk of loose pipe ends jamming under certain conditions and the difficulties of carrying out inspection. Advances in fracture mechanics allowed a better understanding of piping behaviour and it has been demonstrated that postulated small through-wall flaws could be detected by leakage long before the flaws could grow to unstable sizes which might cause a DEGB [66]. For this reason, developing an alternate design criterion was necessary [68], [69]. Further studies have expanded the elaboration of LBB procedures, which were adopted in 1986 by the United States Nuclear Regulatory Commission (USNRC), for the assessments of high energy pipes in Pressurized Water Reactors (PWRs), which provided guidelines (revised in 2007 [70]) for safety evaluation

of the operating and design of Nuclear Power Plant. LBB assessment methods have contributed to a new approach of pressure equipment design. Details about guidance for the implementation, limitations and acceptance criteria for LBB were provided in the late 1980s by the American regulatory authority [70], [71], [72]. Nowadays, this criterion is widely used in the nuclear industry as either validation to remove pipe-whip restraints and jet-impingement shields or as defence-in-depth argument. Outside of the nuclear industry, LBB arguments are sometimes included as part of Fitness-for-Service (FFS) assessments.

3.2 Definition and application

The European Commission [73] defines LBB as "a failure mode of a cracked piping leaking through-wall crack which may by timely and safely detected by the available monitoring systems and which does not challenge the pipe's capability to withstand any design loading". Although inelegantly described, this concept is related to pipe failures and their safety implications and it has been presented as a way to partially relax the common requirements to the postulated DEGB failure. Fracture mechanics principles are used to demonstrate that a flaw will develop through-wall allowing sufficient and stable leakage that it can be detected before catastrophic rupture of the component occurs. This concept may therefore be applied to structures containing a fluid such as pipes or pressure vessels. LBB is applicable to ductile materials which exhibit high toughness and are fracture resistant [73]. These material properties permit a through-wall defect of a certain length to be stable under specified conditions and allow sufficient time for the detection of the resulting leak. A combination of ductile material, benign fluid environment and a reliable leak detection system is therefore necessary.

3.2.1 Basic design formulation

A basic analysis to show the balance of leak conditions and break conditions is presented in [74]. These formulations are used for the design of pressurized thin-walled structures. For example, a thin-walled cylindrical pressure vessel of radius R and thickness t is subject to an internal pressure P. In the basis of design, the maximum hoop stress cannot exceed 2/3 of the yield strength of the material ($\sigma_h \leq 2\sigma_{ys}/3$), but the theoretical thickness t to preclude yielding can be written as:

$$t \geq \frac{P \times R}{\sigma_{ys}} \tag{3.1}$$

In the case of a through-wall crack ($2a_c = t$) where a leak may be detected, the crack will remain stable if :

$$\sigma_h \leq \frac{K_{Ic}}{\sqrt{\pi \times \frac{t}{2}}} \tag{3.2}$$

where K_{Ic} is the plane strain fracture toughness. These two equations lead to a limiting pressure:

$$P \leq \frac{2}{\pi R} \times \frac{K_{Ic}^2}{\sigma_{ys}} \tag{3.3}$$

These basic conditions (more detailed procedures will be discussed in paragraph 3.2.2) are used at the design stage to select materials and they may also be used to ensure that a leak-before-break condition can be feasibly reached. Design engineers select the material yield strength and thickness according to conventional formulae of stress analysis so that the wall thickness is sufficient to withstand the internal pressure. The next step is the selection of the minimum required fracture toughness to meet the leak-before-break criterion. This is followed by the evaluation of cost of material, fabrication, certification, and other technical and economic decisions [75].

3.2.2 Detailed procedures

In a detailed LBB assessment a number of different calculations is required, including those to establish the limiting length of a through wall defect (based on well-established fracture mechanics principles) and those of crack opening area (which allows the fluid to escape). Validation of methods for the calculation of the limiting length of a through wall defect is included in the validation of flaw assessment procedures [76]. The formulation of a Leak-Before-Break argument can be explained with the aid of the following diagram (see Figure 3.1) where (1) and (2) represent the margins applied on leak detection and crack length and flowchart (see Figure 3.2).

During stable crack growth (Crack length < Critical crack length) the penetrating crack will grow to a through-wall crack and form a leak until it reaches the critical length. Catastrophic failure occurs when the crack length reaches its critical length leading to unstable crack growth assuming stresses are load-controlled (generally true for pipes containing high energy fluids). Under fatigue crack growth, defects will grow under the action of cyclic stress mainly due to changes in internal pressure or due to thermal transient load cycles. For example, circumferential defects will grow under cyclic axial stresses and are subject to axial pipe end load, internal pressure and external pipe bending moments [77].

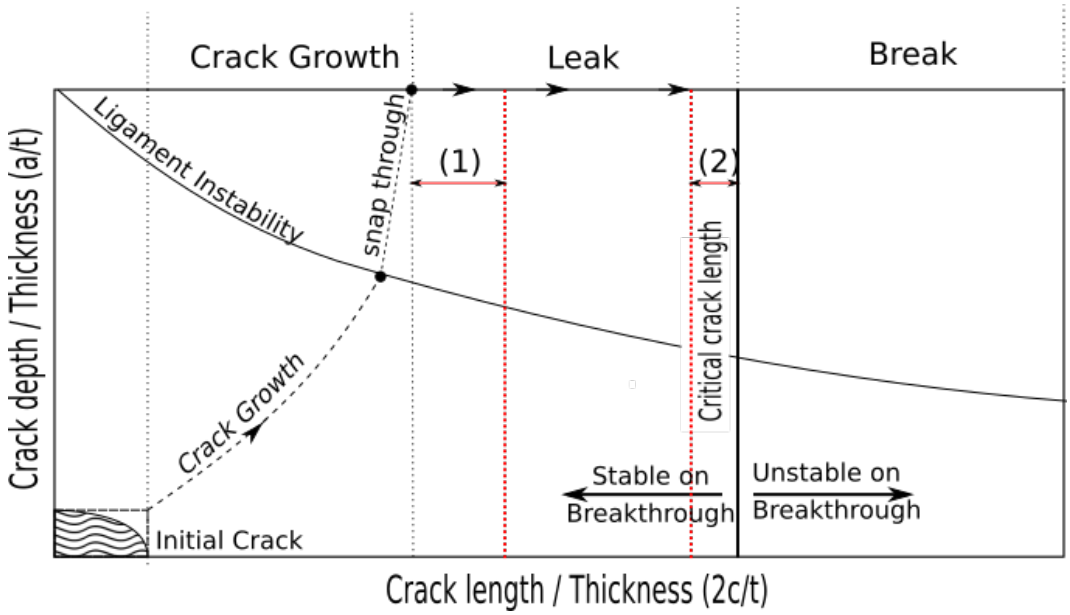

Figure 3.1: LBB Diagram based on [1] (where (1) & (2) represent margins on leak detection and crack length)

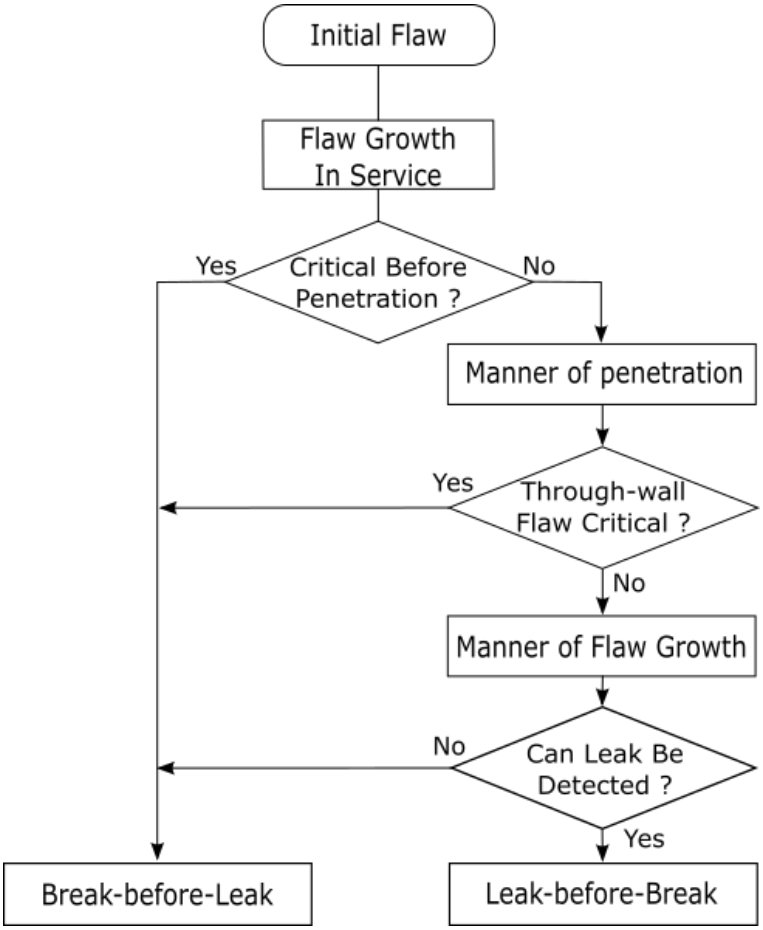

Figure 3.2: Leak-Before-Break flowchart based on [77]

Typical inputs for LBB evaluation include pipe geometry, material properties, crack morphology, cyclic loads, operating pressure and temperature. The different procedures available are explained in the next section. However, having a common origin, some major steps can be summarized as follows (from [1], [60], [78]):

1. **Characterise/Postulate the initial flaw**: Flaw dimensions have to be defined for surface or through-wall flaws. Depending on the procedure used, surface defects may be assessed in addition to through-wall defects by taking crack growth into account.

2. **Determine critical length of the through-wall flaw**: This refers to the length at which the through-wall defect becomes unstable, based on fracture mechanics calculations, assuming stresses are load-controlled.

3. **Estimate the flaw length at breakthrough**: This is carried out by calculating the surface flaw length at which ligament failure is predicted to occur and re-characterising this flaw as a through-wall flaw.

4. **Determine detectable leakage length of the through-wall flaw**: This includes calculation of the Crack Opening Area (COA) associated with the crack length and calculation of the resulting detectable leak rate appropriate to the leak detection system capabilities. Time to detect the leak should be taken into account. The leak rate may be estimated from relevant experimental data if available or computer codes which predict leakage rates for single- or two-phase flows for a wide range of through-wall defects that appropriately account for the surface roughness, number of turns, etc for the crack mechanisms of interest.

5. **Assess the results**: A case for LBB is established provided the calculations in previous steps show that:

   - the flaw length at breakthrough is less than the critical length of the through-wall flaw.
   - the time to detect the leak is less than the time for the flaw to grow to the critical length.

Guidance and established procedures are given in different standards and procedures to resolve each of these steps. Depending on the procedure used, different methodologies can be found with various levels of assessment and explicit margins may be given for each step. This will be further elaborated in Section 3.3.

3.2.3 Limitations

According to the US requirement [70], LBB methodology has to be applied to the worst location (lower material properties, higher stresses, etc.) in an entire system and should not be applied to a particular location along the pipe system alone. The initial crack may arise from different types of defect, and may grow as a result of loading or environment. However, it is generally recommended to demonstrate that certain in-service degradation mechanisms are not present: LBB is not usually applied to systems which experience excessive or unusual loads and is generally limited to piping that is not susceptible to fail from degradation mechanisms such as the following [79]:

- Water hammer
- Creep/ Creep fatigue damage
- Erosion, corrosion or erosion/corrosion
- Stress Corrosion Cracking (SCC) or Inter Granular SCC (IGSCC)
- Thermal ageing
- Brittle fracture
- Potential indirect sources of pipe rupture

Current LBB procedures only consider the case of a single crack. The scenario of multiple cracks was considered by means of Monte Carlo simulation in [80], [81]. It was concluded that this leads to a shorter leak-free time, a shorter allowable response time and that catastrophic failure may also occur without a detectable leak where a large number of initial cracks have a strong crack interaction. Therefore, a multiple crack LBB case would be analysed case by case, and in most cases would probably not be possible. In practice, many service cases of LBB occur with multiple cracks (generally due to Stress Corrosion Cracking), but how to establish the guidelines for assessment of multiple cracks is difficult. Another significant limitation is the requirement on minimum pipe radius. In order to have sufficient margin between the leakage crack size and the critical crack size, pipe dimensions have to be appropriate. In the case of a small pipe, the critical crack length may be reached before the leak detected. In terms of pressure, LBB is generally restricted to high energy components (such as in in the nuclear industry [70] Class 1 and 2, which are the classes containing the highest pressure) in order to improve the leak detection aspect. However, it may also be applied to other significant components when defence-in-depth is invoked.

3.3 Leak-Before-Break Procedures

3.3.1 Nuclear industry

In the last thirty years, LBB has received increased consideration as a criterion for assessing or upgrading the safety of existing plants [82] and has also been applied to optimize the design when large modifications were made. Various countries operating nuclear plant have developed their own procedures regarding LBB applicability taking historic and regulatory aspects into account. Two reports published by the International Atomic Energy Agency (IAEA) in 1993 and 1994 present the application of LBB in different countries [69], [83]. Other publications also provide examples of LBB applications or developments in other countries, for example France [84], [85], Belgium [86], USA [79], Canada [87], [88], Korea [89], India [90] or Czech Republic [91] where the following procedures were used with slight modifications. According to a recent report [92], published in 2012, four distinct approaches of LBB are used throughout Europe in the nuclear industry. All these approaches share some degrees of similarities:

- **Germany - Integrity Concept (IC)**:The LBB procedure is a part of the principle of break preclusion, now included in the overriding safety philosophy for the assessment and structural integrity maintenance of nuclear power plants [78]. The assessment itself is applied only to the most susceptible locations, such as welds, sections of increased load or material degradation. It employs the detectable leak rate to determine the crack size required for confident detection and compares this to the critical crack size. This deterministic approach and defence in depth argument renders probabilistic approaches unnecessary [73].
- **USA - SRP-3.6.3 [70]**: This flaw tolerance approach requires a screening criterion to be met (limitations stated earlier, Section 3.1) to ensure an incredibly low pipe break probability. Similar to other LBB procedures, the basic principle is to use the detectable leak rate to determine the crack size required for confident detection and compares this to the critical crack size to ensure suitable margins exist. LBB is only applicable to the entire section of piping, not individual components or welded joints. The LBB procedure in SRP-3.6.3 can only be applied once the reliability of the detection system has been demonstrated. The US procedure also defines margin coefficients [93]: 10 on leak detection, and either 2 on crack size or 1.4 for (normal and seismic) stresses. These margins have been defined in order to increase the degree of conservatism required in nuclear industry, and account for other uncertainties not explicitly called out in the analyses (i.e., variability of crack morphology parameters, not including cyclic effects from seismic loading on toughness, etc.). Although published in the U.S., this procedure has been adopted by some European countries [94].

- **UK - R6 [60]**: Two approaches are available. The first is a simplified 'detectable leakage approach' used in design and safety studies of a hypothetical through-wall flaw. It aims to demonstrate that a leaking flaw is detectable long before it grows to a limiting length. The second approach is a 'full LBB procedure' that considers the growth of an initial part penetrating surface flaw. In this case, it is necessary to show that the flaw penetrates the pressure boundary before it can lead to disruptive failure and that the resulting through-wall flaw leaks at a sufficient rate to ensure its detection before it grows to a limiting length at which disruptive failure occurs. Heavily based on sensitivity analyses within deterministic calculations, R6 does not apply specific safety margins. The LBB procedure in R6 can usually only be used as part of a defence in depth argument.
- **France - RCC-MRX Appendix 16**: Originally based on the American NUREG-1061 [71], LBB estimates are determined by comparing the crack size that allows the leak to be detected and that which causes component failure. This comparison is quantified by a safety factor of 2 on crack sizes and 10 on the detection capability. Some consideration of the crack dimensions are provided by taking into account different internal and external crack lengths.

According to [92], [94], the German Integrity Concept (IC) and the American Standard Review Plan (SRP) 3.6.3 form the basic foundation of LBB assessment for most countries whereas the UK and French approaches are country-specific. Besides European and USA procedures, Japan has also developed its own procedure:

- **Japan – JSME S ND1**: This guideline provides some unique features but the overall principles are consistent with those previously mentioned. Stability analysis is performed for the larger of the penetrating crack and leakage crack. Guidelines on the crack growth are given and correction of the stress intensity factor at the surface interaction has been included. A factor of 5 is applied to the leak rate and no particular safety factor is specified for the crack length or applied stresses [95].

All LBB procedures described here share the same basis and are underwritten by a large number of studies conducted in the US or Germany. However some differences are noticeable. This may be explained by the different scope of applications. While LBB has been developed in USA as a means to avoid DEGB behaviour and eliminate protections such as pipe-whip restraints and jet-impingement shields; in most European countries it has been used as a defence-in-depth argument. One important aspect to note is the difference in safety factors used. Most countries use a safety factor of 10 on leak detection and 2 on crack length (or applied stresses). Japanese guidelines recommend a factor of 5 on leak detection and 1 on crack length. In contrast, the UK procedure does not provide explicit guidance on the safety factors.

3.3.2 Other industries (Non-nuclear)

In other industries, BS 7910 and API 579 are the most comprehensive, structured and widely accepted FFS standards. They cover a broad range of equipment, and include a LBB methodology which is linked to the assessment of crack-like defects:

- **API 579-1/ ASME FFS-1 (Clause 9.5.2)** [**9**]: Guidance is given to conduct a simplified LBB assessment. Surface defects have to be re-characterized as through-wall defects. Unique Crack-Opening Areas (COA) solutions are explicitly provided for both elastic and elastic-plastic conditions in cylinders and spheres.
- **BS 7910 (Annex F)** [**1**]: LBB procedures are the same than those available in R6 (Detectable leakage approach and full LBB procedure) and guidelines are given for each step. Heavily based on sensitivity analyses, no particular margins are explicitly required.

Both API 579-1/ ASME FFS-1 and BS 7910 provide a procedure for LBB analysis based on Failure Assessment Diagrams (FADs) for evaluating critical crack sizes and three levels of assessment are available. However, there are some differences with respect to parameters such as reference stress solutions and crack-opening-area solutions, both of which can lead to different results. A notable difference is the starting point of the analysis. In API 579-1/ ASME FFS-1, the starting point is a part-penetrating defect, which is then re-characterized as a through-wall defect whereas in BS 7910, depending on the procedure used, the starting point is either a through-wall defect or a part-penetrating defect (consistent with R6). Procedures in these standards are generally limited by their applicability. The assessor is often redirected to other publications or experimental work. The leakage aspect is generally less detailed than the flaw assessment due to fields of applications of these standards. For example, guidance on leak rate calculations is not explicitly provided in API 579-1/ ASME FFS-1. The re-characterization rules used to transform surface flaws to fully through-wall flaws also differ between API 579-1/ ASME FFS-1 and BS 7910. In BS 7910, the length of the re-characterized through-wall flaw, $2c_{TW}$, will be equal to:

$$2c_{TW} = 2c_s + t \tag{3.4}$$

where $2c_s$ is the length of initial surface flaw and t the wall-thickness. In API 579-1/ ASME FFS-1, a more restrictive rule is used:

$$2c_{TW} = 2c_s + 2t \tag{3.5}$$

3.4 Applying LBB to industries other than nuclear

Some available publications provide illustrations where LBB has been applied outside the nuclear industry. A noticeable difference lies in the application of the concept. In the nuclear industry, procedures are strictly followed step-by-step, whereas outside the nuclear industry, each application seems to follow a hybrid procedure, taking aspects from various sources. Some examples are described below:

- A simple case study on a spherical helium storage vessel was conducted [96], where the loading was well within the yield limit of the material (301 stainless steel). LBB demonstrated that the critical depth of a surface defect was larger than the component thickness, for the crack lengths of interest.
- An LBB assessment of vertical cylindrical tanks for oil storage is provided in [97]. Investigations on crack growth are presented to show time margins between inspections. Critical defect length was calculated by means of simple fracture mechanics formulation and time-factor in terms of fatigue (with a safety factor of 20 on fatigue life).
- A large set of experiments were conducted on aluminium beverage cans (ratio of diameter to thickness up to 590) in [98]. A good correlation between plates and cans for axial crack growth was observed and the radial fracture toughness was minimum and constant for crack aspect ratios greater than 70.
- Fitness-for-Service assessment on an ammonia storage tank in [99] used a LBB argument in order to justify an inspection plan.
- A LBB case was compared with a fatigue analysis for an offshore structure [100]. The full development and growth of a circumferential crack in a tubular member from a long deep surface crack to final failure was presented.
- The effect of pre-straining on subsea pipelines was also studied with small/full scale testing in [101] to demonstrate that a LBB case could be made since the initial assessment failed to provide sufficient margins.
- A recent published thesis looked at LBB applications on aerospace components such as high pressure fuel lines and the fuel-to-oil cooler [102].

When LBB is used outside the nuclear field, the major steps detailed in Section 3.2 are followed. However none of established procedures such as those described in Section 3.3 has strictly been followed. Various sources are used and referred to while performing assessments and this can lead to uncertainties (under- or over-estimation) on the final results. Despite such assessment procedures being readily available in general standards such as API 579-1/ ASME FFS-1 or BS 7910, the examples listed in the previous paragraph did not appear to utilise them. It appears that there is a lack of awareness or experience with full LBB general procedures outside the nuclear industry. This might

reflect a perception that they are either too complicated to apply or not sufficiently thorough. In either case, there is a need to expose both established methods more to other industries and to continue research and continuous improvements to these procedures wherever possible.

3.5 Crack Opening Area

Crack Opening Area (COA) is a key element in a LBB assessment of pressurized components. One important parameter in a LBB assessment is the current crack length which governs the leak rate. During service or inspection, through-wall cracks can be detected with a leak within the pressure envelope. Depending on the crack geometry, the leak rate will vary and the relation between the leak-rate and the crack geometry has to be established. This link is given through the Crack Opening Area, which is used to link the leak-rate to the crack length. Therefore, for an accurate establishment between leak-rate and current crack length, the COA has to be accurately predicted for different loading conditions. Different models have been proposed to estimate the values of the COA. They can be classified into three categories:

1. Linear elastic models
2. Elastic models including a small scale plasticity correction
3. Elastic-plastic models

The use of elastic solutions is deemed conservative in terms of leak detection.

3.5.1 Analytical model

The COA is calculated in terms of the crack tip opening displacement (δ) and crack half-length (c) [103]. Most COA models for cylindrical shells are obtained from those for flat plates, with some modifications for curved shells. Using linear elastic theory for a thin-walled component, the COA is determined from the SIF as described below [104]. Its shape is often assumed to be elliptical (See Figure 3.3):

$$COA = \frac{\pi \delta c}{2} \tag{3.6}$$

A diamond-shaped profile may be more appropriate for circumferential cracks of length greater than half the pipe circumference:

$$COA = \delta c \tag{3.7}$$

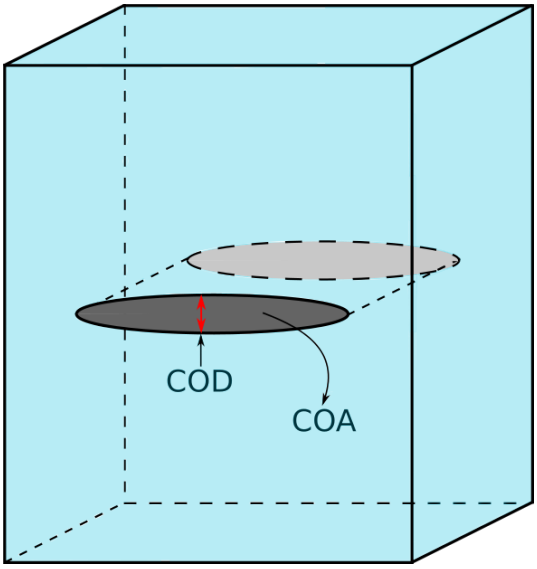

Figure 3.3: Representation of CTOD and COA

The definition for strain energy release rate (G) is related to the potential energy (U) and crack length (a). This can be replaced by two times the crack half-length (c):

$$G = -\frac{1}{t}\frac{\partial U}{\partial a} = -\frac{1}{2t}\frac{\partial U}{\partial c} \tag{3.8}$$

Membrane forces, which play a dominant role in pressure vessels and pipes, can be substituted by surface forces acting along the crack faces as presented on Figure 3.4.

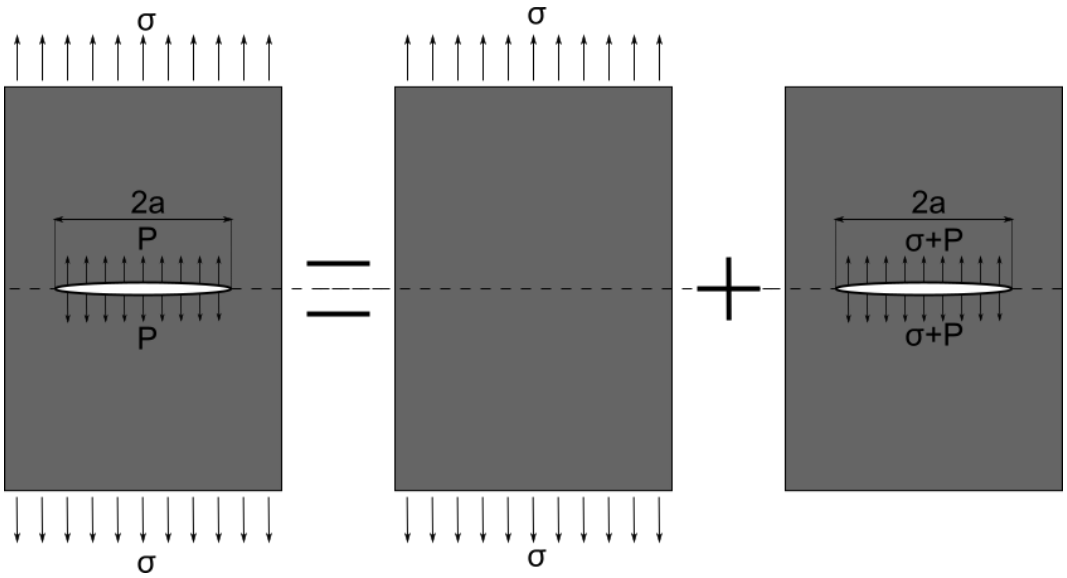

Figure 3.4: Decomposition of forces acting on the crack faces [104]

The strain energy may, therefore, be expressed in the form of the surface integral:

$$W = -\frac{1}{2}\int_{S_c} (T_i \times u_i)\, dS_c \tag{3.9}$$

where T_i and u_i are respectively the surface traction and displacement vectors. The integral extends over the surfaces S_c with non-zero forces, i.e. over the two crack surfaces. In the case of constant membrane stress, σ, and internal pressure, P, the integral becomes:

$$W = -\frac{1}{2} \times (\sigma + P)\int_{S_c} (u_i \times n_i)\, dS_c \tag{3.10}$$

The forces caused by the medium flowing through the crack are usually much lower than the membrane forces and may be neglected for thin-walled vessels. By introducing the average of COA, A, over the wall thickness, it gives:

$$A = \frac{1}{t}\int_{S_c} (u_i \times n_i)\, dS_c \tag{3.11}$$

and the relation between the strain energy release rate, G_I, and the stress intensity factor, K_I, is defined as:

$$G_I = \frac{K_I^2}{E'} \tag{3.12}$$

With this, a relation between the COA and SIF can be established:

$$K_I^2 = \frac{(\sigma + P)E'}{4}\frac{\partial A}{\partial c} \tag{3.13}$$

where E is the Young's Modulus. If the SIF is known, COA can be readily calculated from the integral:

$$A = \frac{4}{(\sigma + P)E'}\int_0^c K_I^2(x)dx \tag{3.14}$$

The derivation shown here does not take into account the fact that, for curved shell geometry, the SIF is dependent on a variable perpendicular to the shell surface [104]. This variable accounts for the bulging effect, which causes the COA to be different on each side of the shell. Using a mean value for the SIF can give an approximate value. In reality COA is affected by geometrical, material and loading parameters. There are extensive literature surveys dedicated to quantifying these effects. For a cylindrical shell, the SIF for a crack is given often expressed in the form of:

$$K_I = M(\lambda) \times (\sigma + P)\sqrt{(\pi a)} \tag{3.15}$$

where the bulging factor, $M(\lambda)$, is a function of the shell parameter which depends on the crack dimension (c), the thickness (t) and the mean radius (R_m):

$$\lambda = Coefficient \times \frac{c}{\sqrt{R_m t}} \tag{3.16}$$

Incorporating (Eq.3.15) into (Eq.3.14), the following expression for COA is obtained:

$$COA = \frac{4\pi(\sigma + P)}{E'} \int_0^a M^2(\lambda) \times a \; da \tag{3.17}$$

3.5.2 Leak rate and COA

In order to carry out an LBB assessment, it is important that the leak is detected before the crack length reaches its critical value. The minimum value of the leak rate Q_{min} is defined by the capability of the leak detection in place. This value is accompanied by a safety factor of 10 in US regulation [93] to allow sufficient margins between the crack length at leak detection and the critical crack length. Therefore the leak rate has to be sufficiently large to be detected by the leak detection system. The leak rate can be estimated as a function of the COA and the pressure difference using the following model [93]:

$$Q = C \times A \sqrt{\frac{2\Delta P}{\rho}} \tag{3.18}$$

where C is an empirical flow coefficient set as 0.6 in terms of l/sec, mm^2, MPa and kg/m^3 units. ΔP is the pressure difference, ρ is the mass density of the fluid and A is the COA, recommended to be determined by using Zahoor's or Paris-Tada's models. Another model is provided in R6 [60] for a single phase flow where C_{dis} a discharge coefficient, W and L are the crack width and length of an equivalent rectangular crack respectively:

$$Q = C_{dis} \sqrt{P \times \rho} \times W \times L \tag{3.19}$$

3.6 Past and future research in LBB

Over the last 30 years, a large number of research activities have been conducted in regards to LBB in the nuclear industry. Various experimental and analytical studies have been carried out on LBB behaviour of nuclear reactor components of non-cylindrical geometries such as tees [105], piping elbows [106], [107] and shell nozzle junctions [108], [109]. A summary of the different development and future research may be found in [94] including attempts to validate LBB using the Integrity Concept, helium environment

experiments, crack shape development, crack length, crack opening area and leak rate. A selection of other research activities is discussed in the following paragraphs.

On one aspect of a LBB procedure, fracture mechanics principles are used to assess important parameters such as crack length at which the leak will be detectable and critical crack length of a through-wall crack. Finite element modelling [110], large scale plate experiments [111] and pipe experiments [112] have been conducted to assess crack shape development. Complex shaped crack analysis can also be found in [113],[114].

On the other aspect of the assessment, fluid mechanics and fluid-structure interactions are also important parameters in a LBB assessment. In order to detect the leak, leak rates through cracks have to be evaluated to validate the leak detection system. Explicit equations for leak rates through narrow cracks (single phase flow) have been developed for four distinct flow regimes [115] using experimental work. The effect of crack morphology and surface roughness are also studied in [116],[117]. It is concluded that improper morphology parameters can result in large errors in the determination of leakage crack size, leading to possible non-conservative margins. Different software codes such as DAFCAT, PICEP, SQUIRT have been developed to calculate leak rates for various crack shapes or fluids as described in [60], [93]. A recent doctorate dissertation [118] shows the effects of thermal interaction between fluid and structure for a leaking fluid. A new finite element was presented to give a convenient way to analyse this effect quickly with good accuracy [119].

The interaction between structural integrity and fluid mechanics is evident in the crack opening area (COA) parameter. Numerous models have been developed for plates, spheres and cylinders with axial and circumferential defects. Three models are available: elastic, elastic with plasticity correction [104], and elastic-plastic models [120]. High temperature effects on the rate of change of the COA have been studied with the help of 2D finite element modelling [121]. Complex geometries such as welded attachments are also taken into account [122]. Simple plate estimations can provide conservative results, which imply that detailed FE analysis may not always be required. A large amount of work has been carried out to improve these deterministic approaches but an important effort has also been undertaken in terms of probabilistic assessments. Probabilistic assessments have been developed to strengthen deterministic assessments (i.e. ProLBB [123]) or to enlarge their applicability (i.e. xLPR (extremely Low Pipe Rupture) [124]), taking into account active degradation mechanisms, such as Primary Water Stress Corrosion Cracking (PWSCC), that are generally out of scope for a standard LBB assessment. A statistical treatment of material data, such as mechanical properties, crack resistance and fatigue crack growth curves is presented in [125]. An example of the application of a probabilistic assessment in accordance with the R6 procedure using Monte Carlo method is provided

in [126]. Application of LBB in CANDU (CANada Deuterium Uranium) reactors is given in [127] or more recently in [128] to assess delayed hydride cracking.

Recent work undertaken to assess the safety aspects of Atucha II nuclear power plant piping system under beyond design basis seismic loading [129], [130] showed surprising results. It was found significant margins due to the LBB assumption that all stresses are load-controlled while the pipe system behaved more like if it was displacement-controlled. The critical flaw size changed from 20% of the circumference with a traditional LBB analysis, to 95% when the full FE model was developed, consistent with IPIRG experimental work [131]. For circumferential flaws in a plant system, there are large margins with the established methodologies where LBB analysis are based on a load-controlled behaviour compared to detailed FE models.

As far as the continuity of LBB assessment is concerned, less work is currently being undertaken and planned to be performed [94] in the near future. Present research is generally limited to the following areas:

- Extension of COA solutions for R6 (high temperature creep and constraint effects)
- Dissimilar Metal Welds application as part of an EPRI/NRC programme
- Extension on probabilistic analysis
- Application of LBB to components which are not suitable for In-Service Inspection including weld overlay

This leaves significant scope for further research to build on the existing knowledge, particularly in the areas of comparing and optimising LBB procedures, assessing the influence of welds on LBB and transition between part-penetrating and through-wall flaws.

3.7 Discussion

LBB is widely recognised as an important methodology for supporting structural integrity safety cases in the nuclear industry. To use LBB as a fail-safe criterion, it has to be demonstrated that that any credible defect would grow through the wall in a stable way and create a detectable leak. The LBB criterion provides an extension to fracture mechanics assessment for pressurized components, by demonstrating that leakage can occur in such components for a certain time period. It is important to note that even for simple cases, LBB assessments may not be straightforward [132]. Detailed procedures are established and numerous applications as defence-in-depth or to allow the non-use of protection equipment can be found. However, performing a robust LBB assessment does not seem to be a regular practice in industries outside nuclear, despite procedures being available.

One reason for this may be that leakage of fluid through a penetrating defect will often not be tolerable, for instance, when the fluid is toxic or flammable, or its leakage has environmental consequences [133]. In the nuclear industry, processing fluids are generally water, a mix of water and air or carbon dioxide. In other industries (such as oil and gas, refinery or petrochemicals), leaking fluids are less acceptable in some circumstances due to their nature: either environmental (pollution) or safety (risk of fire or explosion) aspects cannot be accommodated with these procedures. The time-factor present in LBB procedure, which allows the crack to grow from a detectable length to a critical length, is unacceptable due to the increasing likelihood of ignition and explosion when flammable fluids leak over a period of time. However, water-based products and steam are also common fluids in refineries and these would suit LBB consideration. Another unique feature within the nuclear industry is the confinement of the components. LBB is applied mainly on primary circuit components. In other industries, for example petrochemical and/or oil and gas, fluid-carrying components are generally in the open-air. This difference has a strong influence on the leak detection capacity, since vapour cloud detection will be affected by wind and weather conditions. Insulation of components can also increase the difficulty of leak detection. As far as the fracture mechanics aspect is concerned, examples presented in Section 3.4 show that evaluations are generally limited to estimation of critical length by means of simple formulations, such as the one presented in Section 3.2. Established procedures clearly consider two aspects, namely fracture mechanics and leakage assessment. This second aspect is generally less frequently addressed.

The margins used in LBB assessments are also subject to discussion. Most of the established procedures, based on the American procedures, adopt a margin of 10 on leak detection and a margin of 2 on the crack length. However, Japanese guidelines do not apply any margins on crack length and a margin of 5 on leak detection. Some other procedures do not provide any explicit margins for LBB assessment. The higher the safety margins adopted, the more conservative the assessment will be. However it will be more difficult to satisfy LBB requirements if margins are too high. Load-controlled stresses assumption and moment reductions with the presence of large circumferential flaws also have to be considered in established LBB procedures large margins. The main use of the LBB concept is to provide grounds for the assessment to determine the stability of penetrating defects and hence to use as a forewarning of catastrophic failure for components especially when inspection is not possible or practicable. For the assessment to remain valid the calculated leakage must be detectable and the consequences must be manageable within the context of the overall safety case. It may be useful to determine an upper bound for a part-through flaw that is growing at an unknown rate. In this case, detection of a leak will be an early warning. It is also worth considering the solutions/treatments available. Reference stress and COA solutions are available for homogenous material.

However cracks are mostly found in weldments and such effects have to be taken into account.

3.8 Summary

This chapter focused in details on the different aspects of Leak-Before-Break. Most of the research on Leak-Before-Break has been carried out in the nuclear industry which requires a high level of safety (Section 3.1). This industry has also developed more established procedures (Section 3.3). Numerous situations and types of component have been studied and LBB is generally applied to pressurized components containing benign fluids such as water, steam and carbon dioxide (Section 3.6). Only a few published applications can be found in non-nuclear industries (Section 3.4), certainly due to the limitations discussed in Section 3.7. However, LBB could be further developed in some areas of these industries. When applied to non-nuclear industries, case studies did not appear to follow established LBB procedures such as those presented in API 579-1/ ASME FFS-1 or BS 7910. A mix of different sources was generally used, which could lead to non-consistent results. The margin between the smallest detectable leak size and the critical crack size must be adequate to support LBB. Reliable leak detection methods must be employed to ensure the ultimate success of the technique in order to prevent catastrophic failure.

Chapter 4

LBB parameters - Analysis of current solutions from codes

Contents

4.1 Introduction

A comparison study has been carried out to explore various concepts and standards for pressurised equipment. The objectives of this study are to review and evaluate current analytical solutions at design stage and to conduct Leak-Before-Break analyses on pipes or pressure vessels with both longitudinal and circumferential cracks.

In the first section (Section 4.2), the solutions and relevant safety factors from the most used pressure vessel codes have been evaluated to study their influence on the component thickness at design stage. Important parameters in an LBB assessment have also been reviewed and solutions available in standards and literature have been compared. As discussed in Chapter 3, LBB can be seen as two independent aspects: (i) leakage and (ii) crack stability assessment. Section 4.3 presents the comparison of available COA solutions for both longitudinal and circumferential cracks in cylindrical components. Crack stability assessment solutions are presented in Section 4.4: (i) Failure Assessment Diagram (Section 4.4.2), (ii) Stress Intensity Factor (Section 4.4.3) and (iii) Reference Stress (Section 4.4.4) solutions are discussed. Finally, different cases studies are presented in Section 4.4.5.

For illustration and comparison purpose, a case of an internal pressure of 7.5 MPa is presented. As only elastic COA are presented, the loading has to be kept low in order to reduce the possible error due to the elastic assumption. The following geometric and material parameters have been used.

Geometric parameters

Parameters	**Internal Radius** (R_i)	**Thickness** (t)	**Length** (W)	**Ratio** $\frac{t}{R_i}$
Values	400 mm	20 mm	1000 mm	0.05

Material parameters

Parameters	**Yield Stress** (σ_{ys})	**Ultimate Tensile Stress** (σ_{uts})	**Young's Modulus** (**E**)	**Poisson ratio** (ν)
Values	450 MPa	530 MPa	210000 MPa	0.3

For every solutions presented, a Matlab script has been developed. This allowed to calculate each solutions independently or a full assessment.

4.2 Comparison of formulae for wall-thickness determination

Various pressure vessels design codes are available across the industries. They aim to ensure the component can operate in safe conditions. While the philosophy is similar for all codes, solutions and safety factors provided may differ. As discussed in Chapter 2, pressure vessels have to be designed and built according to the Pressure Equipment Directive (PED) in Europe and ASME Boiler and Pressure Vessel Code in North America. An example of the required wall-thickness calculation using the Design by Rule (DBR) method where the overall dimensions and loads are known is given in this section. Procedures provided by the following codes have been used:

- ASME Section VIII-Boiler & Pressure Vessel Code (Division 1, Division 2) [62]
- EN 13445 - Harmonised European code for unfired pressure vessels [63]
- PD 5500 - Specification for unfired pressure vessels [12]

Table 4.1 lists the different solutions provided by various design codes to calculate the required thickness in cylinders. Also included is the equilibrium equation. Solutions from the codes are compared against the hoop stress equation assuming a maximum stress equal to the yield stress. This will represent the minimum thickness at which plasticity is reached for a given pressure. Distance from this limiting thickness is calculated for each code in order to show the margins applied.

Table 4.1: Required thickness for thin-wall cylinder according to different pressure vessel codes

Codes	Equations (Cylinder, internal pressure)	Conditions
ASME Section VIII Div.1	$t = \frac{PD_i}{2.E.S-1.2P}$	$P < 0.385SE$
(UG-27 + Appendix 1)	$t = \frac{D_i}{2}\left(\sqrt{\frac{SE+P}{SE-P}} - 1\right)$	$P > 0.385SE$
ASME Section VIII Div.2	$t = \frac{PD_i}{2S-P}$	$P < 0.4S$
(AD-201)	$t = \frac{D_i}{2}\left(\exp\left(\frac{P}{2}\right) - 1\right)$	$P > 0.4S$
EN 13445-5	$t = \frac{PD_i}{2ES-P}$	– – –
PD 5500	$t = \frac{PD_i}{2S-P}$	– – –
Cylinder (equilibrium equation)	$t = \frac{PD_i}{2\sigma_{ys}}$	– – –

4.2.1 Calculations of the required thickness

In order to calculate the minimum thickness required, it is necessary to determine the allowable stress based on material properties and safety factors (See Table 2.1). Table 4.2 provides details of allowable stresses, S, for each code using minimum tensile material properties and general safety factors (SF_{ys}, SF_{uts}) as described in Eq.4.1. The allowable

stress to consider for design is defined as:

$$S = min\left(\frac{\sigma_{ys}}{SF_{ys}}, \frac{\sigma_{uts}}{SF_{uts}}\right) \tag{4.1}$$

Table 4.2: Allowable stress calculation

Codes	UTS/SF	YS/SF	Allowable Stress (S)	Units
ASME Section VIII Div.1	151.43	300	151.43	MPa
ASME Section VIII Div.2	220.83	300	220.83	MPa
EN 13445-5	220.83	300	220.83	MPa
PD 5500	225.53	300	225.53	MPa

Once the allowable stresses have been determined, the minimum required thicknesses can be calculated with the different equations given in Table 4.1. Internal diameter is assumed to be equal to 800 mm (consistent with dimensions given in Section 4.1), the weld efficiency factor, E, equals to one and the internal pressure ranges from 1 to 20 MPa. Results are presented in Figure 4.1 for an increasing internal pressure and Table 4.3 for four selected pressures. The y-axis represents the minimum required thickness calculated for each code normalized to the thickness calculated with the equilibrium equation.

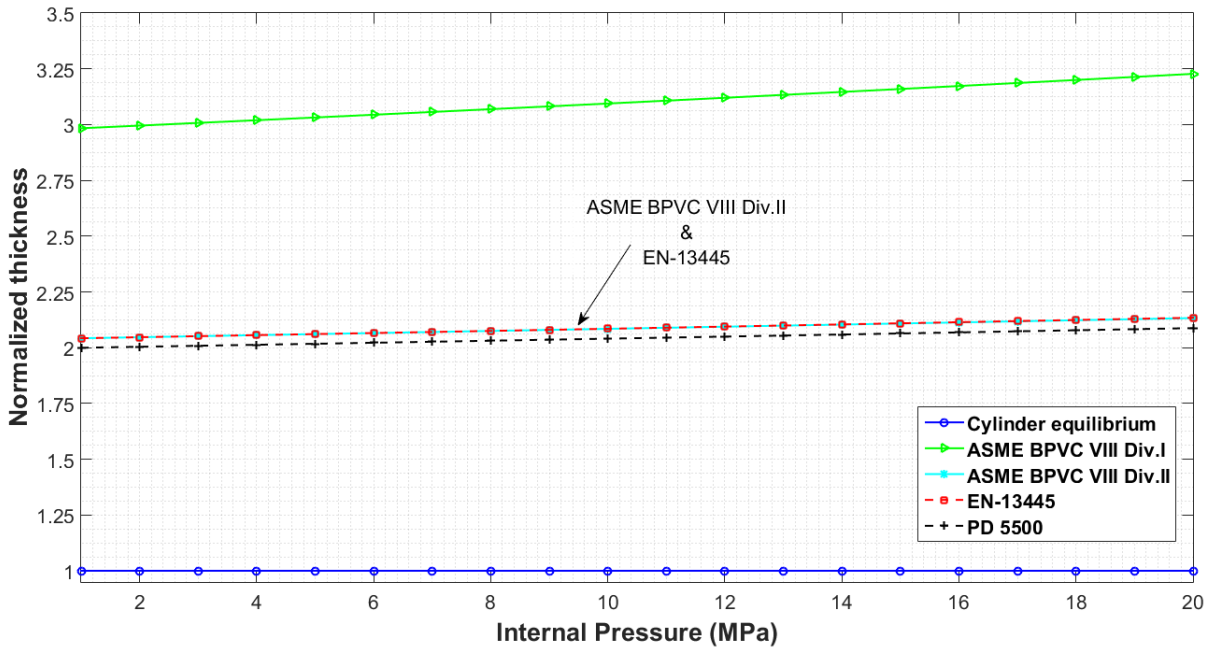

Figure 4.1: Required thickness for different internal pressure normalized to cylinder equilibrium solution

Table 4.3: Required thickness for four internal pressure normalized to cylinder equilibrium solution

Codes	P=2 MPa	P=5 MPa	P=10 MPa	P=20 MPa
ASME BPVC VIII - Div I	3.00	3.03	3.09	3.23
ASME BPVC VIII - Div II	2.05	2.06	2.08	2.13
EN-13445-3	2.05	2.06	2.08	2.13
PD 5500	2.00	2.02	2.04	2.09
Cylinder Equilibrium	1.00	1.00	1.00	1.00

4.2.2 Discussion

Depending on the design code used, safety factors applied to the yield or ultimate stress have an significant impact on the allowable stress as well as on the minimum required thickness. A large amount of comparison work has been conducted between the different codes to update their procedures and to be consistent with each other, which has led to identical values obtained using ASME BPVC Section VIII-Div.II, EN-13445-3 and PD 5500. On the other hand, ASME BPVC VIII-Div.I is known to provide more conservative solutions and higher safety margins, thus requiring a greater minimum thickness. The value of thickness is greater as per ASME BPVC Section VIII-Div.I. This is due to the safety factor used which reduces the allowable stress.

The thickness of the component at a design stage has a great importance in terms of leak-before-break assessments. As seen in Section 3, early concepts were based on the defect size and thickness of the wall. Another remark is that for a given defect size, the fracture behaviour is dependent on the thickness. For a thin structure containing a surface crack, the collapse limit of a ligament is usually the main cause of structure rupture. On the other hand, for a thicker structure, brittle fracture will have to be considered. In a two-parameter assessment such as Failure Assessment Diagram described in the following sections, this can have a significant effect. The final results will be more or less dependent on the couples stress intensity factor/fracture toughness or reference stress/yield strength parameters.

4.3 Comparison of widely used COA models

As discussed in Chapter 3, Leak-Before-Break assessment procedures consider two independent aspects to the potential failure which are respectively fracture mechanics and leakage assessment. On the leakage side of the assessment, one of the main parameters is the calculation of the crack opening area (COA). This parameter links the fracture mechanics side of the assessment to the leakage side. It allows the user to investigate the leak rate to ensure the crack detection or to show that the jet forces do not exceed a critical value. The determination of leak rates is crucial for cracked pressure vessels and pipes and requires the evaluation of the COAs. This has been a widely focused area of research resulting in a wide range of models. This part of the assessment method review focuses on three different elastic models that are available in BS 7910 [1] and API 579-1/ASME-FFS-1 [9] as well as models from the literature recommended by the USNRC guidelines [93]. Both longitudinal and circumferential models are discussed. Plasticity for small scale yielding is also discussed. Equations for the crack opening area discussed in this section are provided in Annex B.1.

4.3.1 Axial cracks

Axial cracks cracks develop along the longitudinal axis of the component. A representation of the different geometrical parameters is given in Figure 4.2. R_i, R_m and R_o being the inner, mid-thickness and outer radius respectively, $2a$, the crack length and δ the crack opening displacement. Considering a long pipe under internal pressure, the membrane stress equals to the hoop stress with the following definition:

$$P_m = \frac{PR_m}{t} \tag{4.2}$$

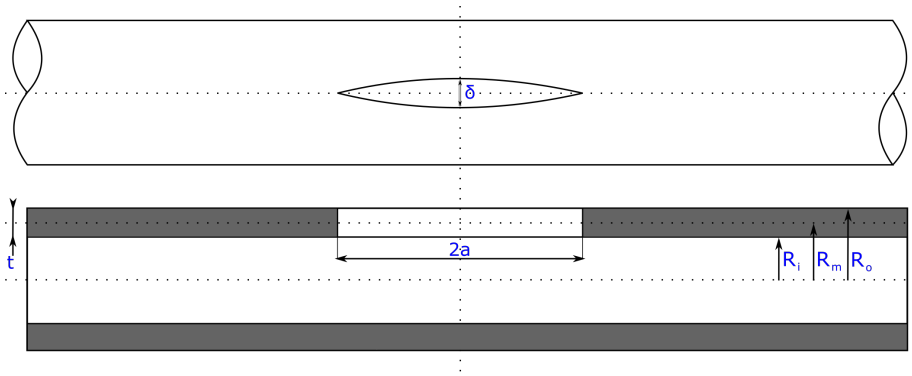

Figure 4.2: Schematic representation of a pipe with a longitudinal through-wall crack

Results of the COA calculations for pipes/cylinders containing axial through thickness defects using the three models discussed earlier are given in Figure 4.3. The x-axis represents crack length, $2a$, normalized to component's length, W, and the y-axis represents the resulting COA. Results are plotted up to the limit of applicability of BS 7910. Note that BS 7910 and Zahoor [134] give unique solutions at mid-thickness, representing the average COA through-thickness. On the other hand, API 579-1/ASME FFS-1 provides solutions for both inner and outer surface. Both BS 7910 and Zahoor's solutions produce similar results at mid-thickness until half of the limit of applicability. These results are also coherent with API 579-1/ASME FFS-1 solutions at inner and outer surfaces. However, when approaching this limit, both solutions tend to give a slightly greater COA. The values from BS 7910 solution approach those of API's solutions at the outer surface. The effect of plasticity have been also evaluated for these axial models (See App.B). Only elastic models are presented and compared against each other in this section. These are known to under-estimate the COA for ductile materials.

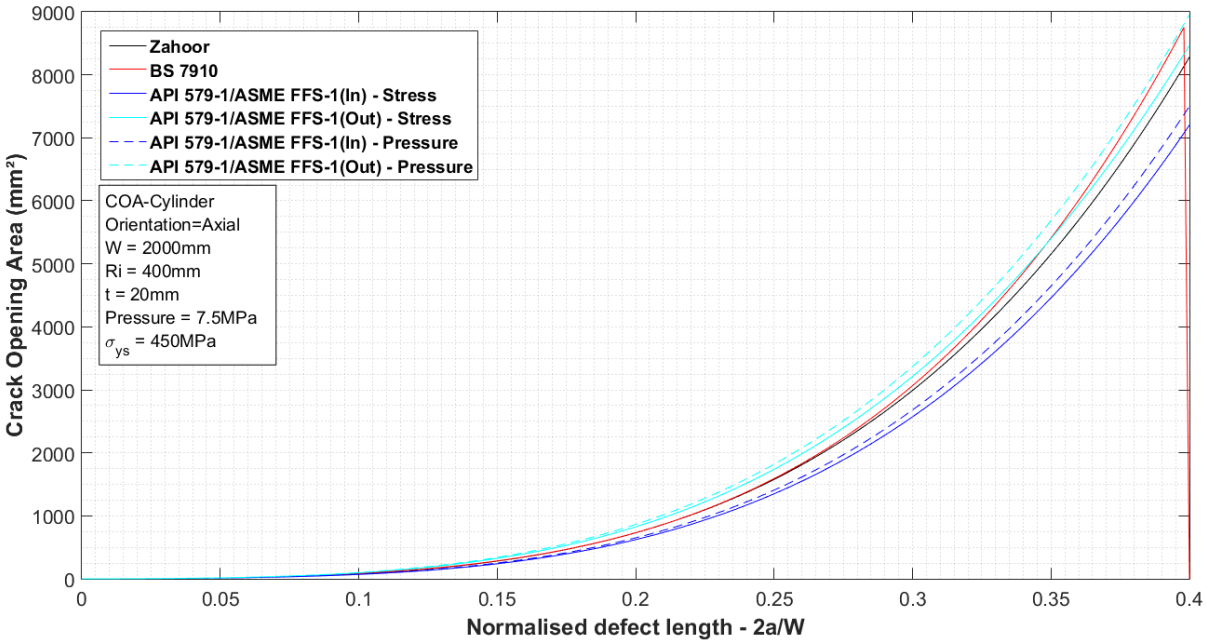

Figure 4.3: Comparison of elastic COA solutions for a longitudinal through-wall crack from API 579-1/ASME FFS-1, BS 7910 and Zahoor

4.3.2 Circumferential cracks

Circumferential cracks cracks develop along the axis of revolution of the component. A representation of the different geometrical parameters is given in Figure 4.4. R_i, R_m and R_o are the inner, mid-thickness and outer surface radius respectively, $2a$, is the crack length and δ is the crack opening displacement. Considering a long pipe under internal pressure, the membrane stress is assumed to be equal to the longitudinal stress with the

following definition:

$$P_m = \frac{PR_m}{2t} \tag{4.3}$$

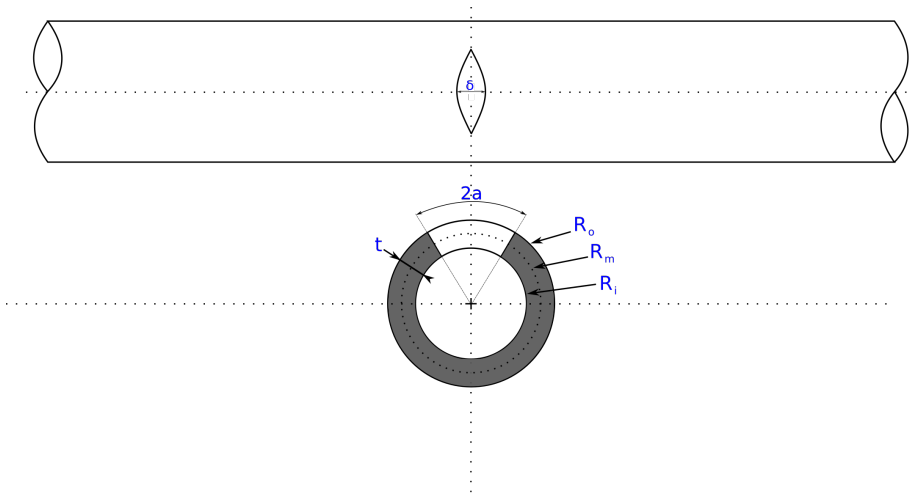

Figure 4.4: Schematic representation of pipe with a circumferential through-wall crack

The results of COA calculations for pipes/cylinders containing circumferential through-thickness defects from the three models discussed earlier are summarised in Figure 4.5. The x-axis represents the crack length, $2a$, normalized to the component's circumference, $2\pi/R_m$, and the y-axis represents the calculated COA. Results are plotted up to the limit of applicability of BS 7910. Note that both BS 7910 and Paris-Tada give an unique solution at mid-thickness, representing the average COA through-thickness. On the other hand, API 579-1/ASME FFS-1 provides solutions for both inner and outer surfaces. As for the axial case, both BS 7910 and Paris-Tada solutions give coherent results as that of API 579-1/ASME FFS-1 solutions until half of the applicability limit. After this, the solutions tend to provide a lower COA values. All over the range, Paris-Tada model is similar to BS 7910 but slighly lower. When approaching this limit, both solutions tend to give a slightly greater COA. BS 7910 solution produces the same values os those of API's at the outer surface. It can be seen that BS 7910's solution is well comprised between the two bounds defined by API 579-1/ASME-FFS-1's solutions.

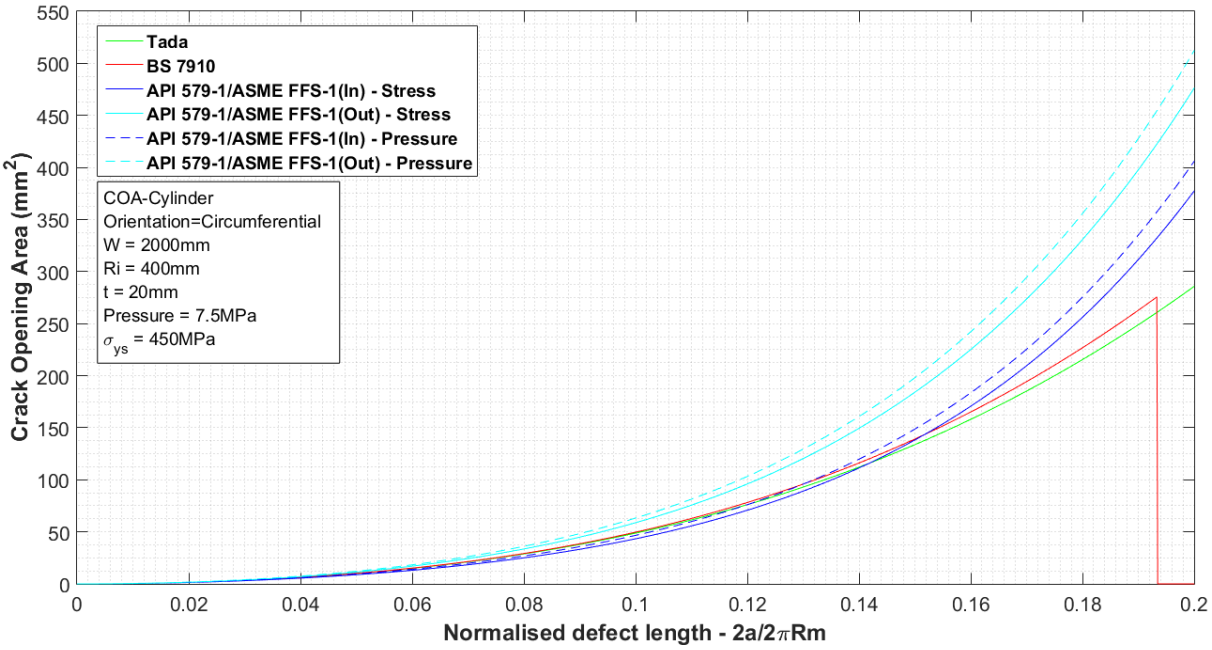

Figure 4.5: Comparison of COA solutions for circumferential through-wall crack from API 579-1/ ASME FFS-1, BS 7910 and Paris-Tada

4.3.3 Discussion

Crack Opening Area models for both axial and circumferential cracks have been compared. In both cases, BS 7910 and the recommended solutions from the USNRC report provide an averaged COA solution at mid-thickness whereas API 579-1/ ASME FFS-1 solutions are available for inner and outer surfaces. The pressure based equations in API 579-1/ ASME FFS-1 solutions,always give a slightly greater values than stress based equations. All solutions are coherent up to about half of the limit of applicability. After this limit, solutions begin to diverge. For a given axial crack, BS 7910 and Zahoor solutions tend to give a greater values with a COA at mid-thickness which is similar to API 579-1/ ASME FFS-1 at the outer surface. For circumferential cracks, BS 7910 and Paris-Tada solutions tend to give lower values than that of API 579-1/ ASME FFS-1 with a COA at mid-thickness lower than API 579-1/ ASME FFS-1 at the inner surface.

The effect of plasticity has been evaluated for axial models. BS 7910 and Zahoor models include correction factors for small-scale yielding while API 579-1/ ASME FFS-1 propose a correction factor based on the plastic collapse. This results in a wider range of application for the latter. It is important to remember that the COA solutions are required to determine leak rate, which is a critical parameter in LBB assessment. An over-estimation of the COA can lead to a non-conservative result (assuming there will be sufficient leakage that could be detected when in reality there is very little) and inversely an under-estimation could lead to a very conservative result. Elastic models are presented here. These are known to under-estimate the real COA for ductile materials. For the

same crack length, the COA for circumferential defects is smaller. This explains why circumferential defects are more critical in a LBB assessment than longitudinal defects. For the same defect length, it will be easier to detect the leak from a longitudinal defect than from a circumferential one.

4.4 Comparison of crack stability assessment solutions

4.4.1 Introduction

Defect assessment procedures such as API 579-1/ASME FFS-1 [9] or BS 7910 [1] can be used to assess the integrity of structures containing flaws, for example pipelines or pressure vessels. The procedures used to assess crack-like flaws require the calculation of the likelihood of failure by both fracture (brittle or ductile) and plastic collapse. In both standards, the interaction between the two is expressed by the use of a Failure Assessment Diagram (FAD). This diagram plots the proximity to fracture (via the fracture ratio, K_r) vertically, and the proximity to plastic collapse (the collapse ratio L_r) horizontally, and an interaction line between the two. An assessment point inside the line is safe, while outside the line is potentially unsafe. Different assessment levels or options are available depending else on the level of qualifications of the assessor or the data available. A default FAD is presented in Figure 4.6

With the use of high toughness materials and relatively low wall-thickness, fracture tends to be a less concern than plastic collapse in modern pipes and pressure vessels. The reference stress solutions used to assess the likelihood of failure by plastic collapse should be safe, but as accurate as possible. With plastic collapse being the subject of recent research, FAD Option 1 equation has been modified in the new BS 7910:2013. This section presents the evaluation of the FAD (Section 4.4.2), SIF (Section 4.4.3) and RS (Section 4.4.4) solutions provided in both procedures.

4.4.2 Failure Assessment Diagrams

One of the ways to assess the safety of structures containing flaws is to evaluate the interaction between the likelihood of failure by both fracture (brittle or ductile) and plastic collapse. In both standards, this is expressed by the use of a Failure Assessment Diagram (FAD). It allows users to assess the critically of a given flaw. Different assessment levels or options are available. Following some harmonization with R6 procedure, BS 7910:2013 offers now three alternative routes, known as “Options”, to carry out frac-

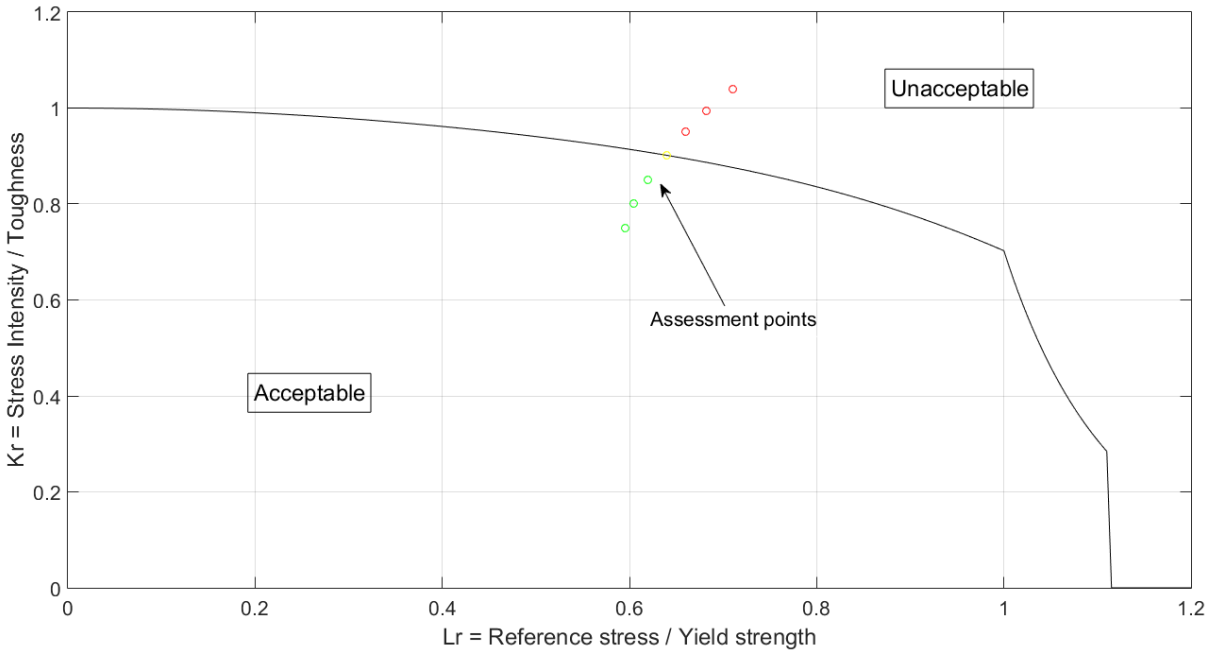

Figure 4.6: Default Failure Assessment Diagram

ture assessments. Option 1 requires basic information and is divided into continuous or discontinuous yielding material, whereas Option 2 requires full stress-strain data for the material under consideration. Option 3 which is recommended for specific cases as an alternative to the two previous, but requires both elastic and elastic-plastic analysis with the aid of numerical analysis to derive crack driving forces. The current edition of API 579-1/ASME FFS-1 offers three "Levels" depending on the available material properties and assessor skills. Level 1 is a quick screening method for the assessment, whereas Level 2 is a more sophisticated analysis using a generic FAD. A Level 2 analysis requires stresses in terms of membrane and bending components and partial safety factors are applied to the independent variables to account for uncertainty. Level 3 offers five methods to provide the best estimate of structural integrity including a method using material's specific FAD similar to BS 7910's Option 2 or elastic plastic analysis similar to Option 3.

The different routes to calculate FADs are presented below. It is worth noting that the equation of API's FAD for a Level 2 assessment is the same than the one in previous edition of BS 7910 (2005). BS 7910 Option 1 (Eq.4.4) and API 579-1/ASME FFS-1 Level 2 (Eq.4.5) can be regarded as equivalent in terms of data requirements. However, it can be observed that BS 7910 formulation is dependent on material properties while API's is only defined via L_r.

BS 7910:2013 (Option 1):

$$K_r = \begin{cases} \frac{0.3+0.7e^{-\mu L_r^6)}}{\sqrt{1+0.5L_r^2}} \text{ for } L_r \leq 1 \\ f_1(1) \times L_r^{\frac{N-1}{2N}} \text{ for } 1 < L_r < L_{rmax} \\ 0 \text{ for } L_r \geq L_{rmax} \end{cases} \tag{4.4}$$

where N is the work hardening coefficient and μ defined by $\mu = \min\left(\frac{0.001E}{\sigma_{ys}}, 0.6\right)$.

API 579-1/ASME-FFS-1:2007 (Level 2):

$$K_r = \begin{cases} \frac{0.3+0.7e^{-0.65L_r^6}}{1-0.14L_r^2} \text{ for } L_r < L_{rmax} \\ 0 \text{ for } L_r \geq L_{rmax} \end{cases} \tag{4.5}$$

In both codes, the cut-off value in terms of Load Ratio is defined in the same way as:

$$L_{rmax} = \frac{\sigma_{flow}}{\sigma_{ys}} \tag{4.6}$$

Parametric studies show the influence of Young's modulus (Figure 4.7), yield strength (Figure 4.8) and ratio of yield strength to ultimate tensile strength (Figure 4.9) on the FAD's shape. In most cases, BS 7910 FAD curve tends to be slightly lower for $0 < L_r < 0.8$, higher for $0.8 < L_r < 1$ and lower for $1 < L_r$ than API 579-1/ASME FFS-1. This allows potential larger flaws in the region just before plasticity when using that of BS 7910, while more conservatism is applied when $L_r > 1$.

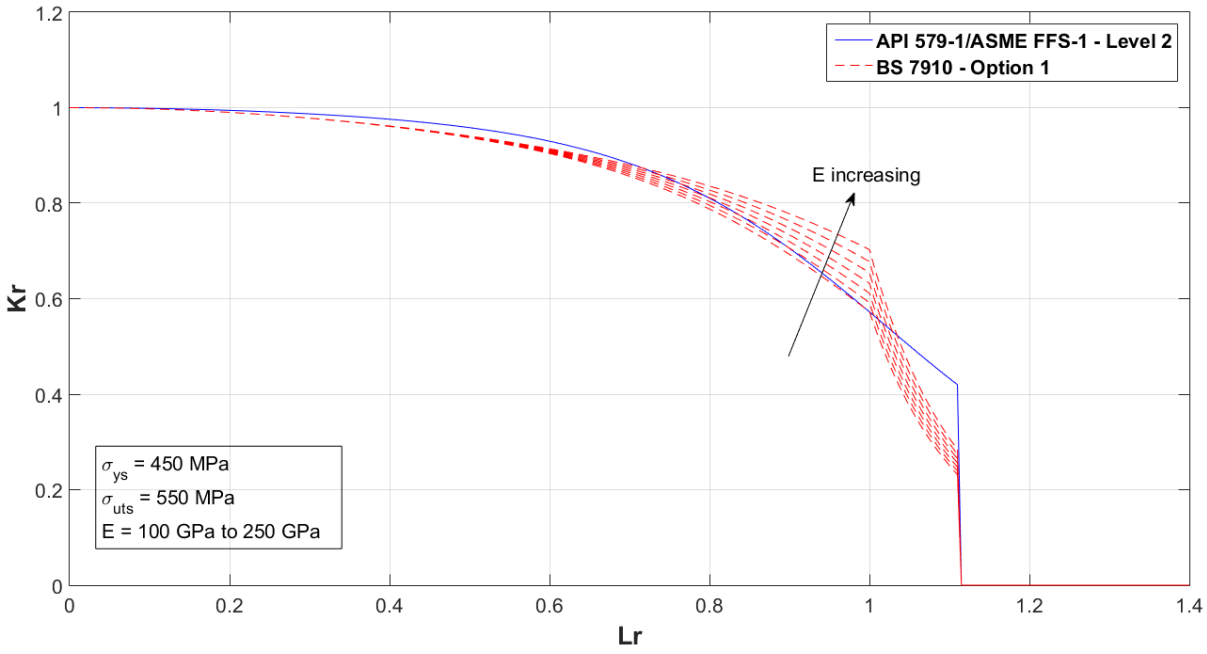

Figure 4.7: Influence of the Young modulus (E) on the shapes of FADs

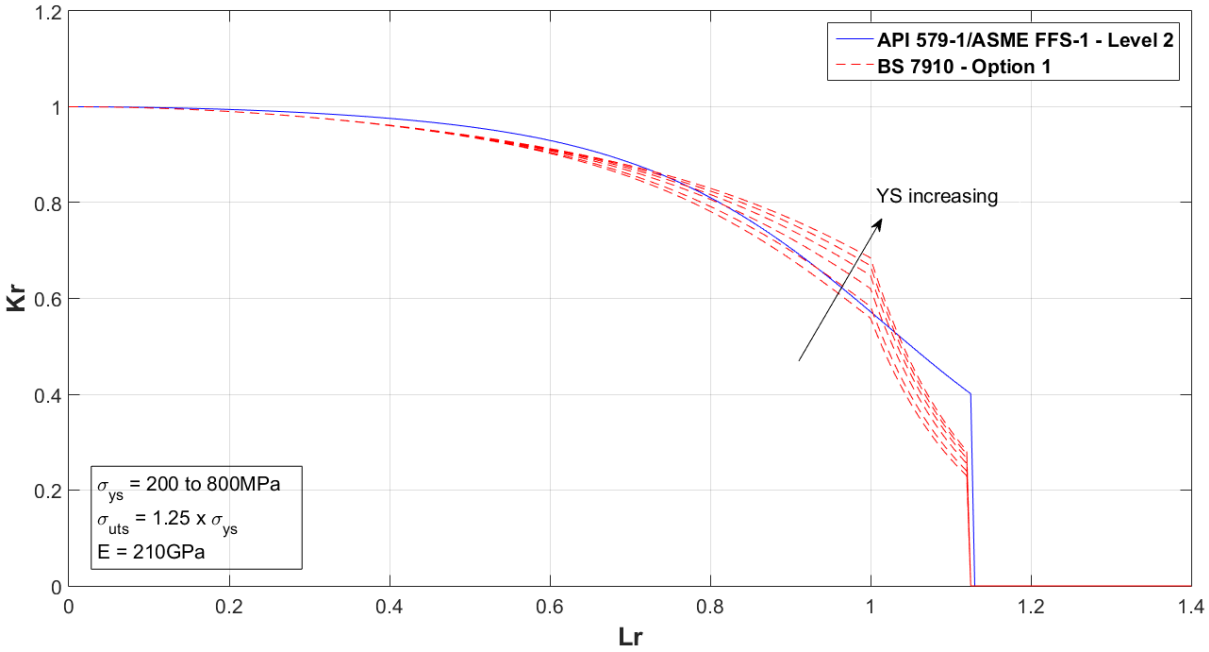

Figure 4.8: Influence of the Yield Stress (YS) on the shapes of FADs

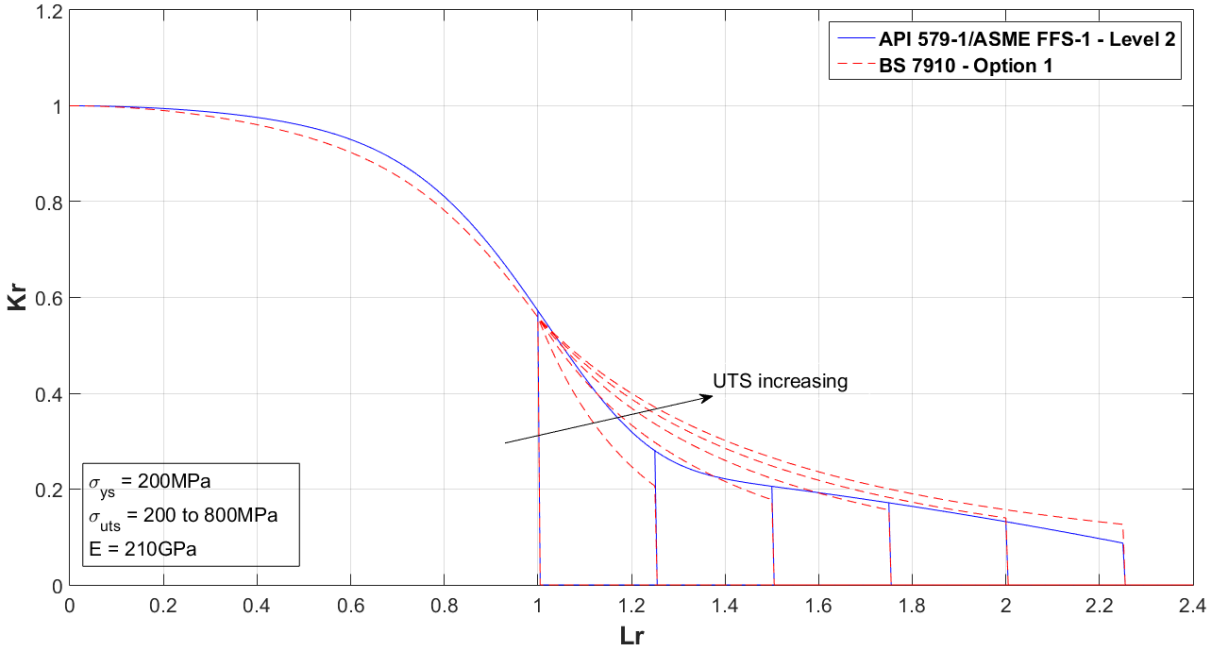

Figure 4.9: Influence of the ultimate tensile strength (UTS) on the shapes of FADs

4.4.3 Stress Intensity Factor solutions

Stress Intensity Factor, K_I, solutions for a wide range of geometry and loading configurations are available in many handbooks or standards. Alternatively, numerical analysis methods may be used to derive solutions. This helps to establish the state of the stress at the location of a crack. A comparison of SIF solutions for various geometries can be found in Ref.[59]. For this reason, only solutions for an axial through-wall crack in a cylinder will be presented and calculations provided in this section. Some remarks will be added to assist the understanding of the assessment method.

Stress Intensity Factor solutions are functions of the applied primary stresses (P_m, P_b), the defect size ($2a$, $2c$) and the structural dimensions (t, W, R_i). Procedures as API 579-1/ASME FFS-1 or BS 7910 contain solutions for many crack geometries that are likely to occur in large range of components including pressurized components. All the SIF equations from API 579-1/ASME FFS-1 or BS 7910 can be found in Annex B.2

Axial through-thickness flaws

Axial through-thickness defects are defined in the same way in both standards. Geometrical parameters such as crack length ($2a$), internal radius (R_i), length (W) and thickness (t) are required. Geometrical parameters are presented in Figure 4.11.

The results of SIF calculations for pipes/cylinders containing a through-thickness defect are summarised in Figure 4.10. All solutions provided similar results. Table 4.4 provides the numerical values for some crack lengths. BS 7910 solution has been taken as reference and compared with API solutions. A maximum difference up to 4% for the stress input solution and up to 2% for the pressure input solution can be observed on the range of study.

Table 4.4: Stress Intensity Factor solutions from API 579-1/ASME FFS-1 and BS 7910 for an axial through-wall crack

2a/W	BS 7910 Eq.B.35 K_I $(MPa.\sqrt{mm})$	API 579-1 Stress - Eq.B.33 K_I $(MPa.\sqrt{mm})$	Diff. (%)	API 579-1 Pressure - Eq.B.36 K_I $(MPa.\sqrt{mm})$	Diff. (%)
0.05	1575.6	1587.6	-0.8	1579.5	-0.2
0.1	2576.4	2668.9	-3.6	2622.3	-1.8
0.25	4949.7	5093.1	-2.9	4973.2	-0.5
0.5	13441	13586	-1.1	13527	-0.6

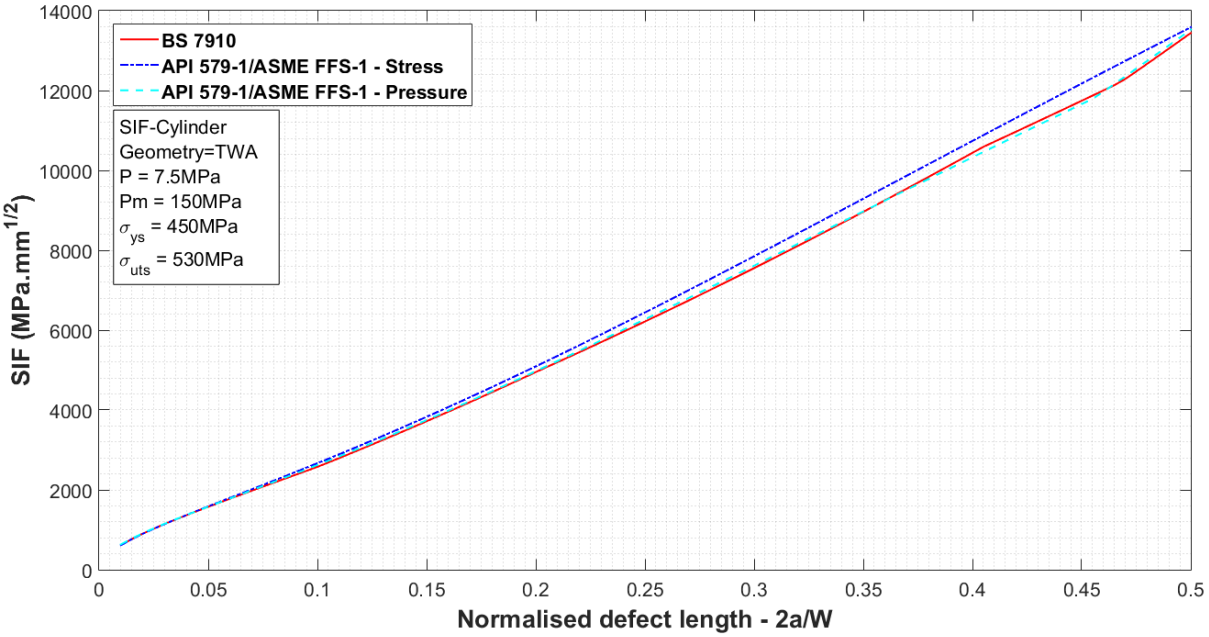

Figure 4.10: Stress Intensity Factor solutions for an axial through-wall crack (API 579-1/ASME FFS-1 and BS 7910)

4.4.4 Reference Stress solutions

The reference stress, σ_{ref}, is a measure of the applied stress in the un-cracked region of a cracked component. It accounts for the loss of cross sectional area in the region containing a flaw. Reference stress solutions are functions of the applied primary stresses (P_m, P_b), the defect size ($2a$, $2c$) and the structural dimensions (t, W, R_i). API 579-1/ASME FFS-1 or BS 7910 provide reference stress solutions for many crack geometries that are likely to occur in pressurized components. As no comparison work has been previously performed for this parameter, the following section includes such discussion for the different geometries. All the SIF equations from API 579-1/ASME FFS-1 or BS 7910 can be found in Annex B.3

4.4.4.1 Axial through-thickness flaws

Axial through-thickness defects are defined in the same way in both standards. Geometrical parameters such as crack length ($2a$), internal radius (R_i), length (W) and thickness (t) are required. Geometrical parameters are presented in Figure 4.11. Equations from BS 7910 and API 579-1/ASME FFS-1 can be found in Annex B.

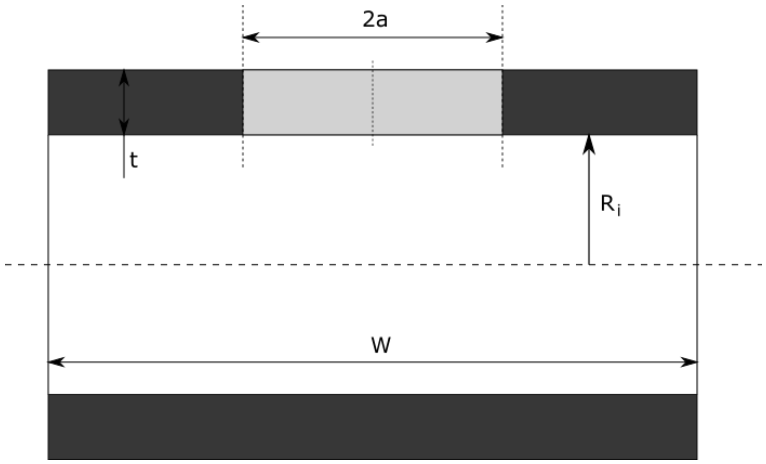

Figure 4.11: Geometry of an axial through-thickness crack in a cylinder

To assess the reference stress for through-thickness defects, both codes refer to Willoughby and Davey [135] which is a solution derived for plates with a correction factor to fit to pipes/cylinders geometries. Two important points may be noted here. In BS 7910 (Eq.B.51), a factor of 1.2 applied to the membrane stress is intended to produce a similar level of conservatism as that is inherent in the flat plate solutions. This increases the reference stress in BS 7910 by 20% compared to that of API 579-1/ASME FFS-1. Assuming a negligible bending stress ($P_b = 0$), reference stress solutions are reduced to:

- BS 7910 (From Eq.B.51)

$$\sigma_{ref(P_b=0)} = 1.2 M_T P_m \tag{4.7}$$

- API 579-1/ASME-FFS1 (From Eq.B.53)

$$\sigma_{ref(P_b=0)} = M_t P_m \tag{4.8}$$

Moreover, the use of surface correction factors leads to further divergences. In BS 7910, a unique surface correction factor, M_T, is provided (Eq.B.52) whereas three different factors are available in API 579-1/ASME FFS-1. Note that (Eq.B.54) is recommended for use in all assessments, this being a best fit to data from different references, (Eq.B.55) is an approximate expression and (Eq.B.56) an upper bound expression. The latter being the same surface correction factor than in BS 7910, (Eq.B.52).

From (Eq.B.57):

$$\lambda^2 = 3.305 \frac{a^2}{R_i t} \tag{4.9}$$

Inserting (Eq.4.9) into (Eq.B.56) leads to:

$$M_{t(API579)} = \sqrt{1 + 0.4845\lambda^2} = \sqrt{1 + 1.5997 \frac{a^2}{R_i t}} \cong \sqrt{1 + 1.6 \frac{a^2}{R_i t}} = M_{T(BS7910)} \tag{4.10}$$

The results of reference stress calculations for pipes/cylinders containing through-wall defect are presented in Figure 4.12 to Figure 4.14. The length of defect, $2a$, was normalized to the length of the pipe/cylinder, W. BS 7910 solution gives higher value of reference stress than all API 579-1/ASME FFS-1 solutions. Removing the 1.2 factor, the modified solution matches with API 579-1/ASME FFS-1 solution using the third surface correction factor (Eq.B.56) and API 579-1/ASME FFS-1 equation. API's two first surface correction factors (Eq.B.54 & Eq.B.55) give similar result. Taking the recommended correction factor, a difference of around 20% is shown for small crack length between BS 7910 and API 579-1/ASME FFS-1. This difference is due to the factor 1.2 on the membrane stress component. As the crack length increases, this difference increases due to the different surface correction factors used. In an example presented here with membrane stress loading only, the difference between BS 7910 and API 579-1/ASME FFS-1 solutions reaches 40% at L_r =1. Assuming only bending stress is present, it has to be noted that API 579-1/ASME FFS-1 equation results in a constant value equal to 0.66 P_b while BS 7910 equation is varying with the defect length.

This means that for all loading cases, BS 7910 is more conservative than API 579-1/ASME FFS-1. It will give a smaller critical flaw sizes before plastic collapse is predicted to occur.

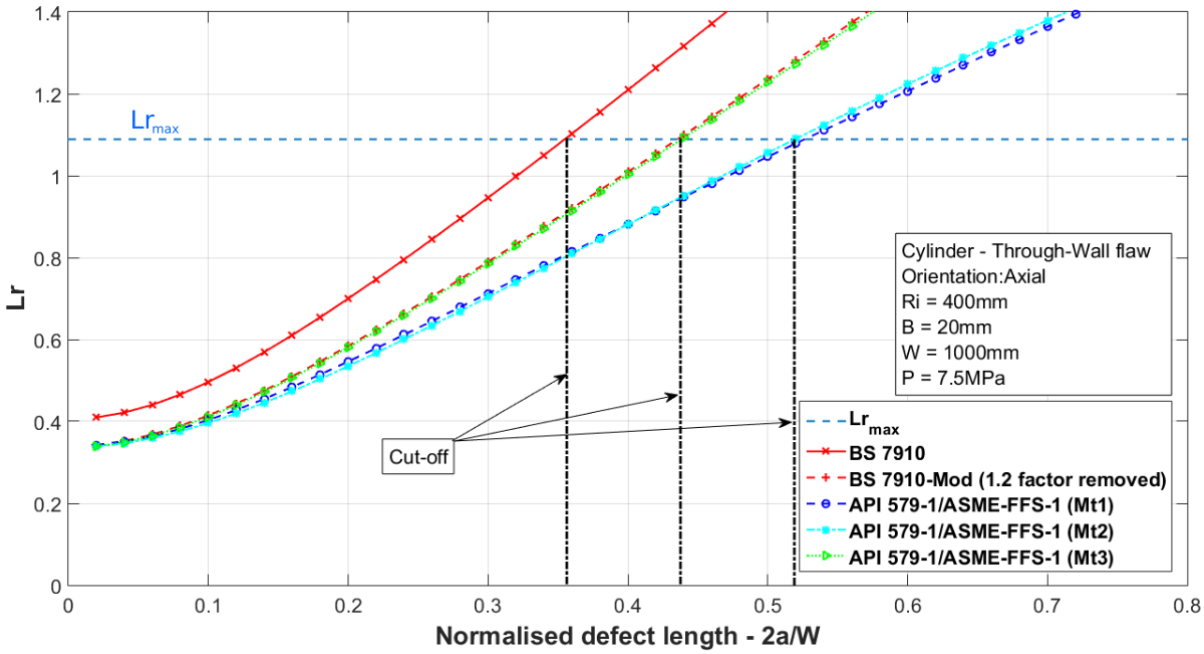

Figure 4.12: RS - Pipe/cylinder containing through-thickness axial defect - Membrane stress only

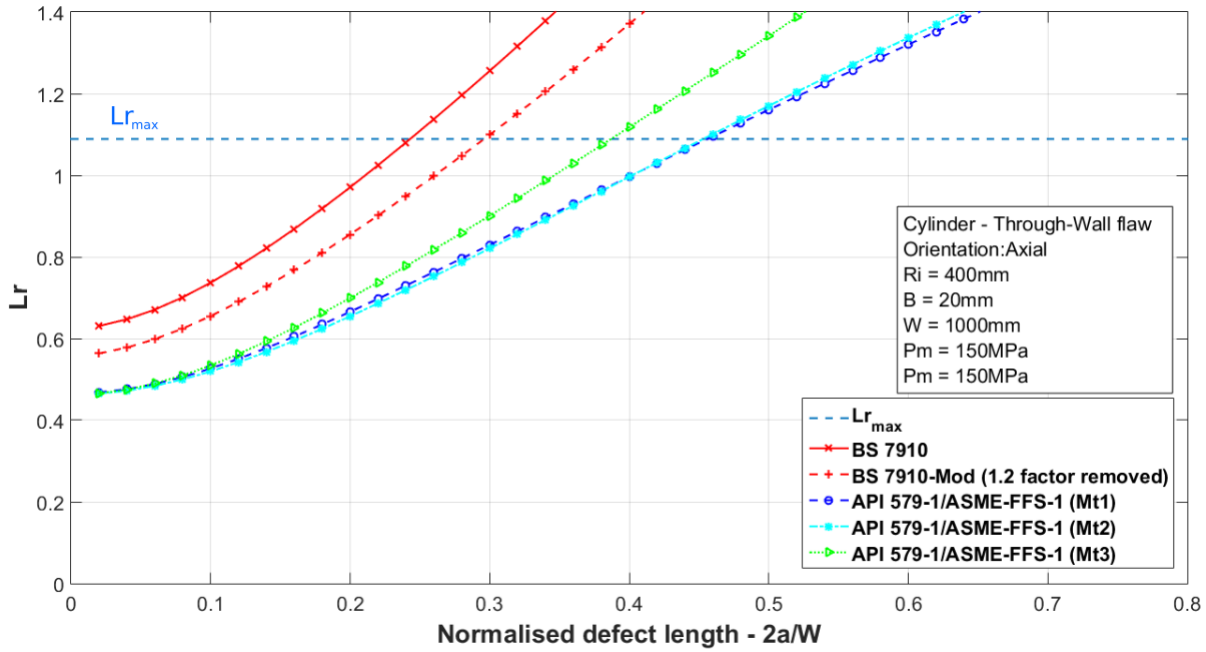

Figure 4.13: RS - Pipe/cylinder containing through-thickness axial defect - Membrane and Bending stress

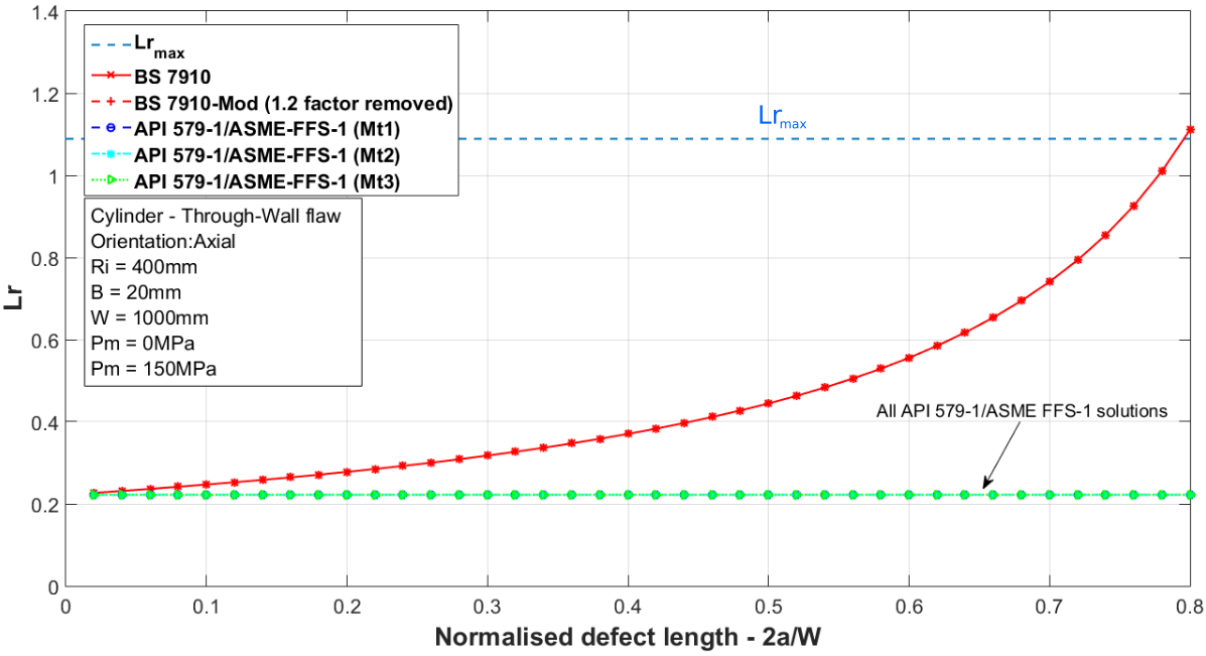

Figure 4.14: RS - Pipe/cylinder containing through-thickness axial defect - Bending stress only

4.4.4.2 Circumferential through-thickness crack

Circumferential through-thickness defects are defined in the same way in both standards. Geometrical parameters such as crack length ($2a$) or crack angle (2θ), internal radius (R_i) and thickness (t) are required. They are presented in Figure 4.15.

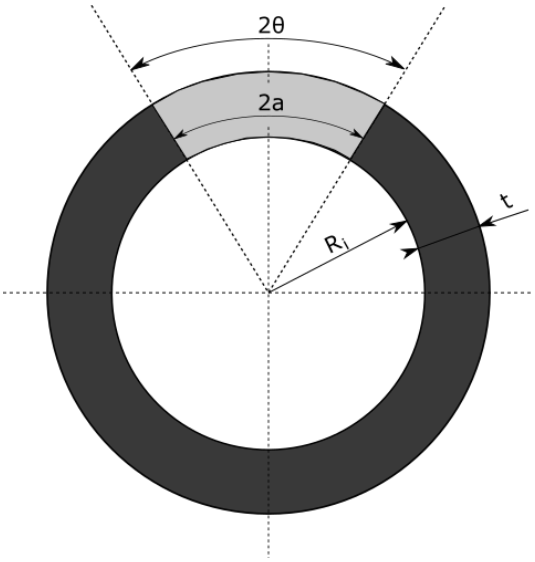

Figure 4.15: Geometry of a circumferential through-thickness crack in a cylinder

The second through-wall geometry examined a circumferential defect in a pipe/cylinder. Since the procedure requires applied loads to be expressed in terms of membrane and bending stresses, the following conversion formulae was used for pressure loading accounting for internal pressure, P and axial force, F [9]:

$$P_m = \frac{PR_i^2}{R_o^2 - R_i^2} + \frac{F}{\pi(R_o^2 - R_i^2)} \tag{4.11}$$

where R_i and R_o are respectively the inner and outer radii. Within this part of the study, pipes/cylinders with the same dimensions and material properties than for axial defects cases have been assumed. The loading conditions considered were membrane and bending stresses of 150 MPa (P_m = 150 MPa, $P_m = P_b$ = 150MPa and P_b = 150 MPa).

Results of the reference stress calculations for pipes/cylinders containing circumferential through-thickness defect are presented in Figure 4.16 to Figure 4.18. For the analysis, BS 7910 (Eq.B.58) and API 579-1/ASME FFS-1 (Eq.B.59) formulae were employed to carry out the assessment. The geometrical normalisation for circumferential flaws is made by the division of the half crack angle, θ, by π. The assessment results of the pipe/cylinder containing a through thickness defect subject to pure tension, combined tension and bending, and in addition to combined tension, bending and internal pressure are summarized in Figure 4.16 , Figure 4.17 and Figure 4.18 respectively.

For the case where through-thickness defects are subject to pure tension (Figure 4.16), both BS 7910 and API 579-1/ASME FFS-1 delivered very similar results. However, significant difference was observed in the assessment of combined tension and bending loading (Figure 4.17). This is mainly due to the definition of α in API 579-1/ASME FFS-1, which

is two times lower than BS 7910 equivalent and the presence of the squared denominator (See equation below). Taking only bending stress into consideration, (Eq.B.58) and (Eq.B.59) were reduced to:

$$\sigma_{ref-BS} = \frac{2P_b}{3(1-\frac{2a}{\pi R_i})} \neq \sigma_{ref-API} = \frac{2P_b}{3(1-\frac{a}{\pi R_m})^2} \tag{4.12}$$

As a whole, BS 7910 produces higher reference stress results. However the evolution of solutions is similar in the range of applicability for both standards. The same observation can be made when internal pressure is taken into account together with tension and bending (Figure 4.18).

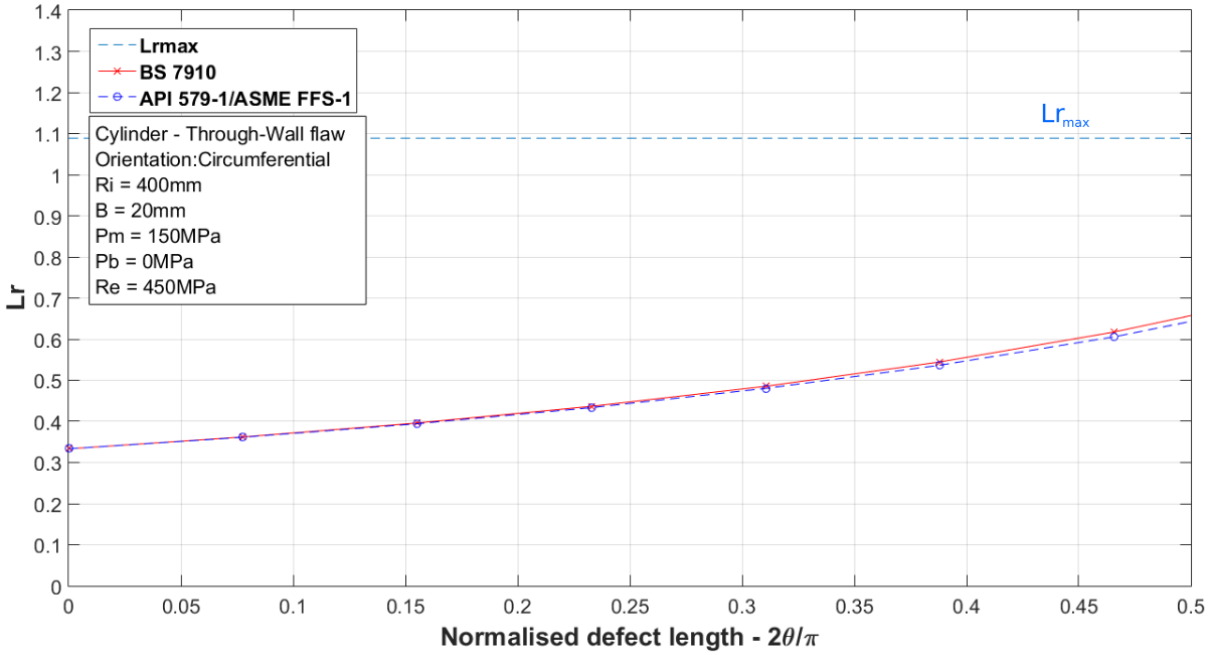

Figure 4.16: RS - Pipe/cylinder containing through-thickness circumferential defect - Pure tension only

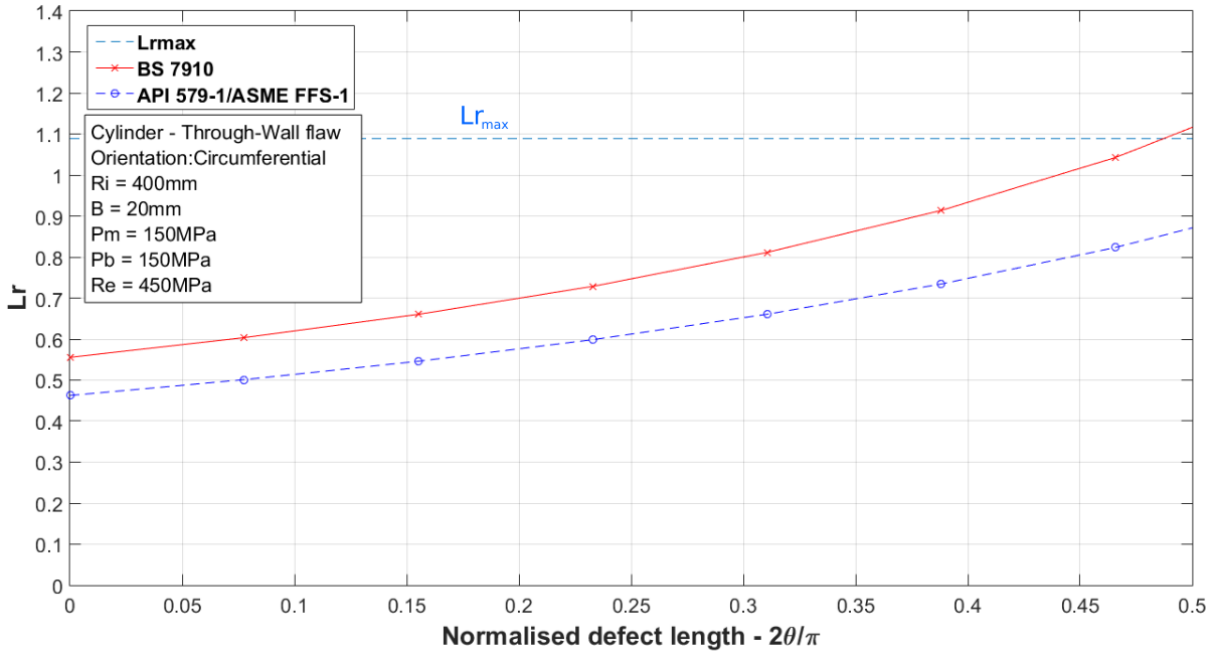

Figure 4.17: RS - Pipe/cylinder containing through-thickness circumferential defect - Membrane and Bending stress

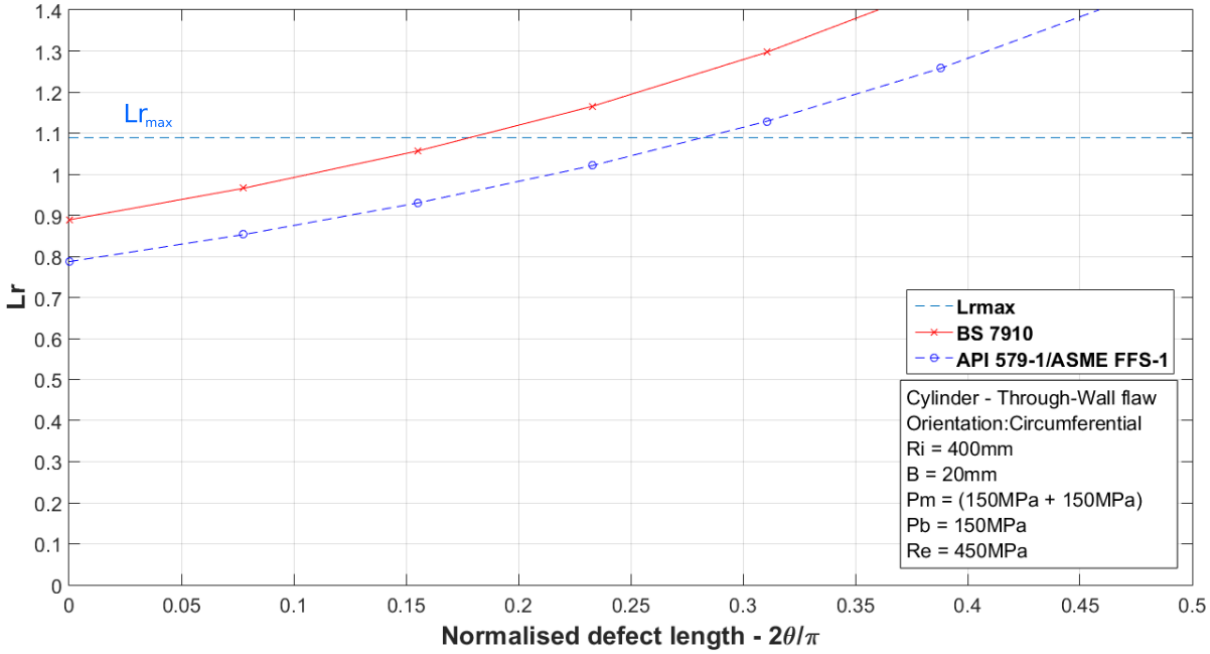

Figure 4.18: RS - Pipe/cylinder containing through-thickness circumferential defect - Combined tension, bending and internal pressure

4.4.4.3 Axial surface defect

Axial surface defects are defined in the same way in both standards. Geometrical parameters such as crack length ($2c$), crack depth (a) internal radius (R_i) and thickness (t) are required. They are presented in Figure 4.19. Equations from BS 7910 and API 579-1/ASME FFS-1 can be found in Annex B.3.3. These solutions are generally applicable for $0< a/t <0.8$.

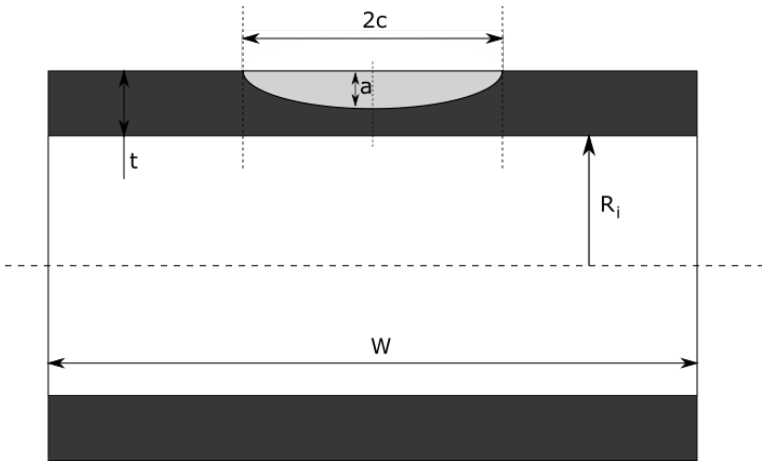

Figure 4.19: Geometry of an axial surface crack in a cylinder

Limit load solutions can be complicated for surface defect assessment as it can be defined as the load corresponding to local yielding ('local' limit load), or net section yielding, ('global' limit load). In the case of a surface defect, in contrast to API 579-1/ASME FFS-1 (Eq.B.68), BS 7910 distinguishes internal and external defects even if the same solution is provided (Eq.B.65). None of the above allows consideration of the defect face pressure when an internal defect is present in a pressurized component. As per through-thickness solution, BS 7910 provides a unique surface correction factor, while API 579-1/ASME FFS-1 provides different solutions. Information given in API 579-1/ASME FFS-1 concludes that the first surface correction factor M_{s1} does not produce consistent results when the crack approaches a through-wall configuration. It is also mentioned that M_{s1} and M_{s2} give similar results up to a ratio $a/t < 0.5$. The formulation M_{s1} with a rectangular shape is the surface correction factor used in BS 7910. Here, the second surface correction factor in API 579-1/ASME FFS-1 M_{s2} will be used to keep the same formulation for different crack depths. Three different cases corresponding to each surface correction factors M_t ((Eq.B.54) to (Eq.B.56)) have been assessed in this work.

The results of reference stress calculation for pipes/cylinders containing surface defect can be seen in Figure 4.20 to Figure 4.23. The length of internal surface defect, $2c$, is normalized to the width, W, of the pipe/cylinder and the defect depth, a, is normalized to the wall-thickness, t. Figure 4.20 shows the effect of surface correction factors available in

API 579-1/ASME FFS-1 on L_r. Calculations presented with Eq.B.71 have been performed using C=0.85. One can see that the recommended equations tend to lower reference stress results. Note that the couple Eq.B.54 and Eq.B.72 are recommended for all assessment. Comparison with the BS 7910 solution will be made using this couple of surface correction factors only.

In Figure 4.21 to Figure 4.23, L_r vs a/t values of membrane only, membrane and bending and bending only cases were plotted against increasing $2c/W$ values. As long as membrane stress is involved, BS 7910 gives higher reference stress values. This is partly due to the 1.2 factor applied on membrane stress as per through-thickness case. Moreover as the crack length increases, the values derived using BS 7910 solution tends to increase more rapidly for defects with a depth superior to the half thickness (Figure 4.21). Another observation can be made regarding the effect of bending stress (Figure 4.22 - Figure 4.23). Values calculated from API 579-1/ASME FFS-1 solutions are lower due to the parameter g. Without this parameter applied on bending stress, solutions give similar results.

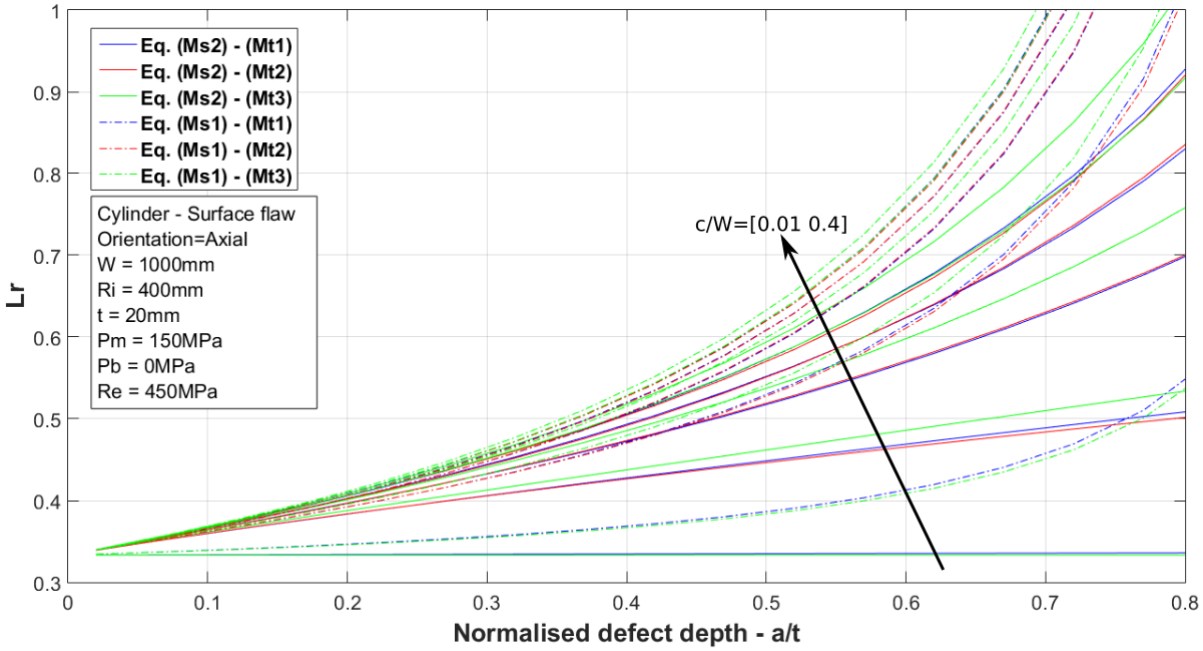

Figure 4.20: RS - Pipe/cylinder containing surface axial defect - API 579-1/ASME FFS-1 - Membrane stress only

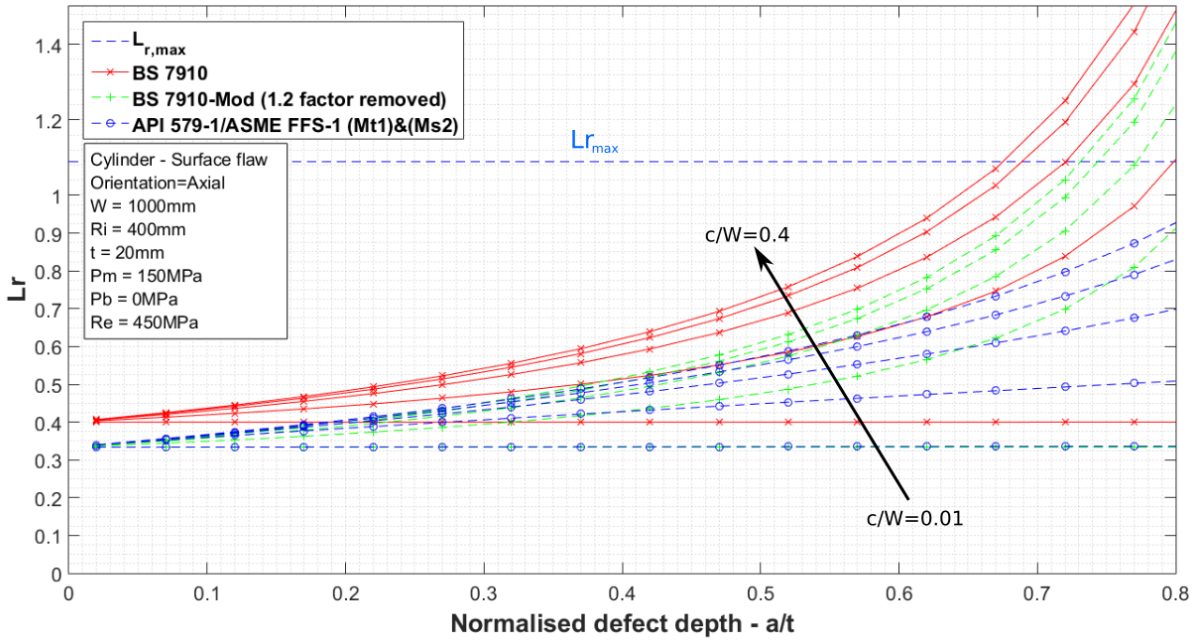

Figure 4.21: RS - Pipe/cylinder containing surface axial defect - Membrane stress only

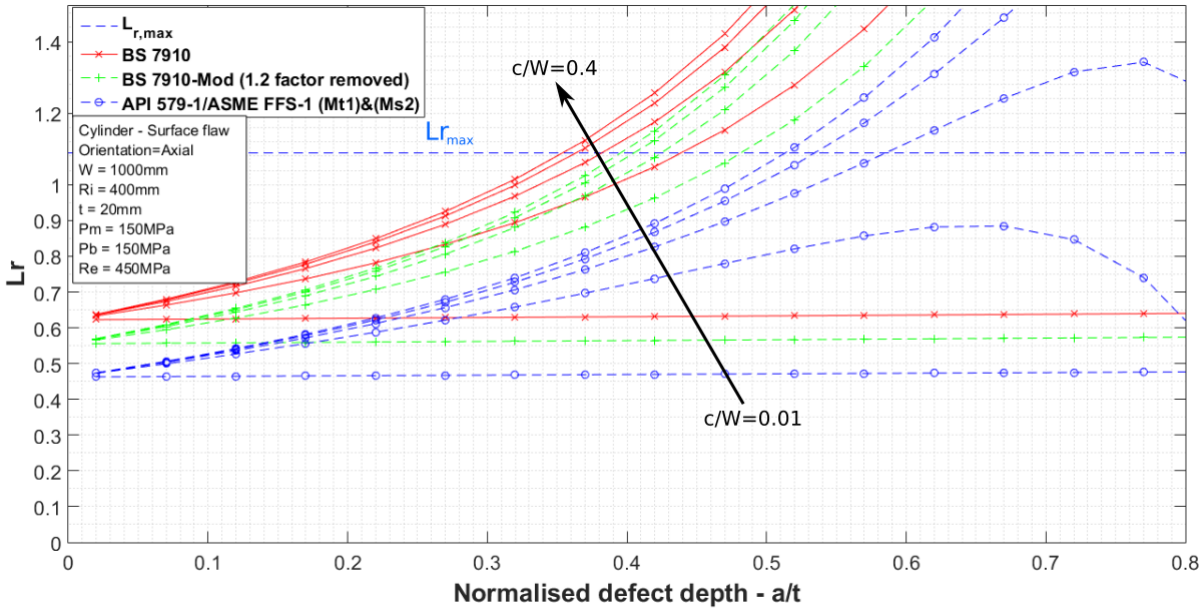

Figure 4.22: RS - Pipe/cylinder containing surface axial defect - Membrane & Bending stress

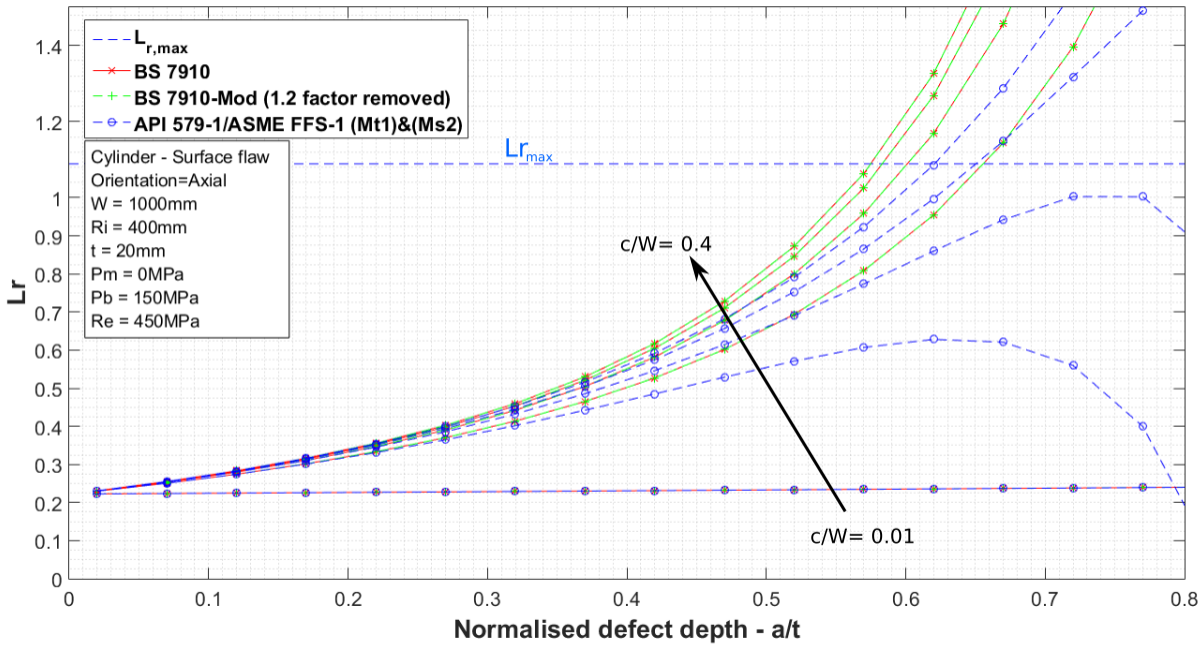

Figure 4.23: RS - Pipe/cylinder containing surface axial defect - Bending stress only

4.4.4.4 Circumferential surface defect

Circumferential surface defects are defined in the same way in both standards. Geometrical parameters such as crack length ($2c$) or crack angle (2θ), crack depth (a) internal radius (R_i) and thickness (t) are required. They are presented in Figure 4.24. Equations from BS 7910 and API 579-1/ASME FFS-1 can be found in Annex B.3.4.

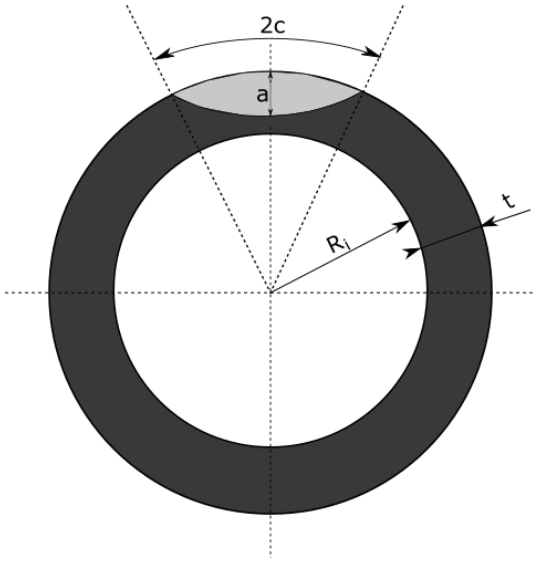

Figure 4.24: Geometry of a circumferential surface crack in a cylinder

Both BS 7910 (Eq.B.74) and API 579-1/ASME FFS-1 (Eq.B.76) distinguish internal and external cases for circumferential surface defects. None of the above allows consid-

eration of defect face pressure in case of an internal defect in a pressurized component. Only internal defect will be illustrated here. The results of reference stress calculation for pipes/cylinders containing circumferential surface defect can be seen in Figure 4.25 to Figure 4.27. The geometrical normalisation for circumferential defect is achieved by the division of the half defect angle, θ, by π and the defect depth, a, is normalized to the wall-thickness, t. The assessment results of pipe/cylinder containing a surface defect subject to membrane, combined membrane and bending, and bending only can be found in Figure 4.25, Figure 4.26 and Figure 4.27 respectively. Considering membrane stress only, both solutions give similar results for small defect depth but diverge significantly as the defect depth increases (Figure 4.25). Solution in API 579-1/ASME FFS-1 increase much slower than BS 7910's one. For combined membrane and bending stress loading, BS 7910 solution gives higher values than that of API 579-1/ASME FFS-1 (Figure 4.26). When only bending stress is considered, both solutions give similar results (Figure 4.27).

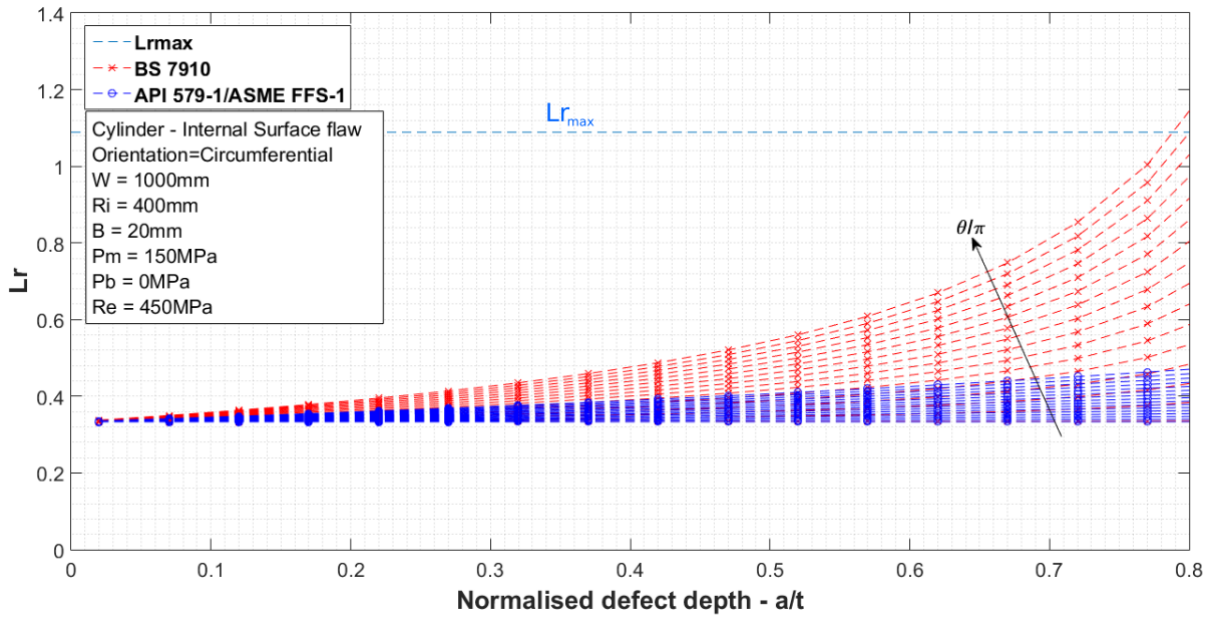

Figure 4.25: RS - Pipe/cylinder containing surface circumferential defect - Membrane stress only

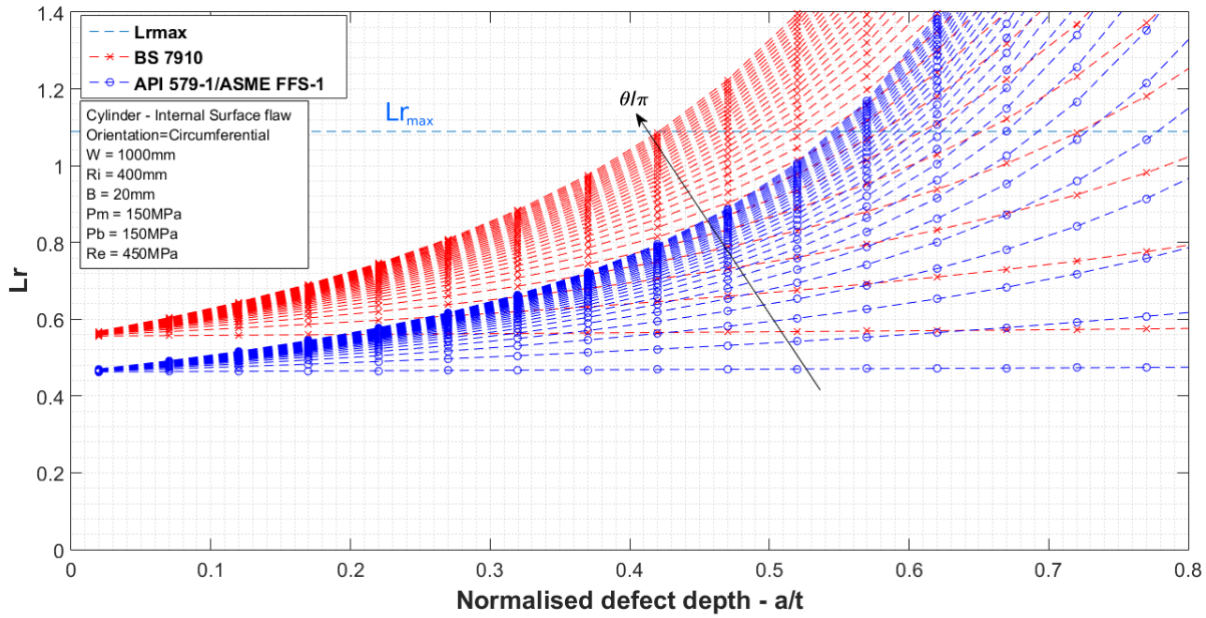

Figure 4.26: RS - Pipe/cylinder containing surface circumferential defect - Membrane & Bending stress

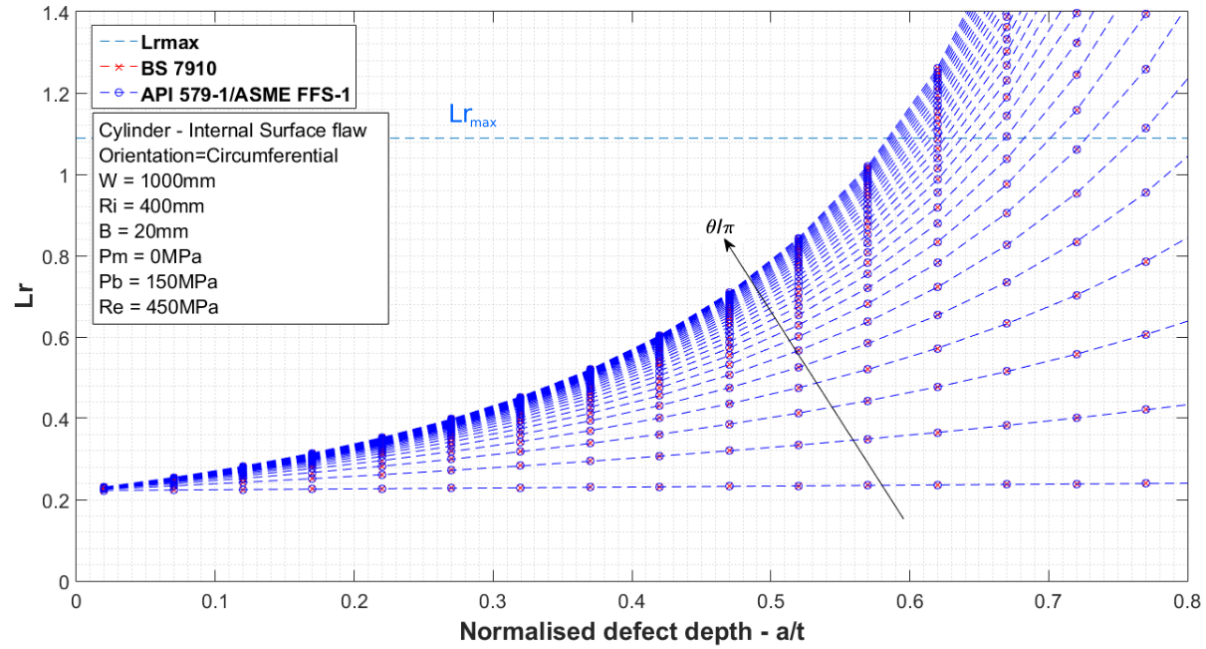

Figure 4.27: RS - Pipe/cylinder containing surface circumferential defect - Bending stress only

4.4.5 Cases study

Three relevant cases studies are provided in this section. In Section 4.4.5.1, a full case study is described including comparison of reference stress, stress intensity factor and final FAD solutions comparison for an axial through-wall defect. The influence of different solutions are discussed. Section 4.4.5.2 provides more details on surface axial defect analytical solutions. The third (Section 4.4.5.3), looks at analytical solutions for a surface axial defect versus experimental data.

4.4.5.1 Axial Through-wall crack - Comparison of the different analytical solution

In order to compare formulations found in both codes, a parametric study on the crack length has been carried out. A case of a pipe with a ratio $t/R_i = 0.05$ under an internal pressure of 2.5 MPa is shown here. In this particular case, the following parameters describing the pipe geometry and loading were used to solve equations from BS 7910 and API 579-1/ASME FFS-1.

Geometric parameters:

Parameters	**Internal Radius** (R_i)	**Thickness** (B)	**Part Length** (W)	**Ratio** $\frac{t}{R_i}$
Values	200 mm	10 mm	1000 mm	0.05

Loading parameters:

Parameters	**Pressure** (P)	**Membrane Stress** (P_m)	**Bending Stress** (P_b)
Values	2.5 MPa	50 MPa	1.25 MPa

Material parameters:

Parameters	**Yield Stress** (σ_{ys})	**Ultimate Tensile Stress** (σ_{uts})	**Fracture Toughness** (K_{mat})	**Cut-off** (L_{rmax})
Values	450 MPa	530 MPa	100 MPa$\sqrt{m}$	1.09

Using different crack lengths, a parametric study can be conducted on the reference stress solutions in API 579-1/ASME FFS-1 and BS 7910. Figure 4.28 shows the reference stress solutions plotted against the normalized crack length, $2a/W$. Five curves are plotted here:

- (I) BS 7910:2013 (Eq.B.51)
- (II) BS 7910:2013-Modified (Eq.B.51 with the 1.2 factor removed)
- (III) API 579-1/ASME FFS-1:2007 (Eq.B.53 with M_{t1} from (Eq.B.54))
- (IV) API 579-1/ASME FFS-1:2007 (Eq.B.53 with M_{t2} from (Eq.B.55))
- (V) API 579-1/ASME FFS-1:2007 (Eq.B.53 with M_{t3} from (Eq.B.56))

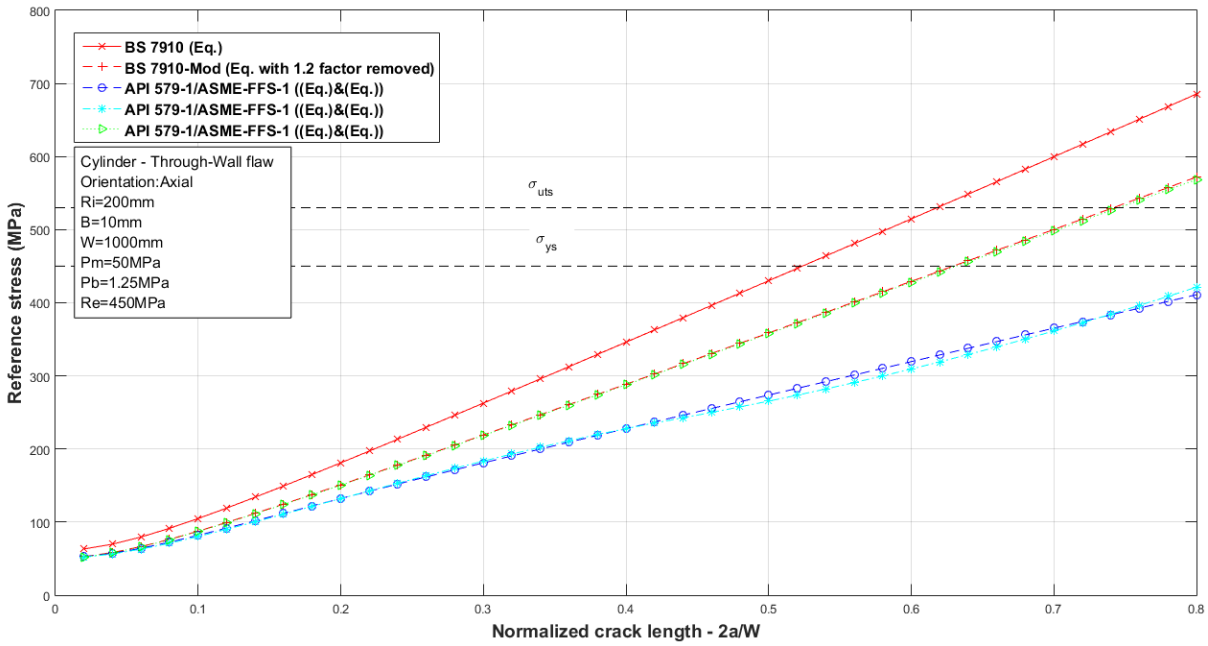

Figure 4.28: Reference stress solutions from BS 7910 and API 579-1/ASME FFS-1 for an axial through-wall crack

Figure 4.28 shows that the BS 7910 solution gives higher values of reference stress than all the API 579-1/ASME FFS-1 solutions. The modified BS 7910 solution matches with API 579-1/ASME FFS-1 solution using the third surface correction factor (Eq.B.56). API 579-1/ASME FFS-1 solution using the two first surface correction factors ((Eq.B.54) & (Eq.B.55)) give approximately the same results. Table 4.5 lists the values of reference stress for some normalized crack lengths. Values obtained from API 579-1/ASME FFS-1 solutions are compared to those obtained by the BS 7910 solutions. A difference of around 20% is shown for small crack lengths. This difference is due to the factor of 1.2 on the membrane stress part in Eq.B.51. As the crack length increases, this difference increases due to the different surface correction factors used. In this example, the difference between the formulation recommended for all assessments in API 579-1/ASME FFS-1 and BS 7910 reaches 40%. Removing the 1.2 factor from the BS 7910 formula, brings the values down to the same as in API 579-1/ASME FFS-1 with the third surface correction factor.

Table 4.5: Comparison of reference stress between BS 7910 and API 579-1/ASME FFS-1 for axial through-wall crack

Normalized crack length	API 579-1/ASME FFS-1 σ_{ref} (MPa)						BS 7910 - Mod σ_{ref} (MPa)		BS 7910 σ_{ref} (MPa)
$(2a/W)$	M_{t1}	%	M_{t2}	%	M_{t3}	%	M_T	%	M_T
0.05	60.7	18.7	59.6	20.2	61.9	17.1	62.4	16.5	74.7
0.1	81.9	21.9	80.2	23.5	87.0	17.0	87.5	16.5	104.8
0.25	156.9	29.2	158.4	28.5	184.2	16.9	184.8	16.6	221.6
0.5	273.7	36.4	265.4	38.3	357.6	16.9	358.7	16.6	430.2
0.75	388.1	39.6	390.4	39.2	533.3	17.0	536.0	16.6	642.6

Figure 4.29 shows the result in terms of load ratio, the value of L_r cut-off being the same in both codes (Eq.4.6). The difference between the reference stress solutions has an effect on the crack length at which the cut-off value is reached.

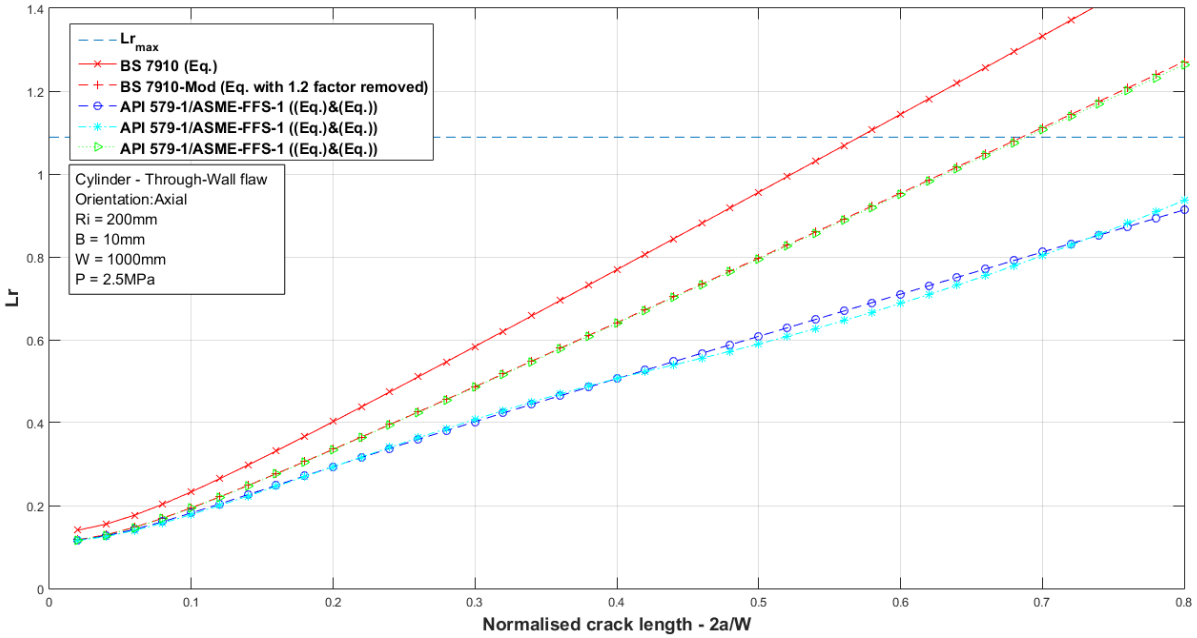

Figure 4.29: Load ratio and cut-off solutions from BS 7910 and API 579-1/ASME FFS-1 for an axial through-wall crack

Here, the cut-off value is a normalised crack half-length of around 0.57 in BS 7910 whereas it reaches a value around 0.95 in API 579-1/ASME FFS-1. With the modified equation of BS 7910, this value reaches approximately 0.68. This is mainly due to the surface correction factor M_t definition. The next step in order to assess the defect in terms of the FAD is the calculation of the fracture ratio K_r. Stress Intensity Factors solutions have to be known for each code (Figure 4.30).

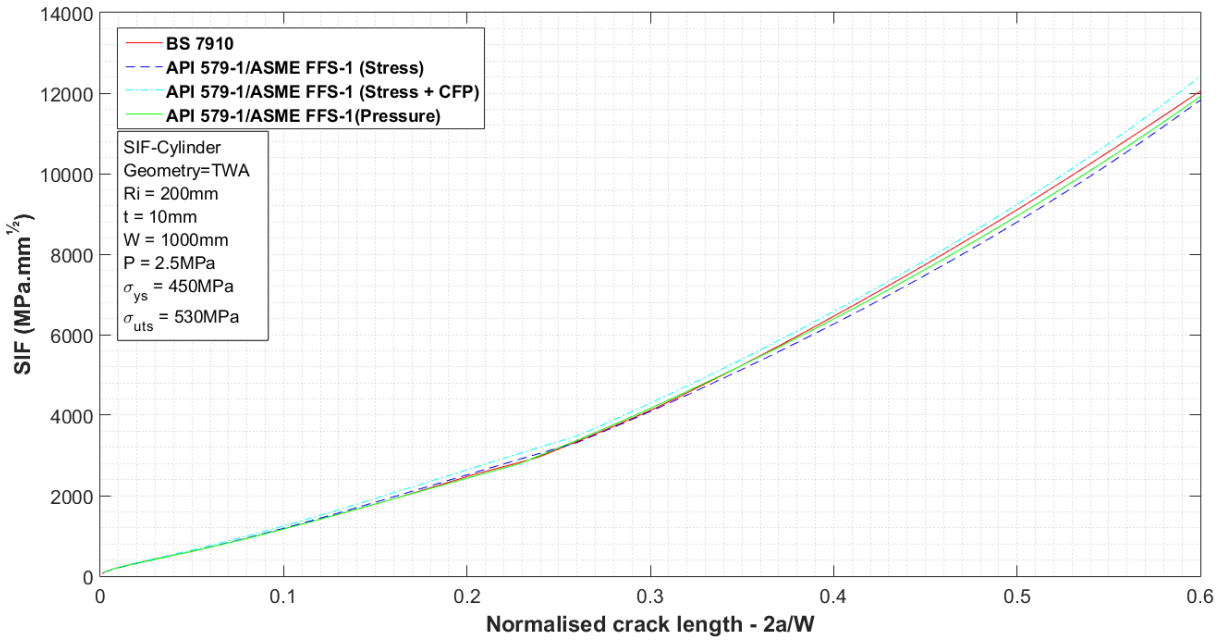

Figure 4.30: Stress Intensity Factor solutions from BS 7910 and API 579-1/ASME FFS-1 for an axial through-wall crack

Table 4.6 gives the values of stress intensity factor for some lambda values obtained from API 579-1/ASME FFS-1 solutions and are compared to those obtained by the BS 7910 solution. Different solutions give approximatively the same result with a maximum difference of 5%.

Table 4.6: Comparison of stress intensity factor, $K_I(MPA\sqrt{m})$, between BS 7910 and API 579-1/ASME FFS-1 for axial through-wall crack

Lambda	API 579-1/ASME FFS-1 (Pressure)		API 579-1/ASME FFS-1 (Stress)		API 579-1/ASME FFS-1 (Stress+P)		BS 7910
(λ)	K_I	%	K_I	%	K_I	%	K_I
0.25	242	1.98	235	4.77	247	0.09	247
0.5	369	2.32	364	3.45	383	1.46	377
1	610	0.55	613	0.09	644	4.97	613
2	1153	1.67	1170	0.24	1229	4.80	1173
4	2394	2.86	2474	0.38	2598	5.43	2464
6	4073	0.63	3998	2.47	4197	2.40	4099
8	6239	2.83	6115	4.76	6420	0.007	6420
10	8730	3.55	8579	5.22	9007	0.48	9051
12	11613	3.10	11511	3.95	12086	0.85	11984

With the previous assumption, the calculation of the fracture ratio K_r is limited to $K_r = K_I^p/K_{mat}$. The following figure shows the evolution of K_r with the crack half-length. The cut-off value in terms of K_r is obtained for K_r=1. The difference between API 579-1/ASME FFS-1 and BS 7910 is small, with a cut-off value around 249 mm in API 579-1/ASME FFS-1 (Pressure, Stress), 237 mm in API 579-1/ASME FFS-1 (Stress + CFP) and 250 mm in BS 7910.

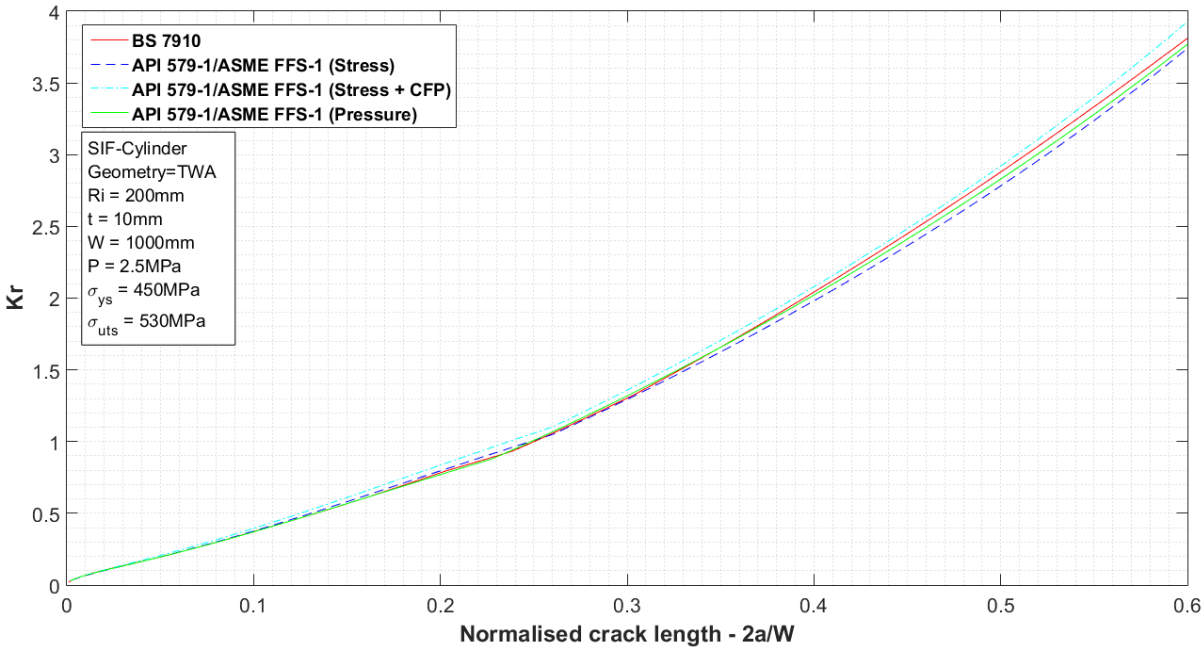

Figure 4.31: Fracture ratio solutions from BS 7910 and API 579-1/ASME FFS-1 for an axial through-wall crack

Having calculated the values of L_r and K_r for different values of crack length, the last step is to plot the FAD. In order to compare results obtained by API 579-1/ASME FFS-1 and BS 7910, a material specific FAD could have been chosen as the same definition in provided both codes. However, here the simplest definition from each code is chosen.

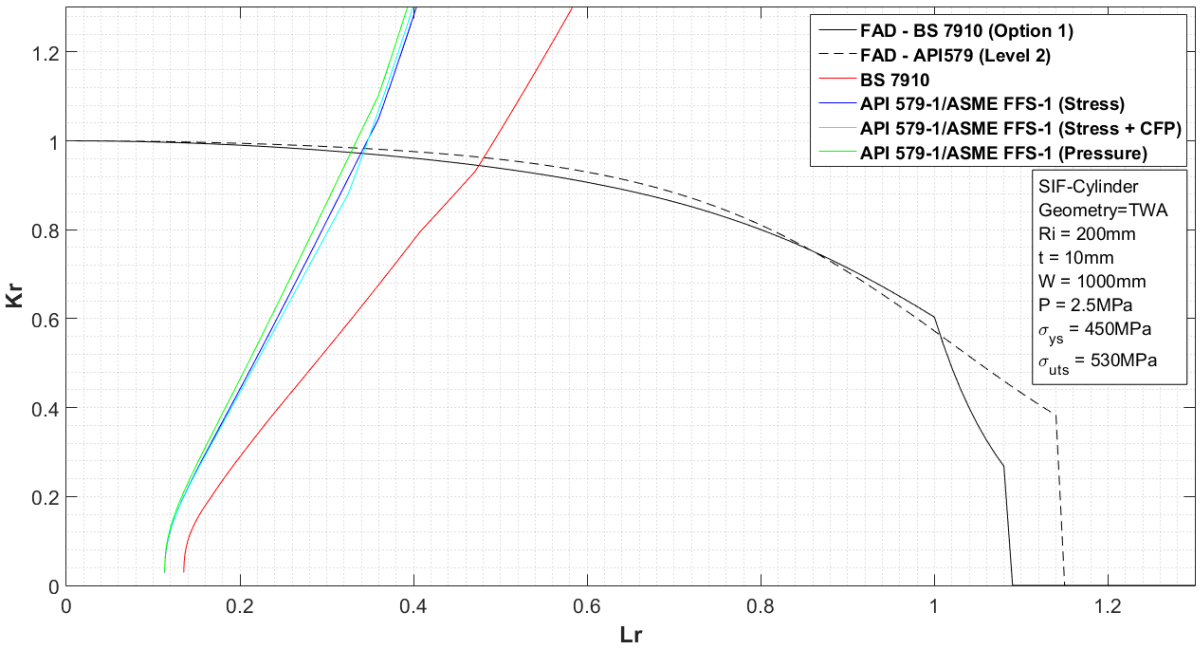

Figure 4.32: FAD comparison between API 579-1/ASME FFS-1 and BS 7910 for an axial through-wall crack

A critical value is reached when assessment point reaches the FAD curve. This critical value is different depending on the code used as shown in Table 4.7:

Table 4.7: Critical length for each standard for axial through-wall crack

Codes	Critical length based on API 579-FAD	Critical length based on BS 7910-FAD
BS 7910 (Eq.B.29 & Eq.B.51)	244 mm	**240 mm**
API 579-1/ASME FFS-1 (Eq.B.34 without CFP & Eq.B.53)	244 mm	242 mm
API 579-1/ASME FFS-1 (Eq.B.34 with CFP & Eq.B.53)	234 mm	230 mm
API 579-1/ASME FFS-1 (Eq.B.36 & Eq.B.53)	**246 mm**	244 mm

Based on API 579-1/ASME FFS-1 (pressure) the critical crack length is determined as 246 mm whereas in BS 7910 the critical value is reached for a crack length of 240 mm. Here a crack length of 243 mm will fail with an assessment using BS 7910 procedures whereas it will be assessed as safe using API 579-1/ASME FFS-1 procedures. One can also notice that using the same input parameters, API 579-1/ASME FFS-1 gives different results depending on the solution used. This difference is due to the assessment of the critical length of the defect and may be a major concern in a LBB case. In a LBB case, the critical length value of a defect is one of the most important parameters to validate the leak detection system and margins associated with the time remaining before failure.

When the different parameters are taken in order to be in the FAD area where the solutions are the more diverging, the choice of the solution may be important. The following case presents the same component as previous in terms of size. However, both material properties and loading have been changed so that plastic collapse becomes dominant. The material is assumed to have a yield strength, $\sigma_{ys} = 275$ MPa and an ultimate tensile strength $\sigma_{ys} = 350$ MPa. The component is subject to an internal pressure of 15 MPa. From these hypothesis, the following FAD can be computed:

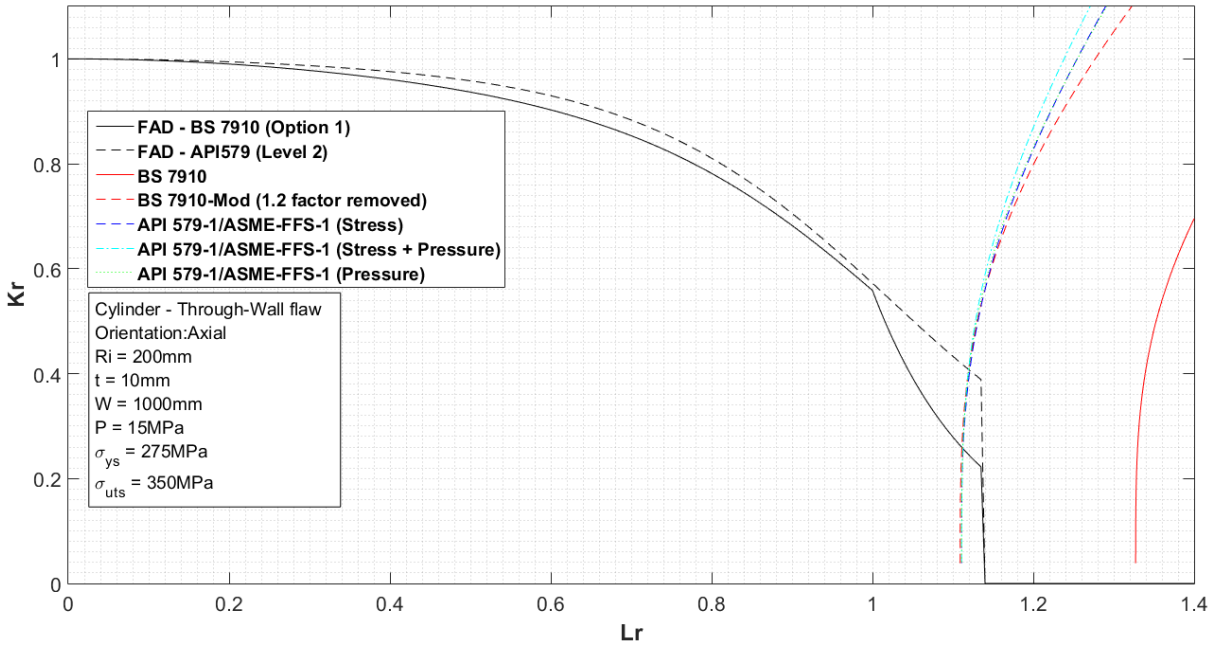

Figure 4.33: FAD comparison between API 579-1/ASME FFS-1 and BS 7910 for an axial through-wall crack

Table 4.8: Critical length for each standard for axial through-wall crack

Codes	Critical length (API 579-FAD)	Critical length (BS 7910-FAD)
BS 7910 (Eq.B.29 & Eq.B.51)	—	—
BS 7910-Mod (Eq.B.29 & Eq.B.51 - 1.2 factor removed)	9.8 mm	**5.3 mm**
API 579-1 (Eq.B.34 without CFP & Eq.B.53)	**10.3 mm**	5.6 mm
API 579-1 (Eq.B.34 with CFP & Eq.B.53)	9.7 mm	5.1 mm
API 579-1 (Eq.B.36 & Eq.B.53)	9.7	5.1 mm

Table 4.8 presents the final results for this selected case. BS 7910 solutions assumes that the component will fail by plastic collapse while API 579-1/ASME FFS-1 allows a through-wall crack to a certain extend. The effect of the FAD shape is also important. Depending on FAD definition, the crack length allowable can be doubled. Removing the 1.2 factor from BS 7910 equations leads to results that are similar to API 579-1/ASME FFS-1.

4.4.5.2 Axial surface defect - Analytical solutions

The reference stress solutions for an axial surface crack are described in this section. In order to maintain the same input parameters as described in Section 4.4.5.1, only internal pressure will be considered for three cases based on the crack depth ($a/t = 0.2, 0.5$ and 0.8). As previously, the curve "BS 7910-Mod" is based on (Eq.B.65) with the factor 1.2 removed.

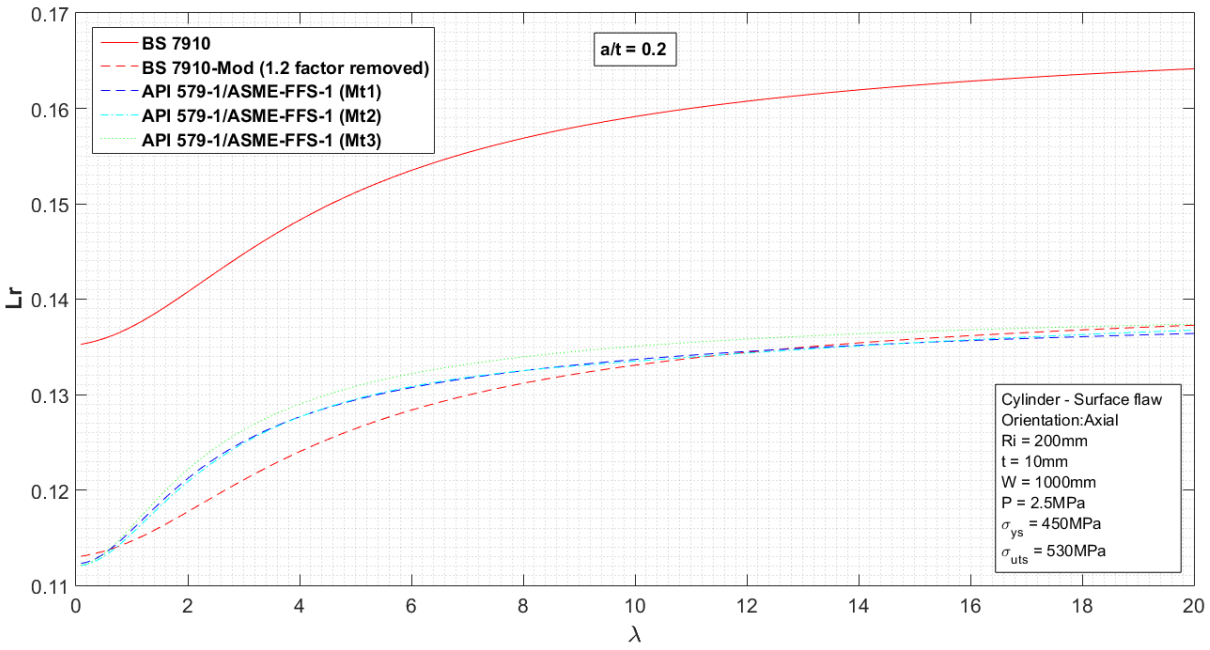

Figure 4.34: Comparison of reference stress between BS 7910 and API 579-1/ASME FFS-1 for axial surface crack (a/t=0.2)

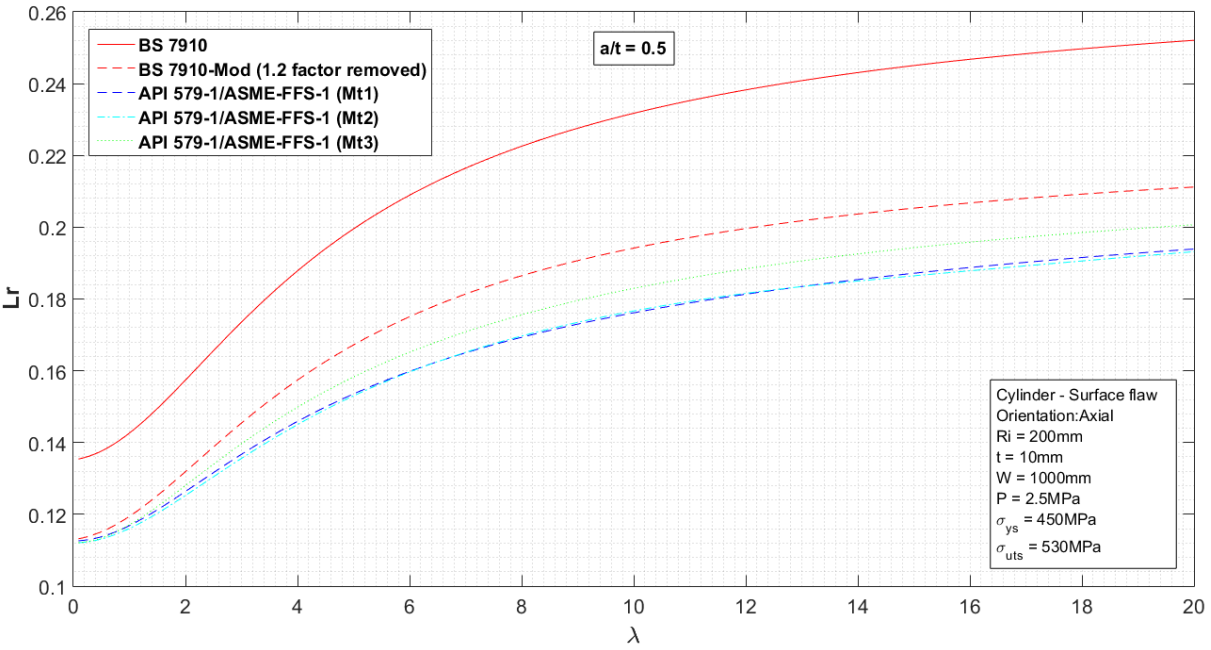

Figure 4.35: Comparison of reference stress between BS 7910 and API 579-1/ASME FFS-1 for axial surface crack (a/t=0.5)

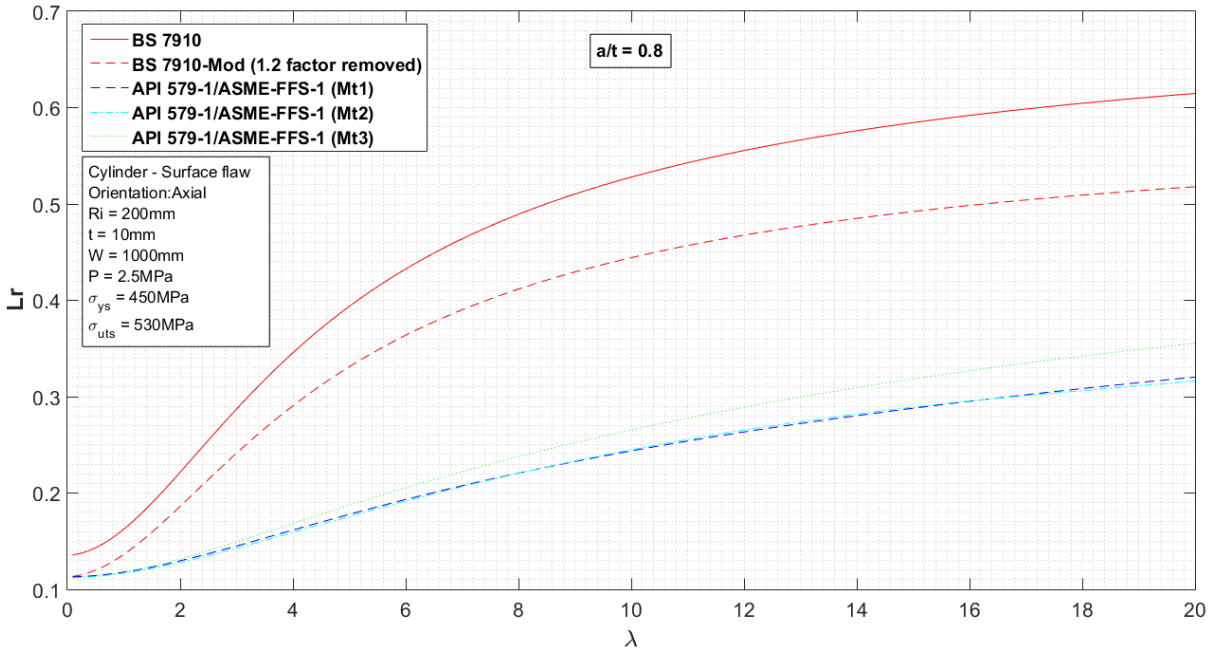

Figure 4.36: Comparison of reference stress between BS 7910 and API 579-1/ASME FFS-1 for axial surface crack (a/t=0.8)

Table 4.9: Comparison of reference stress between BS 7910 and API 579-1/ASME FFS-1 for axial surface crack (a/t=0.2)

Lambda	API 579-1/ASME FFS-1 σ_{ref} (MPa)						BS 7910 - Mod σ_{ref} (MPa)		BS 7910 σ_{ref} (MPa)
	M_{t1}	%	M_{t2}	%	M_{t3}	%	M_T	%	M_T
0.5	51.14	16.40	51.02	16.61	51.15	16.39	51.14	16.40	61.18
1	52.22	15.35	52.05	15.62	52.38	15.08	51.58	16.39	61.69
2	54.69	13.61	54.53	13.85	55.11	12.94	52.94	16.37	63.30
5	58.43	14.01	58.47	13.96	59.07	13.07	56.83	16.37	67.96
10	60.38	15.66	60.30	15.78	61.00	14.80	59.87	16.38	71.60
20	61.61	16.57	61.77	16.36	62.05	15.98	61.75	16.38	73.85

Table 4.10: Comparison of reference stress between BS 7910 and API 579-1/ASME FFS-1 for axial surface crack (a/t=0.5)

Lambda	API 579-1/ASME FFS-1 σ_{ref} (MPa)						BS 7910 - Mod σ_{ref} (MPa)		BS 7910 σ_{ref} (MPa)
	M_{t1}	%	M_{t2}	%	M_{t3}	%	M_T	%	M_T
0.5	51.99	17.73	51.67	18.24	51.98	17.75	52.91	16.29	63.20
1	55.18	18.94	54.72	19.61	55.69	18.20	57.03	16.22	68.08
2	62.32	21.19	61.82	21.82	63.73	19.40	66.27	16.20	79.08
5	76.20	23.73	76.36	23.56	79.01	20.91	83.71	16.21	99.90
10	84.88	23.42	84.48	23.78	88.07	20.54	92.86	16.22	110.84
20	91.33	21.93	92.23	21.17	93.81	19.82	98.02	16.22	117.00

Table 4.11: Comparison of reference stress between BS 7910 and API 579-1/ASME FFS-1 for axial surface crack (a/t=0.8)

Lambda	API 579-1/ASME FFS-1 σ_{ref} (MPa)						BS 7910 - Mod σ_{ref} (MPa)		BS 7910 σ_{ref} (MPa)
	M_{t1}	%	M_{t2}	%	M_{t3}	%	M_T	%	M_T
0.5	53.07	27.12	52.55	27.84	53.03	27.17	61.10	16.10	72.82
1	58.34	41.06	57.54	41.87	59.18	40.21	83.17	15.97	98.98
2	72.69	52.90	71.62	53.59	75.79	50.89	129.75	15.92	154.32
5	110.10	53.60	110.65	53.37	119.99	49.43	199.71	15.84	237.30
10	144.60	47.70	142.74	48.38	160.46	41.97	232.94	15.75	276.50
20	178.79	40.00	184.37	38.13	195.04	34.55	251.24	15.68	297.97

The BS 7910 formulation produces higher reference stress values of approximately 15-20% above API 579-1/ASME FFS-1 for a crack depth between $0 < a/t < 0.5$. This result is contributed by the factor 1.2 on the membrane stress and the surface correction factor based on a rectangular shape (Eq.B.65). Removing this factor, reference stress results reach the API 579-1/ASME FFS-1 solutions. However, as shown on Figure 4.34, removing this factor tends to give smaller reference stress results than that of API 579-1/ASME FFS-1 for small crack length. Care has to be taken in this case. As mentioned in API 579-1/ASME FFS-1, for crack depth to thickness ratio $a/t > 0.5$, the surface correction factor used in BS 7910 gives more conservative results. In the case of $a/t = 0.8$, there is a difference of 35-50% on the reference stress between API 579-1/ASME FFS-1 and BS 7910 solutions. Here, the surface correction factor has a large influence on the final result. Assuming negligible bending stress, (Eq.B.65) and (Eq.B.68) reduce to:

- BS 7910

$$\sigma_{ref(P_b=0)} = 1.2 M_s P_m \tag{4.13}$$

- API 579-1/ASME FFS-1

$$\sigma_{ref(P_b=0)} = M_s P_m \tag{4.14}$$

As discussed previously, the factor 1.2 is applied to produce a similar level of conservatism that is inherent to the flat plate solutions. This increases directly the reference stress in BS 7910 by 20% compared to that in API 579-1/ASME FFS-1. This is shown in Figure 4.34 and Figure 4.35 for $0 < a/t < 0.5$. However for a ratio crack depth to thickness ratio greater than 1/2, surface correction factors used in BS 7910 give different results leading to the increasing difference in the reference stress.

4.4.5.3 Axial Surface Crack - Analytical solutions against experimental data from [136]

Pressure tests have been conducted on cylinders made of 4134V and 4130X steel rated for a 31 MPa service pressure [136]. Sharp, semi-elliptical surface axial cracks (0.076 mm

tip radius) were introduced by Electro-Discharge-Machining and data are summarised in Table 4.12 and Table 4.13. The cylinders were pressurized monotonically to failure with water or nitrogen gas and leak/break failure conditions are reported. The transition between these two failure modes in the experimental data was compared to the predictions based on the reference stress solutions in BS 7910 and API 579-1/ASME FFS-1. Cases have been plotted in a plane of hoop stress versus a/2c. A failure boundary has been developed using reference stress solutions, assuming a constant thickness, t, of 7.5 mm, inner radius, R_i, of 110.94 mm and crack depth, a, of 5.75 mm for the first case. The second case was prepared assuming a constant thickness, t, of 7.25 mm, inner radius, R_i, of 110.87 mm and crack depth, a, of 5.5 mm. Results are plotted in Figure 4.37 and Figure 4.38.

Table 4.12: Case 1 - Experimental data of leak/break tests on 4134V steel from [136]

Test N°	R_o (mm)	t (mm)	a (mm)	c (mm)	Re (MPa)	Rm (MPa)	P_{exp} (MPa)	Leak / Break
5	118.6	7.6	6.2	25.4	1097.1	1179.9	49.3	Leak
8	118.25	7.1	6.1	38.1	1097.1	1179.9	28.8	Leak
9	118.35	7.8	6.5	12.7	1097.1	1179.9	68.5	Leak
11	118.6	7.1	6.1	34.95	1097.1	1179.9	34.8	Leak
12	118.25	7.4	6.7	34.95	1097.1	1179.9	33	Leak
14	118.35	7.4	6.3	34.95	1097.1	1179.9	35.6	Leak
15	118.25	7.4	7.2	34.95	1097.1	1179.9	32.6	Leak
1	118.5	7.6	5.7	25.4	1097.1	1179.9	55.5	Break
2	118.5	7	4.3	12.7	1097.1	1179.9	64.2	Break
3	118.35	7.4	4.6	25.4	1097.1	1179.9	57.5	Break
4	118.35	7.5	5.2	25.4	1097.1	1179.9	52.3	Break
6	118.25	7.4	5.1	38.1	1097.1	1179.9	47.3	Break
7	118.5	7.7	5.5	38.1	1097.1	1179.9	45.1	Break
10	118.25	7.4	5.4	12.7	1097.1	1179.9	70.3	Break
13	118.1	7.5	5.2	34.95	1097.1	1179.9	48.4	Break

Table 4.13: Case 2 - Experimental data of leak/break tests on 4130X steel from [136]

Test N°	R_o (mm)	t (mm)	a (mm)	c (mm)	Re (MPa)	Rm (MPa)	P_{exp} (MPa)	Leak / Break
30747	118.1	7.4	4.9	25.4	648	783	41.5	Break
30835	118.1	6.8	5.2	25.4	648	783	37.1	Break
38444	118.1	7.2	4.8	50.8	648	783	33.2	Break
42934	118.1	6.9	4.6	68.6	648	783	27.9	Break
55172	118.1	7.2	5.5	50.8	648	783	35.7	Break
56792	118.1	7.6	5.1	76.2	648	783	32.7	Break
65284	118.1	7.2	5.5	76.2	648	783	24.6	Break
84065	118.1	7.1	5.4	68.6	648	783	25.2	Break
82915	118.1	7.4	6.3	76.2	648	783	21.4	Leak
83905	118.1	7.2	6.1	68.6	648	783	26.2	Leak
30933	118.1	7.3	6.2	25.4	648	783	38.3	Leak
45491	118.1	7.4	6.4	50.8	648	783	29.5	Leak

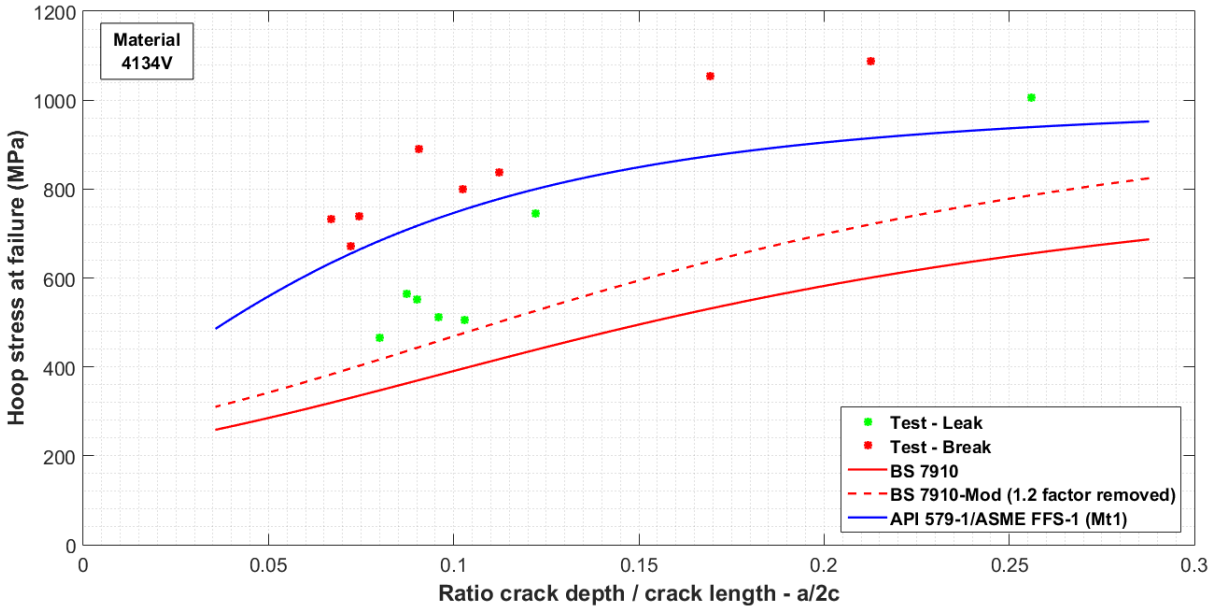

Figure 4.37: Experimental data and failure boundaries as per BS 7910 and API 579-1/ASME FFS-1 - Case 1 - Material = 4134V

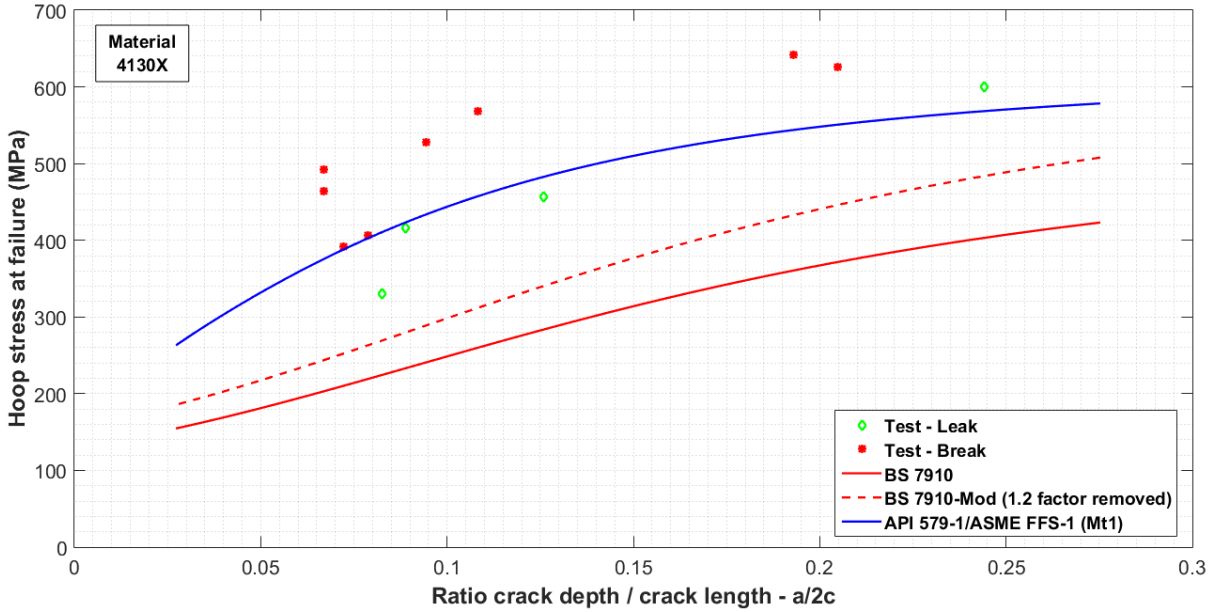

Figure 4.38: Experimental data and failure boundaries as per BS 7910 and API 579-1/ASME FFS-1 - Case 2 - Material = 4130X

The boundary created using recommended reference stress solution in API 579-1/ASME FFS-1 was found to successfully distinguish leak and break cases of the literature test data considered. On the other hand BS 7910 procedure was more conservative assuming leakage as failure. Removing the 1.2 factor applied on membrane stress (Eq.B.65) lead to a less conservative assumption but still excluded leaks ('BS 7910 – Mod').

4.5 Summary

In this chapter, the solutions from both BS7910 and API 579-1/ASME FFS-1, at both design or re-assessment stages have been analysed. All solutions from these standards used in this chapter are summarised in Table 4.14. The influence of the design code and associated safety margins is described in Section 4.2. Depending on the procedure used, the minimum required thickness differs slightly. ASME BPVC Section VIII - Division 1 results in the greatest thickness due to the safety margins employed. The other codes investigated gave similar results to each other. The design may affect the fracture behaviour. For a thin-walled structure containing a surface crack, the collapse limit of a ligament is usually the main cause of structure rupture. On the other hand, for a thicker structure, brittle fracture will have to be considered. In a two-parameter assessment such as the Failure Assessment Diagram, this can have a important effect. The final results will be more or less dependant on the couples stress intensity factor/fracture toughness or reference stress/yield strength parameters.

Leak-before-break parameters as described in established procedures have been evaluated for leakage and crack stability assessment. The COA results (Section 4.3), were provided for both inner & outer surfaces or mid-thickness (representing the averaged COA through-thickness) depending on the solution. All solutions investigated provided coherent results until half of the limit of applicability for both axial and circumferential cracks. It should be noted that BS 7910 solutions were developed for plates and corrected for cylindrical shapes. On the other hand, API 579-1/ASME FFS-1 have been developed for cylinders by FEA. For both axial or circumferential cracks, the stress-based solution from API 579-1/ASME FFS-1 gave greater values of COA than the pressure-based equation. After this limit, solutions begin to diverge. For axial cracks, BS 7910 and Zahoor solutions tend to give greater values of COA at mid-thickness (similar to API 579-1/ ASME FFS-1 at the outer surface). For circumferential cracks, BS 7910 and Paris-Tada solutions tend to give lower values than API 579-1/ ASME FFS-1 with a COA at mid-thickness lower than API 579-1/ ASME FFS-1 at the inner surface. The effect of plasticity has been evaluated for axial models. BS 7910 and Zahoor models include correction factors for small-scale yielding while API 579-1/ ASME FFS-1 propose a correction factor based on the plastic collapse assessment. This results in a wider range of application for the latter. Recalling that COA solution will be used to assess the leak rate which is a critical parameter in a LBB assessment, an over-estimation of the COA can lead to non-conservative result and vice-versa an under-estimation lead to a very conservative result. Only elastic models are presented compared to each other here. They are known to under-estimate the real COA for ductile materials.

In terms of crack stability (Section 4.4), different solutions provided for FAD (Section 4.4.2), SIF (Section 4.4.3) and RS (Section 4.4.4) have been evaluated. Four relevant geometries for LBB assessment have been chosen. For a given axial defect, BS 7910 tends to give greater values of reference stress for both through-thickness and surface defects. The multiplier of 1.2 introduced in the reference stress solutions, as such achieve a certain level of conservatism partially contributed to this observation. It should also be noted that in the original paper, this factor is not present. The other factor leading to an important difference is the correction factor employed. Analyses of the reference stress solutions for axial surface defects versus available experimental data show that API 579-1/ASME FFS-1 is found to successfully distinguish between leak and break cases. On the other hand, BS 7910 gives more conservative results, assuming leak as a fail or fracture result. This is also observed even after the removal of factor 1.2. For circumferential defects, when only membrane stress loading is considered, both standards give similar values in terms of reference stresses. However, when bending stress loading is applied, BS 7910 solutions tend to give higher reference stresses. It is worth noting that reference stress solutions recommended in BS 7910 are mainly from local limit load solutions, as they are more conservative. In leak before break assessments, since that the failure mode is pre-supposed to be ductile, the criteria for break will be based mainly on the reference stress solution. Therefore, BS 7910 is likely to be significantly more conservative than API 579-1/ASME FFS-1 for its break condition.

Table 4.14: Summary of API 579-1/ASME FFS-1 and BS 7910 solutions used in this chapter

Flaw type	Solutions	API 579-1/ASME FFS-1 [9]	BS 7910 [1]
ATWC	COA	Eq.B.12 or Eq.B.13 (Anderson, [137])	Eq.B.7 + Eq.B.8 (Wuthrich, [104])
	SIF	Eq.B.34 or Eq.B.36 (Green, [138])	Eq.B.33 (France, [139])
	RS	Eq.B.53 + (Eq.B.54, B.54 or Eq.B.56) (Miller, [140])	Eq.B.51 + Eq.B.52 (Willoughby, [135])
CTWC	COA	Eq.B.26 or Eq.B.27 (Anderson, [137])	Eq.B.24 + Eq.B.25 (Wuthrich, [104])
	SIF	Eq.B.40 or Eq.B.42 (Green, [138])	Eq.B.39 (France, [139])
	RS	Eq.B.59 (Zahoor, [134])	Eq.B.58 (Kastner, [141])
ASC	SIF	Eq.B.45 or Eq.B.46 (Anderson, [142])	Eq.B.44 (Newman, [143])
	RS	Eq.B.68 + (Eq.B.71 or Eq.B.72) (Willoughby, [135])	Eq.B.65 + Eq.B.66 (Willoughby, [135])
CSC	SIF	Eq.B.48 or Eq.B.49 (Anderson, [142])	Eq.B.29 (Newman, [143])
	RS	Eq.B.76 (Zahoor, [134])	Eq.B.74 (Kastner, [141])

In the light of the results presented within this study, the reference stress solutions for pipes/cylinders containing axial flaws should be re-evaluated in order to enhance the assessment capability. Validation of the solutions against other data from industry or research papers that include leak and break analysis would be beneficial in establishing a more accurate assessment of LBB. Further work to assess the effect of these difference on a full LBB case would be advantageous as well.

Chapter 5

Numerical Methods - Investigation of Ideal Through-Wall Cracks in Plates and Effect of Crack Shape in Cylindrical Components

Contents

5.1 Introduction

As discussed in Chapter 3, a conservative approach of the fracture side of an LBB assessment is to assume a larger flaw size than might be present. In other words, fracture could occur earlier than in reality. However, this exaggeration of crack length would over-estimate the leak rate from an actual crack size, whereas a smaller flaw size than anticipated will give a conservative prediction of leakage. It is therefore very important to determine the behaviour of crack size and shape accurately to ensure the most appropriate fitness-for-service assessment using LBB principles.

In a simplified analysis [60], an idealized through-wall crack with straight crack sides perpendicular to the surface is postulated. Such an assumption simplifies the analysis significantly. However, in reality, a surface crack that grows through the wall thickness and breaks through at its deepest point. At break-through, a given flaw may have a much longer length on the inner surface, and only a small crack length on the outer surface. The crack sides are not perpendicular to the component surface but are more likely to be steeply angled or curved. This results in a through-wall crack with different crack lengths on the internal and external surfaces. This crack eventually grows further to a shape which does become closer to an idealized through-wall crack. This is described more in details in Chapter 6. Experimental works to investigate crack growth shape due to fatigue loading have been carried out [144], [145], [111]. However, stress intensity factors (SIFs) and crack opening areas (COAs) of non-idealized through-wall cracks, which are essential in a LBB assessment, have often been underlooked since there are no available formulae to derive these parameters for non-idealised crack shape. These parameters are essential to predict the growth of an initial surface defect through a pipe wall to final failure.

In this chapter, FE models of idealized through-wall defects will be investigated and compared to existing solutions from BS 7910 and API 579-1/ASME FFS-1. These two procedures provide structural integrity assessment routes with different SIF and COA solutions, including LBB assessment for cylindrical components. The effect of through-wall cracks with shapes yet to become 'idealized' are also examined for their significance in an LBB assessment. Based on the findings, the significance of non-idealised crack is discussed. Table 5.1 gives a summary of all simulation models that are described in this chapter. It is worth pointing out that the consideration of the crack face pressure has been included in the work described in this chapter. If not stated, it is safe to assume that crack-face pressure has not been included.

Table 5.1: A summary of simulation models described in this chapter

Model N°	Description
PTW02	Plate with a through wall crack of 0.2 x Width long
PTW04	Plate with a through wall crack of 0.4 x Width long
PTW06	Plate with a through wall crack of 0.6 x Width long
PTW08	Plate with a through wall crack of 0.8 x Width long
CTWLX_1-X_2	Cylindrical component with a through-wall crack of length equal to $\lambda = X_1$ and ratio inner to outer crack length equal to X_2
X-CFP	Model X including crack face pressure
X-nCFP	Model X not including crack face pressure

5.2 Modelling methods - Benchmark using through-wall cracks in plates

5.2.1 Introduction

Finite Element Method (FEM) is a numerical technique that divides a whole problem domain into simpler and smaller parts, called finite elements. Approximate solutions are numerically integrated for partial differential or integral equations. A continuous physical problem is therefore transformed into a discretised finite element problem with unknown nodal values of a physical field. Values inside finite elements can be recovered using nodal values. The main sources of error are often round-off or discretization errors. Convergence study is often employed to overcome this limitation. Care has to be taken while pre-processing results as errors or bad hypotheses in the input data can produce highly incorrect or inaccurate results that may be easily overlooked or accepted as true. For this reason, in the first part of this work, a simple through-wall cracked plate model was prepared in order to validate the techniques used. All FEA work presented in this thesis has been modelled using Abaqus/CAE software. As with most FE software, Abaqus does not offer a built-in system of units. It allows flexibility to define the desired units. SI-system of mm was employed in this work and the units are given in Table 5.2.

Table 5.2: SI units used in FEA models

Parameter	**Length**	**Time**	**Mass**	**Density**	**Force**	**Pressure/Stress**	**Energy**
Unit	mm	s	tonne	tonne/mm^3	N	MPa	mJ

FEA has proven to be useful for computing custom crack solutions when there are no available solutions for component geometries. These custom solutions can provide more accurate evaluation than a standard simple geometry does. In this section, the methodologies employed for crack modelling are presented. Results obtained from idealised cases are compared to well-established solutions (i.e. BS 7910 or API 579-1/ASME FFS-1).

The parameters of interest are stress intensity factor (SIF), reference stress (RS) and crack opening area (COA). As part of the effort to validate the techniques used and to examine the means of deriving meaningful results and potential difficulties when creating a cracked model, a plate with a through-wall defect has been selected as benchmark. The geometry, material, meshing methodology, loading and boundary conditions are presented in this chapter. Post-processing and validation methods are also given for each parameter using various models. Elastic (for SIF and COA) and elastic-plastic (for RS) FEA have been carried out. The difference in values between analytical solutions and FEA are presented as:

$$\%Difference = 100 \times \frac{|FEA - Analytical|}{Analytical} \tag{5.1}$$

5.2.2 Presentation of models

In order to validate the techniques used to simulate cracked structures, a plate with a through-wall crack has been used as benchmark. The plate length, width and thickness were 400 mm, 100 mm and 15 mm respectively. Four different through-wall cracks were positioned at the middle of the plate, with lengths of 0.2W, 0.4W, 0.6W and 0.8W respectively (Models PTW02, PTW04, PTW06 and PTW08). A far field pressure of 100 MPa equivalent to a force of 150kN was applied as a ramp to both top and bottom surfaces. The material was assumed isotropic. For elastic properties, Young's modulus and Poisson's ratio were estimated to be 217147 MPa and 0.3 respectively (See Chapter 6). Von-Mises yield criteria and isotropic hardening were assumed in all elastic-plastic analyses (Section 5.2.3.2). At the same time, TWI ECA software CrackWISE®5 has been used to generate analytical solutions from BS 7910:2013. Elastic SIF, RS and elastic COA values were extracted for these four cases and compared to handbook solutions.

The step-by-step approach used in the numerical simulation is given in detail in the following section. In order to minimise calculation time but still maintaining sufficient accuracy, different strategies were employed. A solid uncracked plate part and a swept crack box were prepared independently (Figure 5.1). The crack box was then merged with the uncracked plate at the desired location in the assembly module. This allows a great flexibility to duplicate models in an efficient and reliable manner as compared to conventional. The different parameters (i.e. component/crack dimensions, partitions, material properties) can be changed rapidly and a new model re-constructed in seconds, without having to rebuilt a model from early beginning each time. The use of crack box also permits to keep similar features throughout the different models (i.e mesh or partition) and reduce the possibility of making mistake. Python scripting were used to develop plug-ins for this purpose. The use of symmetry planes allows users to model only one fourth of the whole plate (Figure 5.2). Another symmetry plane could have

been used (Z-symm), however, for other models presented later in the thesis, only quarter model reduction is possible. Another methodology is to impose a mesh transition from a fine mesh along the crack and around the crack-tip to a coarser mesh far from the crack. Partition toolset was used to divide the plate into different regions. Two swept regions were created to generate mesh transition through the thickness (y-z plane) and on the surface (x-y plane). This reduces significantly the number of elements and maintains a fine mesh in the area of interest.

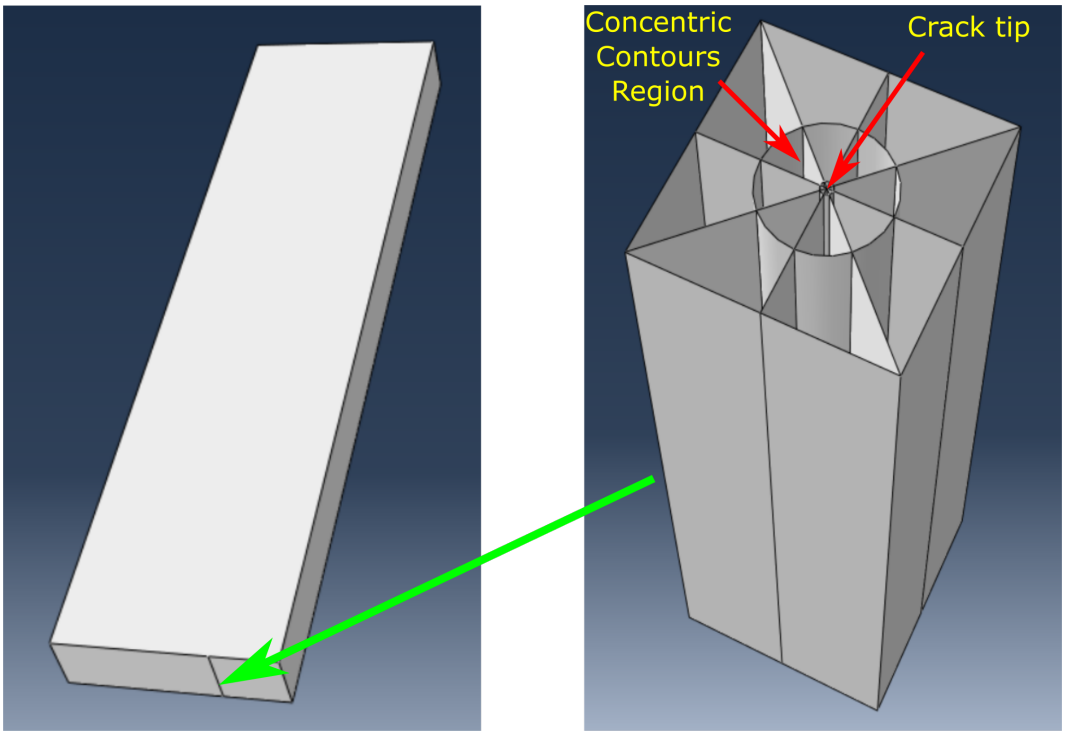

Figure 5.1: Modelling technique: (i) Uncracked plate and (ii) Crack Box

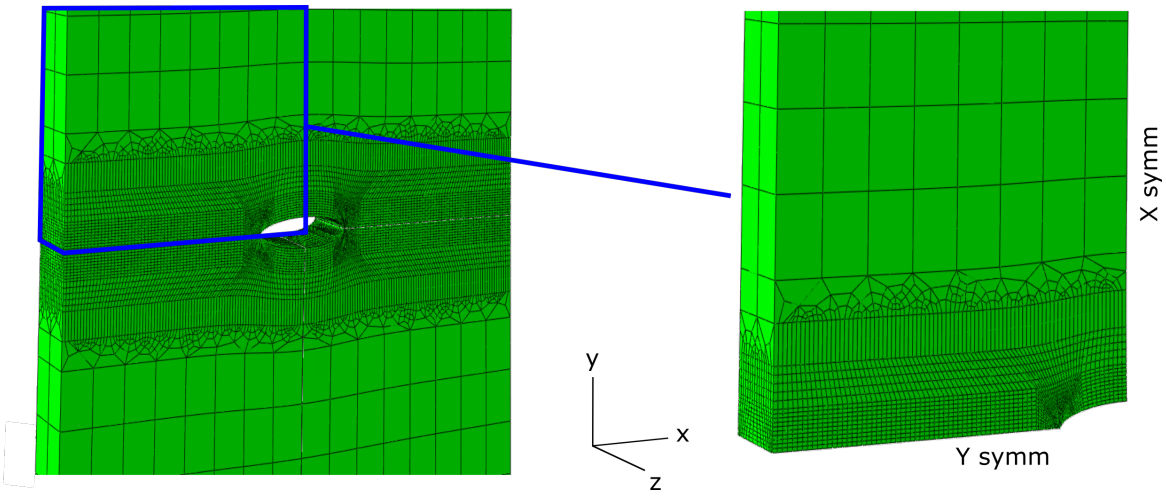

Figure 5.2: From full model to quarter model using symmetry plans - Model PTW02

For typical crack modelling, the most efficient mesh design for crack-tip region is spider-web configuration [146]. The model in Figure 5.3 consists of concentric rings of structured hexagonal quadratic elements (C3D20R) surrounding the first ring of swept wedge

quadratic element (C3D15) at the crack tip. In the first ring, a singularity was introduced to get more accurate stress/strain results at crack tip. Mid-side nodes were located at 1/4 element size from the crack tip for elastic models. When elastic-plastic conditions were considered, this singularity was moved to 1/2 element size as recommended in Abaqus documentation [146]. In addition, spider-web configuration was introduced to allow a smooth transition from a fine mesh at the crack tip (required to get accurate displacement fields) to a coarser mesh in the remaining bulk body. This resulted in concentric contours (integration domains). Eight different contours have been employed to compute J-integral, SIF and COA. As J-integral estimates may vary for different contours due to the approximate nature of finite element solutions. For this reason, the accuracy of these outputs had to be verified. One of the ways to do so was to examine the values of J-Integral across a few contours. Good accuracy in the results was observed as J-Integral values appeared approximately constant from one contour to the next. An example of convergence study is given in Section 5.2.3.1. Significant variations in J-Integral values may indicate errors in the definition of contour integral, and a finer mesh would be required to produce a more gradual change in the values. If plasticity were taken into account, the contour integral domain would have to include the whole plastic zone. Similar mesh pattern was used for other models (PTW04, PTW06 and PTW08). A mesh convergence study has been performed to verify the adequacy of this mesh.

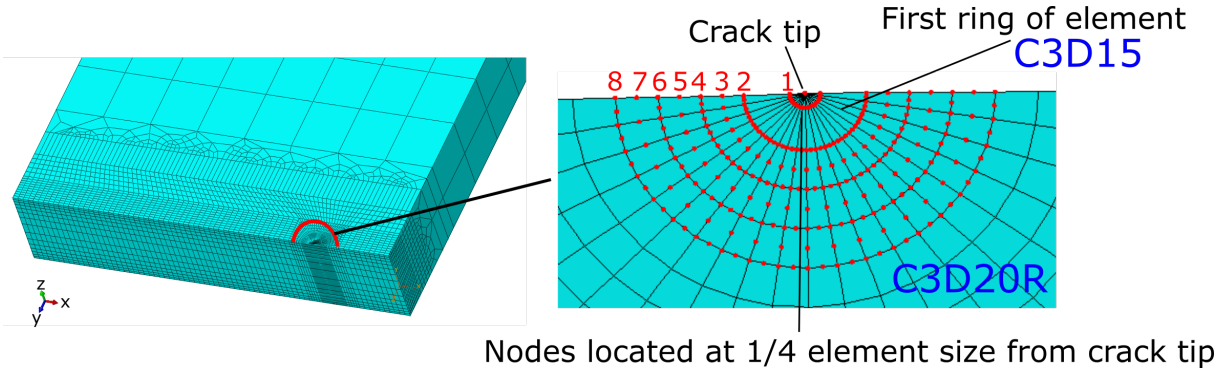

Figure 5.3: Mesh refinement, elements and contours used to compute SIFs - Model PTW02

5.2.3 Parameters investigated

5.2.3.1 Stress intensity factor (SIF)

Elastic SIF values were extracted at each node through the thickness for all the 8 contours using J-integral, assuming plane strain conditions, using the following equation:

$$K_I = \sqrt{\frac{E.J}{1-\nu^2}} \tag{5.2}$$

Convergence was also checked. For example, tabulated values of SIF for the model PTW02 with a crack length of 0.2W are given in Table 5.3 and the convergence for different contours is shown in Table 5.4. In both tables, the results are given for a normalized position through thickness. The nodes spacing is not constant due to the bias ratio employed in the mesh seeds. This mesh repartition allows more elements approaching the plate surfaces, where there is a greater variation in output values. This technique permits the introduction of more elements (i.e. more data points) where needed. As expected, Contours 1 and 2 do not present a stabilized solution as there is some difference in SIF values between these contours. Stabilization and path independence can be considered as acceptable when approaching Contours 3-4 with less than 0.1% variation and was fully stabilized in the 8th contour.

Figure 5.4 presents the SIFs values from FEA (PTW02, PTW04, PTW06 and PTW08) versus handbook solutions. These values were normalized at 1. The horizontal axis represents the normalized thickness and the vertical axis, the normalized stress intensity factors from FEA to those of BS 7910. It can be seen that results obtained from FEA are well in agreement with BS 7910 analytical solution. The mean difference is approximatively 0.2% excluding edge effects. Edge effects were expected as J-integral estimates may be inaccurate at the crack front ends due to the skewness of the external layers of elements [146] but this does not affect the accuracy at neighboring node sets. The last elements (two nodes) on both surfaces were then excluded. Numerical values for all the four cases are given in Table 5.5. The maximum values obtained using FEA are in good agreement with those obtained using BS 7910 handbook solutions.

Table 5.3: SIF values for 8 integral contours for model PTW02 (2a=0.2W)

Location	**FEA**								**CW5**	**Diff.**
(Norm)	**Ctr 1**	**Ctr 2**	**Ctr 3**	**Ctr 4**	**Ctr 5**	**Ctr 6**	**Ctr 7**	**Ctr 8**	**BS 7910**	**(%)**
0.00	625.8	642.8	645.2	645.7	645.7	645.5	645.2	644.9	703.9	8.38
0.03	645.0	670.9	671.9	672.4	672.7	672.9	673.0	673.1	703.9	4.37
0.06	662.0	691.8	693.9	694.2	694.3	694.3	694.3	694.3	703.9	1.36
0.11	668.1	697.2	699.5	700.1	700.3	700.4	700.4	700.4	703.9	0.49
0.16	671.5	700.6	702.9	703.6	703.9	704.0	704.1	704.1	703.9	0.03
0.23	672.7	701.7	704.2	704.9	705.2	705.4	705.5	705.5	703.9	0.23
0.32	673.0	701.9	704.5	705.2	705.6	705.7	705.8	705.9	703.9	0.28
0.43	673.0	701.7	704.3	705.2	705.5	705.7	705.8	705.9	703.9	0.28
0.57	673.0	701.7	704.3	705.2	705.5	705.7	705.8	705.9	703.9	0.28
0.68	673.1	701.9	704.5	705.2	705.6	705.8	705.9	705.9	703.9	0.29
0.77	672.7	701.7	704.2	704.9	705.3	705.4	705.5	705.5	703.9	0.23
0.84	671.5	700.6	702.9	703.6	703.9	704.0	704.1	704.1	703.9	0.03
0.89	668.2	697.3	699.5	700.2	700.4	700.4	700.4	700.5	703.9	0.49
0.94	662.0	691.8	693.9	694.2	694.3	694.3	694.3	694.4	703.9	1.35
0.97	645.0	670.9	672.0	672.4	672.7	672.9	673.1	673.2	703.9	4.37
1.00	625.9	642.8	645.2	645.8	645.7	645.5	645.2	644.9	703.9	8.38

Table 5.4: Contour independence validation for model PTW02 (2a=0.2W)

Location	Absolute difference between contours (%)						
	C1-C2	**C2-C3**	**C3-C4**	**C4-C5**	**C5-C6**	**C6-C7**	**C7-C8**
0.00	2.63	0.38	0.08	0.01	0.03	0.04	0.05
0.03	3.87	0.15	0.07	0.05	0.03	0.02	0.01
0.06	4.31	0.30	0.05	0.01	0.00	0.00	0.00
0.11	4.17	0.32	0.09	0.03	0.01	0.00	0.00
0.16	4.15	0.33	0.10	0.04	0.02	0.01	0.00
0.23	4.13	0.35	0.10	0.04	0.02	0.01	0.01
0.32	4.11	0.36	0.11	0.05	0.02	0.01	0.01
0.43	4.09	0.37	0.11	0.05	0.03	0.02	0.01
0.57	4.09	0.37	0.11	0.05	0.03	0.02	0.01
0.68	4.11	0.36	0.11	0.05	0.02	0.01	0.01
0.77	4.13	0.35	0.10	0.04	0.02	0.01	0.01
0.84	4.15	0.33	0.10	0.04	0.02	0.01	0.00
0.89	4.17	0.32	0.09	0.03	0.01	0.00	0.00
0.94	4.31	0.30	0.05	0.01	0.00	0.00	0.00
0.97	3.86	0.15	0.07	0.05	0.03	0.02	0.01
1.00	2.63	0.38	0.08	0.01	0.03	0.04	0.05

Table 5.5: Comparison of results from FEA and BS 7910 handbook solutions

Normalized crack length	FEA - Abaqus 6.13 ($MPa.\sqrt{mm}$)	BS 7910 - CrackWISE®5 ($MPa.\sqrt{mm}$)	Difference (%)
0.2	705.9	703.9	0.28
0.4	1088.9	1079.3	0.89
0.6	1569.3	1550.9	1.19
0.8	2522.9	2469.8	2.15

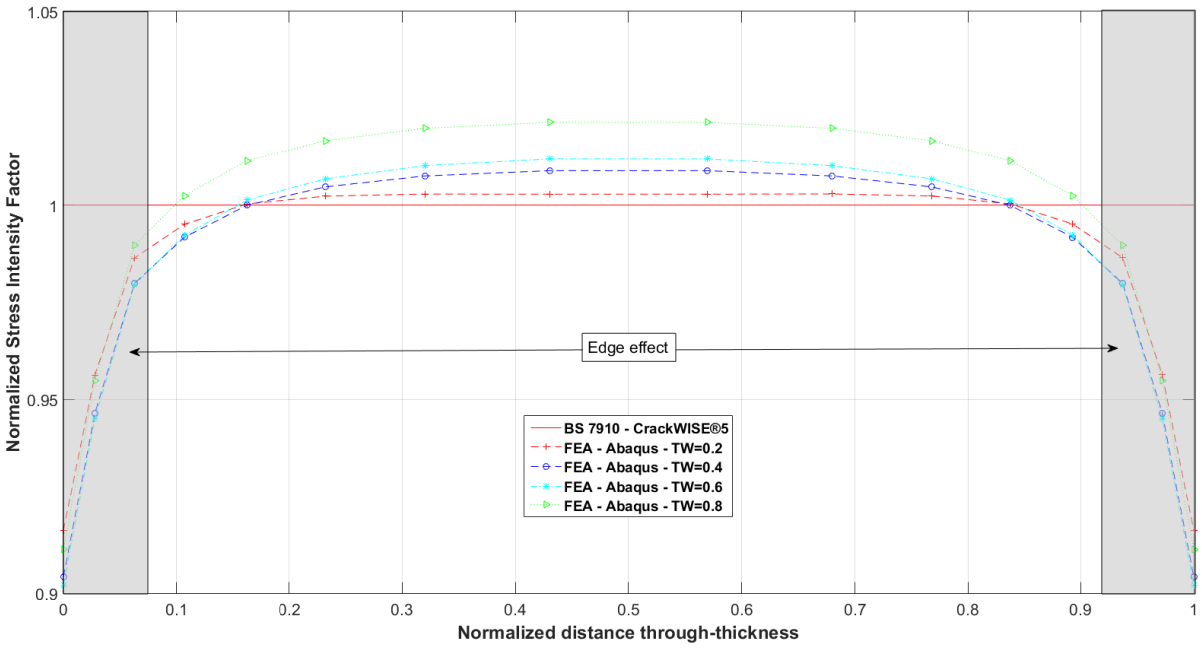

Figure 5.4: Comparison of normalized SIF determined from FEA and normalized BS 7910 handbook solutions

5.2.3.2 Reference stress (RS)

Calculation of reference stress solutions requires the elastic-plastic models. In order to compute elastic-plastic J-integral along the crack front, actual stress-strain data of the material are required. A common difficulty often encountered is to achieve sufficient convergence in analysis. Different calculation tasks that were used to compute reference stress from J-Integral values are presented in this section. Computed reference stress was used to determine plastic collapse ratio, L_r. When a tolerable crack is found during routine inspection, or when there is a need to evaluate a critical crack size for a given service life, ECA is performed by means of FAD. Plastic properties have been curve-fitted to be implemented into Abaqus. Analysis difficulties can occur when too many data points are used. It is important that plastic strain must stay in an ascending order, otherwise the analysis will not run. The best approach is to sample the strain-hardening data until a representative and acceptable curve is achieved. Figure 5.5 presents of plot of plastic strain versus true stress data used in Abaqus and the selected values are given in Table 5.6.

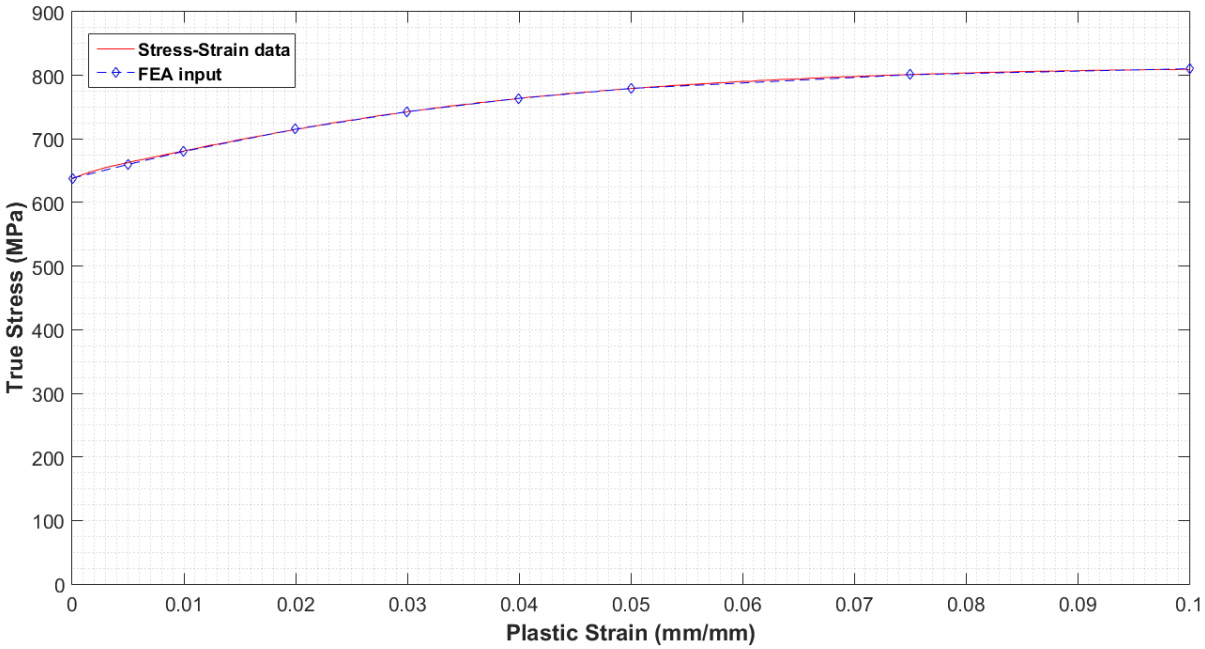

Figure 5.5: True stress – plastic strain curve for elastic-plastic finite element analysis

Table 5.6: Plastic properties employed for elastic-plastic models

True stress (MPa)	638.2	659.9	680.5	715.4	742.9	763.9	779.4	801.5	810.4
Plastic strain (mm/mm)	0	0.005	0.01	0.02	0.03	0.04	0.05	0.075	0.1

The elastic region of the total elastic-plastic J-integral plot. This was obtained by applying curve-fitting to the first few load increments of J-Integral values at a specific crack front location. The calculations can be performed for every node position at crack

front . Only at the crack front where J-Integral results were maximum at the final loading step were of interest. A quadratic curve fit was expected since J^2 is proportional to SIF, K, which is linear in the elastic region. Figure 5.6 shows a close-up of the first few increments of J-Integral (0 to 50 MPa). Quadratic curve fit has been applied to the first few data points (open red circles). The elastic J trend was computed using a second order polynomial fit. It was compared to the next several J increments (blue cross data points) to verify that these results were in the expected elastic range and that the curve-fit was valid.

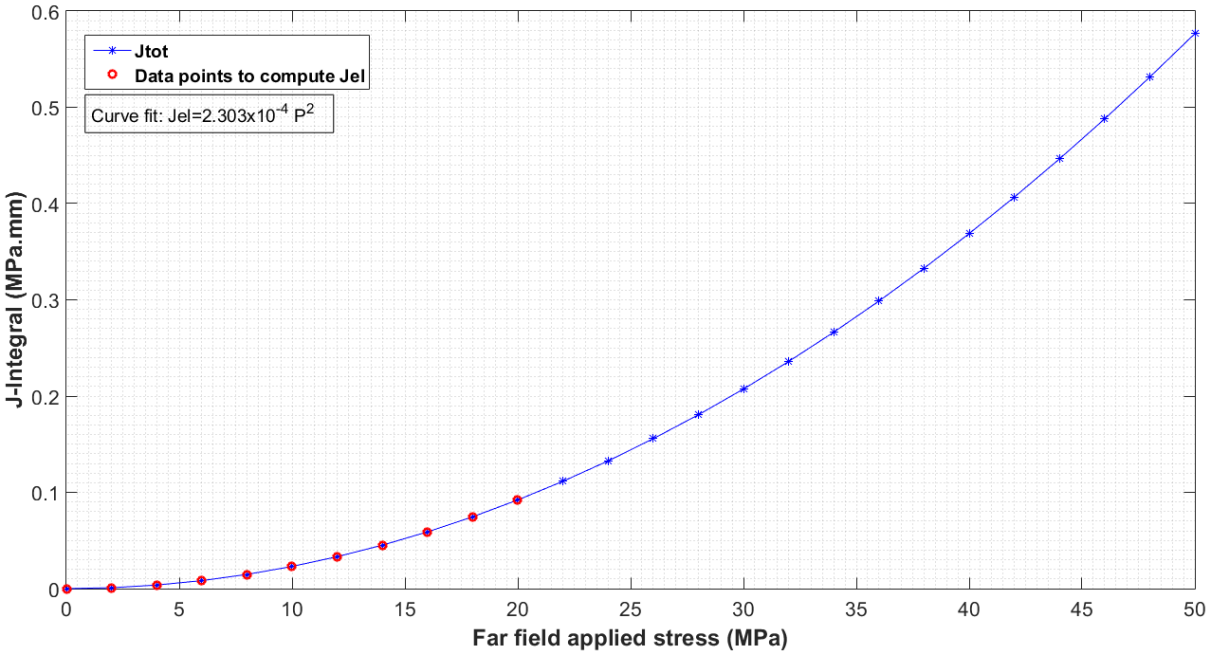

Figure 5.6: J-Integral quadratic curve fit to estimate elastic region - Model PTW02

As an effort to validate the curve fitting exercise, computed elastic J-Integral from an elastic-plastic model has been compared with a fully elastic model. Figure 5.7 shows both elastic J-Integral obtained from the first few data points of an elastic-plastic model with curve fitting (blue line) and from a fully elastic model (red line).

In a typical elastic-plastic analysis without a crack, the initial load increments can be large due to equilibrium convergence. However, for an elastic-plastic fracture analysis with a crack, several small load increments are required at the beginning of the analysis to ensure that it is posible to derive J-Integral values within the elastic range. The maximum load must be sufficiently high to create yielding at the crack front, which usually requires a much higher load than the operating or design load. In this work, the pressure applied at the plate ends for the elastic-plastic case has been increased to 800 MPa (i.e. a pressure of 100 MPa only was used for the elastic analysis). Figure 5.8 shows the elastic and elastic plastic J-Integral which are used to estimate the reference stress.

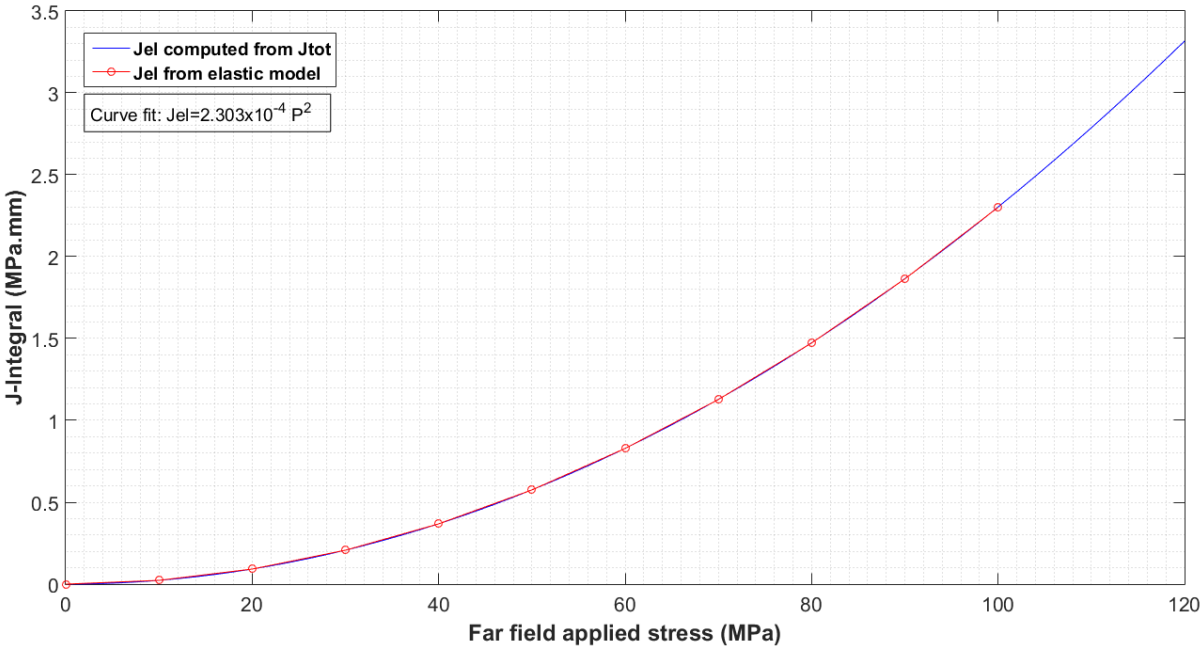

Figure 5.7: Comparison of elastic J-Integral from curve fit and FEA - Model PTW02

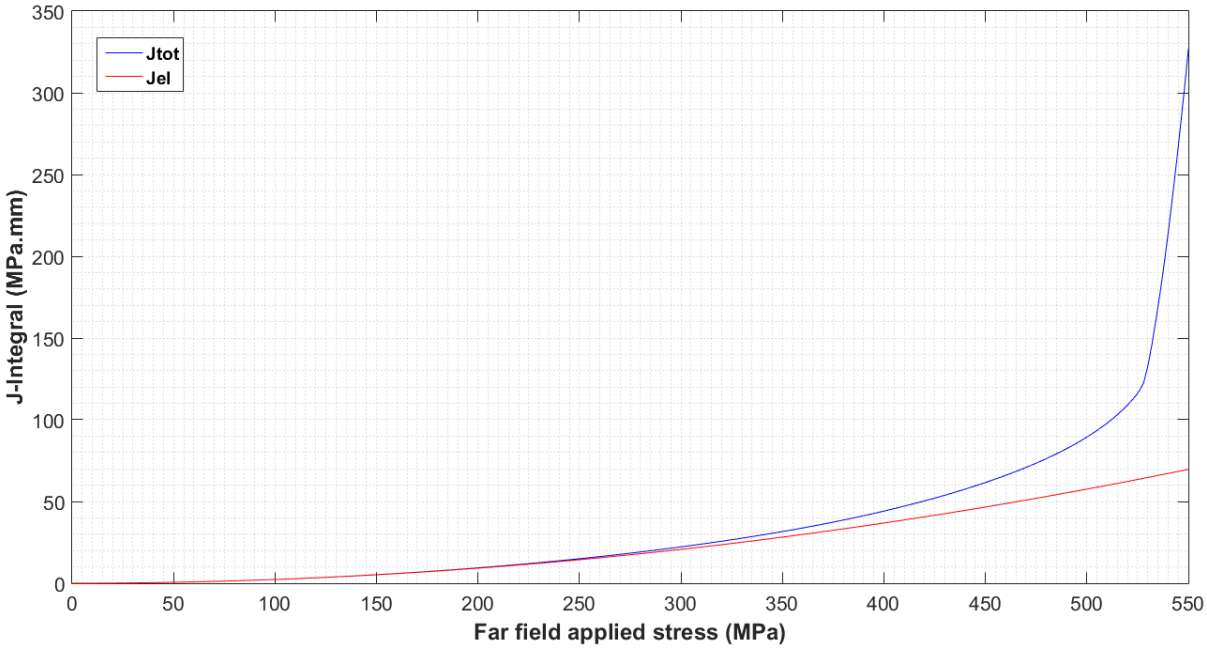

Figure 5.8: Illustration of the J_{total} and computed $J_{elastic}$ curves - Model PTW02

The nominal load value was obtained using the material-specific FAD equation evaluated at L_r=1 (nominal plastic collapse) [1]:

$$f(L_r) = \left(\frac{E\epsilon_{ref}}{L_r\sigma_{ys}} + \frac{L_r^3\sigma_{ys}}{2E\epsilon_{ref}} \right)^{-1/2} \tag{5.3}$$

When the material-specific FAD curve equation is evaluated at L_r=1, it results in:

$$\frac{J_{total}}{J_{elastic}}|_{L_r=1} = 1 + \frac{0.002E}{\sigma_{ys}} + \frac{1}{2\left(1 + \frac{0.002E}{\sigma_{ys}}\right)} \tag{5.4}$$

The value of $J_{total}/J_{elastic}$ evaluated at L_r=1 was calculated using modulus of elasticity, E, and yield strength, σ_{ys}. 0.002 is the nominal 0.2% offset strain at yield. This gives a $J_{total}/J_{elastic}$ ratio value of 1.978 using material properties described earlier. The nominal load was obtained at the intersection of this ratio with the $J_{total}/J_{elastic}$ ratio curve. In Figure 5.9 the material-specific ratio is shown by the horizontal red line, J-Integral ratio curve is the blue line, and the vertical green line represents nominal load value at the intersection between blue and red lines. In this analysis, nominal load of 528.75 MPa was applied to FEA models. If the maximum applied load was not high enough, elastic-plastic J-Integral values would not sufficiently large to obtain the intersection with material-specific J ratio. If the maximum J was not large enough, then elastic-plastic analysis was repeated with a higher maximum load so that J increases accordingly to evaluate the intersection point and thus obtain the nominal load. The nominal load was derived from the expected load at which L_r=1, where nominal plastic collapse occurs. The nominal load is typically higher than operating load. The nominal load was used to normalize the plastic collapse ratios.

The reference stress geometry factor, Y, is defined as the ratio of yield strength, σ_{ys}, to nominal load obtained at L_r=1, $\sigma_{nominal}|_{L_r=1}$

$$Y = \frac{\sigma_{ys}}{\sigma_{nominal}|_{L_r=1}} \tag{5.5}$$

The nominal load value, $\sigma_{nominal}|_{L_r=1}$, obtained from the intersection point in Figure 5.9, determines the reference stress that satisfies the material-specific FAD equation at L_r=1. It was also used to normalize the values at L_r axis. In this analysis the geometry factor Y is 1.207. Reference stress and L_r values can now be computed for each analysis increment to obtain case-specific and material-specific FAD values. The reference stress, σ_{ref}, at each load increment is given by:

$$\sigma_{ref} = Y\sigma_i \tag{5.6}$$

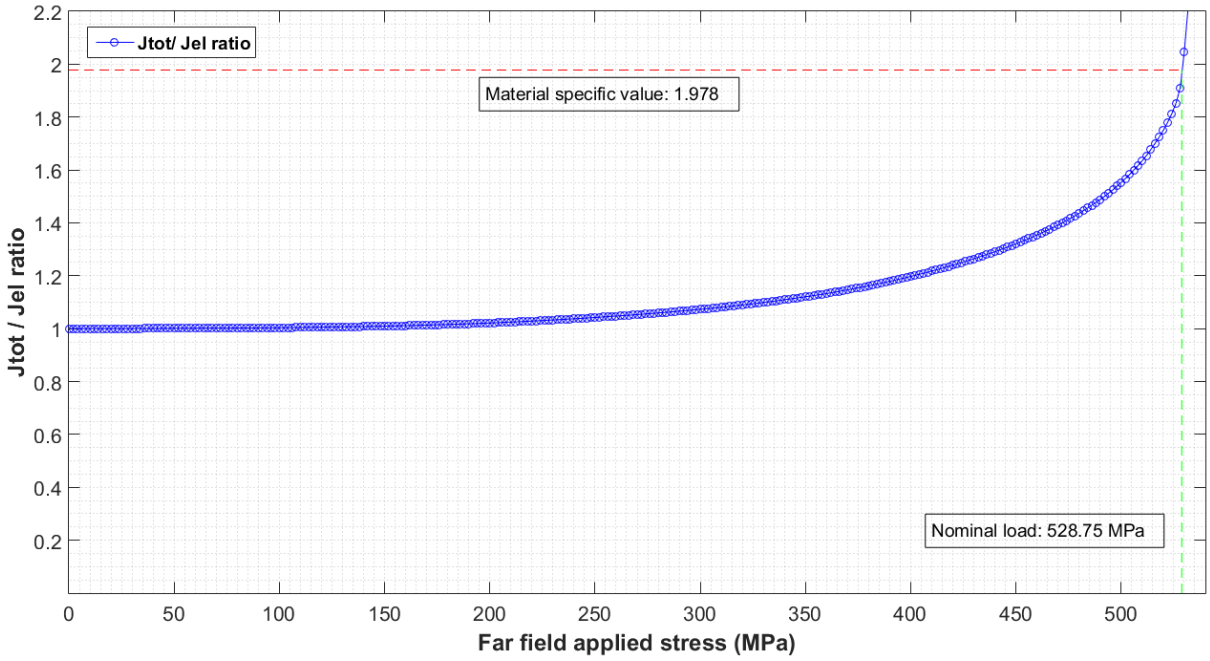

Figure 5.9: Derivation of the intersection between $J_{total}/J_{elastic}$ ratio and the material-specific value - Model PTW02

where σ_i is the load value at each load increment i. Reference stress can be computed for different loadings for a given geometry. Table 5.7 and Figure **??** present the results for the four plate geometries of interest.

Table 5.7: Comparison of reference stress determined from FEA and BS 7910 handbook solutions

Normalized crack length	Nom. Load (MPa)	Geom. factor Y	FEA - Abaqus 6.13 (MPa)	BS 7910 - CW5 (MPa)	Diff. (%)
0.2	528.75	1.21	120.70	125	3.44
0.4	406.42	1.57	157.03	166.67	5.78
0.6	271.08	2.35	235.43	250	5.83
0.8	137.60	4.64	463.81	500	7.24

5.2.3.3 Crack opening area (COA)

The calculation of COA is also not as direct as that of SIF. Displacements at every nodes along the crack would need to be extracted. Figure 5.10 presents a selection of the elements where the displacements were extracted. An accurate evaluation of the crack tip opening displacement (CTOD) around the crack tip is crucial as most of the crack opening will occur in this area. The mesh refinement in this area is therefore important. On the other hand, variation in the displacement is limited as it goes further.

As an example, a detailed description of the post-processing of FEA outputs is given for Model PTW02. In order to derive crack opening area, the CTODs have been extracted

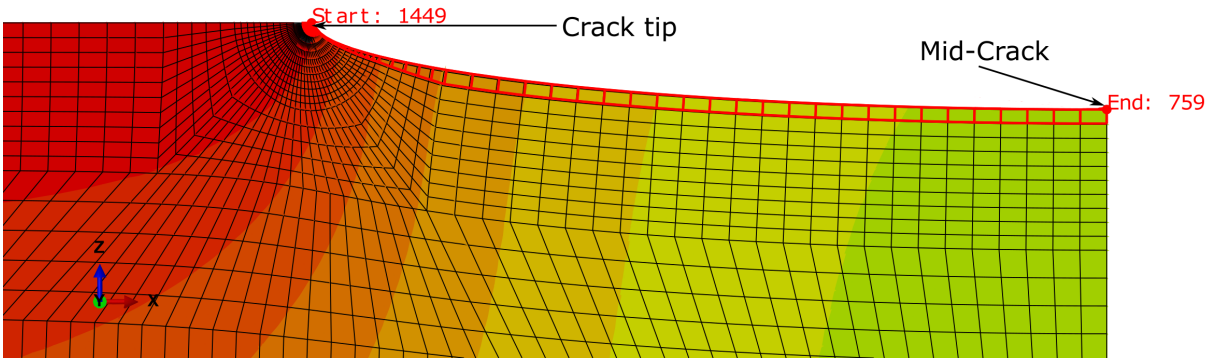

Figure 5.10: Displacement field along the half-crack length from FEA

for each nodes along the half-crack length. As previously mentioned, the COA from FEA was determined by integrating these CTOD values along the crack length. As the CTODs values are dependent on the mesh, cubic data interpolation has been used to reduce the distance between each extracted value. This allows a more accurate area calculation using trapezoidale rule. An example is provided in Figure 5.11.

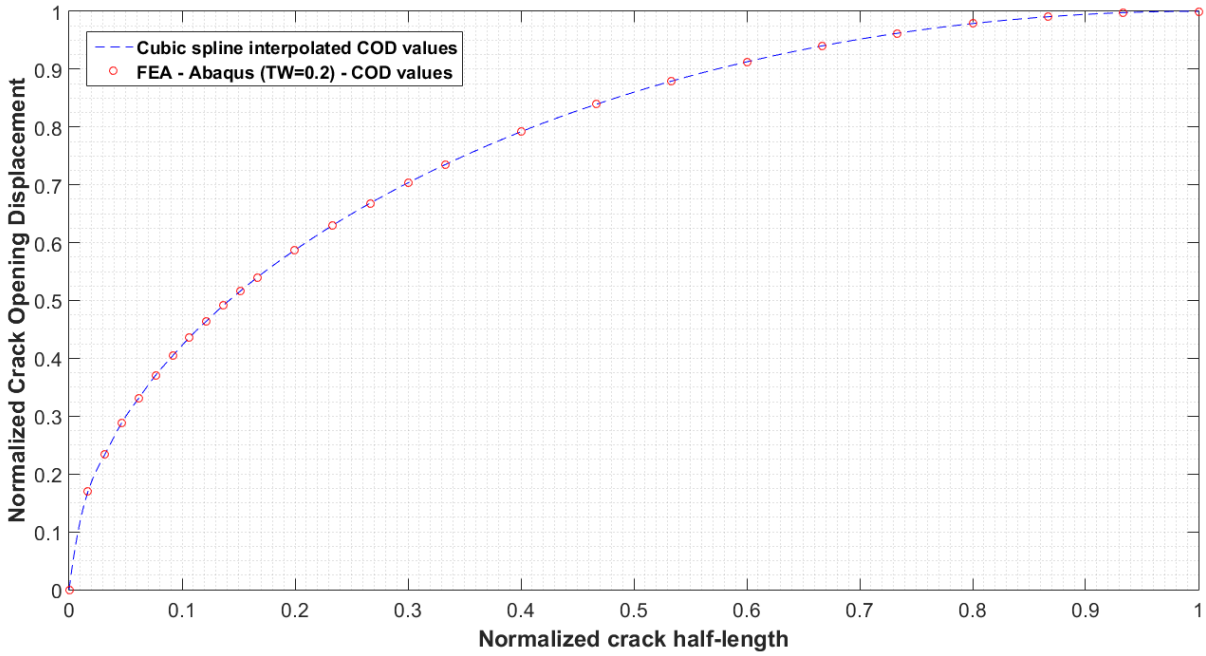

Figure 5.11: Crack opening displacements extracted from FEA and cubic spline interpolation along the crack half-length - Model PTW02

From the interpolated values of CTODs, a trapezoidale rule (Eq.5.7) has been used to calculate the opening area between each extracted values along the crack half-length. The distance between two location is defined by a segment [a,b] and its corresponding CTODs by the couple [f(a),f(b)].

$$Area = (b-a)\left(\frac{f(a)+f(b)}{2}\right) \tag{5.7}$$

The sum of these small increment areas is only a quarter of the total value of crack opening area. This required multiplication by four due to the symmetrical assumptions in the FEA models. Assuming an elliptical shape, the crack opening area is often calculated with Eq.3.6 (See section 3.5).

Table 5.8: Comparison of analytical solution from BS 7910 and FEA results for COA calculation

Crack length $2a/W$	Analytical COA (mm^2)	COA from FEA (mm^2)	Difference (%)
0.2	0.68	0.67	0.84
0.4	2.96	2.94	0.51
0.6	7.77	7.77	0.10
0.8	18.50	18.73	1.25

5.2.4 Discussion

Different techniques have been employed to calculate the parameters of interest in a LBB assessment. A plate with a through-wall crack has been taken as benchmark to compare the results obtained using FEA with existing solutions from BS 7910. Four different crack sizes have been considered (PTW02, PTW04, PTW06 and PTW08). A summary of the findings is given below:

- Model preparation: Different strategies have been used in this validation section to create FEA models. The utilization of symmetries and mesh strategy have been detailed. Symmetries have been used to reduce model size. Partitions and mesh swept also helped to reduce the number of elements in the models, focussing on the region of interest. An efficient manner to prepare the models was to create two parts independently, namely: (i) uncracked plate and (ii) crack box (See Section 5.2.2). This allows quick modification to the position of the through-wall crack in the plate without having to repeat the effort to create models. Development of Python script offers users a great flexibility in model generation and is extremely time-effective when similar models are required.

- Stress intensity factor: Stress intensity factors have been determined from J-Integral values. These values have been compared with SIF from Abaqus/CAE output. Convergence study on eight contours has been detailed. Results were similar to those using analytical solutions of BS 7910 with a maximum difference of 2% for the longest crack.

- Reference stress: Plastic properties were required for calculation of reference stress. Loading was applied in excess to achieve the desired nominal load. The elastic region of J-Integral was inferred by curve-fitting from elastic-plastic J-Integral. Material-specific FAD curve equation was established at L_r=1 to determine the nominal load required for the calculation of reference stress. The values were slightly lower than those determined using handbook solutions of BS 7910 with a maximum difference of 7% for the longest crack.

- Crack opening area: Crack opening area was calculated from crack opening displacements along the crack front. Cubic spline data interpolation has been used to sample the extracted displacement into a finer set of values. The area of the crack opening was then estimated using trapezoidal rule. These values were similar to the analytical solution in BS 7910 Annex F with a maximum difference of 1% for the longest crack.

- Post-processing: All three parameters described above requires post-processing of FEA output. Excel and Matlab spreadsheets have been prepared to assist the synthesis of Abaqus outputs. SIF have been calculated using J-Integral values and had to be converted using the relationship between them. RS calculation requires several steps to determine the nominal load for the material and specific case. COA were calculated from CTOD and integration was necessary.

This first section focussed on the modelling techniques and their validation compared to analytical solution. The different parameters of interest have been calculated with confidence from FEA with the methodologies described above. Post-processing of FEA output was performed using Excel or Matlab. Based on observations from Chapter 4, SIF and COA solutions from FEA were found in good agreement with analytical solutions. However reference stress solutions showed more discrepancy in values. The development of plug-ins using Python script proved to be highly time-saving and offers great flexibility in model generation. The next section will focus on cylindrical components. Similar techniques will be detailed to validate solutions for idealized through-wall cracks. Investigation on the effect of crack shape on SIF and COA will also be discussed.

5.3 Investigation of crack shape influence (cylinders)

5.3.1 Models transformation - From plate to cylinder

Two techniques were employed to generate cylindrical component models: (i) a similar plug-in for cylinder or (ii) transform plate model into cylinder by mapping the coordinates. The first technique was presented in detail in Section 5.2.2. Similar plug-in was developed for cylinders. The second technique is presented in this section. An initial plate model has been created based on the final desired cylinder geometry using the plug-in developed and described in Section 5.2.2. Once meshed, the plate model was transformed into cylinder by mapping the mesh into a cylindrical system as seen in Figure 5.12.

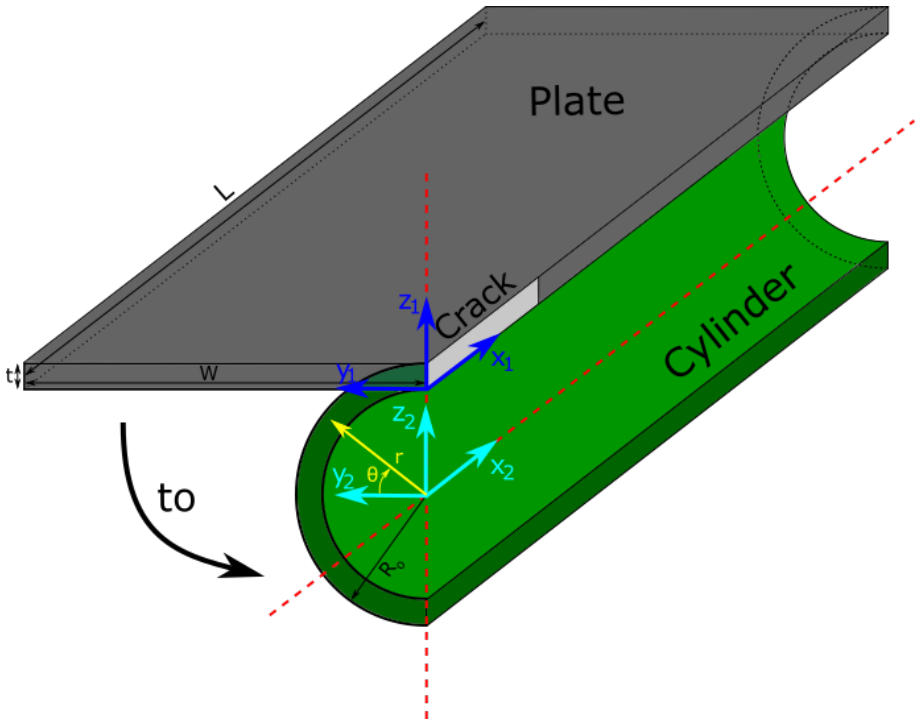

Figure 5.12: Strategy from to transform plate geometry into cylinder geometry

Because the cylinder was generated from a plate model, the dimensions had to be defined accordingly. The plate length, L, and thickness, t, had to be equal to the cylinder dimensions. The plate width, W, should be half the circumference of the cylinder:

$$W = \pi R_o \tag{5.8}$$

Only the y–z cross section was transformed. The cracked face of the plate was fixed and the other end was bent into a cylinder. This allows a convenient location as a reference point for the local plate-coordinate system (x_1, y_1, z_1) in the global pipe-coordinate system

(x_2, y_2, z_2). Figure 5.12 gives an overview of the coordinate systems. The mathematical transformations followed the steps below:

1. The coordinate system of the plate was moved from the corner of the plate to the center of the cylinder:

$$y_2 = y_1 - R_o + t \tag{5.9}$$

2. The nodes were converted from the plate coordinate system (dark blue) to the cylindrical one (yellow):

$$r = R_i + y \tag{5.10}$$

$$\theta = \frac{y_1}{W} + \frac{\pi}{2} \tag{5.11}$$

3. The nodes coordinates must also be transferred from the cylindrical coordinate system (yellow) to the global rectangular one (cyan):

$$y_2 = rsin(\theta) \tag{5.12}$$

$$z_2 = rcos(\theta) \tag{5.13}$$

As the cracked face was kept stationary, the coordinates on x-axis remained the same:

$$x_2 = x_1 \tag{5.14}$$

It is worth pointing out, that special attention must be paid to the final coordinates of the nodes. Due to rounding errors resulting from the multiplication by pi, some values have to be correct to construct a proper cylinder. Numerical adjustment had to be implemented for very small values.

5.3.2 An ideal axial through-wall crack in cylinders

5.3.2.1 Presentation of models

In an LBB assessment, one of the recommended methods is to re-categorize a surface crack approaching through-thickness (about 80% wall-thickness) as a through-wall crack. This section will focus on axial through-wall cracks in cylindrical components. The same material properties and techniques used in the assessment of plates in Section 5.2.2 were employed. Numerical results were compared with handbook solutions for SIF and COA given in both BS 7910 and API 579-1/ASME FFS-1. Three locations of concern are referred as: (A) at internal radius, (B) at mid-thickness and (C) at external radius (see

Figure 5.13). TWI software CrackWISE®5 was used to generate BS 7910 handbook solutions, while API 579-1/ASME FFS-1 solutions were performed using Matlab.

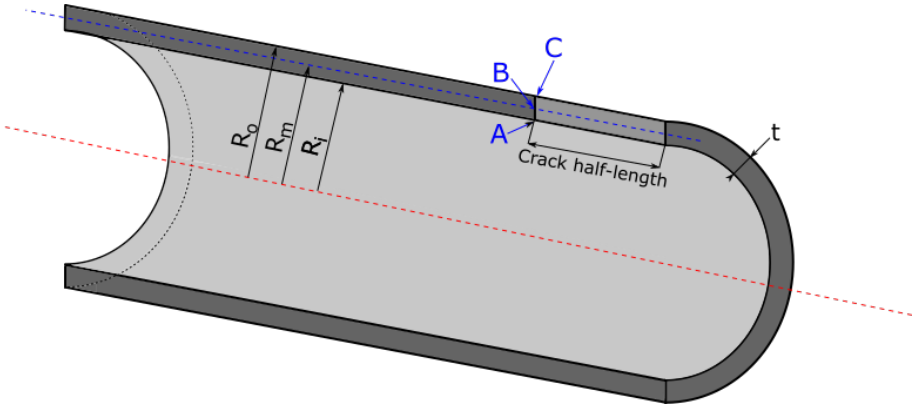

Figure 5.13: Illustration of various geometrical parameters of interest

Three-dimensional, elastic FE analyses were carried out using ABAQUS 6.13. Figure 5.14 illustrates a cylinder with idealized and non-idealized axial through-wall defects of different flaw dimensions. The inner radius,R_i, and wall-thickness, t, were assumed to be 200 mm and 10 mm respectively. The non-idealized defect was characterized by its length on each side of the cylinder ($2a_i$ and $2a_o$) while the idealized by its length, $2a$. In both cases, the crack front was assumed as a straight line and the crack length was normalized as:

$$\lambda = \frac{a}{\sqrt{R_m t}} \tag{5.15}$$

Three different crack lengths (λ = 1,2 and 4) have been studied with different a_o to a_i ratios. A plug-in has been prepared using Abaqus GUI toolkit [146], to facilitate model generation in a more time-efficient manner. This plug-in offers the advantage to define the main parameters which the user wishes to modify without the need to re-construct a new model. Mesh has also been optimized to reduce the number of elements and to increase accuracy. Sensitivity study has shown that a better option was to reduce the number of elements per contour and to use double bias seed (Abaqus function) along the thickness, such that the stress distribution through the thickness could be captured.

Figure 5.15 shows a typical FE mesh used for the cylindrical models described in this section. Quarter models were employed by exploiting the advantage of the symmetrical boundaries. Reduced integration 20-nodes brick elements (C3D20R) were used for the model. The crack-tip was modelled with a spider-web configuration consisting of swept wedge quadratic element (C3D15). Homogeneous, isotropic linear elastic material was assumed with a Young's modulus of 217 GPa and a Poisson's ratio of 0.3. Internal pressure, P, of 2.5 MPa was applied to the inner surface of the cylinder. The elastic J-integral along the crack front was determined as the mean value of the 4th–5th contours.

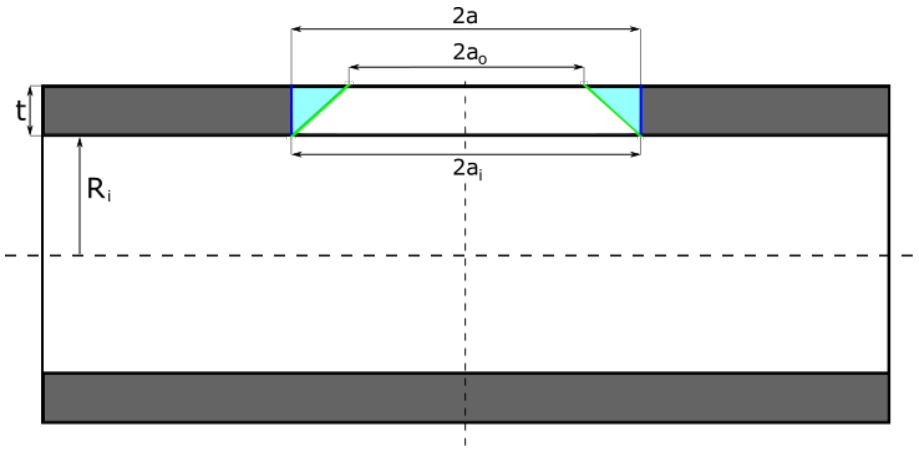

Figure 5.14: Schematics of ideal and non-ideal axial through-wall cracks in a cylinder

Path independence was achieved with a difference of up to 1%. The elastic SIF was then determined assuming plane strain conditions.

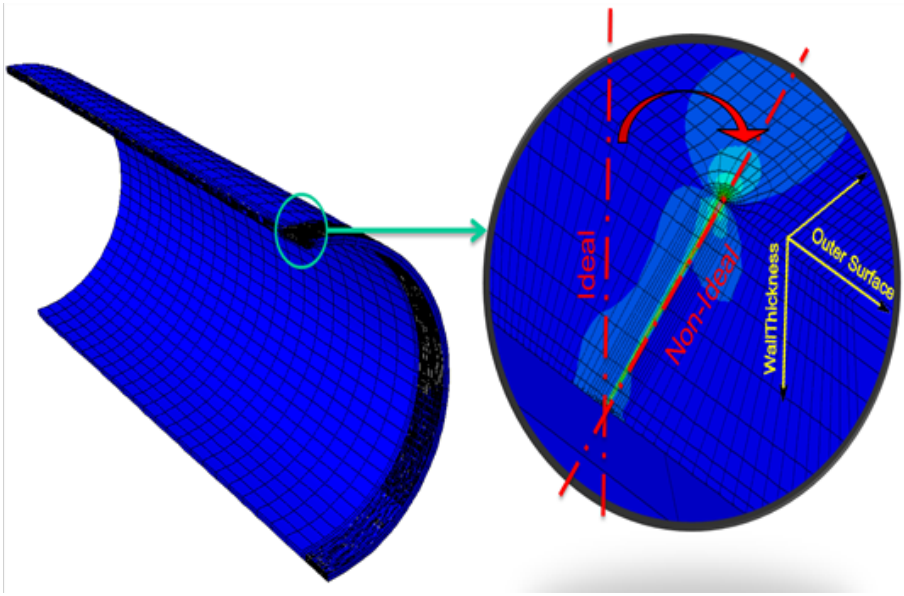

Figure 5.15: Typical FE mesh employed in this Chapter

The elastic COA was determined at the inner, mid and outer surfaces by integrating the crack opening displacements along the crack length. SIF and COA values obtained from idealized through-wall crack were compared with the existing solutions. TWI software CrackWISE®5 and Matlab have been used to generate BS 7910 and API 579-1/ASME FFS-1 solutions. Equations employed can be found in Appendix B respectively.

5.3.2.2 Discussion on handbook formulations

Based on the comparison work presented in Chapter 4, the following observations have been made:

- Stress intensity factors solutions given in both procedures are expressed in the same manner i.e. membrane and bending stresses with correction factors derived from FEA. They are defined as M and G in BS 7910 and API 579-1/ASME FFS-1 respectively.
- API 579-1/ASME FFS-1 solutions also include a crack face pressure term (p_c). BS 7910 explicitly states that its solutions do not account for this effect, considering it negligible. The effects of crack face pressure were included and studied in some cases.
- API 579-1/ASME FFS-1 solution for internal pressure only has included this crack face pressure by incorporating external radius in its formulation.
- The formula given in BS 7910 employs mean radius whereas API 579-1/ASME FFS-1 solutions are generally accounting for internal radius

The implication of using either mean radius or internal radius ought to be investigated prior to progressing into more complicated solutions. As far as internal pressure is concerned, the bending stress can be assumed to be negligible and the membrane stress is equal to hoop stress using thin shell theory which is given as (PR)/t. However, depending on the procedure, the use of which radius to use was questioned. While API 579-1/ASME FFS-1 recommends calculating membrane stress using the internal radius, the mean radius is implicit in thin shell theory. Simulations have been conducted using the following three formulae:

- Case 1: $P_m = (PR_i)/t = 50$ MPa
- Case 2: $P_m = (PR_m)/t = 51.25$MPa
- Case 3: $P_m = (PR_o)/t = 52.5$ MPa

The following trends can be observed from evaluations previously discussed:

- When comparing P_m derived from internal, mean or external radius, a higher membrane stress produces a similar gradient in the SIFs through the component thickness but with an offset at a higher value.
- Variation of SIF through the thickness does not exhibit the same behaviour when assessed using both procedures. Using BS 7910 solution as reference, API 579-1/ASME FFS-1 solutions show more significant variation through the thickness, giving lower values than those of BS 7910 at the internal surface and larger at the external surface.
- Assuming the stresses are higher at the external surface, it is apparent that BS 7910 solution (Case 2) and API 579-1/ASME FFS-1 solutions (Case 1) give almost identical values at the outer surface.
- BS 7910 provides a list of different references for different COA models and a solution at mid-thickness from the literature is given. SIF calculations were derived assuming mean radius.

- API 579-1/ASME FFS-1 provides its own COA solutions, for both internal and external surfaces of an idealized crack.

5.3.2.3 Validation of cylindrical models and CFP effect

Based on the geometrical and loading conditions described earlier, two different simulations (models X-CFP and models X-nCFP) have been prepared with and without crack face pressure (Figure 5.16). In model CTWL2-Id-nCFP, internal pressure was applied only to the internal surface of the cylinder and the crack face was kept free of loading .

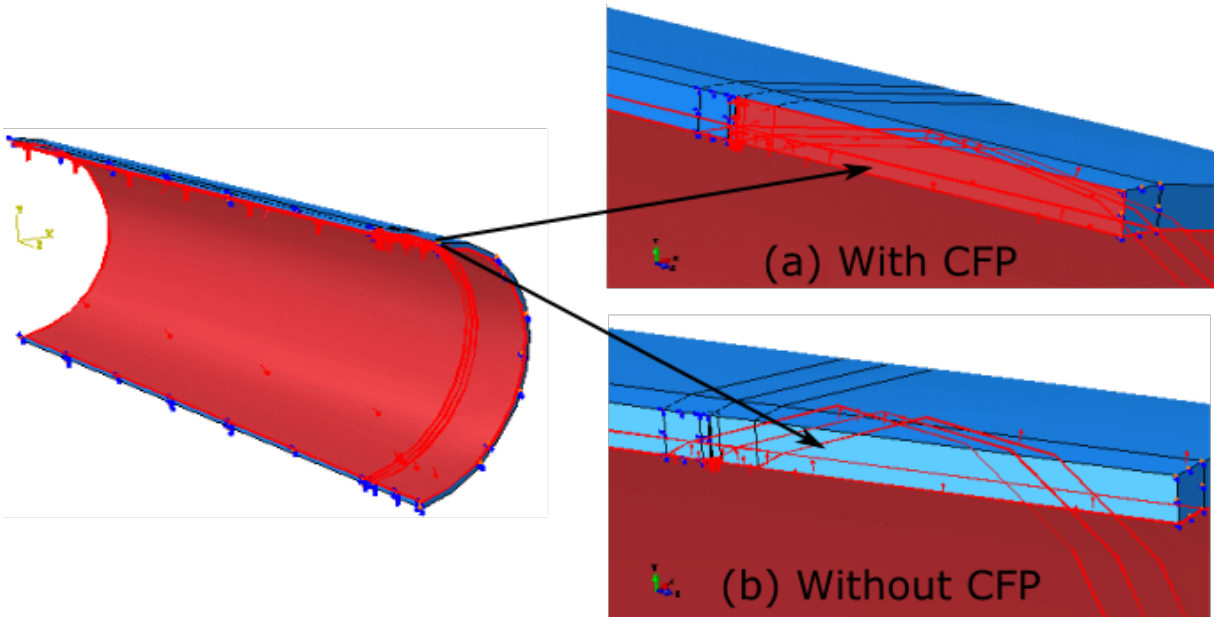

Figure 5.16: Cylindrical component under internal pressure: (a) with crack face pressure and (b) without crack face pressure

Abaqus allows the extraction of both SIF K_I values directly or J-Integral along the crack front. Figure 5.17 shows a typical through-thickness SIF profile. Both direct K_I and J-integral extraction are presented: the red line is SIF derived from J and the blue line is the direct K_I extraction. Both results show very identical values through section thickness. As the values of K_I and SIF derived from J are very close, only J-Integral results based on the fifth contour are presented here.

Using the normalized values of FEA-derived SIFs as reference, Figure 5.18 presents the solutions given in both procedures for Case 1 and Case 2 (as defined in Section 5.3.2.2). BS 7910 solution (using mean radius, R_m) gives the closest value to that of FEA all along the thickness, while API 579-1/ASME FFS-1 solution(R_m) solution agrees up to 60% thickness. It is also evident that API 579-1/ASME FFS-1 (R_i) solution converges to BS 7910 (R_m) solution as it approaches the external radius.

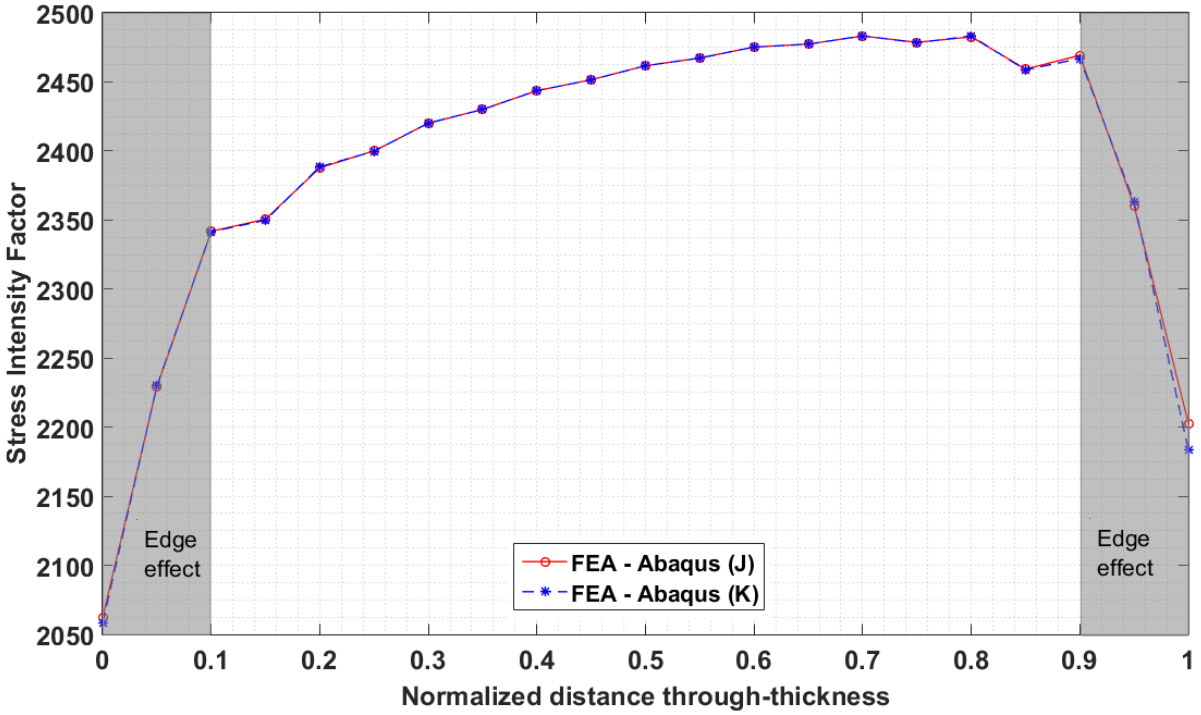

Figure 5.17: Typical FEA computed SIF (K_I and J) for a through-wall crack in a cylindrical component

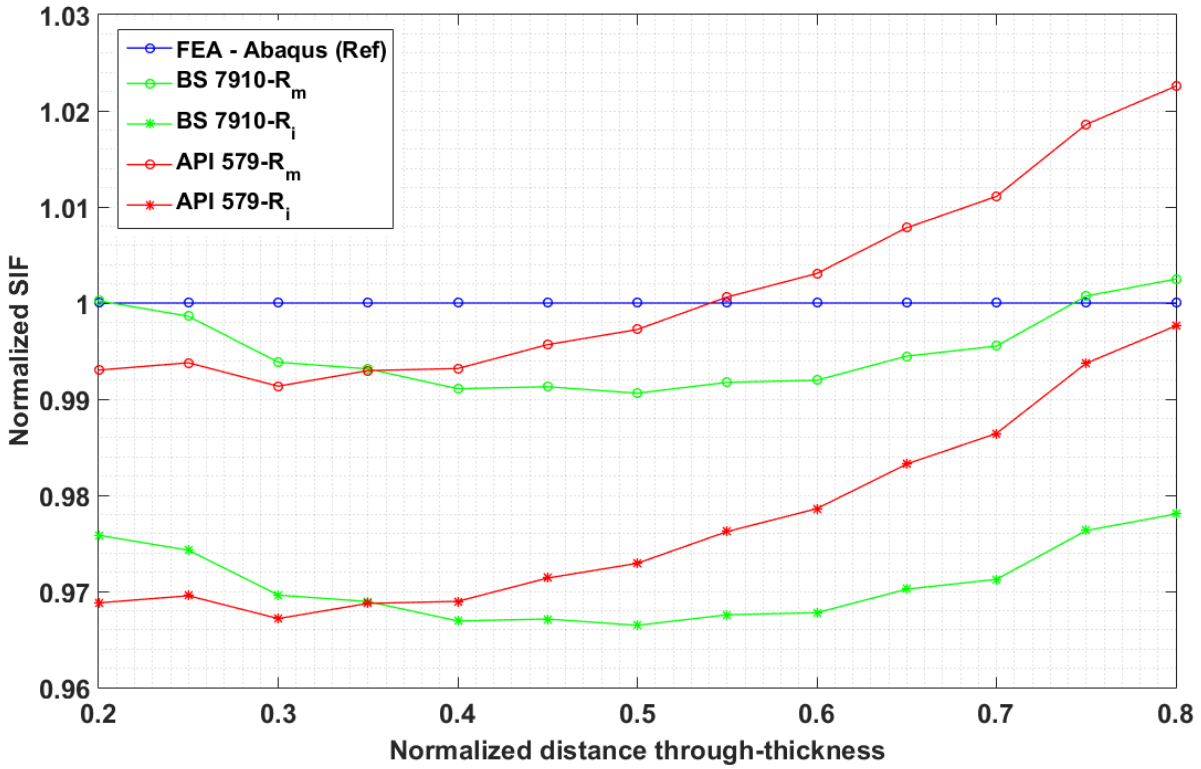

Figure 5.18: A comparison between FEA-derived and handbook SIF solutions (No CFP)

The crack face pressure term is often associated with membrane stress component in API 579-1/ASME FFS-1 solution. The addition of crack face pressure was expected to increase the SIF values compared to the solution without crack face pressure. Figure 5.19 presents the FEA results concerning the aspect of solutions through the thickness. Values derived from both handbook solutions and FEA were normalized and plotted along the thickness. Similar observations reported in Section 5.3.2.3 can be made. As expected, if crack face pressure has been included, API 579-1/ASME FFS-1 solutions are able account for it while BS 7910 solution do not. The values derived using BS 7910 solutions are therefore the lowest among those of FEA and API 579-1/ASME FFS-1 with additional crack face pressure which produces the highest value.

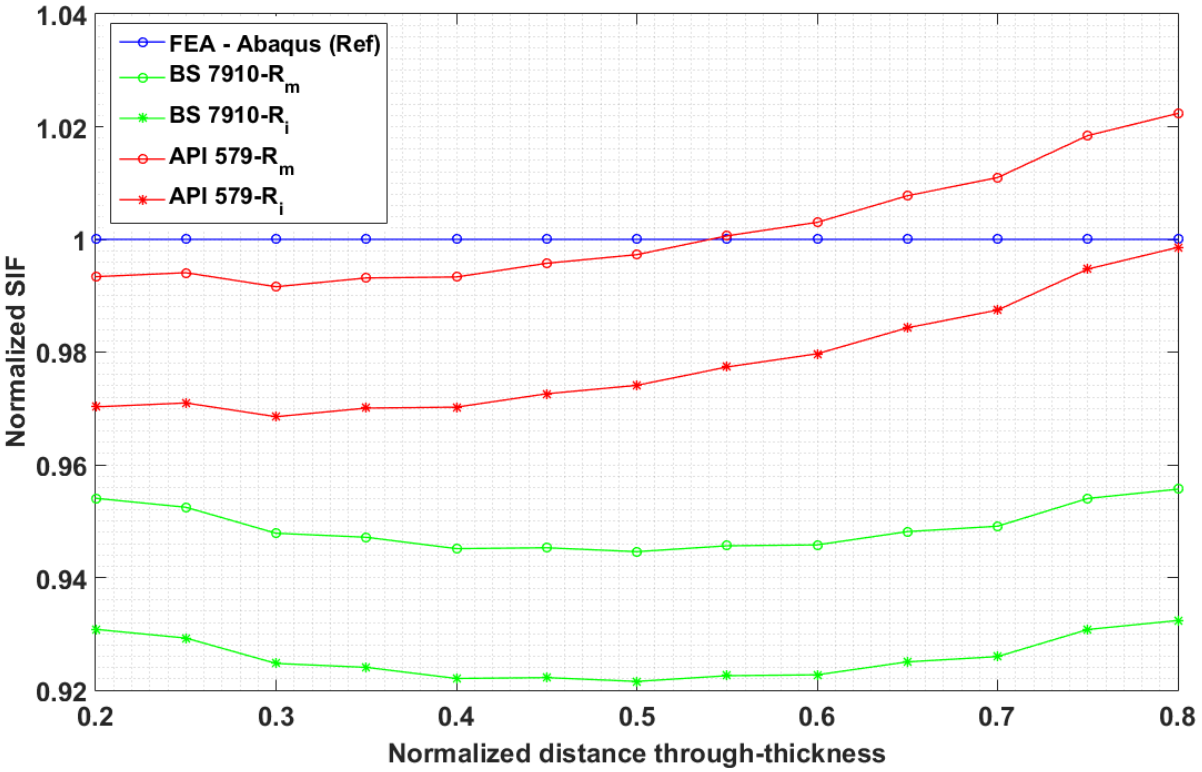

Figure 5.19: A comparison between FEA-derived and handbook SIF solutions (CFP)

Current capabilities of Abaqus/CAE does not allow users to acquire the values of COA directly from simulation model as in the case for SIF. In an effort to determine COA from FEA, displacements have been extracted at every node along the crack length at three locations (A, B and C) shown in Figure 5.13. Analytical COAs were calculated at locations (A) and (C) using API 579-1/ASME FFS-1 solutions with and without crack face pressure and using BS 7910 solution at location (B) without crack face pressure. As shown in Figure 5.20, the results from both procedures are well in agreement with the models with or without application of crack face pressure. A mid-thickness COA with crack face pressure can be easily extrapolated. Although BS 7910 and API 579-1/ASME FFS-1 offer dissimilar COA solutions for different locations and employ different principles

with respect to crack face pressure, the two procedures are essentially consistent with each other. Both offer accurate predictions of crack opening area which could be used for a LBB assessment.

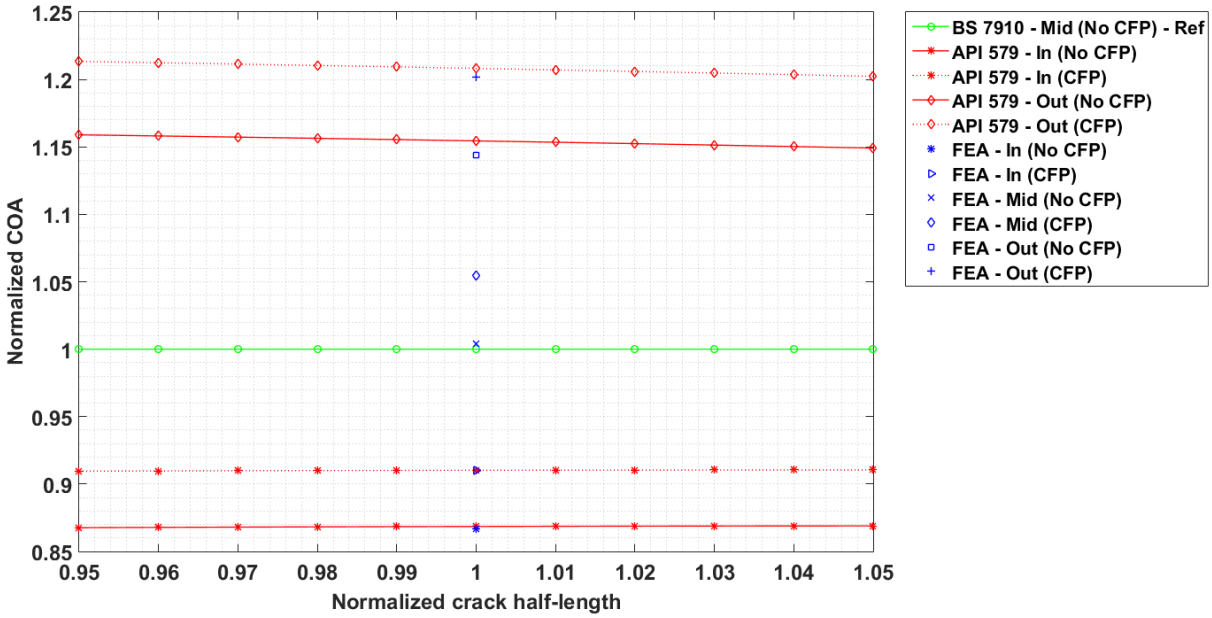

Figure 5.20: A comparison between FEA-derived and handbook COA solutions

5.3.2.4 Results

For the three crack lengths under investigation, three ideal models have been prepared and validated (CTWL1-Id, CTWL2-Id and CTWL4-Id). Figure 5.21 and Figure 5.22 present the values of SIF and COA obtained from FEA versus those determined using handbook solutions respectively.

Stress intensity factor (SIF)

Figure 5.21 presents SIF values at inner (a) and outer (b) surfaces. As J-integral tends to be unreliable at free surfaces [9], SIF at inner and outer surface were estimated using a fourth-order polynomial fit. As shown in Table 5.9, the present FE results are in good agreement with handbook solutions, given only a maximum difference of 3% and 5% at inner and outer surfaces respectively. As the crack length increase, the SIF values increase. The effect of crack face pressure is not presented in this part. However, it is worth noting that when crack face pressure is considered, API 579-1/ASME FFS-1 solutions take this effect into account while BS 7910 explicitly do not.

Table 5.9: A comparison of SIF values between FEA and handbook solutions (S: stress based equations, P: pressure based equations)

	λ	FEA	BS 7910	Diff. (%)	API 579-1 - (S)	Diff (%)	API 579-1 - (P)	Diff. (%)
Inner	1	510.3	510	0.1	503.3	1.4	499.6	2.1
	2	964.4	963.3	0.1	940.8	2.4	922	4.4
	4	2310.7	2354.9	1.9	2315.3	0.2	2250.9	2.6
Outer	1	612.3	622.5	1.7	644.8	5.3	603.4	1.5
	2	1190.3	1195.8	0.5	1230.5	3.4	1144.3	3.9
	4	2458	2522.3	2.6	2594.5	5.6	2376.5	3.3

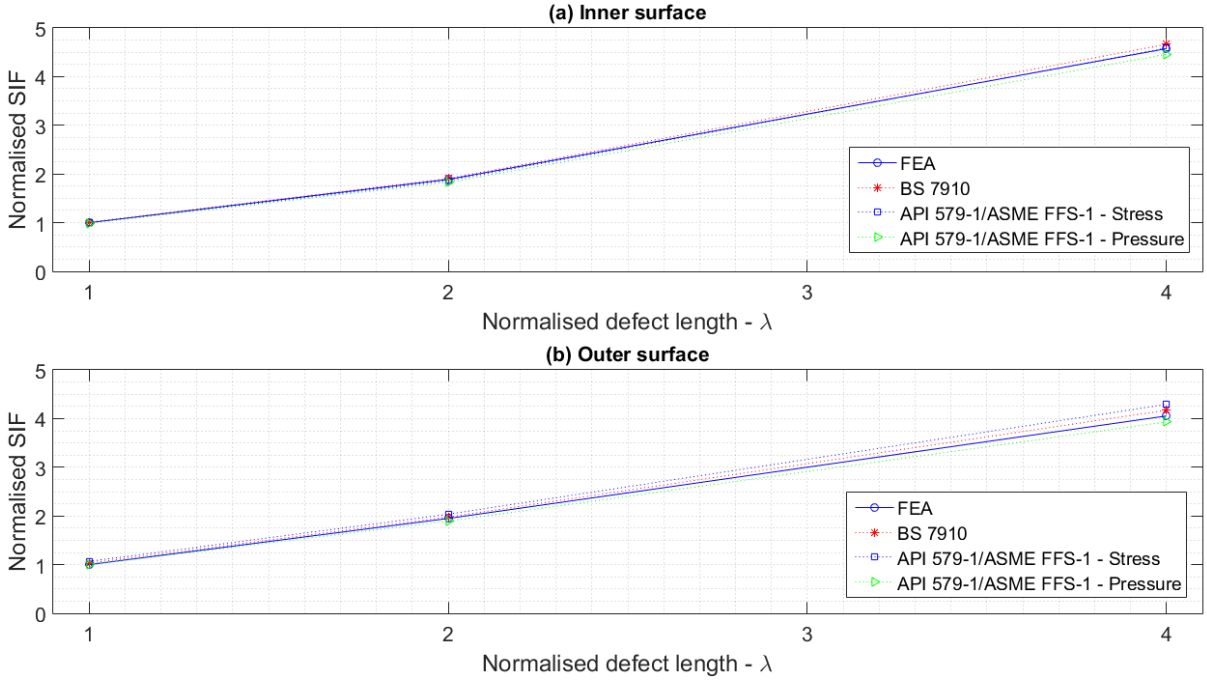

Figure 5.21: A comparison of SIF values between FEA and handbook solutions for an ideal axial through-wall crack in a cylindrical component

Crack opening area (COA)

Figure 5.22 presents COA results at three selected locations, namely inner (a), mid (b) and outer (c) surfaces. As shown in Table 5.10, FEA results agree well with handbook solutions. Only a maximum difference of 2%, 1% and 2% at inner, mid and outer surfaces respectively has been observed. As the crack length increases, the COA increases steeply. The effect of crack face pressure has not been included in all FEA models. API 579-1/ASME FFS-1 solutions take into account crack face pressure while BS 7910's explicitly do not.

Table 5.10: A comparison of COA values between FEA and handbook solutions (S: stress based equations, P: pressure based equations)

	λ	FEA	BS 7910	Diff. (%)	API 579-1 - (S)	Diff. (%)	API 579-1 - (P)	Diff. (%)
Inner	1	1	—	—	1	2	1.1	4.2
	2	5.9	—	—	5.8	1.5	6.1	4.2
	4	51.6	—	—	51.7	0.1	54.2	5
Mid	1	1.2	1.2	0.9	—	—	—	—
	2	6.9	6.9	0.3	—	—	—	—
	4	59.8	59.6	0.4	—	—	—	—
Outer	1	1.3	—	—	1.3	2.3	1.4	6.1
	2	7.9	—	—	8	0.6	8.3	5.2
	4	68.1	—	—	68.9	1.2	72	5.6

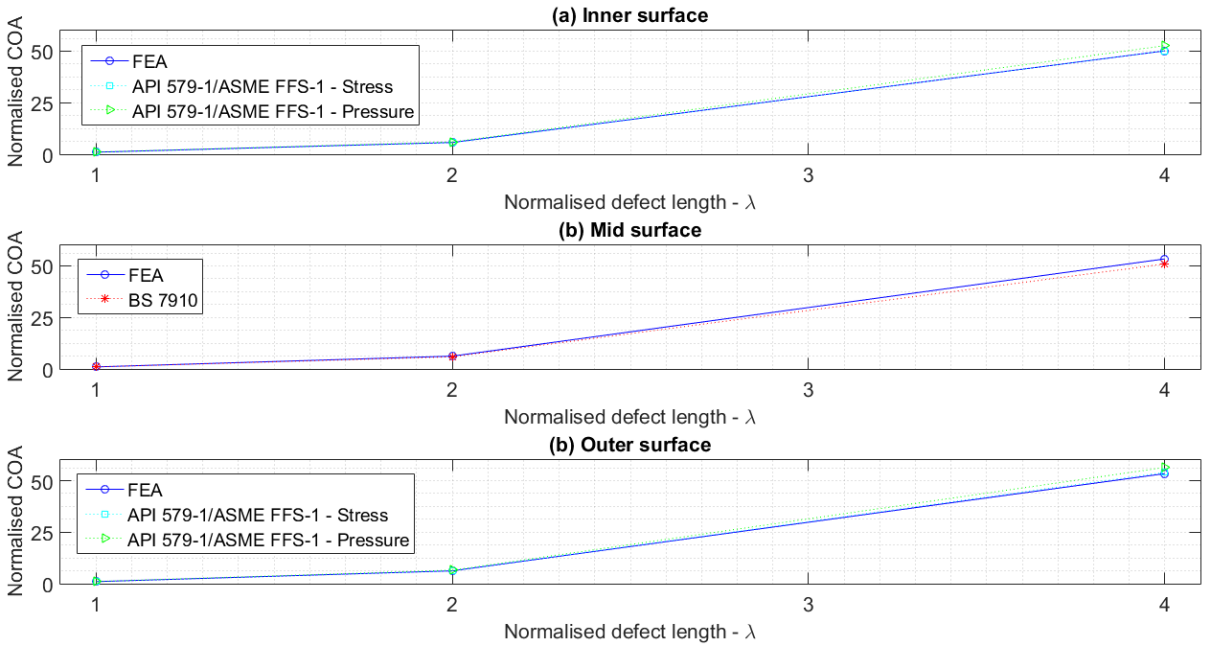

Figure 5.22: A comparison of COA values between FEA and handbook solutions for an ideal axial through-wall crack in a cylindrical component

5.3.2.5 Discussion

As previously mentioned (See Section5.3.2.2), BS 7910 provides one solution for both SIF and COA. API 579-1/ASME FFS-1 provides two solutions for both SIF and COA depending on the input data (stress or pressure). For COA, BS 7910 provides a solution at mid-thickness and API 579-1/ASME FFS-1 at inner and outer surfaces. The validation of techniques for SIF extraction through the section thickness with and without crack face pressure show that for an idealized flaw, FEA models are in good agreement with the solutions from procedures. The validation of techniques for COA calculation with and without crack face pressure show that for idealized cases, FEA models are also in good agreement with the solutions from procedures. Other aspects such as non-idealized crack shape were investigated using previously described techniques to study their effect on LBB assessment in Section 5.3.3 of this chapter.

5.3.3 Non-ideal axial through-wall crack in cylinders

5.3.3.1 Preliminary study

Introduction

An assumption of an idealized crack shape with perfectly straight crack sides oriented perpendicular to the wall is a common practice in a LBB assessment. This assumption helps to reduce the amount of analytical effort needed and is intended to be conservative. A typically postulated shape for a through-wall crack is a crack with its front perpendicular to the component thickness. The largest dimension of the real crack is often assumed (Figure 5.23).

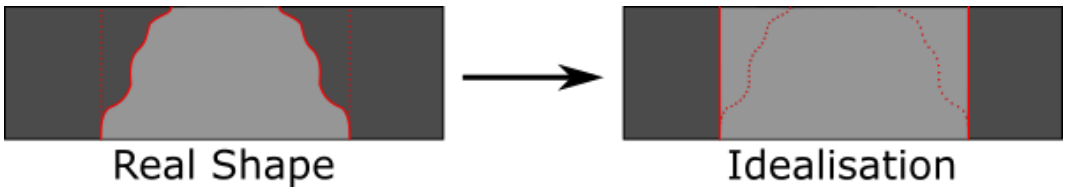

Figure 5.23: Through-wall crack idealisation with API 579-1/ASME FFS-1 and BS 7910

However, assumptions that are valid and conservative for the fracture mechanics aspect of a LBB assessment can have an opposite effect on the calculation of leakage. In reality, a crack grows through the thickness and partially penetrates at the deepest point, resulting in a through-wall crack with different crack lengths at the inner and outer surface. Both scenarios of a crack developing from the inner or outer surface were considered in this preliminary study. This crack idealization overestimates the SIF and underestimates the COA. However, it is obvious that an idealized crack with the largest dimension of the real

crack size may well overestimate the SIF but will also overestimate the COA, therefore the resulting leak rate prediction will be non-conservative.

SIF and COA solutions have been derived for five individual analysis cases:

- Three idealised through-wall cracks with crack half-lengths of 0.95a (Case 1), a (Case 2) and 1.05a (Case 3) - See Figure 5.24
- One 45° slanted cracks from inside to outside with crack half-lengths through the component thickness of 0.95a, a and 1.05a (Case 4) - See Figure 5.25
- One 45° slanted cracks from outside to inside with crack half-lengths through the component thickness of 0.95a, a and 1.05a (Case 5) - See Figure 5.26

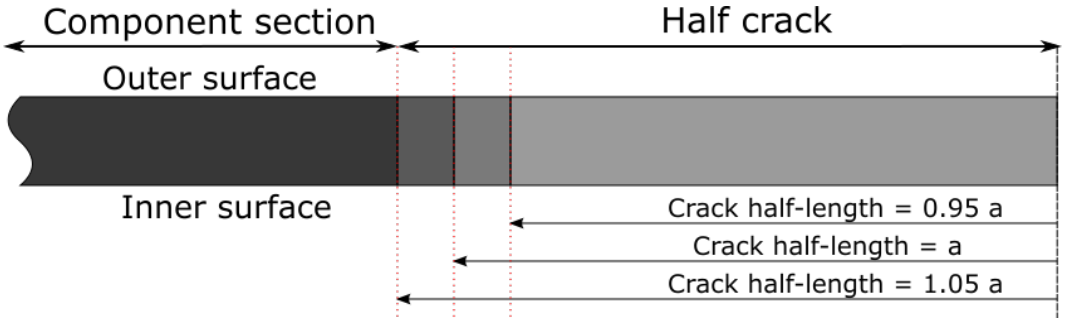

Figure 5.24: Three ideal through-wall cracks with crack half-length of 0.95a (Case 1), a (Case 2) and 1.05a (Case 3)

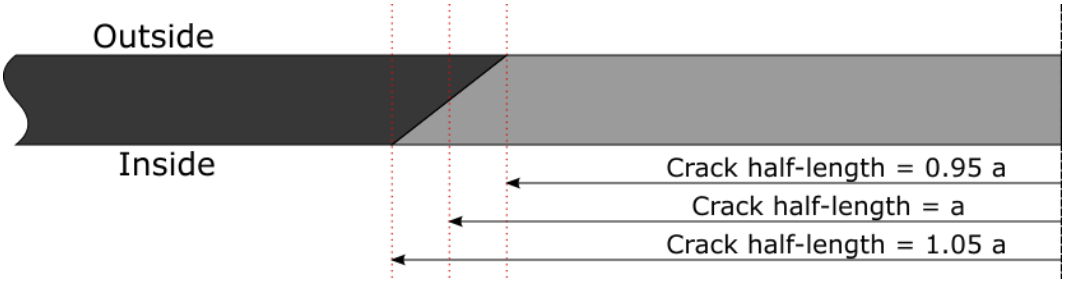

Figure 5.25: Slanted through-wall crack with internal crack half-length=1.05a and external crack half-length=0.95a (Case 4)

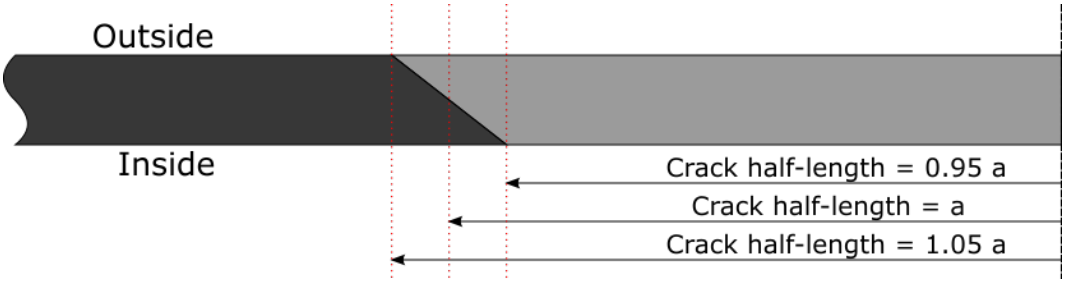

Figure 5.26: Slanted through-wall crack with internal crack half-length=0.95a and external crack half-length=1.05a (Case 5)

Results

SIFs along the crack front from the inner to the outer surface were determined. The three ideal cases, i.e. Cases 1, 2 and 3, have been normalized with the SIF values from Case 1 (crack half-length = a) and Cases 4 and 5 have been normalized with SIFs values from the three ideal cases in order to establish the significance of crack idealization (Figure 5.27). The calculted SIFs were higher at locations where the crack length was shorter, which was consistent with experimental observations. Normalizing by the largest ideal through-wall crack (which is equal to the largest crack length of a non-ideal crack) resulted in a conservative assumption along the crack front.

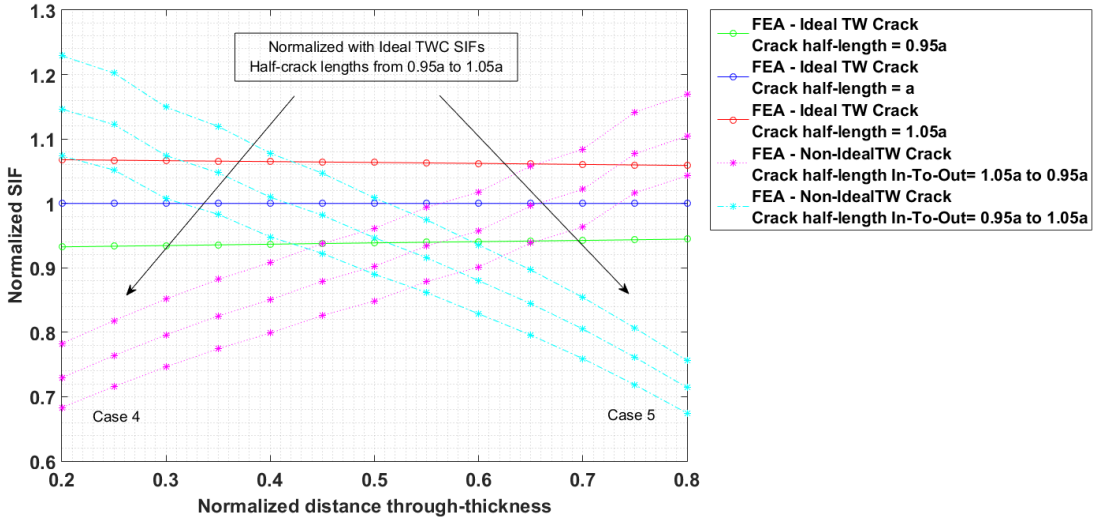

Figure 5.27: SIFs of both idealized and developing through-wall cracks

Idealization of a through-wall crack leads to a conservative estimate of SIF. The highest SIF along the crack front for a slanted crack will be covered by the SIF from the idealized shape (See Figure 5.28).

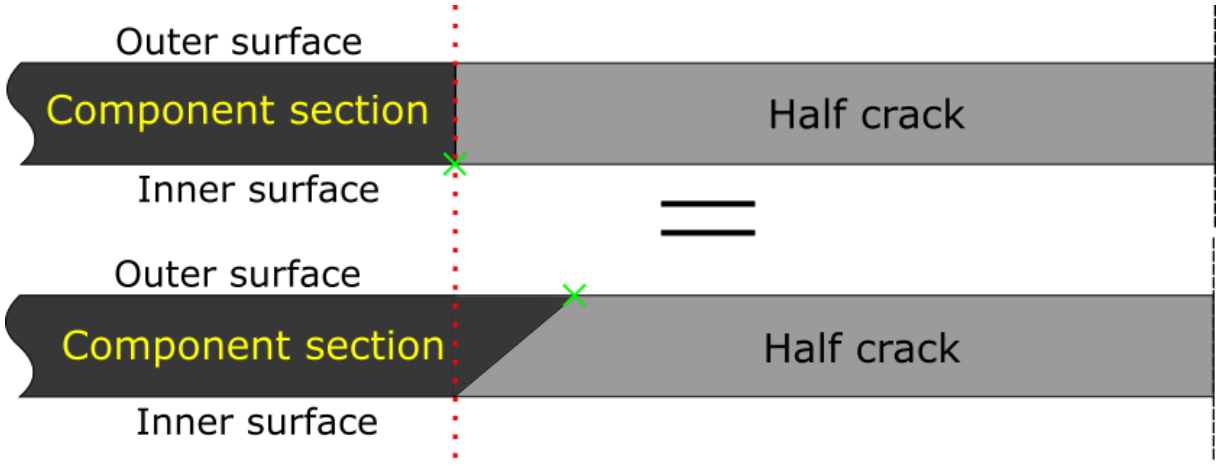

Figure 5.28: Schematics of both idealized and developing through-wall cracks and equivalent SIF position

However, as far as COA is concerned, this idealisation of crack as through-thickness does not produce conservative results (Figure 5.29). While an idealized crack with a crack half-length of 1.05a, COA of the slanted crack will be definitively lower, resulting in a lower leak rate.

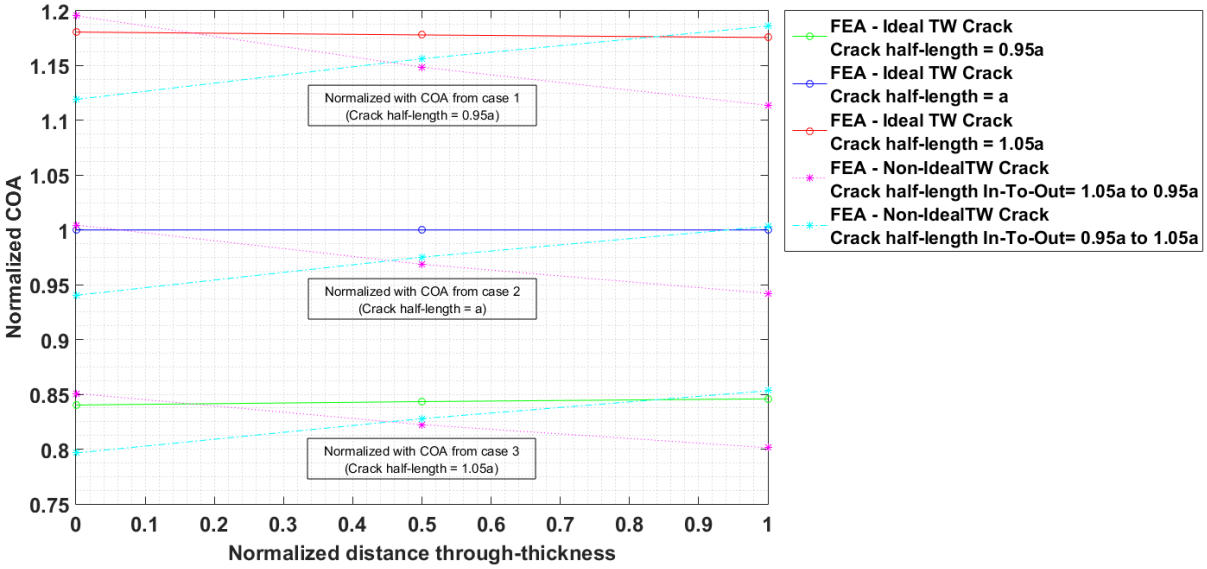

Figure 5.29: COAs of both idealized and growing through-wall cracks

Concluding remarks from this preliminary study

Based on this preliminary study, the following observations can be drawn:

- The values of SIF and COA of ideal through-wall crack agree well with handbook solutions. For slanted through-wall cracks, idealization of a growing crack to an ideal crack with the largest dimensions gives conservative SIF values up to 80% through the thickness. Further work is needed to expand crack transformation behaviour on the first and last 20% (simulation vs. experiment)
- For slanted through-wall cracks, idealization of a growing crack to an ideal crack with the largest dimensions leads to possibly un-conservative results in term of COA values. Assumption of a largest crack size overestimates the current COA, and therefore the current leak rate.
- Taking the minimum crack size to idealize a through-wall crack is likely to produce more realistic results. However as shown in Figure 5.29, a slanted crack also leads to a variation of COA through section thickness compared to an ideal case. This is further studied in the next section.

5.3.3.2 Numerical models

In order further evaluate the effect of these ideal/non-ideal crack shapes on LBB assessments, various FE models were prepared with different crack sizes and ratios of inner crack size (kept constant) to outer crack size. These cases are presented in Figure 5.30. Both SIFs and COAs have been derived for each model. Note that as the crack length increases, the slant angle from the inner and outer surface increases at a constant ratio of a_{out}/a_{int}. However, the application of this technique was however limited due to Abaqus/CAE model generation. This is the reason why as λ increases, this ratio is limited as shown on Figure 5.31.

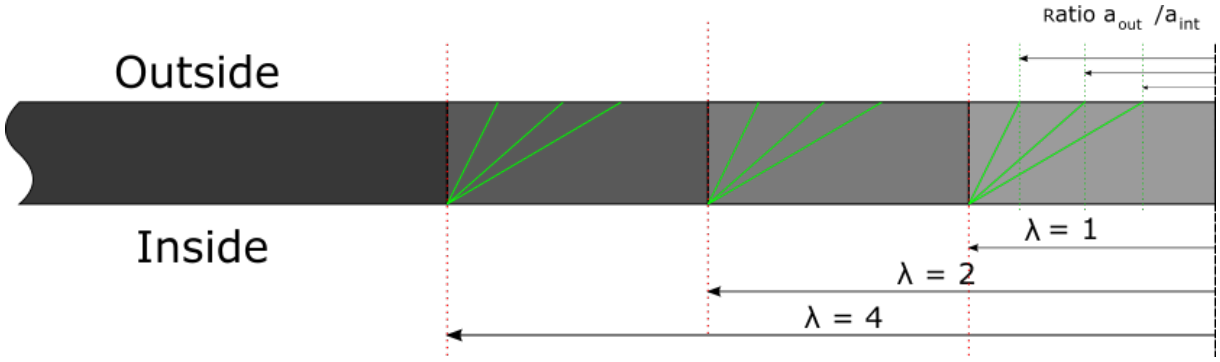

Figure 5.30: Principle of the different case studied

Cases			
Ratios(a_{out}/a_{int})	λ=1	λ=2	λ=4
1 (Ideal)			
0.95			
0.9			
0.85			
0.8			
0.75			
0.7			
0.6			

Figure 5.31: Summary of the different cases presented

5.3.4 Results

Both SIF values for the three reference crack lengths $\lambda = 1$ (Figure 5.32), $\lambda = 2$ (Figure 5.33) and $\lambda = 4$ (Figure 5.34)and COA solutions for $\lambda = 1$ (Figure 5.35), $\lambda = 2$ (Figure 5.36) and $\lambda = 4$ (Figure 5.37) from FEA are presented.

Stress intensity factors

In this section, stress intensity factors for non-idealized axial through-wall cracks are investigated. To improve confidence in the present results, the SIF values derived

from FEA models for an idealized geometry have been compared to handbook solutions and are presented in Section 5.3.2.3. Both BS 7910 and API 579-1/ASME FFS-1 provide a general SIF solution and membrane stress due to internal pressure is given as:

$$P_m = \frac{PR}{t} \tag{5.16}$$

The following paragraph, discusses the results from non-idealized crack geometry. SIFs derived for λ=1, 2 and 4 are presented in Figure 5.32 to Figure 5.34 respectively. The SIFs values of non-idealized geometries (dotted lines) were normalized to the corresponding idealized geometry (blue plain line). An idealized through-wall crack length is equal to the longer crack length (inner crack length, $2a_i$) for each model (CTWL1-Id, CTWL2-Id and CTWL4-Id). The SIF results from idealized case were normalized to 1 and the results of non-idealized models were directly normalized to the value of idealized models. The horizontal axis represents normalized through-thickness distance. For all the cases, the same trend has been observed i.e. SIF is greater at the outer surface whereas lowest value at the inner surface. Moreover this effect became more pronounced with an increasing outer to inner crack length ratio, a_o to a_i. As the difference in length between the inner and outer surfaces increases, SIF values at the inner surface decrease and increase at the outer surface. This can be explained by the fact that as the ratio between inner and outer crack lengths increase, the inner surface undergoes more local constraint than at the outer surface. This contributes to a greater stress field at the outer surface. Note that at the outer surface, SIF values are greater than those of an idealized model. Further observations have been given in Section 5.3.5.

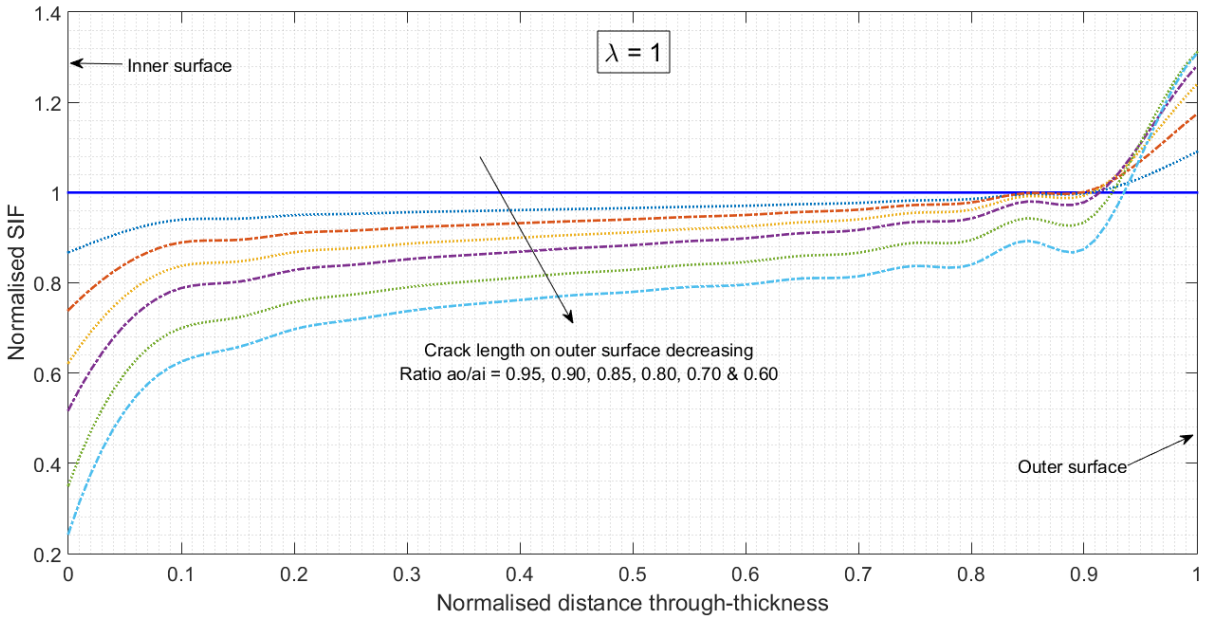

Figure 5.32: Evolution of SIF through section thickness for λ = 1

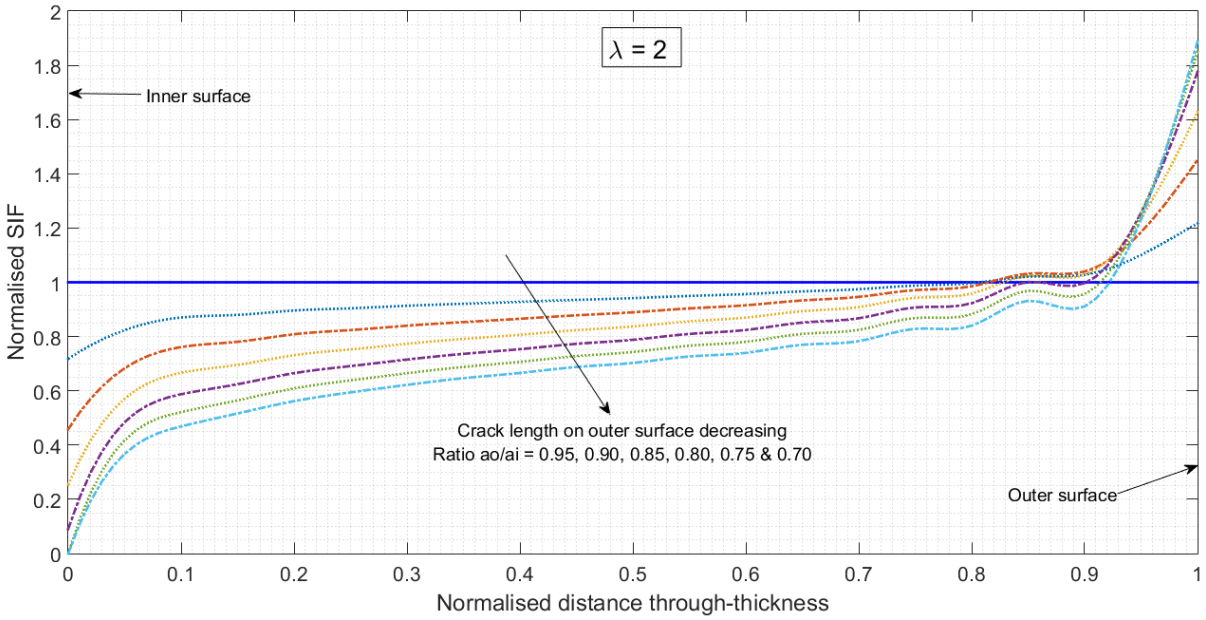

Figure 5.33: Evolution of SIF through section thickness for $\lambda = 2$

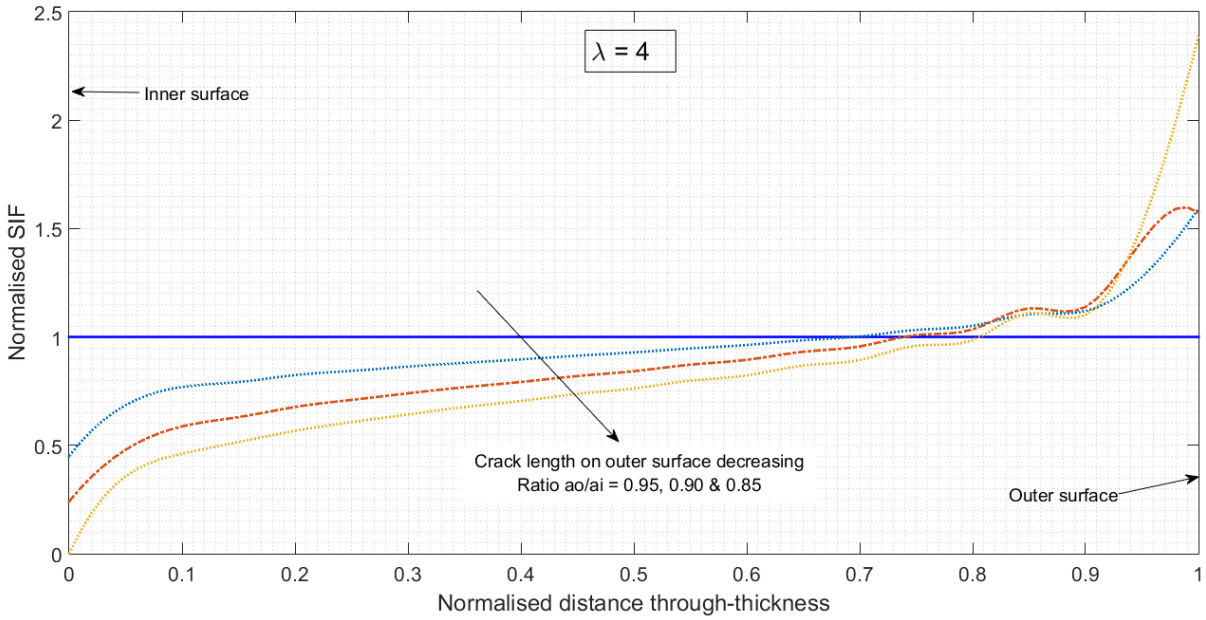

Figure 5.34: Evolution of SIF through section thickness for $\lambda = 4$

Crack opening areas

In this section, the crack opening areas for non-idealized axial through-wall cracks are investigated. To assure confidence in the present results, the COA values derived from FEA for an idealized geometry have been compared to handbook solutions. Note that BS 7910 gives a solution for mid-thickness while API 579-1/ASME FFS-1 provides solutions for inner and outer surface. CTODs were directly determined from FE displacements along the crack length at the inner surface, outer surface and mid-thickness. These values were then integrated and multiplied by four (due to the symmetric conditions) to get a final COA value for each model under consideration. The results of the reference lengths $\lambda = 1$, 2 and 4 are presented in Figure 5.35 to Figure 5.37. The horizontal axis represents the difference between the inner and outer crack lengths. The COAs results obtained for each model at inner (blue) mid-thickness (green) and outer surfaces (red) have been normalised to the values derived from an ideal geometry. The COA values for an idealized cases were normalized to 1 for each location. For an idealized through-wall crack, COAs are larger at the outer surface than at the inner surface (see Figure 5.22 and Table 5.10). However, COAs at outer surface and mid-thickness decrease with shorter outer crack lengths while SIFs become greater (see Section 5.3.4). COAs also decrease at the inner surface while the inner crack length is kept constant for each respective case. Due to the higher local constraint at the inner surface, the displacement at the inner surface tends to be larger than that at the outer surface. This is particularly apparent for relatively short crack (Figure 5.35). Further observations are given in Section 5.3.5.

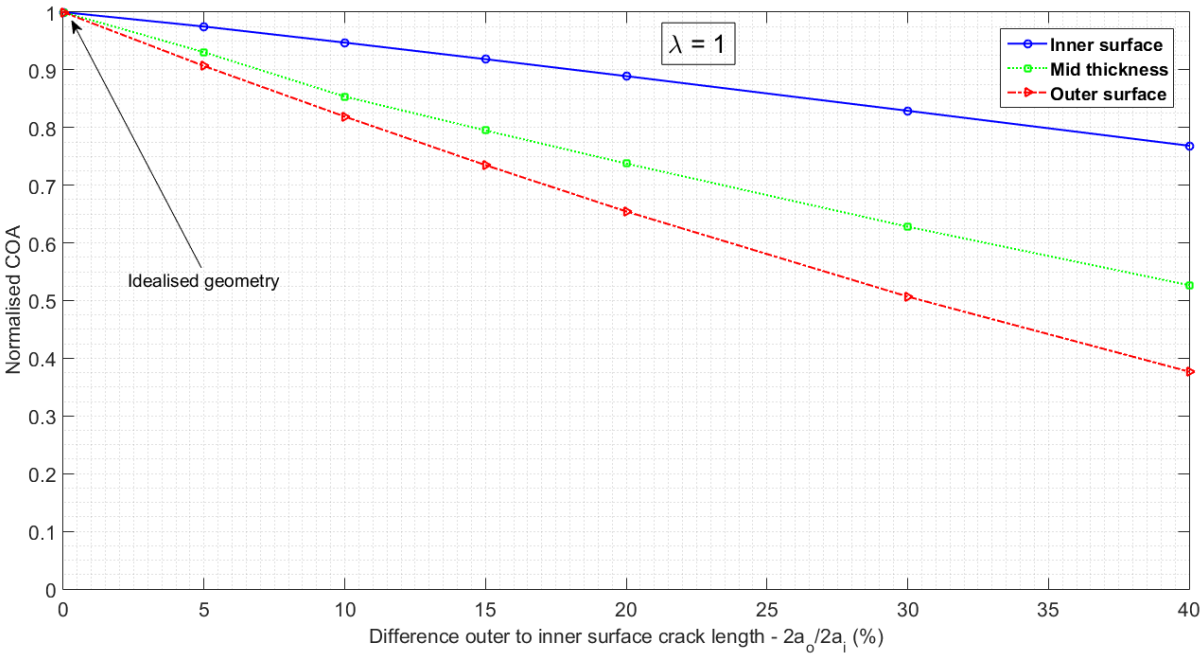

Figure 5.35: Evolution of COA at inner, mid and outer surfaces for $\lambda = 1$

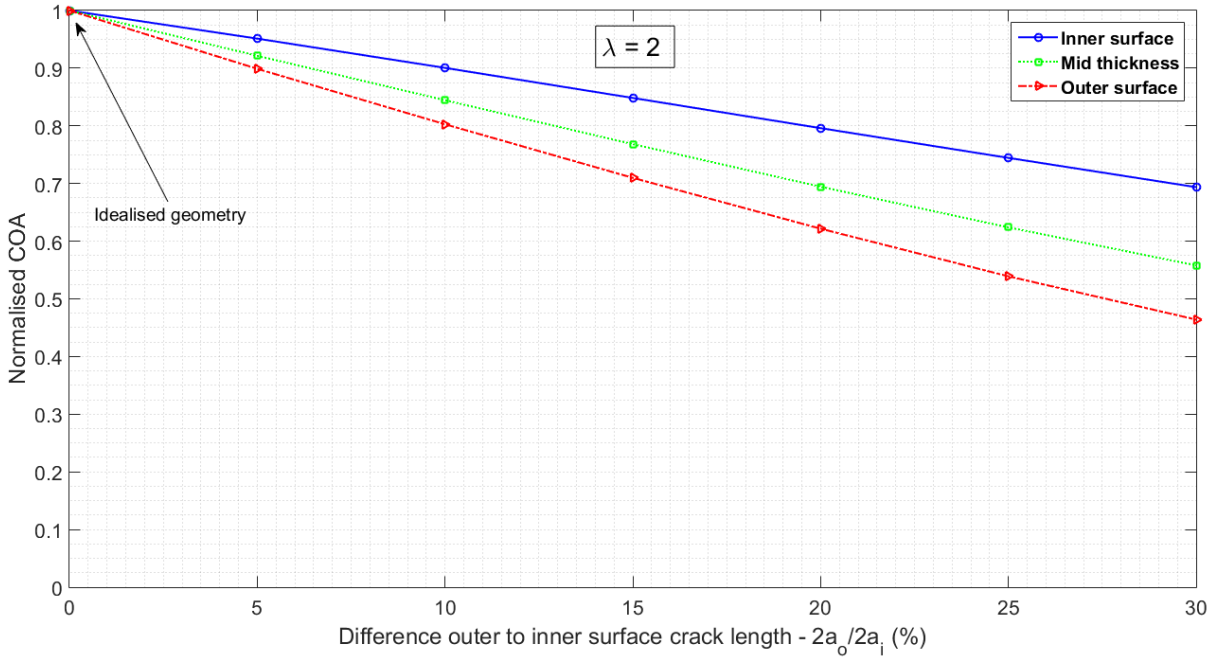

Figure 5.36: Evolution of COA at inner, mid and outer surfaces for $\lambda = 2$

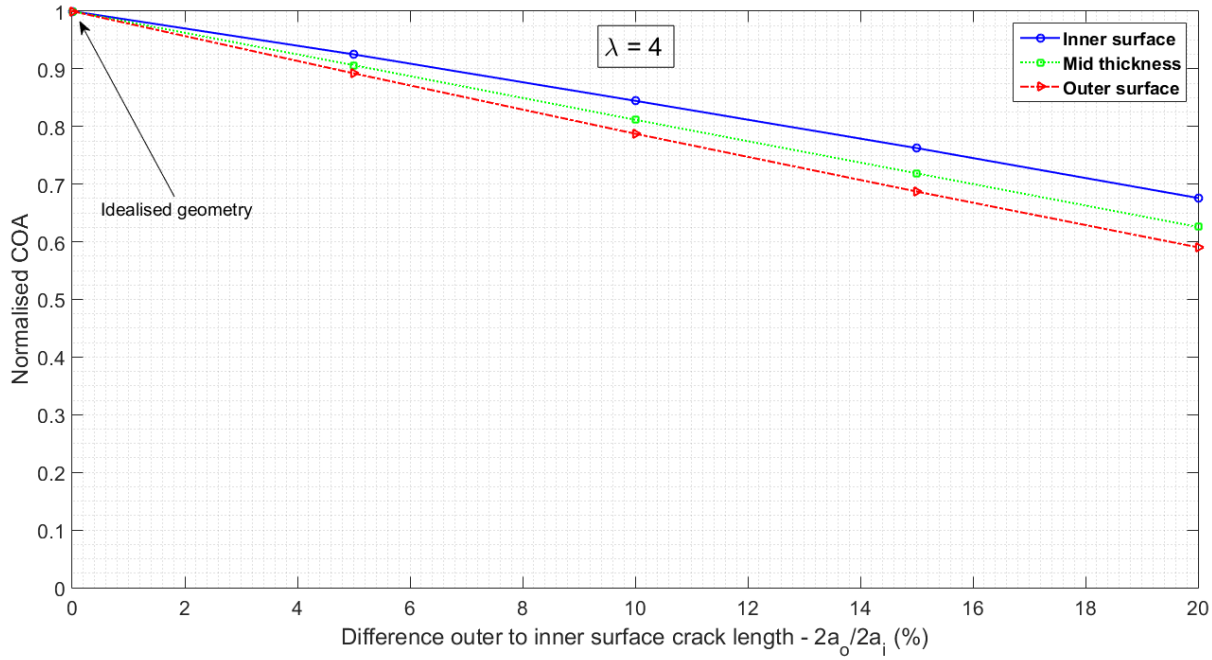

Figure 5.37: Evolution of COA at inner, mid and outer surfaces for $\lambda = 4$

5.3.5 Discussion

The SIF and COA solutions for idealized and non-idealized axial through-wall crack in a cylindrical component under internal pressure were investigated.

Stress intensity factors

Figure 5.38 summarizes the SIFs values derived from axial through-wall cracks with shapes yet to become 'idealized' (i.e. difference between inner/outer crack length $\leq 15\%$) for three different reference lengths (λ). It can be seen that as the reference crack length increases, the effect of non-idealization becomes more significant. In all models, as the ratio of a_{out}/a_{int} decreases, the absolute values of SIF decrease but the gradient along the thickness begins to develop. For longer cracks (i.e. λ=4), SIF at the inner surface is much lower than at the outer surface. Under these circumstances, the crack is expected to grow much faster on the outer surface. With a difference of only 15% between inner and outer surface crack lengths, SIF is close to zero, resulting in a crack growth only at the outer surface. At the outer surface, the SIF values can reach up to two times the values of an idealized geometry. For shorter crack (i.e. λ=1), the variation of SIF along the thickness is still present but at a much lower scale. It is safe to say that for a given non-idealized crack, crack growth is dominated by the outer surface. Based on such observation, it can be argued that a non-idealized crack will grow into an idealized through-wall crack at some point during components service life, which is consistent with the experimental observations (Chapter 6). The crack presented can be considered as relatively short. It can be observed that the crack growth takes place at both inner and outer surface.

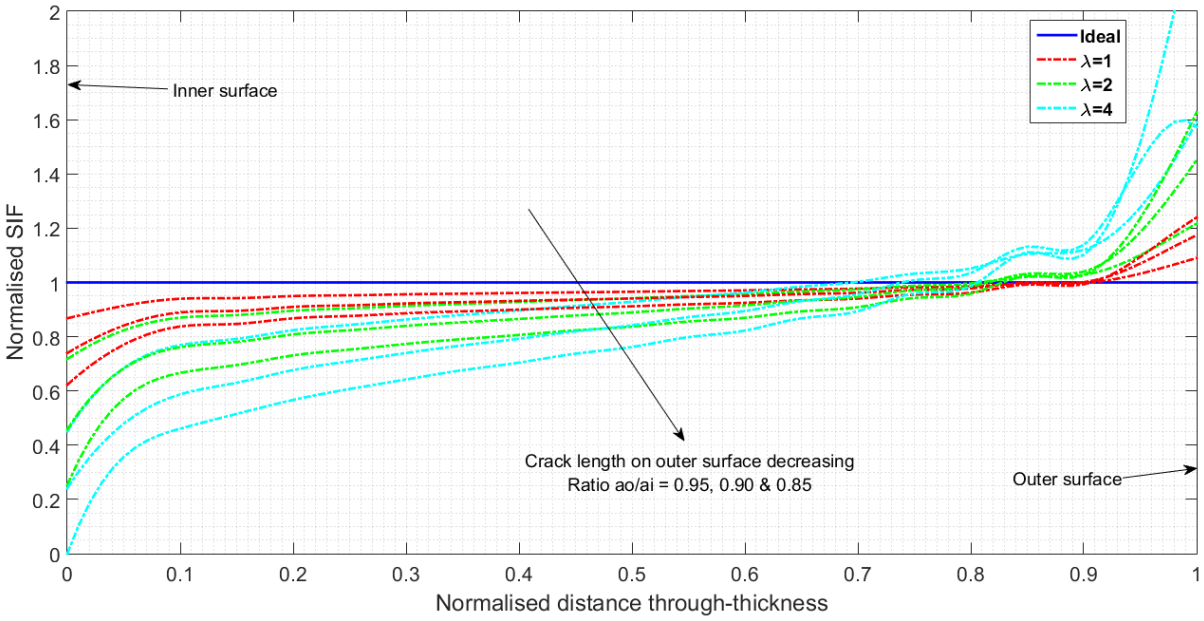

Figure 5.38: The effect of crack shapes on SIF profiles through-thickness for different reference crack lengths, λ

Crack opening areas

In a typical LBB assessment, an estimation of crack length corresponding to a detectable leak-rate is required. This is achieved by determining COA values that relates leak rate to corresponding crack length. Figure 5.39 summarizes COAs values of through-wall cracks with shapes yet to become 'idealized' (with a difference of less than 20% between inner and outer crack length) for the three reference lengths (λ). It can be seen that as the reference crack length increases, the effect of non-idealization becomes more apparent but the difference in COA between inner and outer surface is less pronounced. Assuming a linear trend for each curve, the slope of the inner and outer surface is more pronounced for smaller cracks (λ=1) than that of longer cracks (λ=4). Shape idealization for cracks 'yet' to become fully idealized can rapidly lead to an overestimation of COA. This results in an overestimation of leak rate which is one of the most important parameters in a LBB assessment. There is a risk of producing un-conservative prediction. A better evaluation of the COA would have helped to reduce margins applied on leak rate determination.

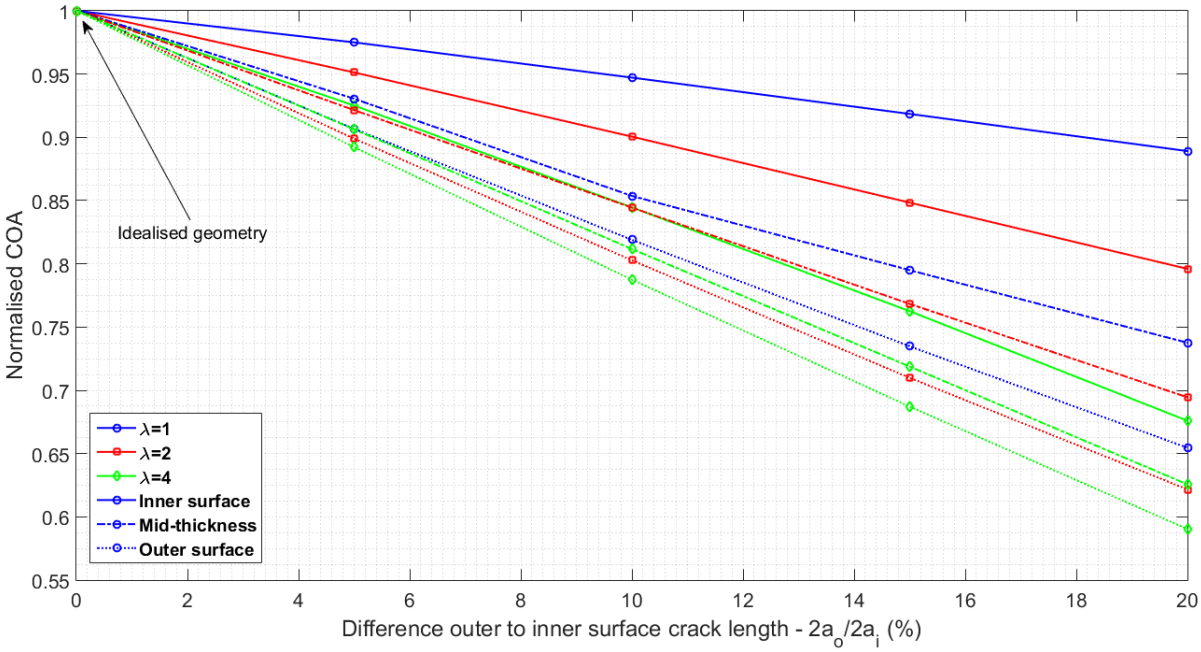

Figure 5.39: The effect of crack shapes on COA profiles for different reference crack lengths, λ

5.4 Summary

This chapter validated the solutions for through-wall cracks in plates and cylindrical components. The calculation of various solutions has been detailed for plates, with step-by-step methodologies and post-processing to generate models and results.

In order to generate numerous models in a time-efficient manner, different plug-ins have been created using Python script. Cracks have been introduced into un-cracked bodies (plate or cylinder) in the assembly step, using a crack-box. This permitted to generate the models changing only the desired parameters. FE results in this work were found in good agreement with solutions available in procedures for idealized shape models.

The effect of crack idealization on SIF and COA solutions has been investigated for axial through-wall cracks in a cylindrical component under internal pressure using detailed 3D elastic FE analyses. Idealization of a through wall crack with its largest dimension tends to be conservative when it comes to deriving SIF. However, in a LBB assessment, both crack stability and leakage have to be evaluated. Crack idealization rapidly increases COA estimation leading to an over-estimation of detectable leak rate. This implies that for a given crack size, its idealisation will be conservative in terms of SIF but the estimated resulting leak rate over-estimated. The leak detection can therefore be distorted.

Models and analyses employed in this work were validated against existing solutions for SIF and COA given in BS 7910 and API 579-1/ASME FFS-1. The work presented in the second part of this chapter (Section 5.3) permits to extend the understanding on non-idealised cracks. Different reference crack length (inner surface) have been selected in order to cover various crack sizes. The observations on SIF and COA for various crack geometries can be used to carry out sensitivity studies while assessing LBB cases. The effect of non-idealized geometry on both SIF and COA could be included to assess cracks 'yet' to become idealized using the observations presented in this work. The analysis showed that a non-idealized crack at break-through (from surface to through-wall) will grow and finally evolve into an ideal shape. LBB assessment in this transition region is generally limited due to a lack of existing solutions. The effect of crack shape on SIF solutions can be used in fatigue assessment to examine cracks growing under cyclic loading. The modification on COA solutions can improve the leak rate calculation more accurately. This is an important aspect of the assessment often overlooked, while the variation is important in the transition region. Further work to investigate more realistic crack shapes (i.e. non-straight crack front) and development of correction factors for existing solutions would be beneficial in establishing a more refined assessment of LBB.

Chapter 6

Experimental Work - Stress-Strain Field on the Back Surface of Surface Cracked Plate During Crack Transition

Contents

6.1 Introduction

This chapter describes the work carried out to examine the transition from surface-breaking to through-thickness crack. Besides FE simulations, experimental tests were performed using Perspex and high strength steel plates. The test on Perspex specimens was used as a preliminary study to semi-qualitatively examine crack transition behaviour. Analysis of the fracture surface provided an insight of the crack transition between surface-breaking to through-thickness cracks. For the metallic samples, strain gauges were attached to the back surface of the plates to capture the change in strain at several locations adjacent to expected breakthrough position during the crack growth and transition from 80% to 100% through-thickness. Crack lengths were recorded at the same time to determine crack growth rate of both surfaces during transition.

6.2 Semi-qualitative study of crack transition - Perspex specimens

6.2.1 Preparation of Perspex samples

A set of 20 Perspex samples were prepared with semi-elliptical cracks. Figure 6.1 shows the schematic of sample geometry. Actual dimensions are given in Table 6.1. Four different geometries have been selected, including two different thickness. All samples were free of internal defects (pores, cracks,etc) and were assumed homogeneous under visual inspection. The cracks have been artificially introduced with a 36mm diameter, 1mm thick acrylic cutting disc at 3500rpm. It was also necessary to introduce a pre-crack, to simulate a natural flaw with a sharp crack tip. Two widely adopted methods for polymers are to either tap or press a razor blade tool into the machined notches. As the experiment aimed to look at surface cracks, assumed to have an elliptical shape, the latter procedure has been selected for simplicity. Both procedures are known to produce similar results when applied to PMMA [147]. Deep cracks and razor edges have been introduced respectively to reach about 70% - 80% of the sample thickness.

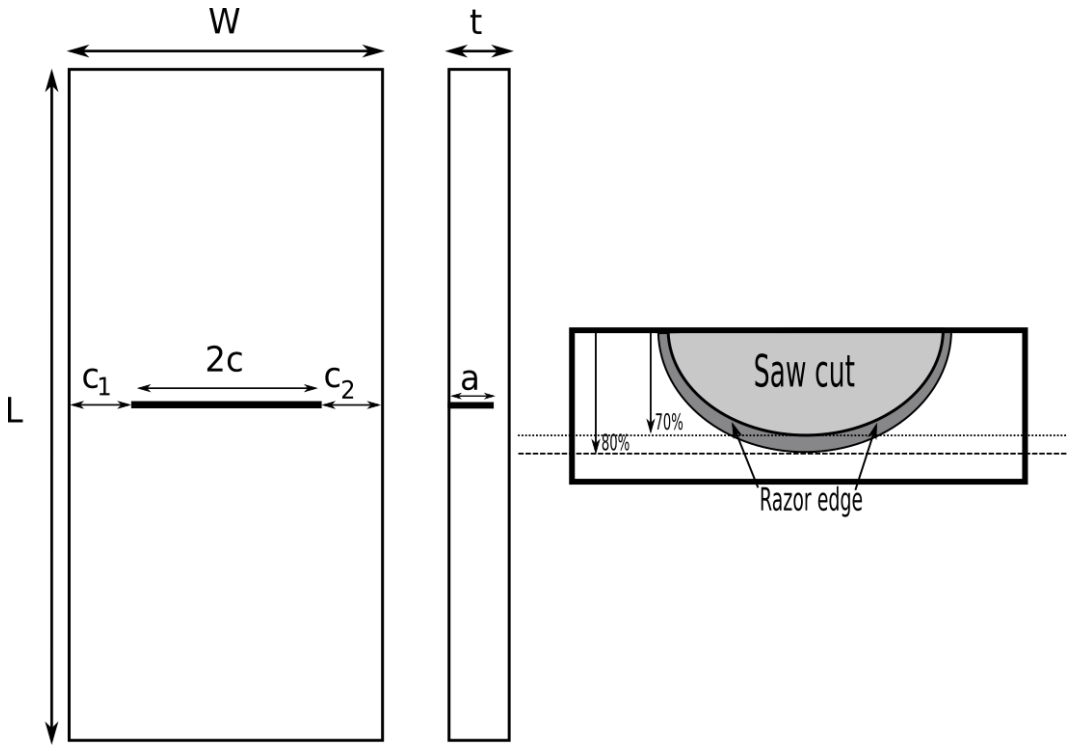

Figure 6.1: Perspex sample

Table 6.1: Dimensions of Perspex samples

Test	L (mm)	c1 (mm)	c2 (mm)	2c (mm)	a (mm)	w (mm)	t (mm)	a/t (—)	RA (mm^2)	RA (%)
Specimen 100x50x10										
S11	100.1	10.45	10.25	29.8	7	1.75	9.54	0.73	317.94	65.99
S12	100.1	10.5	10.2	30.0	6.9	1.5	9.85	0.7	336.82	67.45
S13	100.3	11.2	9.3	30.3	6.6	1.5	9.73	0.68	337.22	68.22
S14	100.3	10.2	9.4	31.2	7.1	1.5	9.64	0.74	315.73	64.47
S15	100.5	9.7	10.6	30.1	7.2	1.5	9.5	0.76	308.59	64.45
Specimen 100x50x15										
S21	100.2	7.1	8.2	34.7	10.1	2.0	14.38	0.7	443.74	61.72
S22	100.3	8.5	7.7	33.8	9.7	2.0	14.35	0.68	460 v	64.11
S23	100.1	5.8	8.1	36.4	10.1	1.5	14.31	0.71	431.05	59.89
S24	100.4	7	6.7	36.4	11.1	2.0	14.08	0.79	388.08	55.01
S25	—	—	—	—	—	—	—	—	—	—
Specimen 100x75x10										
S31	100.1	21.9	23.8	30.1	7.1	1.5	9.72	0.73	568.93	77.22
S32	100.4	22.8	22.2	31.0	7.1	1.5	9.71	0.73	565.09	76.58
S33	100.3	21.9	21.6	32.0	7	1.5	9.48	0.74	539.81	75.42
S34	100.3	21.7	24.1	30.3	6.7	1.5	9.68	0.69	577.2	78.36
S35	100.4	21.7	22.4	31.7	7.2	1.5	9.65	0.75	552.21	75.49
Specimen 100x75x15										
S41	100.3	19.6	20.5	35.2	10.1	1.5	14.36	0.7	802.08	74.18
S42	100.5	20.3	18.3	36.7	10.3	1.5	14.34	0.72	782.91	72.51
S43	100.2	20	20.0	35.2	10.8	1.5	14.42	0.75	785.81	72.47
S44	100.2	20.3	19.9	34.9	10.3	2.0	14.44	0.71	802.12	73.97
S45	100.2	20	19.8	35.5	10.3	1.5	14.15	0.73	778.31	73.05

6.2.2 Test setup

PMMA samples (cast Perspex) have been used as preliminary study specimens as they provided the possibility to acquire a visual representation of crack propagation through thickness. It is one of the few brittle amorphous thermoplastic materials with a glass transition temperature T_g around 100°C. However, since PMMA is a viscoelastic material, this means fatigue behaviour is different from conventional metallic materials. Two notable differences are the sensitivity to temperature and cyclic frequency [148]. In order to duplicate the fatigue behaviour of metallic material, the test frequency was maintained at a very low level. This prevented localized plastic deformation and at the same time allowed the generated heat (due to loading) to dissipate quickly enough to avoid crack-tip blunting. It had been observed that the effect of temperature rise on fatigue behaviour was insignificant at frequencies less than 0.5Hz. Moreover, a consistent conclusion from experiments is that fatigue crack propagation decreases with frequency. To prevent samples from buckling under compressive loading, tension to tension loading was applied for all tests. The cyclic plastic zone is known to be only about one quarter of the size of the monotonic plastic zone [149].

Table 6.2: Assumed material properties for preliminary parametric calculations

Density [150]	**Youngs's modulus** [150]	**Tensile strength** [150]	**Poisson's ratio** [148]	**Fracture Toughness** [147]
1.19 g/cm^3	3210 MPa	75 MPa	0.41	1.1 MPa.$\sqrt{m}$

As described previously, surface cracks and pre-cracks have been introduced in Perspex samples (Stage 1 on Figure 6.2). Fatigue testing was carried out until the surface crack grew through thickness, i.e. breakthrough (Stage 2 on Figure 6.2). All tests were conducted in the air with an Instron machine Model 5967 and accompanying Instron Bluehill software. Tensile cyclic loadings were applied in axial direction and applied stresses ranged from 3 to 4 MPa. Test was continued (Stage 3 on Figure 6.2) until a through-thickness crack had developed with its edges parallel to each other or until specimen ruptured (Stage 4 on Figure 6.2).

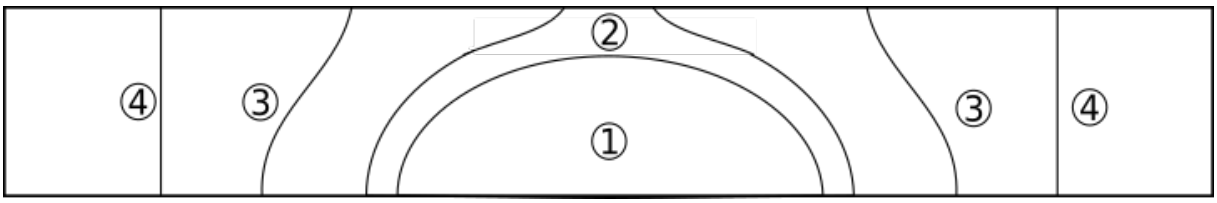

Figure 6.2: Expected fatigue crack growth in perspex samples

Tests parameters used were:

- Stress ratio, $R = \sigma_{min}/\sigma_{max}$=0.
- Frequency kept under 0.5 Hz
- Amplitude from 0 to σ_{max}
- Triangular waveform
- Test carried out in Load Control

6.2.3 Observations from tested plates

Fracture surface for all tested samples can be found in Annex A. A representative photo of the different behaviour observed is provided in the discussion.

6.2.3.1 Series 1 (10x50x100mm)

Series 1 was the smallest specimen size series to be tested with a thickness and width of 10 mm and 50 mm respectively. All samples suffered from non-symmetric crack growth. This was assumed to be caused by a misaligned gripping of the samples in the testing machine. Sample S12 is given as reference for this series in Figure 6.3. Similar behaviour was observed for The other samples.The blue area (Area 1) represents the initial crack introduced in the sample. Fatigue crack growth is represented by the red area (Area 2). As a result of the misaligned gripping, on all specimens, crack growth mainly took place in one direction. Crack growth on one side continued until it reached the sample edge. Test was stopped when sudden rupture occurred (Area 3) and the fracture surface was found to be flat and clear. Specimen S15 was used for calibration purpose. As a result, only a small amount of fatigue crack growth has been observed. Few cycles have been tried under an increasing loading of 125N, 250N, 500N, 1000N, 2000N and 3000N. Specimen suffered from sudden rupture has at loads just under 3000N. A flat and clear fracture surface could be observed. A summary of the specimens is given below:

- Sample S11 - Crack growth only on one side until it reached edge
- Sample S12 - Crack growth mainly on one side until it reached edge, no growth in thickness direction
- Sample S13 - Crack growth mainly on one side until it reached edge
- Sample S14 - Crack growth mainly on one side until it reached edge
- Sample S15 - Crack growth only one side until instability

6.2.3.2 Series 2 (15x50x100mm)

The specimens thickness of series 2 was greater, i.e. 15mm, while the other dimensions remained the same than series 1. With this increased thickness the samples were able to

sustain higher load with an increased cross section area. Samples S21 suffered from the misaligned gripping leading to a crack growth only on one side (Figure 6.3). Different observations can be made on Sample S23 (Figure A.8). Firstly, the crack was not exactly located in the middle of the sample ($d_1 < d_2$). Moreover, the initial crack shape was not exactly semi-elliptical as shown with the green dots on the initial crack shape. This caused crack growth to reach the edge prematurely, leading to a sudden rupture. However, compared to previous tests, as loading was applied perpendicular to the crack, the resultant crack growth was fairly uniform. Both specimens S22 and S24 (Figure 6.4) achieved the expected fatigue growth pattern (Figure 6.2). The initial crack (Area 1) grew by fatigue until it reached the back surface (Area 2). Then rapid crack growth occurred and the crack became an idealised through-wall crack shape (Area 3). Final rupture occurred at the boundary between Areas 3 and 4, giving a clear and flat surface. A summary of the specimens is given below:

- Sample S21 - Crack growth only on one side until it reached edge
- Sample S22 - Expected crack growth mainly in thickness direction
- Sample S23 - Crack growth mainly on one side until it reached edge
- Sample S24 - Expected crack growth mainly in thickness direction
- Sample S25 - Not tested

6.2.3.3 Series 3 (10x75x100mm)

The specimens width from series 3 was greater (75mm) while thickness was similar to series 1. Different level of loading were investigated, leading to a large number of specimens failure. Sample S35 was used to calibrate the test for this series. As a result no fatigue can be observed. The failure observed in the specimens was assumed to have initiated from the area shown on the figure (Figure A.13). Similar to series 1, Sample S34 also suffered from misaligned gripping (Figure 6.3). This results in a non-symmetric crack growth reaching the sample's edge and fails. The next two samples suffered from bending due to the geometry. As a result, fatigue crack growth was first observed in the thickness direction up to a certain stage during the test. Then fatigue crack growth was observed to occur only on surface direction until instability. A summary of the specimens is given below:

- Sample S31 - Crack growth quicker on one side until it reached edge
- Sample S32 - Not tested
- Sample S33 - Crack growth quicker on one side until it reached instability
- Sample S34 - Crack growth only on one side until instability
- Sample S35 - Fracture without fatigue crack growth

6.2.3.4 Series 4 (15x75x100mm)

The specimens from series 4 were the largest tested with a thickness of 15 mm and width of 75 mm. Like specimens from series 1, Sample S45 also showed effect due to misaligned gripping (Figure 6.3). Non-symmetric crack growth was evident from initial crack until the sample's edge. Sample S42 was the first to reach the expected crack evolution (Figure 6.4). Fatigue crack growth was observed until it reached the back surface (Area 2). Breakthrough was observed as well (Area 3). However, the sample failed rapidly after breakthrough (Area 4). Loading has been reduced for the next samples tested. Other samples from this series achieved the expected crack shape evolution. A first stage of fatigue crack growth can be observed (Area 2). When the crack reached the back surface, it breakthrough and a rapid crack extension may be observed (Area 3). From this point, another stage of fatigue crack growth could be identified (Area 4) before the final failure (Area 5). Another observation on samples S41 and S44 was that after breakthrough (Area 3), another area could be observed (Area 4). The fracture surface was similar to sample S42 where overloading was assumed. Compared to FEA models prepared for non-ideal through-wall crack, this was realistic as the SIF was found higher on the back surface. Once the crack shape reached an "ideal" through-wall crack shape, fatigue surface (Area 5) was observed until failure (Area 6). A summary of the specimens is given below:

- Sample S41 - Expected crack growth mainly in thickness direction
- Sample S42 - Expected crack growth mainly in thickness direction, rupture soon after break-through
- Sample S43 - Expected crack growth mainly in thickness direction, through-wall crack growth mainly in one direction
- Sample S44 - Expected crack growth
- Sample S45 - Crack growth quicker on one side until it reached instability

6.2.4 Summary of the test results

Different observations have been noted based on the experimental work on Perspex samples:

- If the sample was not loaded strictly perpendicular to the applied load, fatigue crack growth resulted in a non-symmetric pattern. This lead to rapid extension of the crack size on one side. It reached rapidly the specimen edge and failed prematurely (S11, S12, S13, S14, S15, S21, S34, S45).
- Thicker samples allowed the crack growth through-thickness. Desired crack shape evolution has been observed for Samples from Series 2 and 4 which were 15mm thick.

- Samples from Series 3 experienced from bending during the tests. This resulted in an increase in crack length on surface and crack growth arrest in the thickness direction.
- Samples from Series 4 achieved expected crack shape evolution. Once the crack had broken through, a rapid crack growth was observed until the crack shape reached an "idealised" through-wall shape. This has been confirmed by the FEA work carried on previously, (see Chapter 5), of which a high SIF values was predicted at the back surface of a non-idealised through-wall crack.

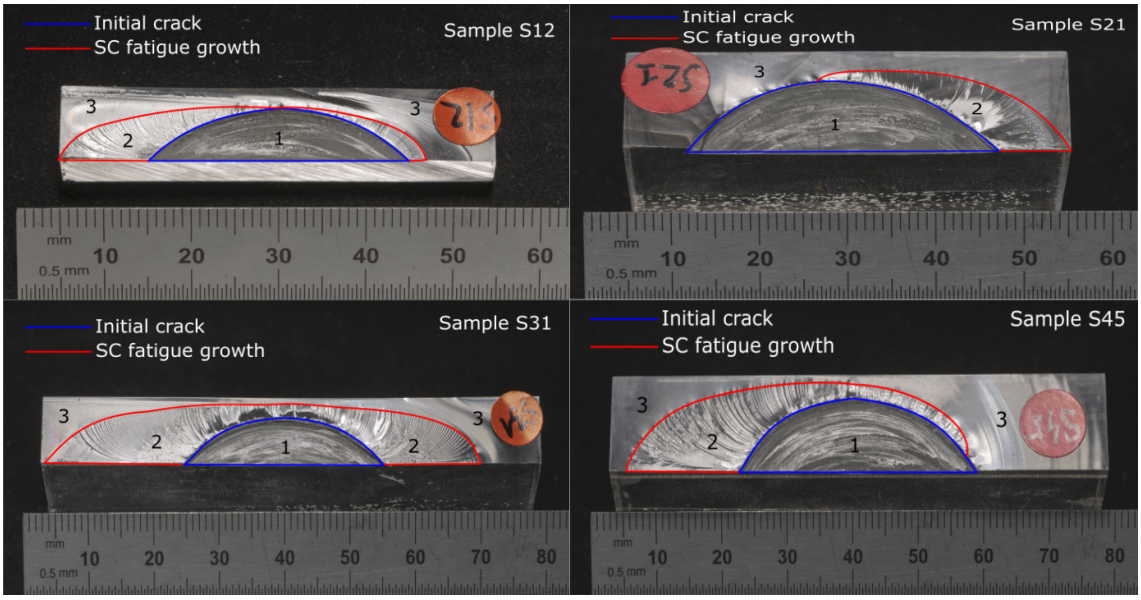

Figure 6.3: Fracture surface of samples with a non-symmetric fatigue crack growth (Samples S12, S21, S31 & S45)

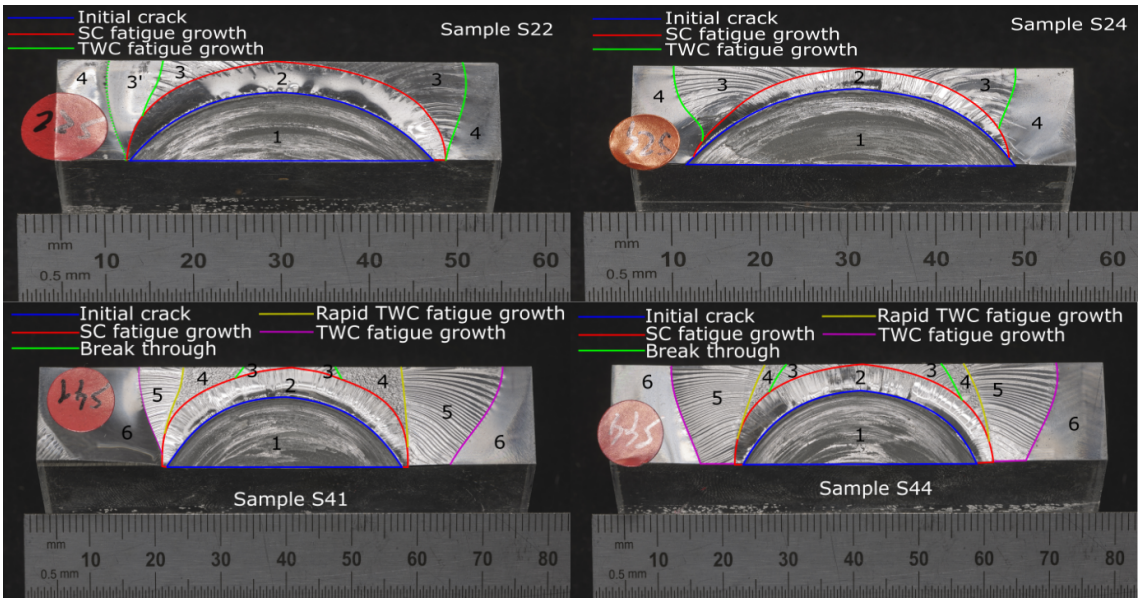

Figure 6.4: Fracture surface of samples with an expected fatigue crack growth pattern (Samples S22, S24, S41 & S44)

Table 6.3: Summary of test results

Specimen	Non-Symmetric loading	Fatigue+Breakthrough	Fatigue+Break	Break
S11	X			
S12	X			
S13	X			
S14	X			
S15	X			
S21	X			
S22		X		
S23			X	
S24		X		
S31			X (Bend)	
S33			X (Bend)	
S34	X			
S35				X
S41		X		
S42		X		
S43		X		
S44		X		
S45	X			

6.2.5 Crack shape re-categorization

Once the surface crack depth reached 80% of the wall thickness by fatigue crack growth, current available procedures recommend re-characterization as through-thickness to evaluate its acceptance when considering LBB condition. The re-categorization as a through-wall crack consists of the combination of the surface crack length plus an additional length based on the thickness or remaining ligament. The formulation for re-characterization in three procedures are given:

- General method in API 579-1/ASME-1 FFS [9]:

$$2c_t = 2c_s + 2(t - a_s) \tag{6.1}$$

  where $2c_t$ is the re-categorized through-wall crack length equal to the sum of the surface crack length 2 c_s plus twice the remaining ligament with a_s the surface crack depth, and t is the wall thickness.
- The recommended formula for LBB analysis in API 579-1/ASME FFS-1 [9]:

$$2c_t = 2c_s + 2t \tag{6.2}$$

  The re-categorized crack length is longer because the thickness is added twice to the surface crack length, instead of using the remaining ligament length.

- The re-categorization formula given in Annex E of BS 7910 [1]:

$$2c_t = 2c_s + t \tag{6.3}$$

  This re-categorization of a surface crack falls in between the two API 579-1/ASME FFS-1 equations by adding one thickness to the surface crack length.

Using the three equations above to re-categorize the surface crack, the recommended through thickness crack lengths, are given in Table 6.4. Only samples that resulted in the expected penetration were assessed.

Table 6.4: Re-categorization through-wall crack length as per BS 7910 and API 579-1/ASME FFS-1

Specimen	API 579 - Eq.6.1	API 579 - Eq.6.2	BS 7910 - Eq.6.3
S22	41.10	62.50	48.15
S24	41.36	64.56	50.48
S41	41.72	63.92	49.56
S42	42.78	65.38	51.04
S43	40.44	64.04	49.62
S44	41.18	63.78	49.34

6.3 Evaluation of stress-strain field on back surface using high strength steel specimens

Several experimental works to investigate the crack growth shape due to fatigue loading have been carried out [144], [145], [111]. The focus is often on stress or strain field at crack-tip and stress intensity factor (SIF) derivation [151], [152], [153], [154]. With regard to the influence of the geometric characteristics of the crack, in the case of tension, the SIF was shown to be maximum at the centre of the crack front for cracks with low aspect ratio and at the surface point for cracks with high aspect ratio. However, for deeper cracks for (a/t $>$ 0.8) the accuracy of solutions has not been well established. The crack front progression was also studied by means of numerical methods [155], [156] based on Paris law [157]. It was shown that cracks would try to grow with a SIF remaining constant along the front, but such behaviour fail when the cracks become deeper and approach the free surface [158]. This section deals with the propagation of deep surface cracks (a/t $>$ 0.8) in plates subjected to cyclic tension. Four flat plate specimens were produced from high strength steel samples (400x150x22mm). All specimens notched with part-penetrating cracks were subject to uni-axial tensile fatigue loading. Propagation from 80% thickness surface cracks to fully through-thickness shape was investigated. Strain variation during the fatigue crack growth has been analysed for two different crack aspect ratios. Material properties, test arrangement and results are presented in the following sections.

6.3.1 Material properties

This section summarises the properties of the specimens. Material properties are required as basic input for integrity assessment. All the tests were carried out using facilities at TWI, in accordance with the respective testing standards and accreditations. The samples for chemical analysis were analysed using optical emission spectroscopy, OES (also known as direct spark analysis). The composition is given in Table 6.5.

Table 6.5: Chemical composition of high strength steel

Element	C	Si	Mn	P	S	Cr	Mo	Ni
Wt. (%)	0.2	0.31	1.43	0.007	0.005	0.22	0.53	0.59

Mechanical properties have been measured using tensile test in accordance with BS EN ISO 6892-1:2009 B [159]. Round tensile samples were machined from one of the available plates as shown in Figure 6.5. The specimen dimensions and results of tensile tests are given in Table 6.6 and the associated stress/strain curve is presented in Figure 6.6.

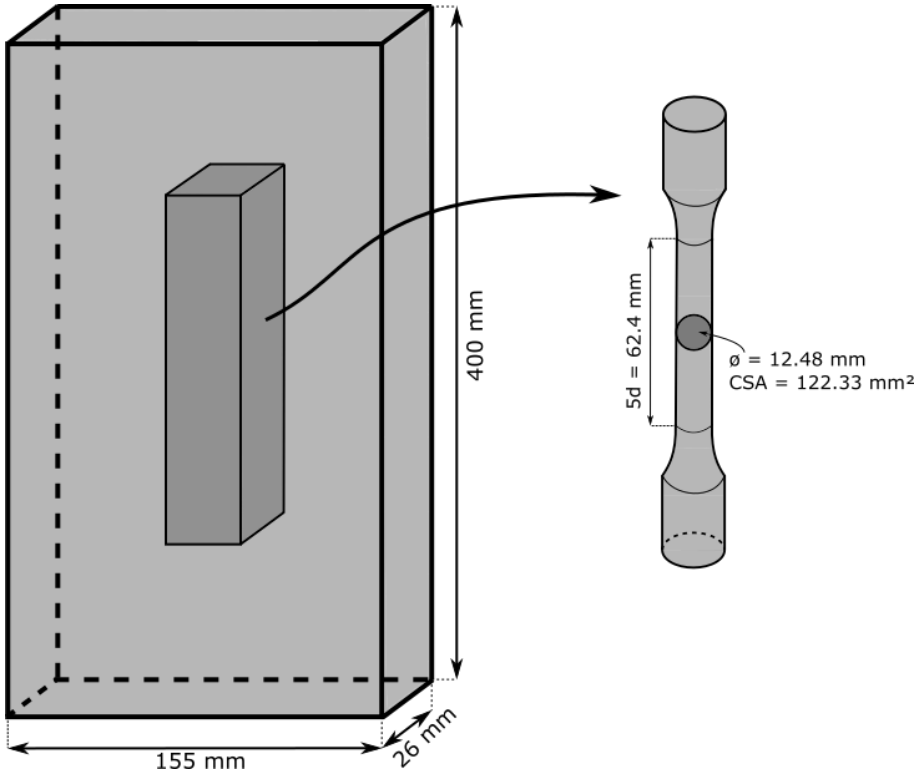

Figure 6.5: Schematic of cutting plan for tensile specimens

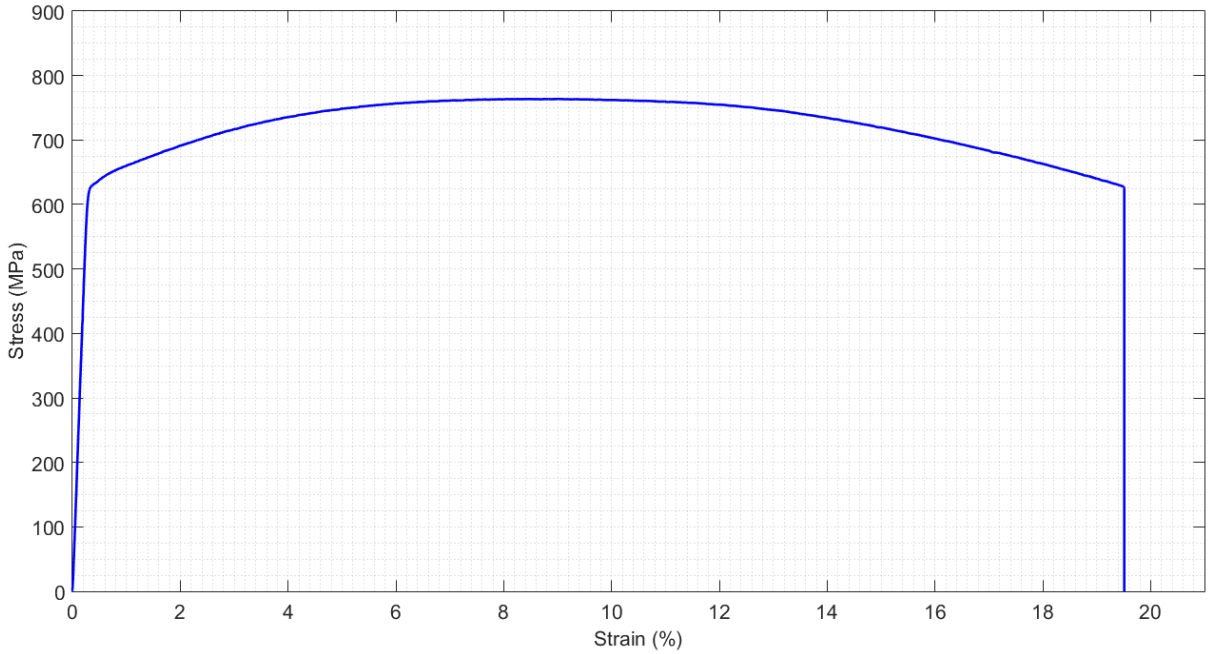

Figure 6.6: Stress-strain curve derived from tensile specimens

Table 6.6: Mechanical properties derived from tensile test

Yield strength		Ultimate tensile strength		Young's Modulus	Poisson's ratio
Load (kN)	Stress (MPa)	Load (kN)	Stress (MPa)	MPa	—
78.07	638.2	93.42	763.7	217147	0.3

6.3.2 Test specimens

Test specimens (400x150x22mm) consist of flat plates machined to dog-bone shape with semi-elliptical surface-breaking notches. All specimens were notched to a depth about 80% of the plate thickness using electro-discharge machining (EDM). A pure copper electrode with thickness of 0.1 mm has been prepared to be used in the spark procedure. Figure 6.7 presents the dimensions of machined specimens and details of notch. Specimens edges have been radiied to avoid fatigue initiation at an undesired location. A total of four plates have been manufactured. Two different crack geometries were examined (later described as "short" and "long" cracks). Numbering and respective geometric details of the test specimens are given in Table 6.7.

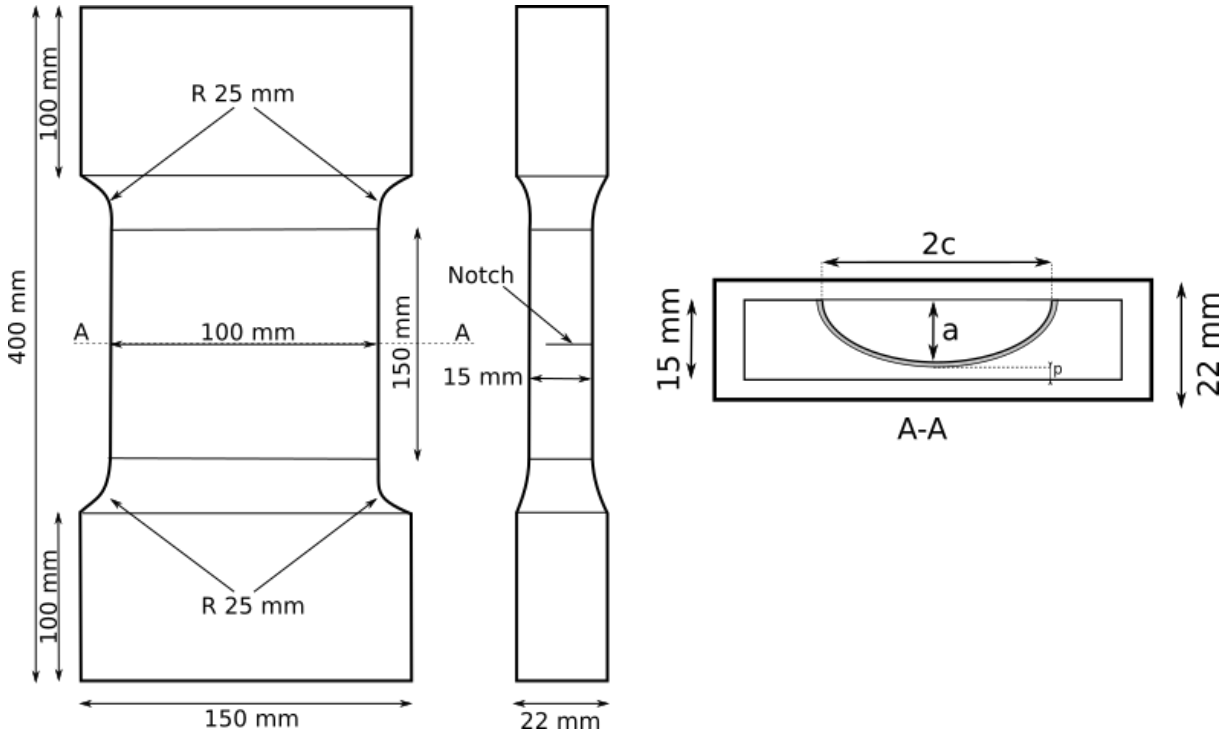

Figure 6.7: Schematic drawing of dog-bone shaped specimens with artificially-induced cracks

Table 6.7: Test specimens numbering and dimensions

Geometry	Specimen No	Width (mm)	Thickness (mm)	Crack depth a (mm)	Crack length 2c (mm)	Ligament p (mm)
Long	M01-01	100.6	14.80	12.1	57.9	2.7
Crack	M01-02	100.1	15.79	11.9	58.9	3.9
Short	M01-03	100.4	14.67	12.1	23.8	2.6
Crack	M01-04	100.1	15.82	12.4	24.0	3.5

6.3.3 Test arrangement

Electrical resistance strain gauges were attached on to the back surface of the plates. A 6 mm uni-axial strain gauge (TML FLA-6-11) and sixteen 1 mm uni-axial strain gauges (TML FLA-1-11) were positioned as shown in Figure 6.8 as seen in specimen M01-01. The distance between strain gauges was established to be 10 mm. The strain gauge at the centre carried a resistance of 120 Ω with a gauge length and width of 6 mm and 2.2 mm respectively. The other strain gauges carried a resistance of 120 Ω with a length and width of 1 mm and 1.3 mm respectively. They have been adhesively bonded to the plates using cyanoacrylate adhesive. They were wired with a quarter bridge configuration to a NI 9235 module (Logging rate = 10kS/s/ch) for data acquisition. Three types of strain were monitored during testing:

- Strain along the plane parallel to the crack - X-axis (SG 1/7/8/9/10/11/12/13/14)
- Strain along the plane perpendicular to the crack - Y-axis (SG 2/3/4/5/6)
- Strain along the diagonal axis (SG 15/16/17)

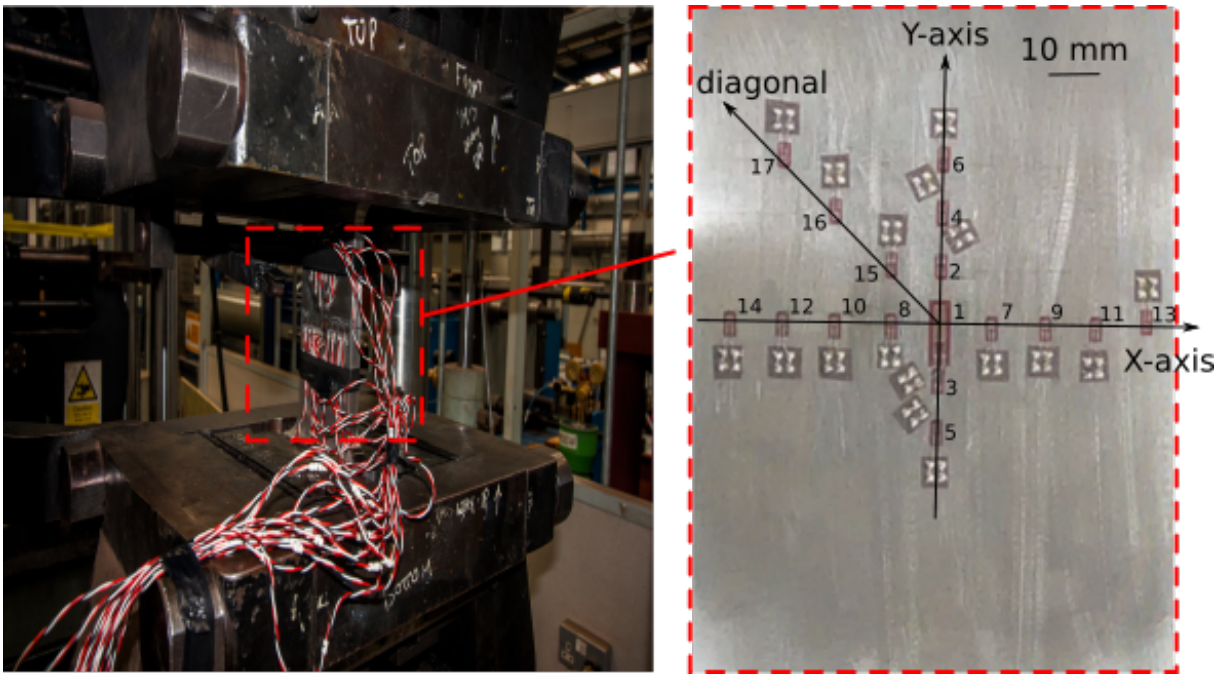

Figure 6.8: Set-up for fatigue test with strain gauges attached onto the back surface of specimen. Notch was introduced on the opposite surface

A static test was performed for each specimen for the purpose of calibrating the strain gauges. Specimens were then subject to fatigue loading at room temperature in air using a Mayes servo-hydraulic test machine with a 500kN capacity load cell. All tests were conducted using load control with a constant sinusoidal fluctuating tensile mean load of 135kN with a load ratio R=0.1. This resulted in a cross section tensile mean stress of 82.5 MPa (≈13% x material's yield strength). The maximum applied stress of 150kN (100 MPa), was well below the yield strength (≈ 15% x σ_{ys}). The tests were monitored using a computer software and all loading history was recorded. Fatigue tests were considered achieved when the through-wall crack reached one of the last strain gauges along X-axis (SG13/SG14). The specimen was then removed from the machine and pulled apart to have access to the fracture surface. Results of both static and fatigue test are provided in the following two sections.

6.3.4 Static tests

A static test had been performed for each specimen for the purpose of calibrating the strain gauges. Specimens were subject to different loads and the strains were recorded. Calibration was divided into five stages: ie (i) 0kN, (ii) 15kN, (iii) 50kN, (iv) 100kN

and (v) 150kN. The strains measured at each stage were logged and readings were used to set the various trip values implemented to stop the fatigue tests at desired crack development. Far field elastic strain was estimated for each specimens based on their respective dimensions:

- $\epsilon_{M01-01} = \frac{F}{A_{M01-01}E} = 463.96\mu\epsilon$
- $\epsilon_{M01-02} = \frac{F}{A_{M01-02}E} = 437.04\mu\epsilon$
- $\epsilon_{M01-03} = \frac{F}{A_{M01-03}E} = 469.24\mu\epsilon$
- $\epsilon_{M01-04} = \frac{F}{A_{M01-04}E} = 436.21\mu\epsilon$

where F is the force applied, E the Young's modulus and A the cross section for each specimen. Static test recorded strain are provided for long crack geometry (M01-01/M01-02). Data from short crack geometry (M01-03/M01-04) are provided in AnnnexA.2.1. The recorded values of strain in the three directions for M01-01 & M01-02 are given in the following figures:

- Figure 6.9 - X-axis
- Figure 6.10 - Y axis
- Figure 6.11 - Diagonal axis

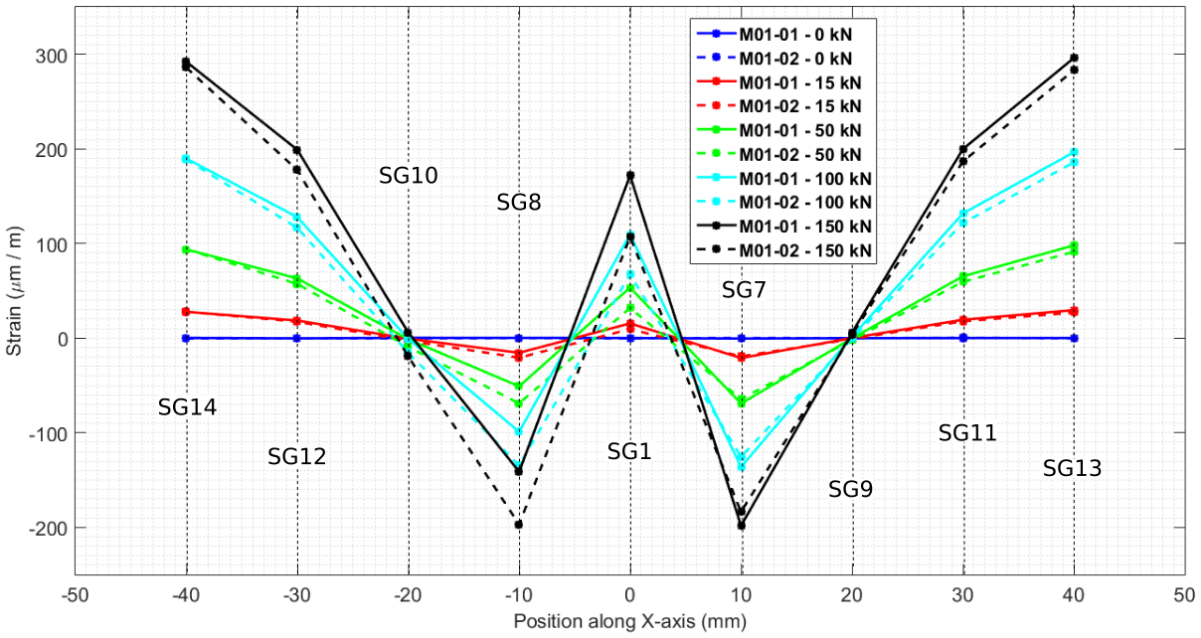

Figure 6.9: Evolution of strains along X-axis under increasing static loads: 0kN, 15kN, 50kN, 100kN and 150kN for Specimens M01-01 & M01-02

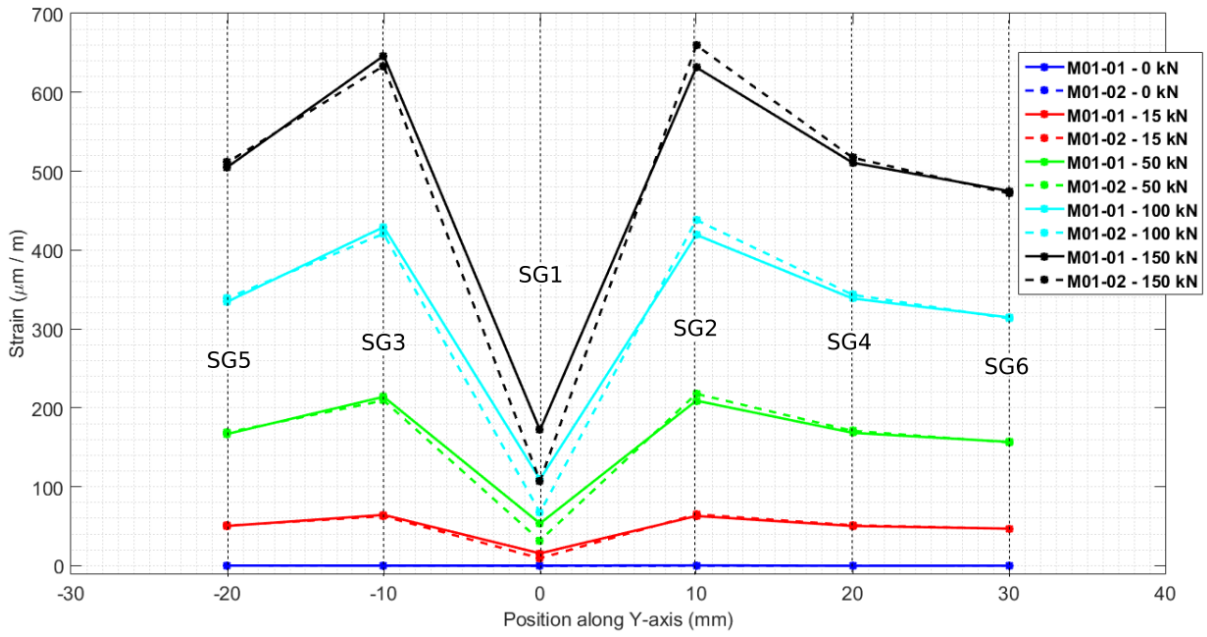

Figure 6.10: Evolution of strains along Y-axis under increasing static loads: 0kN, 15kN, 50kN, 100kN and 150kN for Specimens M01-01 & M01-02

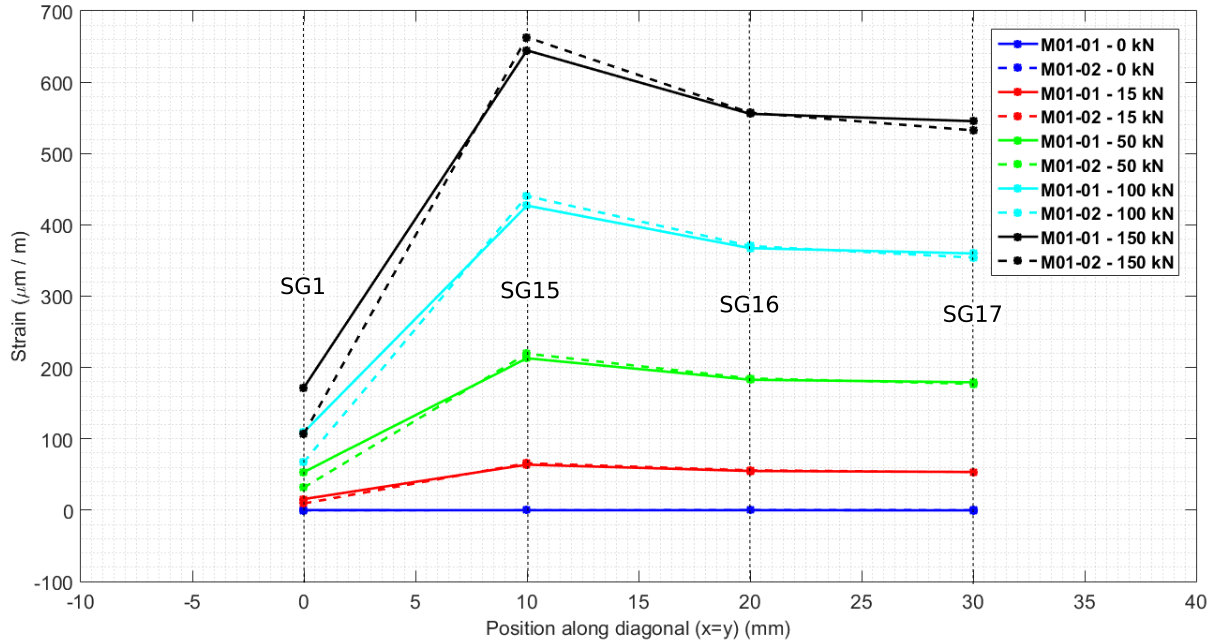

Figure 6.11: Evolution of strains along the diagonal direction under increasing static loads: 0kN, 15kN, 50kN, 100kN and 150kN for Specimens M01-01 & M01-02

The profiles of static tests were observed to be similar for both geometries (short"/"long cracks). However, recorded values differed greatly. For short cracks, the variation of strains is limited due to the dimensions (c=a) and area of the notch ($\approx$ 15% of the specimen CSA). For long cracks, the area of the crack is larger ($\approx$ 35% of the specimen CSA) and the length longer. This led to some bending (not measured) that needs to be balanced. It is worth to note that strain values are measured at a particular location along each axis. Further details are provided in the next chapter (Section 7.3) where numerical model were developed.

6.3.5 Fatigue tests

All tests were carried out using load control with a constant sinusoidal fluctuating stress where σ_{max} was 100 MPa, σ_{min} was 15 MPa and σ_{mean} was 82.5 MPa, as presented in Figure 6.12 and Table 6.8.

Table 6.8: Cyclic loading parameters

Parameter	Max. Load (kN)	Min. Load (kN)	Load range (kN)	Mean Load (kN)	Load Ratio (–)	Freq. (Hz)
Value	150	15	135	82.5	0.1	3

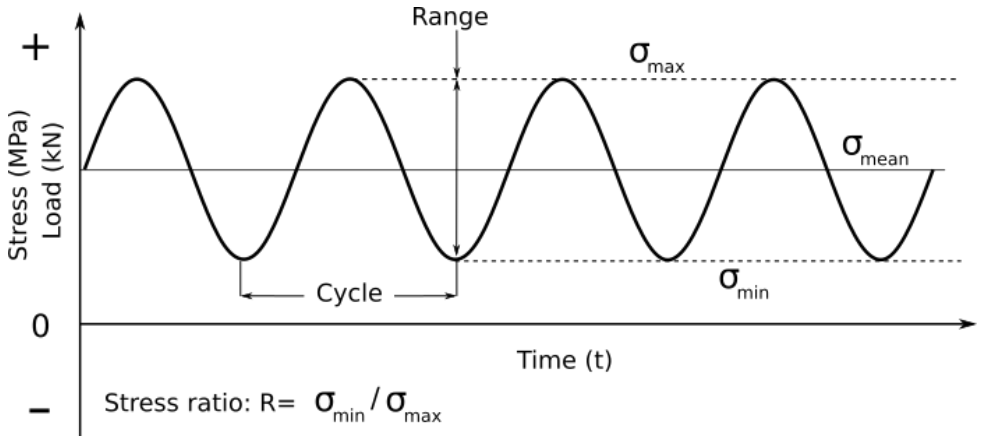

Figure 6.12: Schematic graph illustrating cyclic loading applied during testing

The plots obtained from specimens fatigue test on M01-01 are presented in this section. Strain evolution during tests for the other specimens can be found in Annex A.2. Strain gauges numbering can be found in Figure 6.8. Strain evolution on the back surface of the plates is given in:

- Figure 6.13 - Strain evolution along the X-axis
- Figure 6.14 - Strain evolution along the Y-axis
- Figure 6.15 - Strain evolution in the diagonal direction

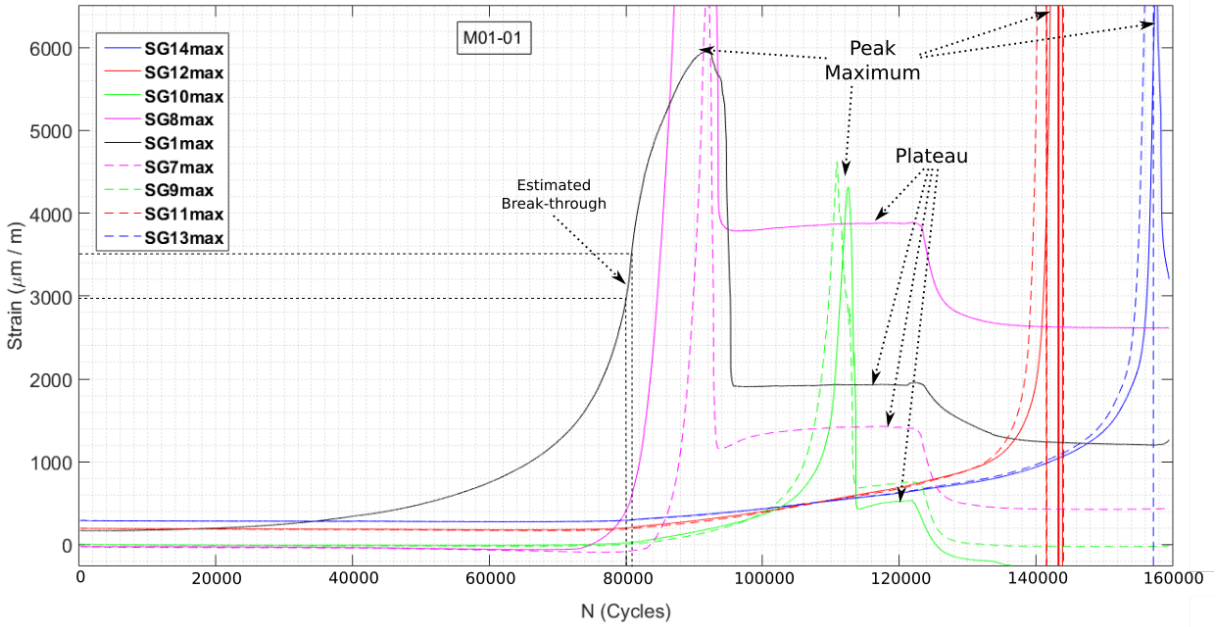

Figure 6.13: Evolution of the strains along the X-axis during fatigue test - M01-01

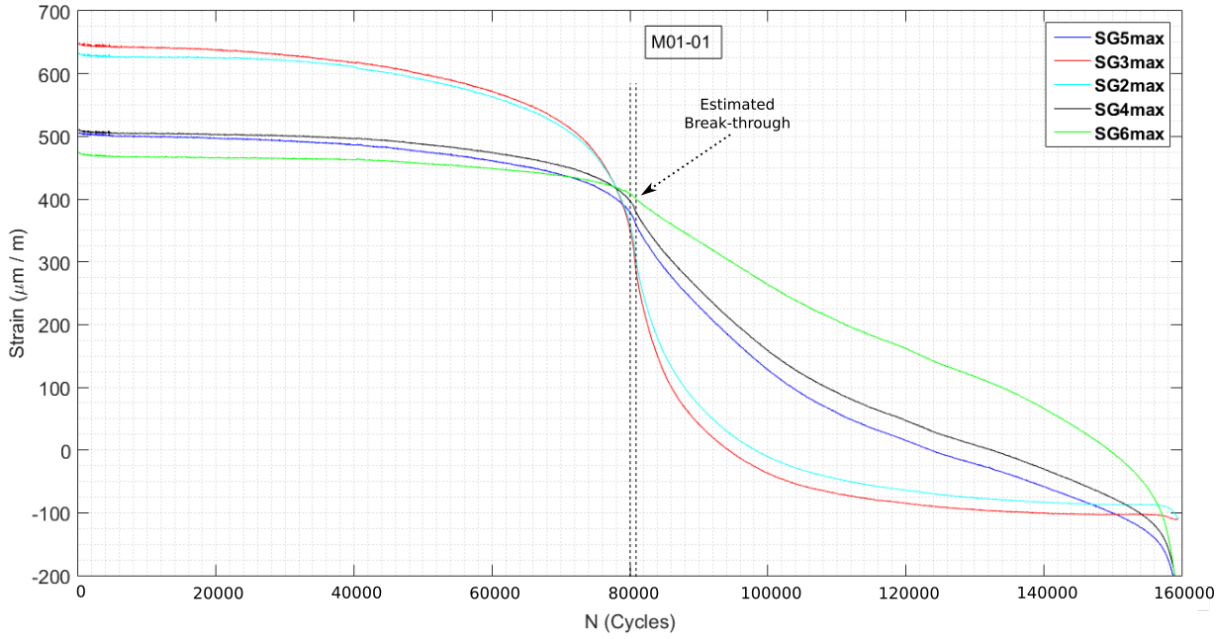

Figure 6.14: Evolution of the strains along the Y-axis during fatigue test - M01-01

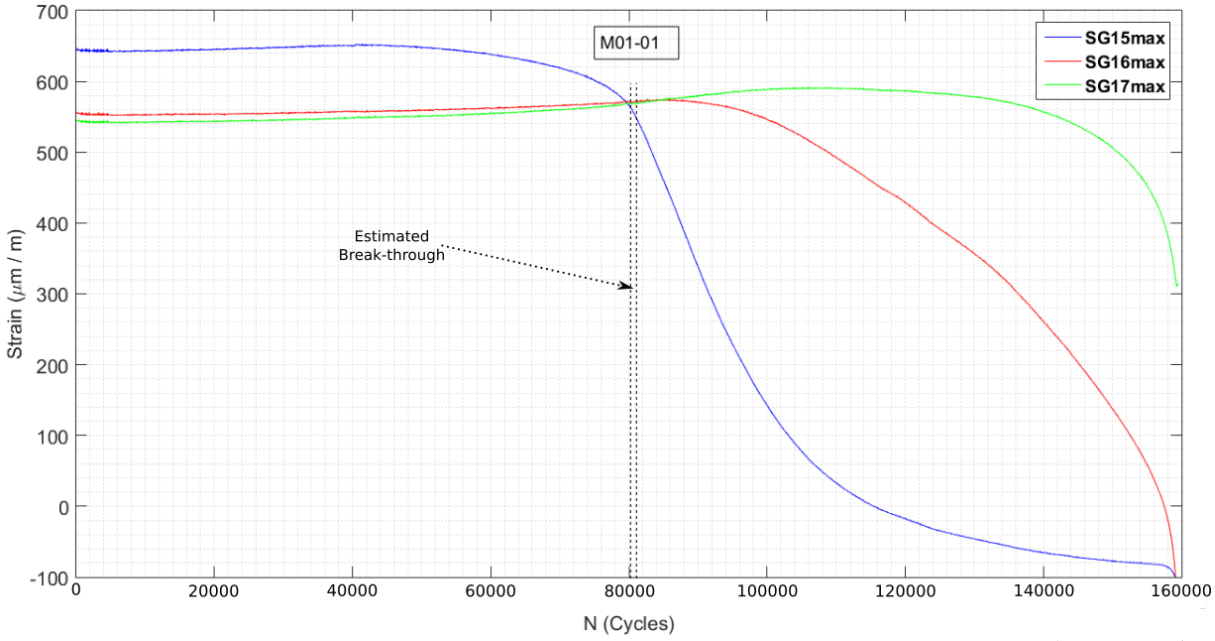

Figure 6.15: Evolution of the strains for the diagonal strain gauges during fatigue test - M01-01

The final number of cycles for each specimens tested is given in Table 6.9. For "long" crack specimens, the number of cycles is fairly similar (between 140k-160k cycles). For "short" crack specimens, a large discrepancy can be observed (ranging from 470k to 710k cycles). A stabilisation of the strain evolution for about 200k cycles has been observed from the strain data for sample M01-04. This was assumed to be due to the notch insertion resulting in a lighter condition at crack-tip.

Table 6.9: Number of cycles until failure for all tests

Geometry	Specimen No	N (Cycles)
Long crack	M01-01	159629
	M01-02	139704
Short crack	M01-03	468656
	M01-04	709870

Figure 6.13 presents the strain variations along X-axis as the crack propagated. Initial strains were in good agreement with static tests carried out earlier. The difference in the peak maximum and plateau observed for the strain gauges SG1, SG7, SG8, SG9 and SG10 is due to the failure of the adhesive before the strain gauge. When rupture of the strain gauge occurs before debonding, the maximum strain dropped instantly (i.e. SG11, SG12, SG13 and SG14). The first variation has been observed in SG1, located where the ligament was the thinnest (i.e. X=0mm), after ≈20000 cycles. Other strain gauges remained stable until SG1 value reached ≈3000 μm/m. Break-through was estimated to occur when strain values from SG1 were ≈3000-3500 $\mu\epsilon$ (≈80000 cycles). Afterwards, all recorded values

from strain gauges started to increase along X-axis. It can be observed for the couple SG7/SG8 showed an increase in recorded strain values at the approximate cycles where breakthrough occurred. This implies that break-through did not occur exactly at the centre of the plate where SG1 was attached (i.e X=0mm) but at a distance offset from it. This effect was less pronounced for the couple SG9/SG10, indicating that soon after crack penetration, crack growth occurred at a higher rate on one side to grow in a symmetric way for the remaining.

Figure 6.14 presents the strain variations along Y-axis as the crack propagated. Similar to the observation along X-axis, the break-through was estimated to have occurred after ≈80000 cycles. The higher variation rate for strain gauges close to the crack plane (SG2 and SG3) and a sudden change in the slope of the recorded values for strain gauges far from the crack plane (SG4, SG5 and SG6) has been observed. Opposite to observations along X-axis, strain values decreased as the crack grew. Close to the crack plane (SG2/SG3), the first variations were observed after ≈ 20000 cycles (similar to SG1 behaviour along X-axis) with descending values of recorded strain. While recorded strains from SG1 showed a sharp increase from 60000 to 80000 cycles, strain values for SG2/SG3 showed increased descending rate. For strain gauges located further away from the crack plane (SG4/SG5/SG6), there was a gradual decrease in strain between 60k and 80k cycles but a swifter decrease only occurred after breakthrough (similar to observations along X-axis).

Figure 6.15 presents the strain variations along the diagonal direction as the crack propagated. Unlike the observations along X and Y axes, the effect of break-through was not significant and really captured. It is provided based on previous observations. However, similar behaviour as that along Y-axis has been observed. The recorded strain for the strain gauge closest to the crack plane (SG15) showed decrease first, while for strain gauges located further, the drop in recorded strain was more gradual, with SG16's strain profile being between SG15 and SG17.

6.3.6 Discussion

Based on the observations made on the strain data recorded during the tests for each geometry, different aspect have been investigated:

- From Figure 6.13, break-through was estimated to occur when strain values from SG1 were ≈3000-3500 μm/m. The strains at yield (Eq.6.4) and ultimate tensile stress (Eq.6.5) were calculated using uni-axial Hooke's law:

$$\epsilon_{ys} = \frac{\sigma_{ys}}{E} = 2984\mu\epsilon \tag{6.4}$$

$$\epsilon_{uts} = \frac{\sigma_{uts}}{E} = 3518\mu\epsilon \tag{6.5}$$

The graphically estimated location of break-through corresponds to a value located between yield and ultimate tensile strains. These closest recorded values were used as boundaries to estimate the number of cycles range when break-through happened:

- Strain=2984 $\Leftrightarrow$ Cycle=80093
- Strain=3522 $\Leftrightarrow$ Cycle=80865

- From Figure 6.14, break-through was estimated to occur when:
  - Strain gauges close to the crack plane (SG2 and SG3) shown their higher variation rate
  - Strain gauges far from the crack plane (SG4, SG5 and SG6) shown a sudden change in strain variation

  Variation in strains was calculated for all strain gauges along Y-axis. Value of the tangent was calculated at each data point based on strain values within a defined set of 50 cycles. Since the recorded reading of strain exhibited high level of noise, the strain variation rates presented in Figure 6.16 were filtered using MatLab-incorporated moving average function (rloess method). Actual data were used to estimate the number of cycles where minimum variation was observed. Similar calculations were carried out for SG1 along X-axis. In both cases, SG1 (i.e. X=0mm) and SG2/SG3 (i.e. Y=10mm) exhibited greater variation rate in strain values with a maximum at cycle N=80596. As seen previously, this corresponds to a strain value between yield and ultimate tensile strains.

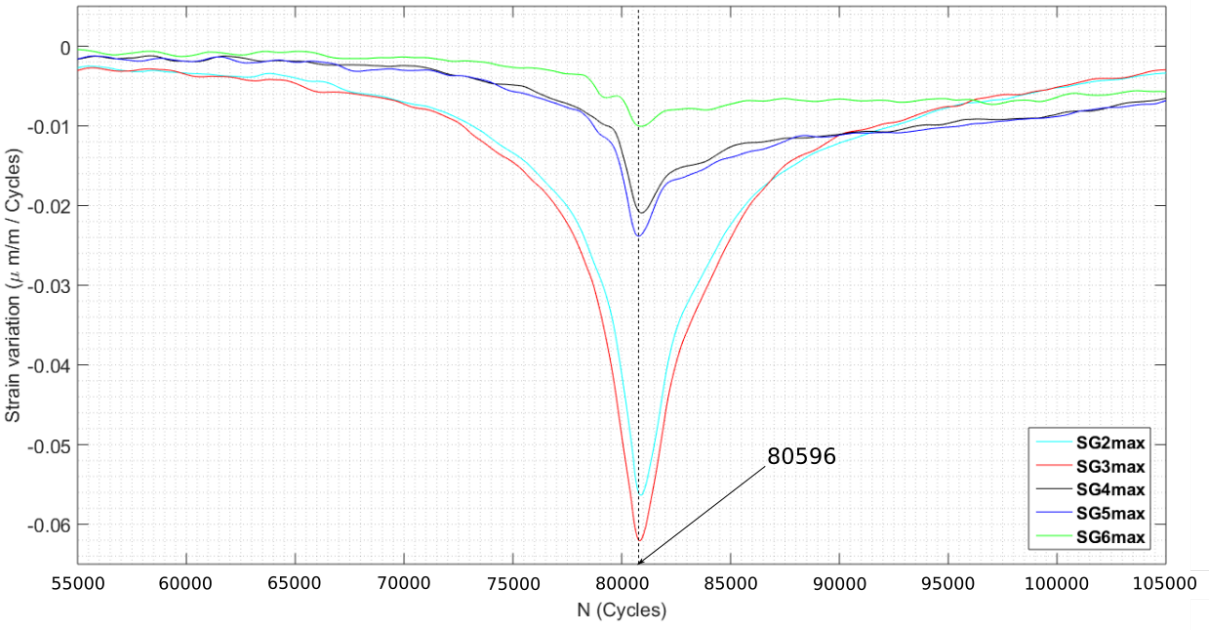

Figure 6.16: Evolution of the strain variation along Y-axis

- As discussed previously, strain variation profiles were similar for both geometries but the recorded values were different. The initial aspect ratio was found to influence the number of cycles for the crack to grow from one strain gauges to another. Table 6.10 provides the recorded values for Specimen M01-01. Figure 6.17 shows the number of cycles when strain gauges measurement reached the estimated yield strain along X-axis for both geometries. The number of cycle was normalised against the central strain gauges (SG1) and calibrated at 0 cycles. The averaged crack growth rate between strain gauges based on the yield strain value is also provided in Figure 6.18.

Table 6.10: Number of cycles against strains at yield and ultimate tensile stress along X-axis - M01-01

M01-01	YS		UTS	
	Cycles	Strains	Cycles	Strains
SG1	80093	2984	80865	3522
SG7	89875	2983	90235	3514
SG8	84603	2978	85053	3505
SG9	109730	2989	110150	3536
SG10	111410	2990	111800	3535
SG11	139294	2984	139535	3513
SG12	141127	2981	141382	3513
SG13	154656	2986	154971	3500
SG14	156276	2988	156561	3531

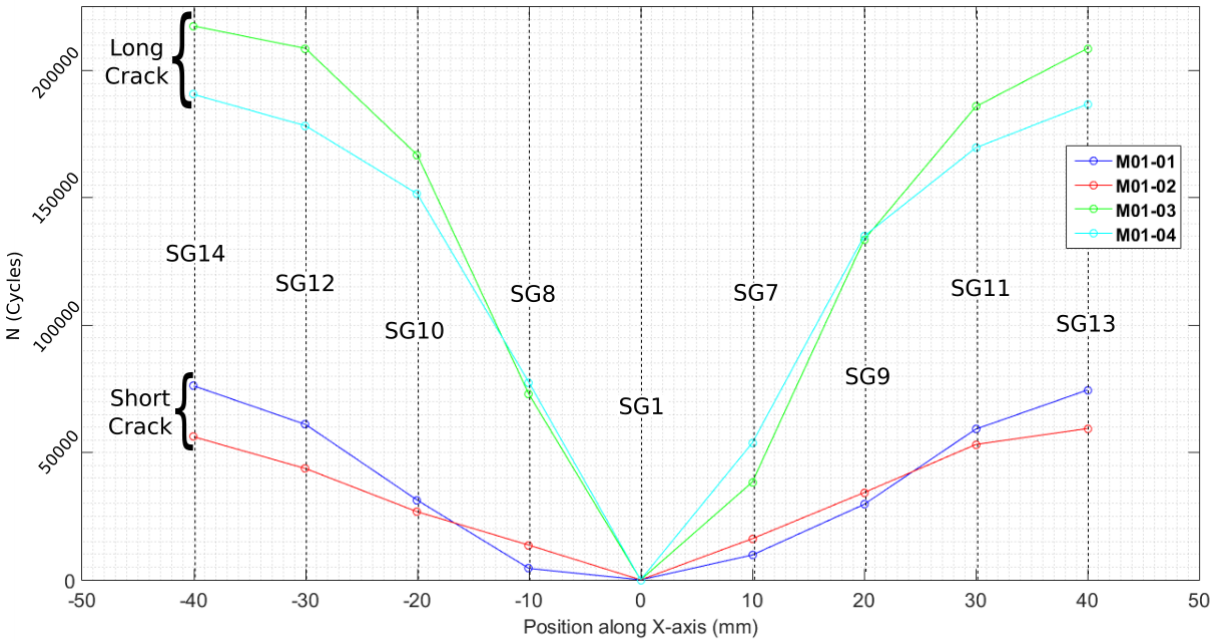

Figure 6.17: Evolution of crack growth rate along X-axis for all specimens (Cycles)

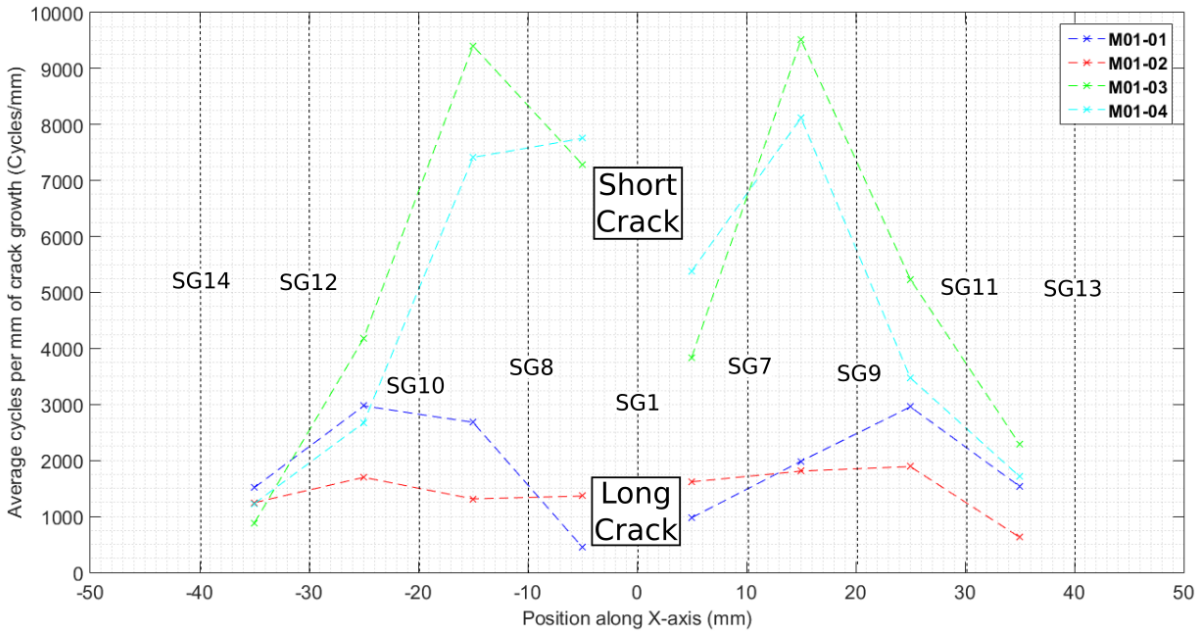

Figure 6.18: Evolution of the crack growth rate along X-axis for all specimens (Cycles/mm)

6.3.7 Observations from tested plates

Fatigue tests were terminated when the through-wall cracks reached one of the last strain gauges along X-axis (SG13/SG14). The specimen was then removed from the machine and pulled apart to examine to the fracture surface.

6.3.7.1 Photographs of fracture surfaces

Photographic record of each geometry is presented in this section. Figure 6.19 presents the fracture surface from M01-01 which is a long crack and Figure 6.20 presents the fracture surface from M01-03 which is a short crack. Photographs of the remaining two specimens can be found in Annex A.3.1.

Four areas were identified on the associated fracture surfaces:

- 1 - Initial crack (blue)
- 2 - Estimated shape at breakthrough (red)
- 3 - Through-wall crack growth (green)
- 4 - Final rupture (pink)

Tests were stopped at different strain levels to introduce a mix of soap and water solution in the crack. This offered the advantage of identifying the stage at which the crack penetrated the back surface by the formation of bubbles. This also introduced oxidation on crack surfaces, leaving beach marks to give a history of the crack shape.

This is particularly relevant to specimen M01-03 where the test has been stopped many times and sufficient time was allowed before to restart.

For long cracks (M01-01/M01-02) as seen in Figure 6.19, the crack growth occurred primarily in the depth direction. The initial crack length remained the same until break-through and followed by some through-thickness growth. Upon break-through, the crack length at the back surface continued to grow from the region bounded by the red line in the width direction (B to B') but the initial crack length only underwent very little extension (A to A'). Fatigue crack growth continued until an almost uniform through-thickness flaw shape was achieved, with a similar length on both side of the plate.

For short cracks (M01-03/M01-04) as seen in Figure 6.20, the crack growth was uniform in both depth and length direction until breakthrough. Crack length increased at a higher rate on the back surface (B to B') until a similar length was observed on both side. However, unlike the long crack, the initial surface crack length always increased during the test (A to A').

It was evident from Figure 6.19 and Figure 6.20 that the evolution from break-through to non-idealised flaw (post break-through) was dependent on the aspect ratio/geometry of the initial flaw size.

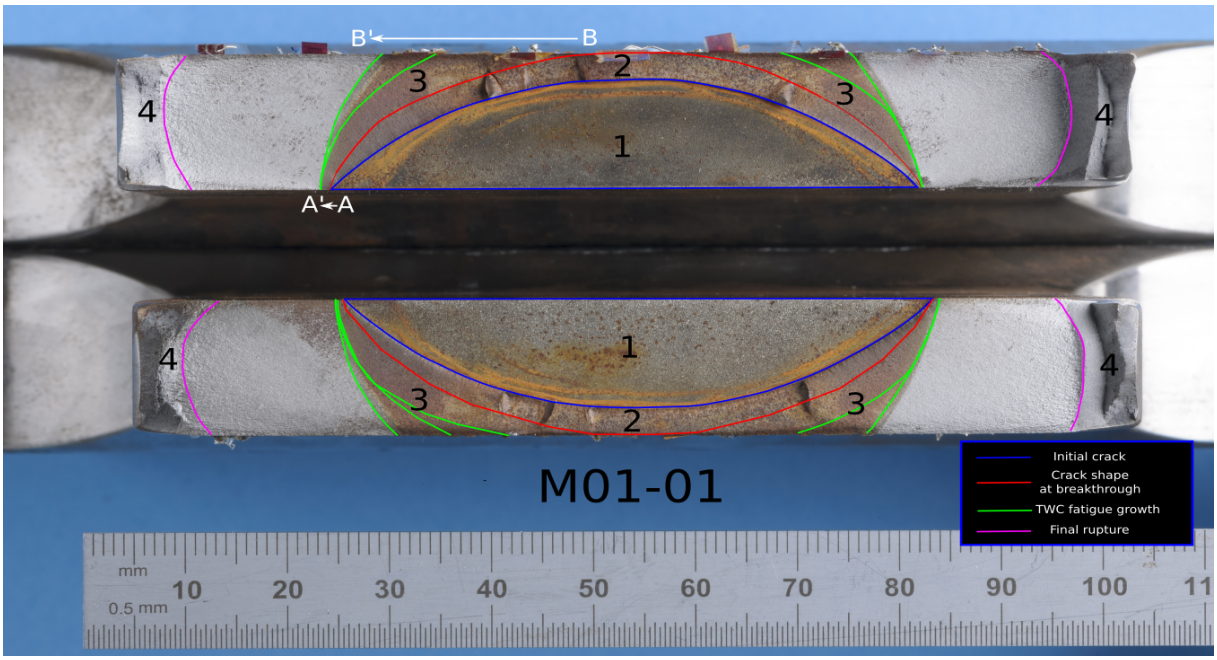

Figure 6.19: Fracture surface of Specimen M01-01

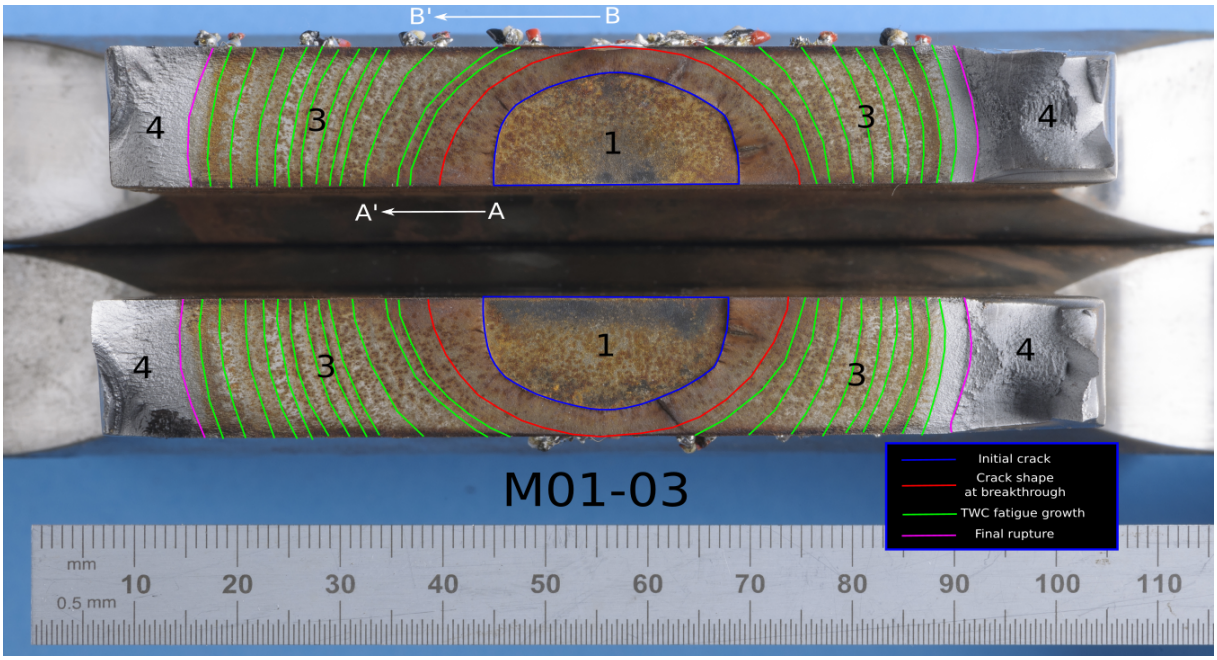

Figure 6.20: Fracture surface of Specimen M01-03

6.3.7.2 Scanning Electron Microscope (SEM) photographs

As part of the effort to get a better understanding of the behaviour during the crack evolution, SEM analysis were carried out with a Zeiss EVO LS15 microscope. Specimens M01-02 and M01-04 were chosen to represent long and short cracks respectively and were less corroded than those presented in Figures 6.19 and Figure 6.20. Fracture surface was carefully cleaned before analysis. However, the use of water/soap solution has oxidised the fracture surface significantly. For this reason, most of the physical feature of the fatigue crack growth were either not available or difficult to detect. Majority of the areas could not be thoroughly examined so only general observations were made. Observation of crack growth on both specimens were similar to those of M01-01 and M01-03. Figure 6.21 gives a schematic of the location where the photographs where taken. Four areas were considered:

1. Transition between initial notch and cross section
2. Break-through location
3. Some distance after break-through
4. Region away from initial notch

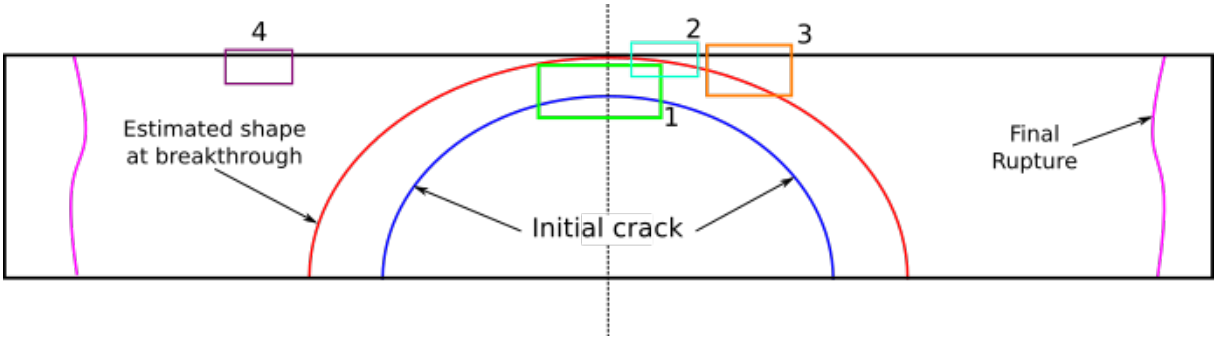

Figure 6.21: Schematic of the location of photographs from SEM analysis

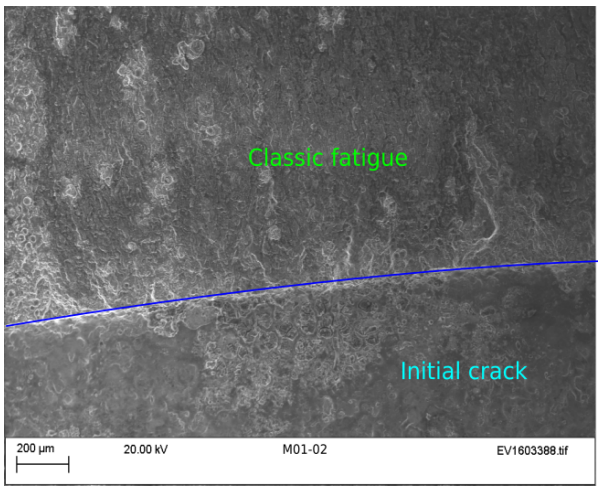

(a) Location 1

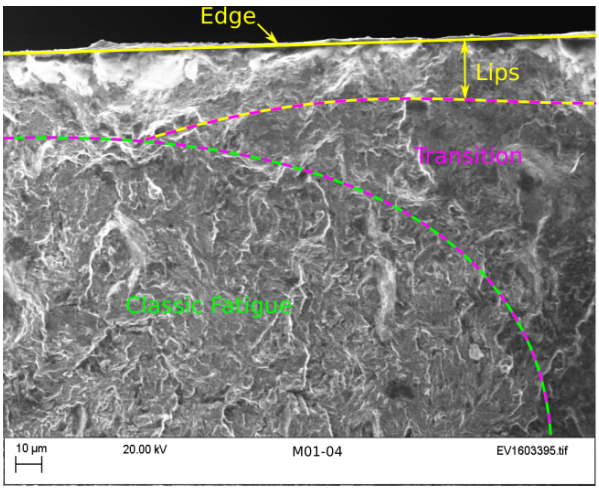

(b) Location 2

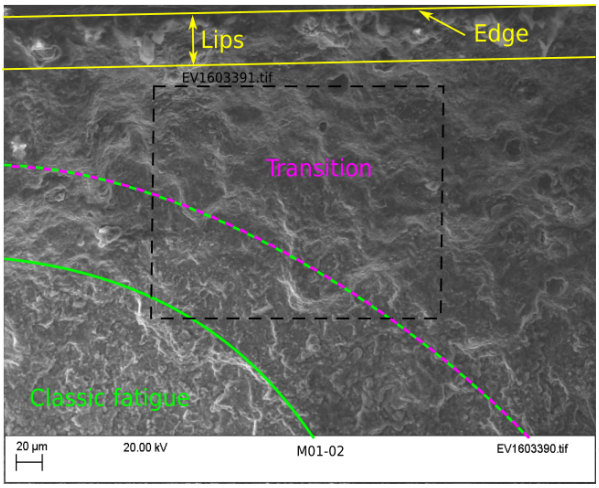

(c) Location 3

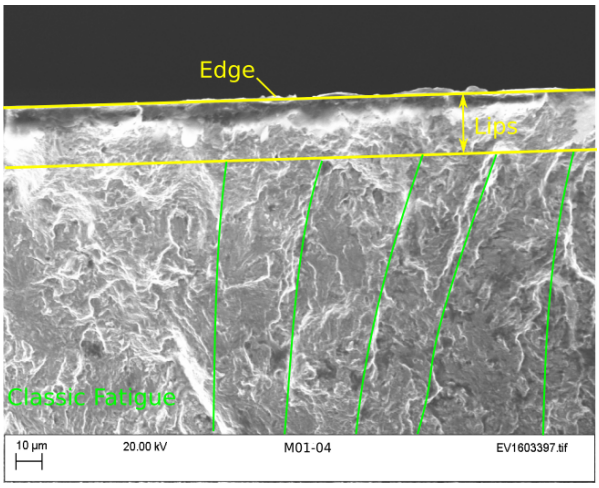

(d) Location 4

Figure 6.22: Photographs from SEM analysis

Figure 6.22a shows a general view (200 μm) between the initial crack and the cross section at initial crack-tip front. Typical initiation of fatigue can be observed along the boundary. Severe corrosion can be noted with the presence of numerous pits. Figure 6.22b shows the area adjacent to the break-through. Three distinct regions were observed. Classic fatigue pattern could be seen until the last stage of propagation. Once the crack broke through, another area of transition (flat, blunt) was observed as well as the formation of a lip. Figure 6.22c shows the transition area. Classic fatigue pattern could still be observed from the initial crack. A transition of classic fatigue, crack blunting and corrosion was also evident. Figure 6.22d was taken at a region away from the transition stage. Propagation was dominated by classic fatigue only before the end of the test.

6.3.7.3 Crack shape recategorisation

Similarly to calculations in Section 6.2.5, the dimensions of recategorised through-wall cracks as per BS 7910 and API 579 were determined. Using equations Eq.6.1 to Eq.6.3, the calculated values are given in Table 6.11. A photograph of M01-02 (Figure 6.23) and M01-03 (Figure 6.23) are provided to represent both geometries. Other specimens can be found in Annex A.3.2 .

Table 6.11: Recategorised through-wall crack length (mm) as per BS 7910 and API 579-1/ASME FFS-1

Equations	Specimens			
	M01-01	M01-02	M01-03	M01-04
API 579 - Eq.6.1	63.3	66.6	29.0	30.9
API 579 - Eq.6.2	87.5	90.5	53.2	55.6
BS 7910 - Eq.6.3	72.7	74.7	38.5	39.8

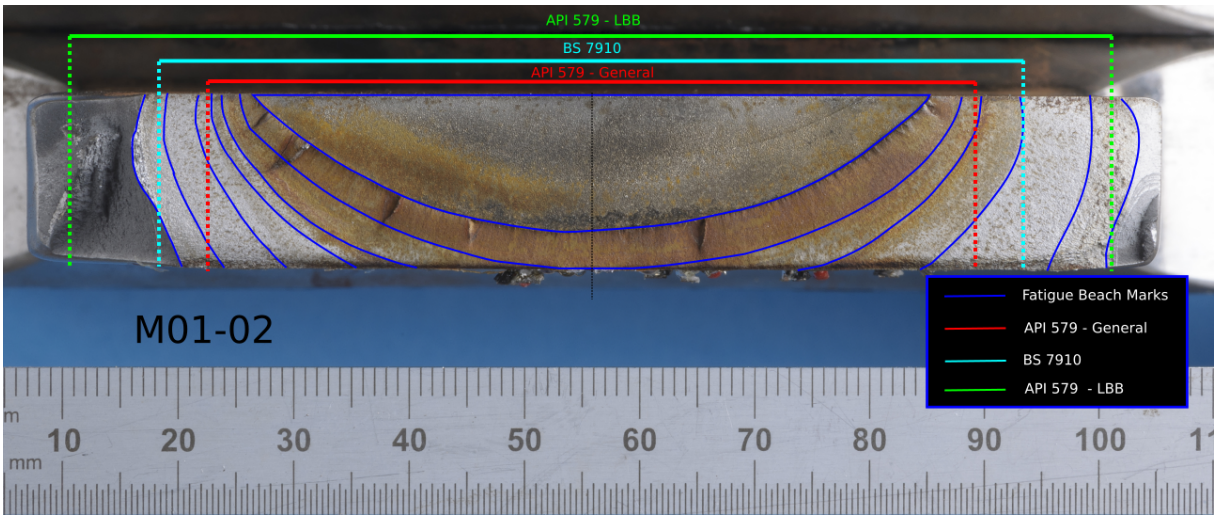

Figure 6.23: Recategorisation into through-wall crack for Specimen M01-02

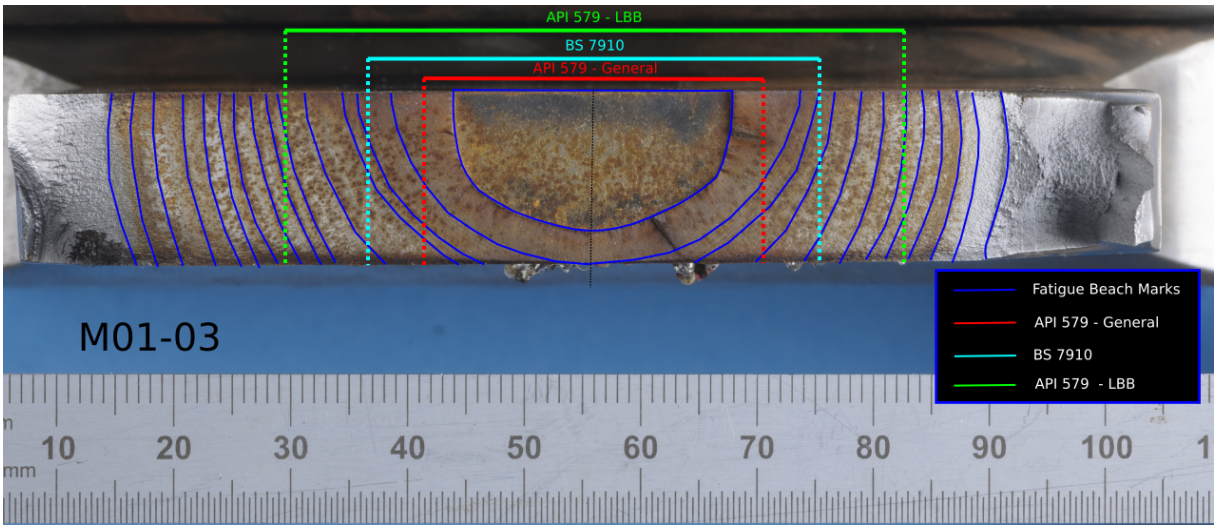

Figure 6.24: Recategorisation into through-wall crack for Specimen M01-03

As described in Section 6.2.5, recategorisation as per BS 7910 falls between the values derived using API 579's general and LBB formulae. For both aspect ratios, the general equation in API 579-1/ASME FFS-1 predicts a smaller through-wall crack when compared to the observed actual shape, especially for short cracks (i.e. Figure 6.24). On the other hand, API's solution recommended in a LBB assessment appears to over-estimate the flaw size for long cracks. The same has been observed in Perspex samples. In terms of recategorisation, BS 7910 rule appears to be more adequate than those of API 579-1/ASME FFS-1. However, based on the observations made in Chapter 5, assessment of COA could still be over-estimated.

6.4 Conclusions

In this chapter, experimental work undertaken was presented. As a semi-qualitative test, fatigue testing on surface cracked Perspex plate specimens showed that: (a) If the sample was not loaded strictly perpendicular to the applied load, fatigue crack growth resulted in a non-symmetric pattern. This led to rapid extension of the crack size on one side and the specimen failed prematurely; (b) Thinner samples experienced bending during the tests. This resulted in an increase in crack length on surface and crack growth arrest in the thickness direction; and (c) Thicker samples allowed the crack to grow through-thickness. They achieved expected crack shape evolution. Once the crack had broken through, a rapid crack growth was observed until the crack shape reached an "idealised" through-wall shape. This has been confirmed by the FEA work carried on previously, (see Chapter 5), of which a high SIF values was predicted at the back surface of a non-idealised through-wall crack.

Two different crack geometries were examined using metallic specimens to represent short and long cracks and the following are concluded: (a) The measured strains allowed the accurate prediction of break-through when recorded strains where between yield and ultimate strain of the material and (b) Observations along three axes (i.e. parallel/perpendicular/diagonal) of the crack showed that break-through can be estimated with a rapid increase of the strain variation on the back surface.

Fracture surfaces from both Perspex (Series 2 & 4) and metallic specimens showed similar behaviour at break through. While the materials are different, further test on Perspex would permit an easier way to characterise the transition from part-penetrating to through thickness crack with direct observations during the test. Metallic specimens showed a change in propagation behaviour during the transition but could not be precisely established due to the corrosion. Similar observation was made on Perspex specimens. Recent advance in testing such as DIC measurement [160] would permit a better understanding on metallic specimens with a full field characterisation of the strain evolution on back surface.

Observations made on the fracture surfaces also showed the importance of the aspect ratio in the LBB assessment: (a) For long cracks, the propagation was primarily in the depth direction. Upon break-through, the crack length increased rapidly on the back surface. Once similar length was reached on both sides, propagation of through-thickness crack occurred at same rate; (b) For short cracks, the initial shape remained the same until break-through. The change in shape occurred during the through-thickness propagation and (c) The transition and growth from a part-penetrating flaw to through-thickness is dependent on the aspect ratio of the initial flaw.

Chapter 7

Numerical Simulation - Stress-Strain Field on the Back Surface of Surface Cracked Plate During Crack Transition

Contents

7.1 Introduction

This chapter describes the work undertaken to examine the transition of crack from surface-breaking to through-thickness. The validation of available solutions for through-thickness cracks and investigation on the crack shape have been discussed in Chapter 5. In this chapter, FEA were carried out to investigate the stress/strain field on the back surface of a plate with a part-penetrating crack. Various FE models have been constructed to evaluate the stress field on the back surface of cracks from 20% to 95% thickness. Two crack geometries have been selected to represent "short" and "long" cracks. The change in stress along the axis of the crack and the one perpendicular to it were also examined.

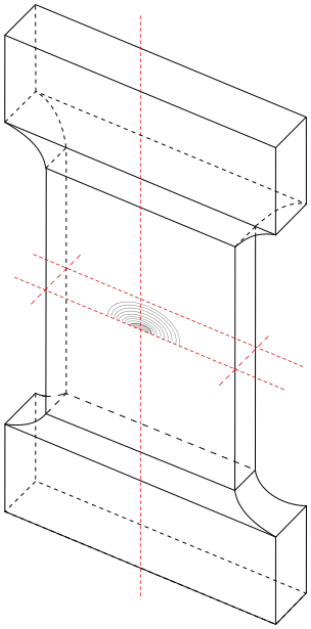

Figure 7.1: Schematic of a cracked plate with crack growth through-thickness

7.2 Models description

7.2.1 Plate and cracks geometry

Various models with crack depths ranging from 20% to 95% thickness have been created for cracks to capture all the possible scenarios during crack evolution. Two crack geometries have been selected to represent 'short' and 'long' cracks. The dimensions of the cracks and plates have been designed to correspond to the experiments described in the previous chapter. Plates were 15 mm thick and 100 mm wide. Crack dimensions were varied. Taking advantage of the symmetries, only 1/4 of the plate of interest was modelled. A typical model used in this work for both geometries is illustrated in Figure 7.2. A crack was introduced in the middle of the plate. Different simulations were pre-

pared for each geometry to include crack depth ranging from 20% to 90-95% of thickness. Crack aspect ratios were kept constant: (i) c=a for Geometry 1, (ii) c≃2a for Geometry 2. A tensile load of 100 MPa (150 kN) was applied to the ends of the plate. The key outputs derived from crack simulations include Von Mises stresses along two axes (as seen on Figure 7.2):

- (i) X-axis which is in plane with the crack
- (ii) Y-axis which is perpendicular to the crack

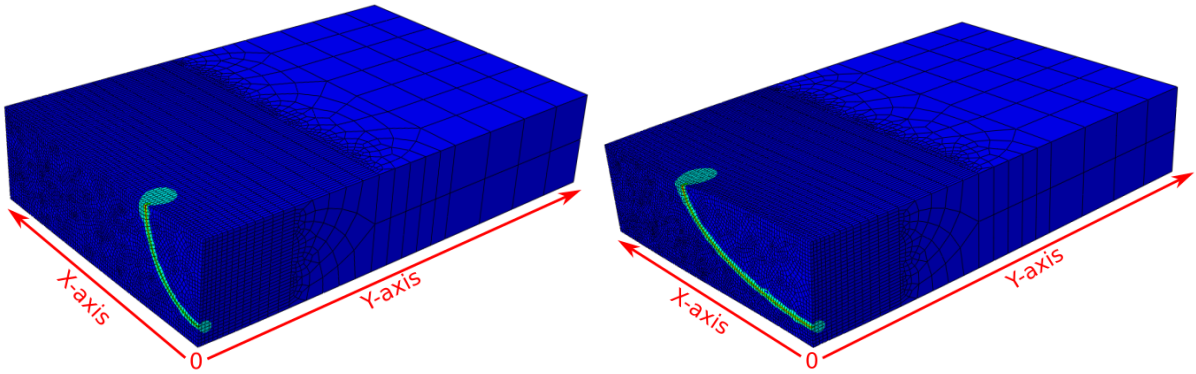

(a) Geometry 1 - Short crack **(b)** Geometry 2 - Long crack

Figure 7.2: FE models for the two crack aspect ratios

7.2.2 The effect of crack geometry on back surface stress field

As a preliminary study, models have been prepared with a crack depth of 80% thickness. This was selected to duplicate the dimensions and geometry of the metallic specimens in Chapter 6. The crack-tip radius was modelled to investigate the effect of a possible blunted notch that can occur in experiments, depending on the notch introduction. Four different notch radii thought to be relevant were included (Figure 7.3):

- Sharp crack
- Blunt notch - Radius=0.125mm
- Blunt notch - Radius=0.25mm
- Blunt notch - Radius=0.50mm

The resultant stress profiles along X-axis and Y-axis are presented in Figure 7.4.

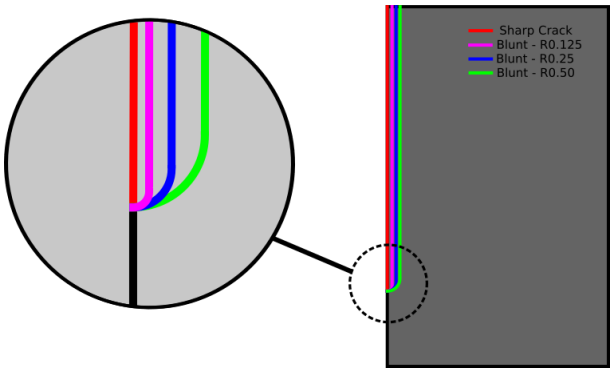

Figure 7.3: Schematics of sharp crack and blunt notches geometry investigated

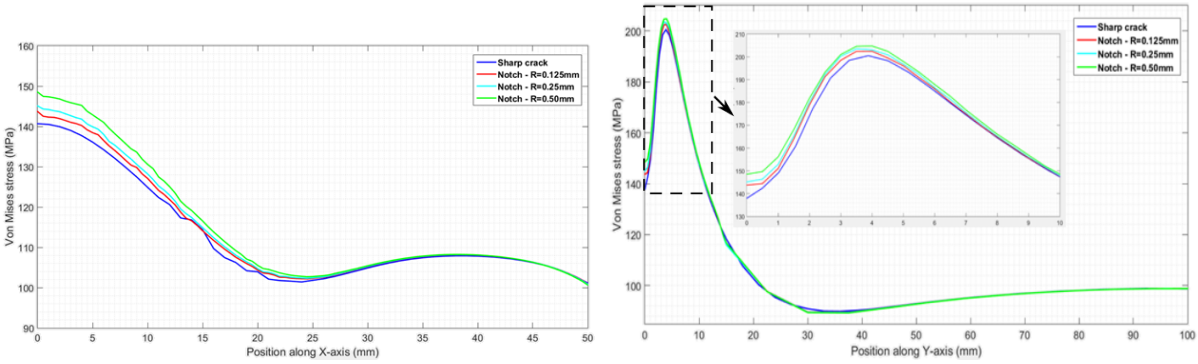

(a) X-axis **(b)** Y-axis

Figure 7.4: Comparison between sharp crack and blunt notches

It can been seen that models with sharp crack and blunt notches displayed very similar back surface stress profiles on the of the plate. Models with blunt notches showed a slight increase in the stress field on back surface. However this was not thought to have a significant impact on the work described in this chapter. The larger the notch radius produced higher Von Mises stress on back surface.

7.2.3 Mesh sensitivity study

Sensitivity studies have been carried out to improve confidence in the output data. For both aspect ratios, four mesh sizes have been included for a 80% deep crack. Table 7.1 provides a list of models, mesh size and number of elements employed. Mesh sensitivity studies were carried out on both X- and Y-axes. A coarse mesh (i.e. 2 mm) was first introduced. The mesh size was then refined from 2 mm to 0.25 mm to highlight the inaccuracy issues when using a coarser mesh. This also helped to decide which mesh size was adequate.

Figure 7.5 and Figure 7.6 present the plots of Von Mises stresses along X-axis when different mesh sizes were employed, whereas Figure 7.7 and Figure 7.8 on the Y-axis, for

Table 7.1: Number of elements in the various models used for mesh sensitivity study

Mesh size (mm)	Number of elements	
	Geometry 1 (Short crack)	Geometry 2 (Long crack)
2	2634	2546
1	16054	15837
0.5	50272	44036
0.25	191293	173892

both crack aspect ratios respectively. Numerical values of Von Mises stress are given in Table 7.2 for X-axis and Table 7.3 for Y-axis.

From the sensitivity studies, models with a mesh size of 0.5 mm were created. The stress values derived from models with this mesh size were identical to those from the finest mesh (i.e. 0.25mm) with a maximum variation of 0.5% on X-axis (See Table 7.2) and 1% on Y-axis (See Table 7.3). For all mesh sizes under consideration, the maximum deviation in stress along X-axis has been observed in the first 15 mm in a 'short' crack. Beyond 15 mm from the crack tip, as seen in Figure 7.5, similar results were obtained from all four mesh sizes. The model with a 'long' crack (Figure 7.6) demonstrates that consistency in Von Mises stress was achieved when a mesh of 0.5 mm or finer was used and mesh refinement was required within 25 mm of crack tip. With a mesh size of 0.5 mm, models were still manageable in terms of running time and considered to be accurate.

Table 7.2: Mesh sensitivity study along X-axis - Values of Von Mises stresses

	X (mm)	2 mm	Diff. (%)	1 mm	Diff. (%)	0.5 mm	Diff. (%)	0.25 mm
Geometry 1	0	121.7	1.51	116.1	3.09	119.3	0.45	119.9
	10	98.6	0.66	98.9	0.43	99.2	0.12	99.3
	20	101.6	0.17	101.7	0.07	101.8	0.02	101.8
	30	102.6	0.1	102.7	0.05	102.7	0.02	102.7
	40	102.1	0.07	102.2	0.03	102.2	0.01	102.2
	50	100.4	0.002	100.4	0.02	100.4	0.004	100.4
Geometry 2	0	142.8	1.02	136.8	3.14	140.8	0.28	141.2
	10	129.5	3.05	124.5	0.92	125.4	0.21	125.6
	20	103.3	0.75	103.4	0.57	104.0	0.07	104.0
	30	104.7	0.36	104.9	0.13	104.7	0.34	105.0
	40	107.7	0.20	107.9	0.09	107.9	0.02	107.9
	50	101.2	0.06	101.1	0.02	101.2	0.002	101.2

Table 7.3: Mesh sensitivity study on Y-axis - Values of Von Mises stresses

	Y (mm)	2 mm	Diff. (%)	1 mm	Diff. (%)	0.5 mm	Diff. (%)	0.25 mm
Geometry 1	0	121.662	1.51	116.139	3.09	119.311	0.45	119.847
	10	116.656	0.61	114.378	1.35	115.002	0.82	115.947
	25	96.129	1.60	94.431	0.20	94.675	0.06	94.618
	50	97.637	0.08	96.414	1.18	97.575	0.015	97.561
	100	99.546	0.014	99.549	0.018	99.535	0.003	99.532
Geometry 2	0	142.67	1.02	136.794	3.14	140.834	0.28	141.234
	10	151.774	2.10	147.205	0.98	148.728	0.05	148.657
	25	98.034	4.05	97.525	3.51	95.277	1.13	94.215
	50	93.852	0.16	93.766	0.07	93.717	0.014	93.705
	100	98.788	0.03	98.772	0.012	98.762	0.0025	98.760

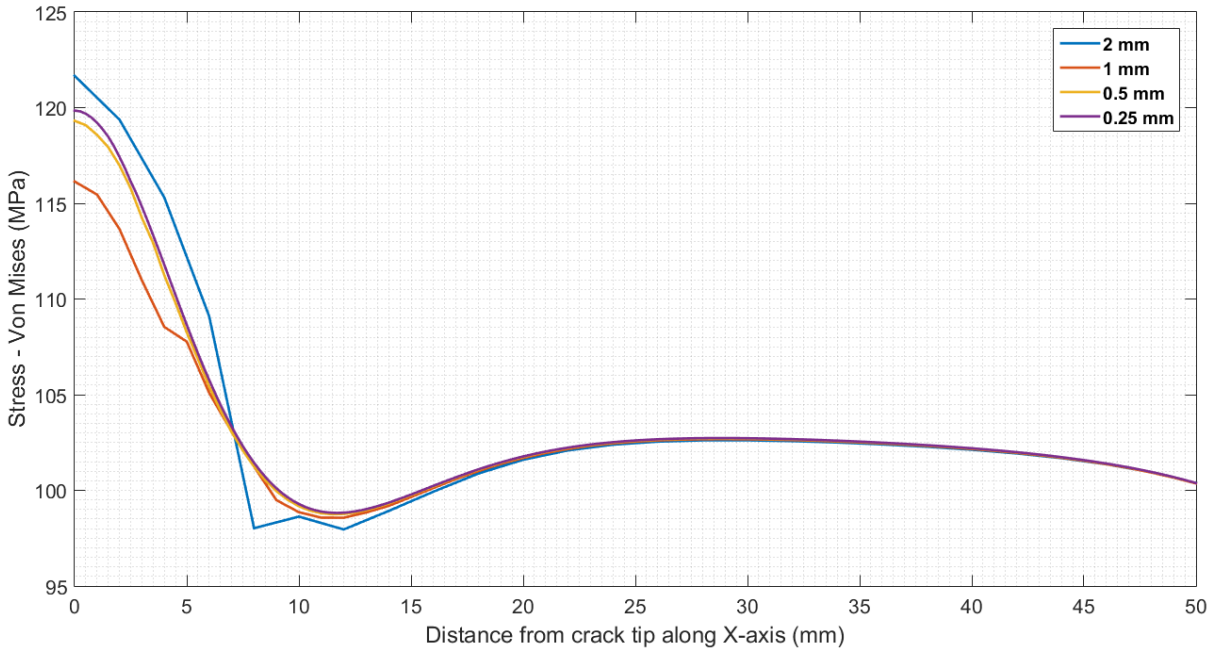

Figure 7.5: Mesh sensitivity study on X-axis - Geometry 1 (Short crack)

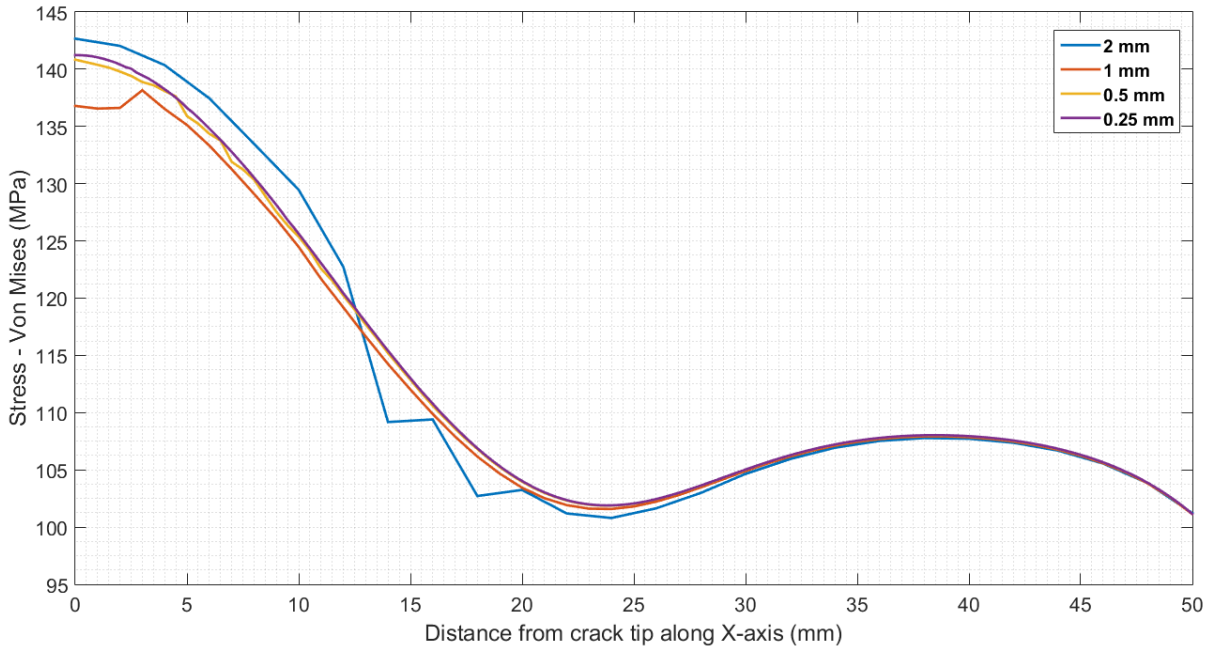

Figure 7.6: Mesh sensitivity study on X-axis - Geometry 2 (Long crack)

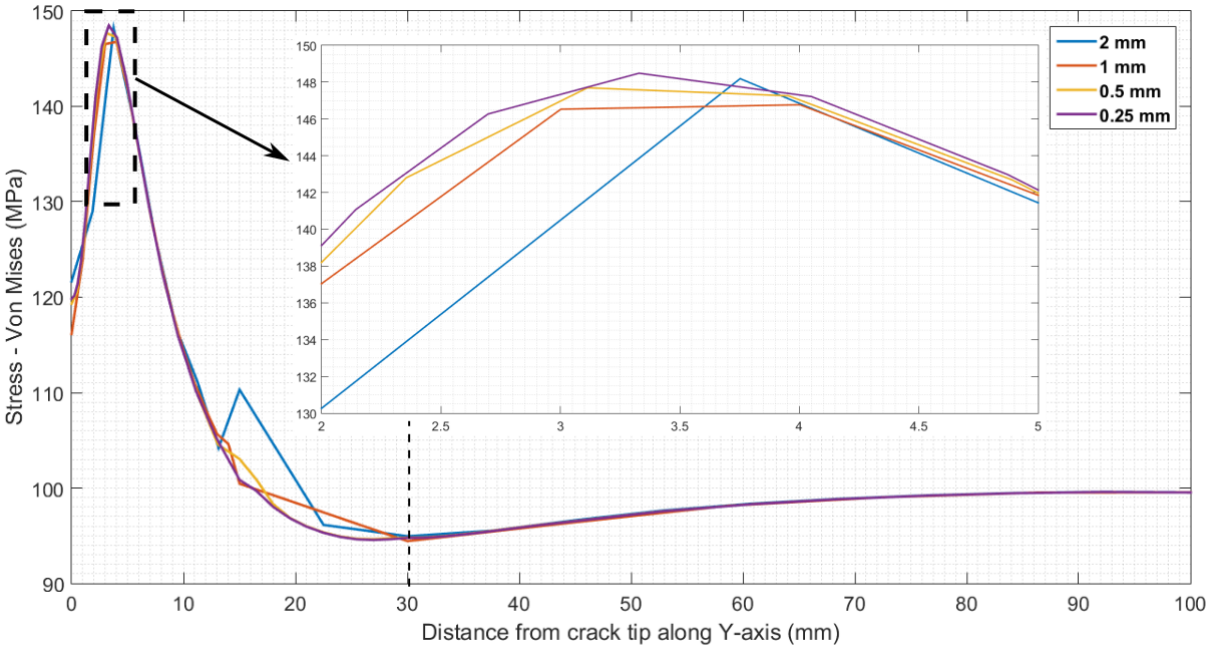

Figure 7.7: Mesh sensitivity study on Y-axis - Geometry 1 (Short crack)

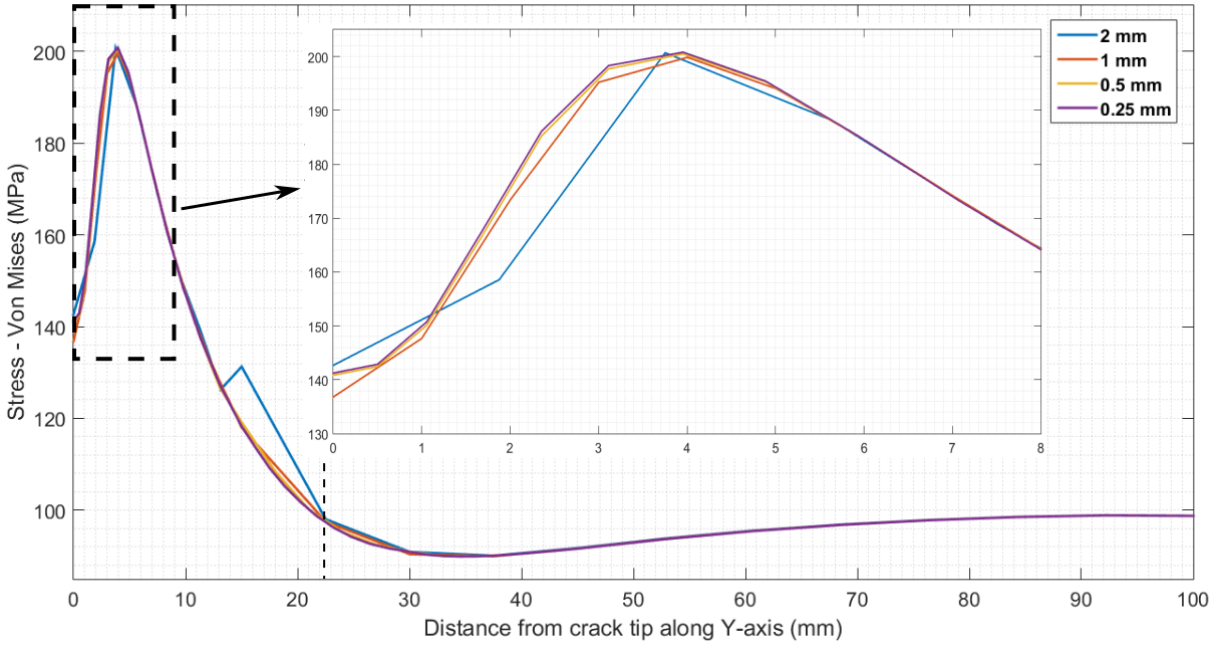

Figure 7.8: Mesh sensitivity study on Y-axis - Geometry 2 (Long crack)

7.3 Validation against experimental data

7.3.1 Model geometries and results

In this section, the recorded strain values from static test undertaken prior to the fatigue testing (See Section 6.3.4) for the four plates have been compared against numerical values. Experimental values were recorded by the strain gauges mentioned on figures and location can be found in Figure 6.8. Numerical values have been obtained from two models: (i) FEAgeom1 and (ii) FEAgeom2. Models dimensions and properties are defined in Table 7.4.

Table 7.4: Models for validation against experimental results

Model	Crack length 2c (mm)	Crack depth a (mm)	Min. element size		Nb. of elements
			X-axis (mm)	Y-axis (mm)	
FEAgeom1	24	12	0.5	0.5	48980
FEAgeom2	56	12	0.5	0.5	49218

The continuous FEA estimated strain values are presented in :

- Figure 7.9 - X-axis (Density=0.5mm all along the axis)
- Figure 7.10 - Y-axis (Density=0.5mm at crack-tip and increasing gradually)

and the averaged values from FEA are given in:

- Figure 7.11 - X-axis for FEAgeom1 (M01-03/M01-04)
- Figure 7.12 - Y-axis for FEAgeom1 (M01-03/M01-04)

- Figure 7.13 - X-axis for FEAgeom2 (M01-01/M01-02)
- Figure 7.14 - Y-axis for FEAgeom2 (M01-01/M01-02)

7.3.2 Discussion

Figure 7.9 and Figure 7.10 are included to show the continuous form of the FE-derived strains. It can be seen that values are close to the far field strains for position far from the deepest point of the crack (i.e [-50 -20] and [20 50]) especially along Y-axis. When it comes closer to the deepest point of the crack (i.e 0 mm), the strain is varying the more. These continuous values could not be compared directly to the experimental readings as the sampling areas were different, so FE values were averaged with respect to strain gauges sampling areas. This is particularly important for the strain gauge SG1 at the centre, which was 6 mm long. Averaged FEA values were then compared to the static experimental values (see Section 6.3.4). It can be seen that FE models and experiments are in good agreement. The difference could be explained by the fact that FE models simulated idealised dimensions for both plates and cracks. However the exact dimensions from the specimens varied slightly from these idealised values.

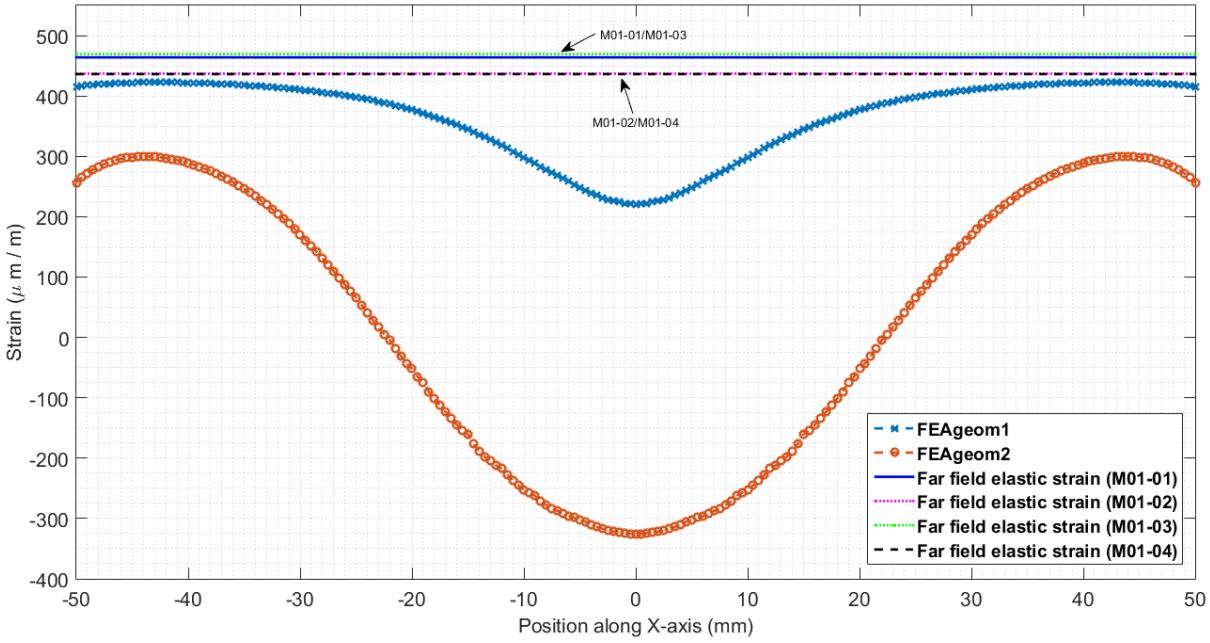

Figure 7.9: FEA continuous values on X-axis - Geometry 1 & Geometry 2 (Both crack)

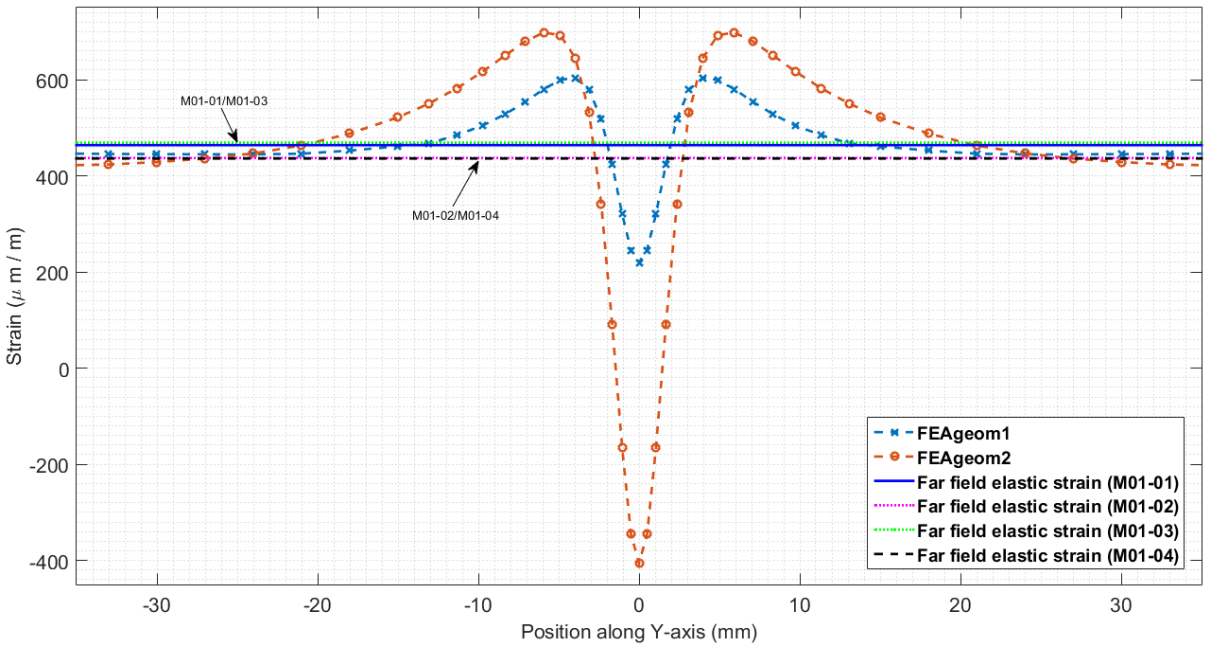

Figure 7.10: FEA continuous values on Y-axis - Geometry 1 & Geometry 2 (Both crack)

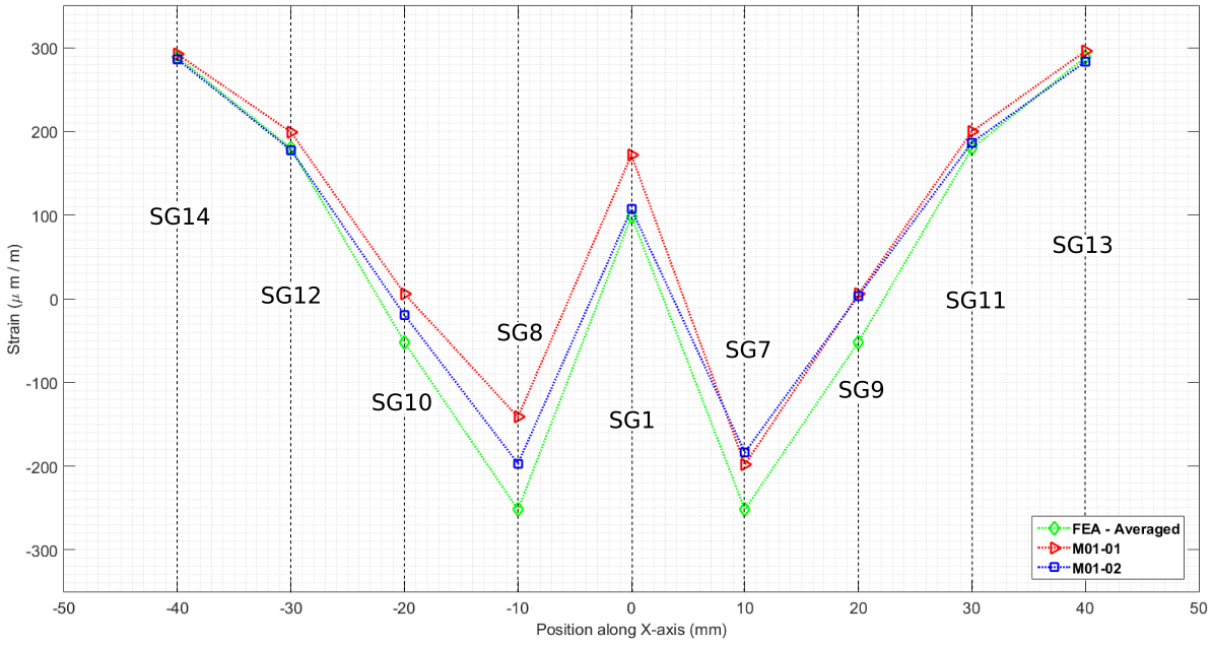

Figure 7.11: Averaged strain values derived from FEA vs. Experimental readings on X-axis - Geometry 1 (Short crack)

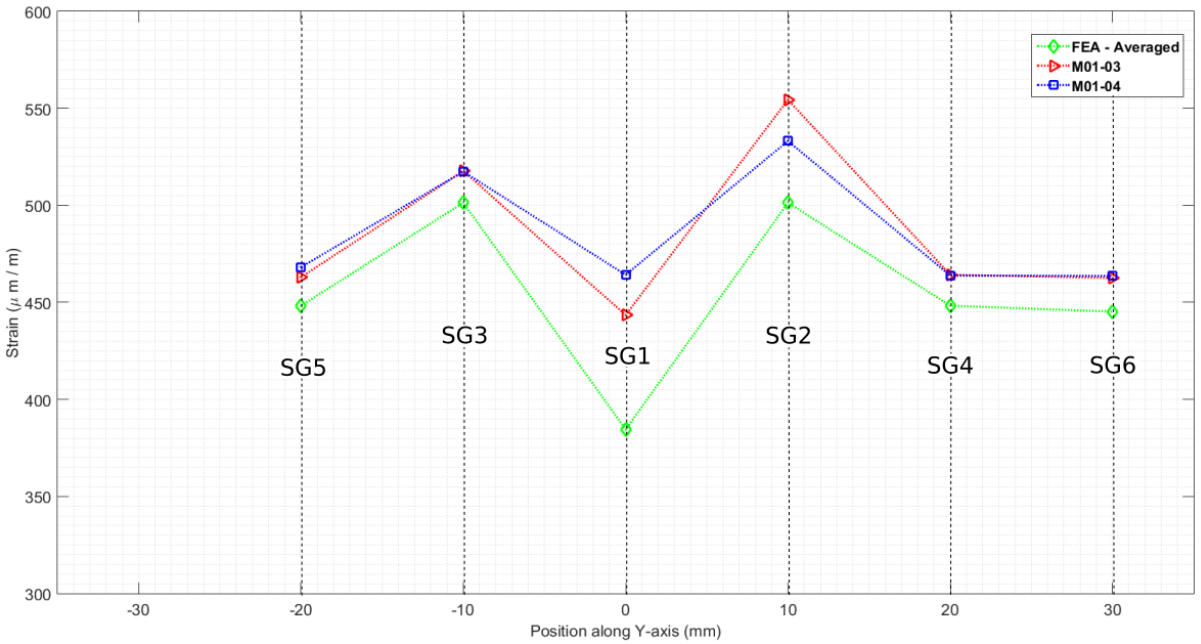

Figure 7.12: Averaged strain values derived from FEA vs. Experimental readings on Y-axis - Geometry 1 (Short crack)

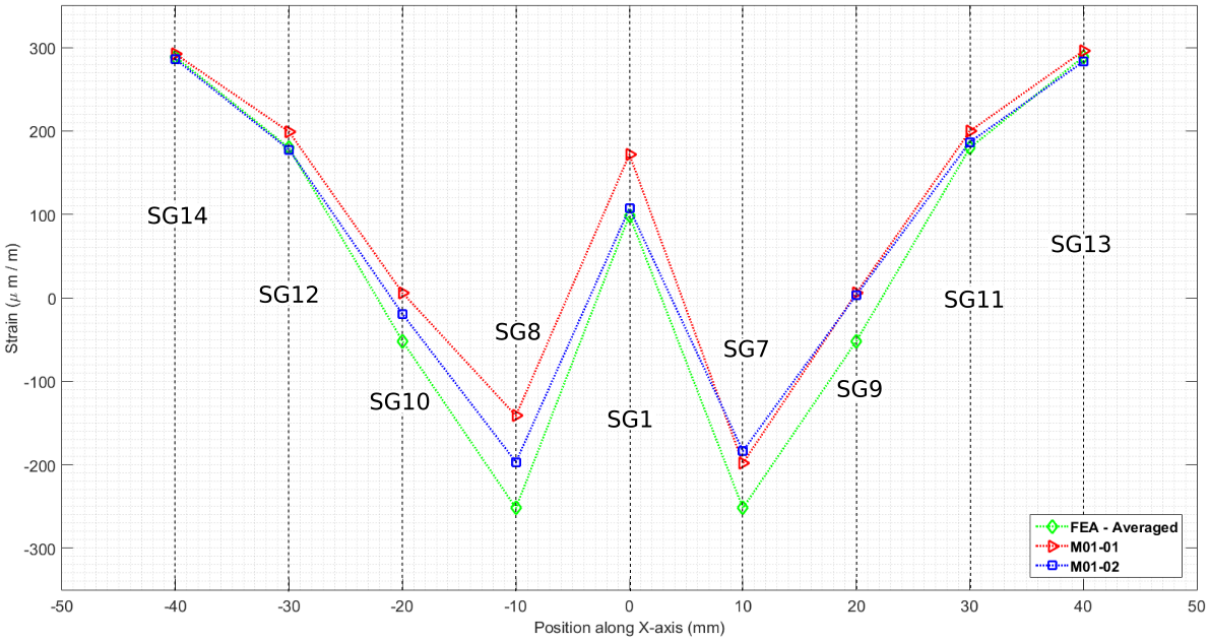

Figure 7.13: Averaged strain values derived from FEA vs. Experimental readings on X-axis - Geometry 2 (Long crack)

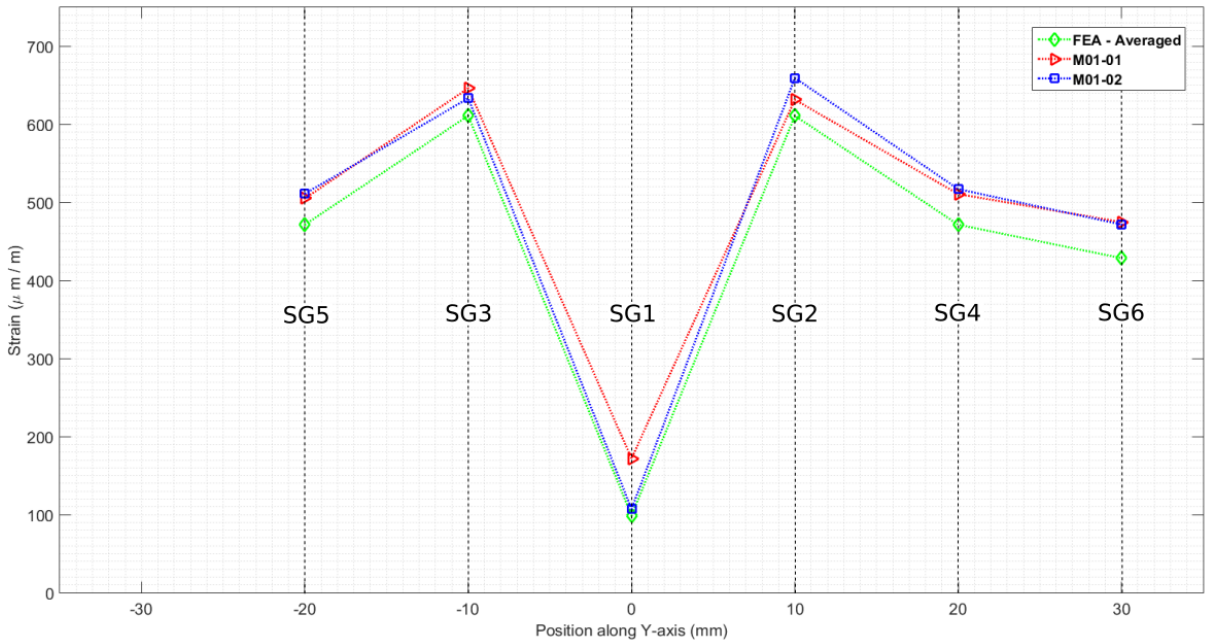

Figure 7.14: Averaged strain values derived from FEA vs. Experimental readings on Y-axis - Geometry 2 (Long crack)

7.4 Stress analyses along axes parallel and perpendicular to crack

A matrix of the cases investigated is given in Table 7.5.

Table 7.5: FEA matrix of the models for part-penetrating crack

a/t	Geometry 1 (Short crack)		Geometry 2 (Long crack)	
	a	c	a	c
0.20	3	3	3	7
0.40	6	6	6	14
0.50	7.5	7.5	7.5	17.5
0.60	9	9	9	21
0.65	9.75	9.75	9.75	22.75
0.70	10.5	10.5	10.5	24.5
0.75	11.25	11.25	11.25	26.25
0.80	12	12	12	28
0.825	12.375	12.375	12.375	28.875
0.85	12.75	12.75	12.75	29.75
0.875	13.125	13.125	13.125	30.625
0.90	13.5	13.5	13.5	31.5
0.925	13.875	13.875	13.875	32.375
0.95	14.25	14.25	14.25	33.25

7.4.1 Stress analyses along X-axis

This section discusses the analysis of stresses evolution along the X-axis of both crack aspect ratios. This is the axis which is in plane with the crack. The stresses on the back surface of the plate are plotted along this axis from the deepest point at the crack tip (X = 0 mm) to the edge of the plate (X = 50 mm).

7.4.1.1 Geometry 1 - Short crack with c=a

This first case considers a crack having an half crack length equal to its crack depth (c=a). A schematic of a typical crack evolution is given in Figure 7.15 and an example of a typical mesh is given in Figure 7.16 for a crack equal to 80% thickness. This aspect ratio of c=a has been kept constant for crack depths ranging from 20% to 95% through-thickness.

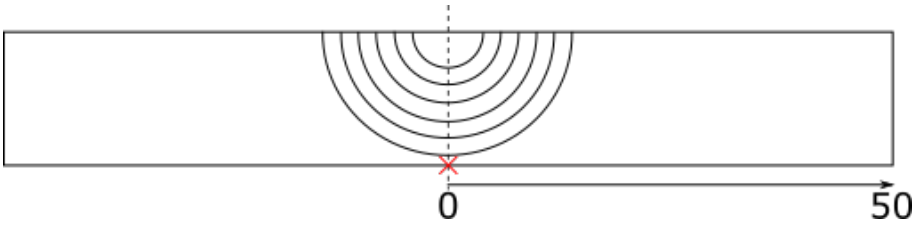

Figure 7.15: Schematics of the first geometry crack depths

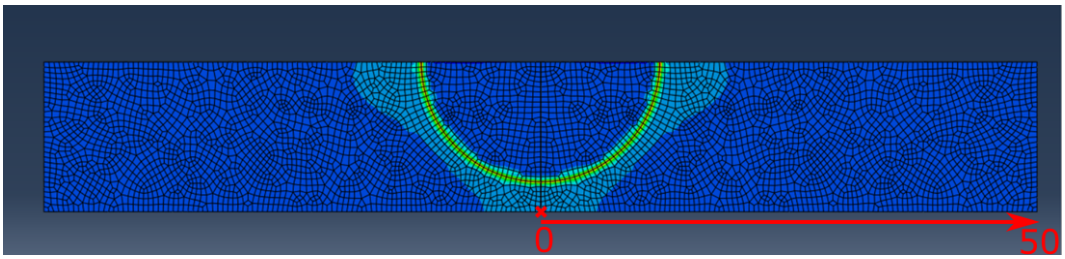

Figure 7.16: Typical mesh for the first geometry where crack depth a=0.8t

Figure 7.17 presents the Von Mises stresses along the X-axis for different crack depths. The horizontal axis represents the distance along the X-axis from the deepest point at the crack tip (X = 0 mm) to the edge of the plate (X = 50 mm). The vertical axis shows the Von Mises stresses derived from FEA. A close-up of the first 10 mm is provided as the stresses further away from the crack tip do not exhibit significant changes with increasing crack depth. Below 0.7t crack depth, the difference in the far field stresses is hardly visible. The stresses at X = 0 mm tend to be even slightly lower than that of the far field stress. The elastic stress field at advancing crack tip only became visible on the back surface when the crack was at least 75% deep.

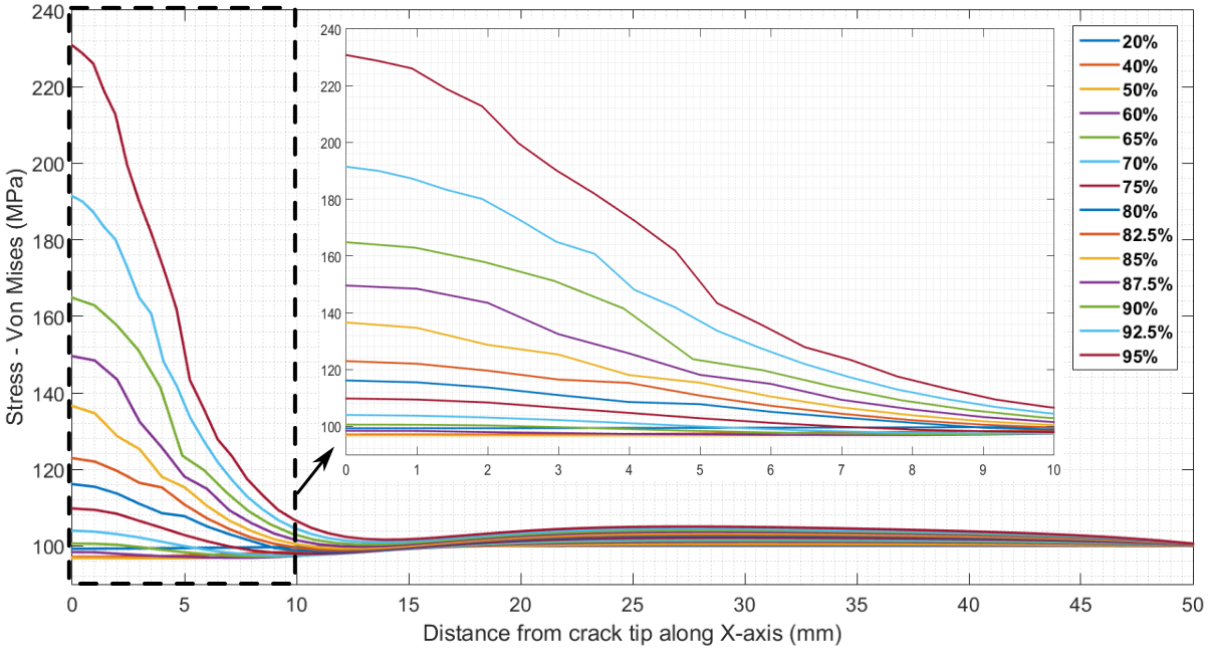

Figure 7.17: Von Mises stresses along the X-axis for various crack depths - Geometry 1 (Short crack)

The maximum Von Mises stress value on the back surface of the plate was obtained at the front of the deepest point of the crack tip (X = 0 mm). The results are given in Table 7.6 for a/t ranging from 0.2 to 0.95. The difference between the estimated Von Mises stress and far field stress has also been included. Figure 7.18 presents the values plotted against a/t ratios. As expected, there is a sharp increase in stress field at the back surface when the crack tip advances deeper (70%) into the component section.

Table 7.6: Von Mises stresses along the X-axis for various crack depths - Geometry 1 (Short crack)

a/t (%)	20	40	50	60	70	75	80	82.5	85	87.5	90	92.5	95
Von Mises (MPa)	99	97	97	98	104	110	116	123	137	150	165	191	231
Diff. (%)	1	3	3	2	4	10	16	23	37	50	65	91	131

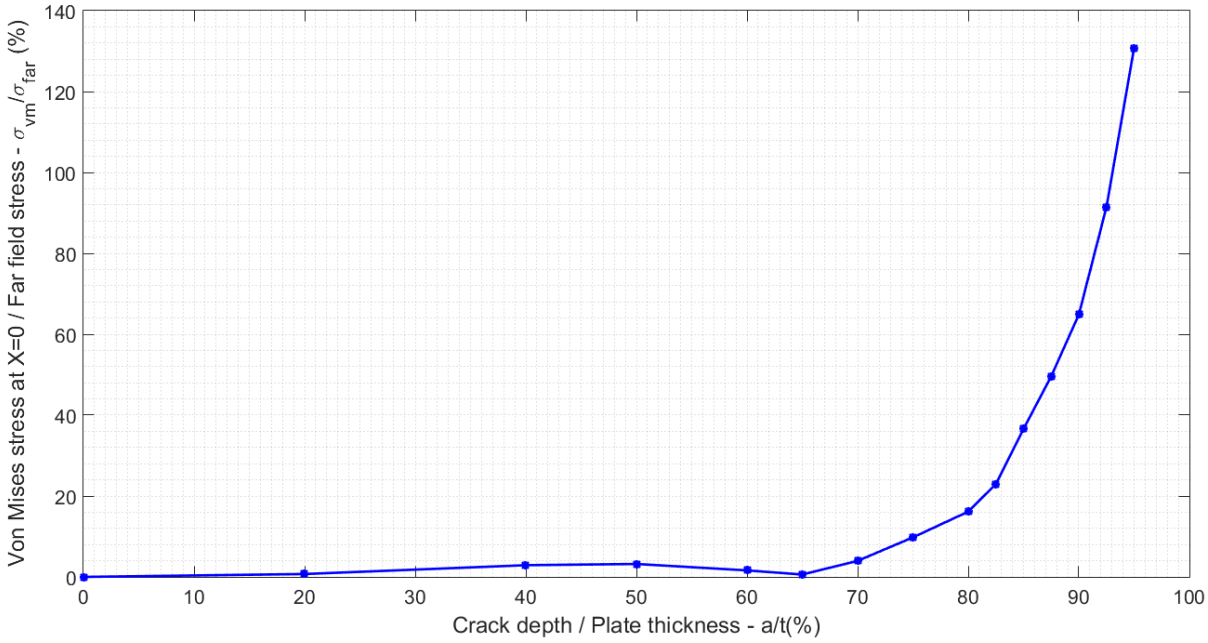

Figure 7.18: Maximum Von Mises stresses along the X-axis for various crack depths - Geometry 1 (Short crack)

7.4.1.2 Geometry 2 - Long crack with c≃2a

The second FEA model considered a crack having an half-length close to two times the crack depth (c≃2a). The schematic of a typical crack evolution is given in Figure 7.19 and an example of a typical mesh is given in Figure 7.20 for a crack depth of 80% thickness . The crack ratio has been kept constant for crack depth ranging from 20% to 92.5% through-thickness.

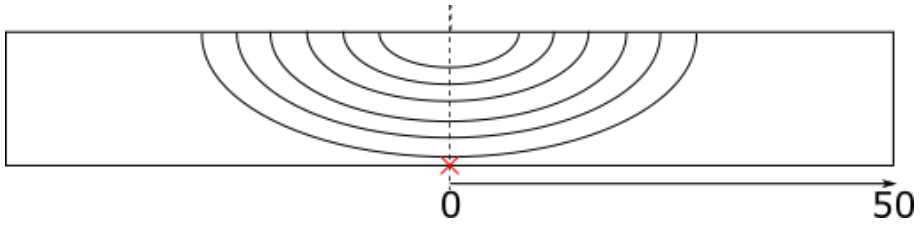

Figure 7.19: Schematics of the second geometry crack depths

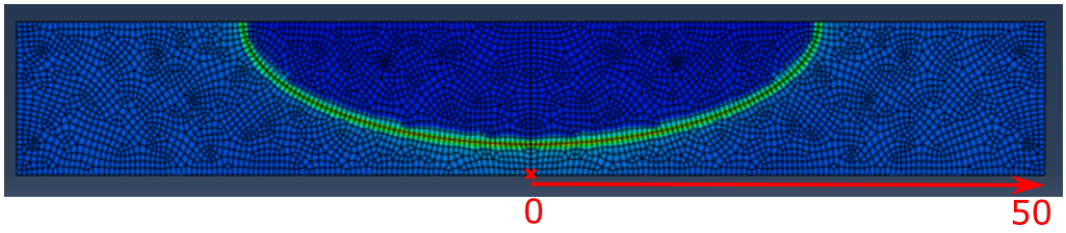

Figure 7.20: Typical mesh for the second geometry where crack depth a=0.8t

Figure 7.21 presents the Von Mises stresses along the X-axis for various crack depths. The horizontal axis represents the distance along the X-axis from the deepest point at the crack tip (X = 0 mm) to the edge of the plate (X = 50 mm). The vertical axis shows the Von Mises stresses. A close-up of the first 20 mm is provided as the stresses further away from the crack tip do not experience significant changes with increasing crack depth. Similar to 'short' crack model (Section 7.4.1.1), below 0.7t crack depth, the difference in the far field stresses was limited. The stresses at X = 0 mm tend to be even slightly lower than that of the far field stress. The elastic stress field at advancing crack tip reaches a maximum of about 260 MPa when the crack is at 0.925t. Again, as observed in short crack models, the effect of crack tip stress field is visible at the back surface when crack depth is at least 0.7t.

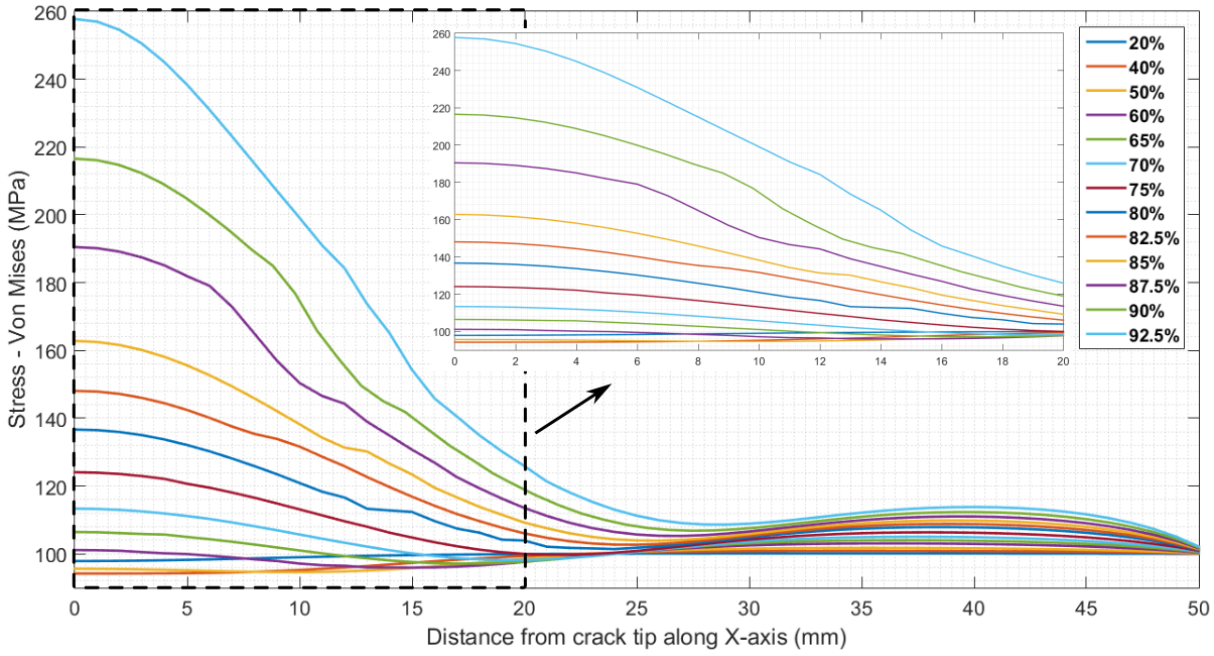

Figure 7.21: Von Mises stresses along the X-axis for various crack depths - Geometry 2 (Long crack)

The maximum value of Von Mises stress was obtained in front of the deepest point of the crack tip (X = 0 mm).The results are presented in Table 7.7. The difference between the estimated Von Mises stress and far field stress has also been included. Figure 7.22 presents these values plotted against increasing a/t ratios.

Table 7.7: Maximum Von Mises stresses along the X-axis for various crack depths - Geometry 2 (Long crack)

a/t (%)	20	40	50	60	70	75	80	82.5	85	87.5	90	92.5
Von Mises (MPa)	98	94	96	101	113	124	137	148	163	191	217	258
Diff. (%)	2	6	4	1	13	24	37	48	63	91	117	158

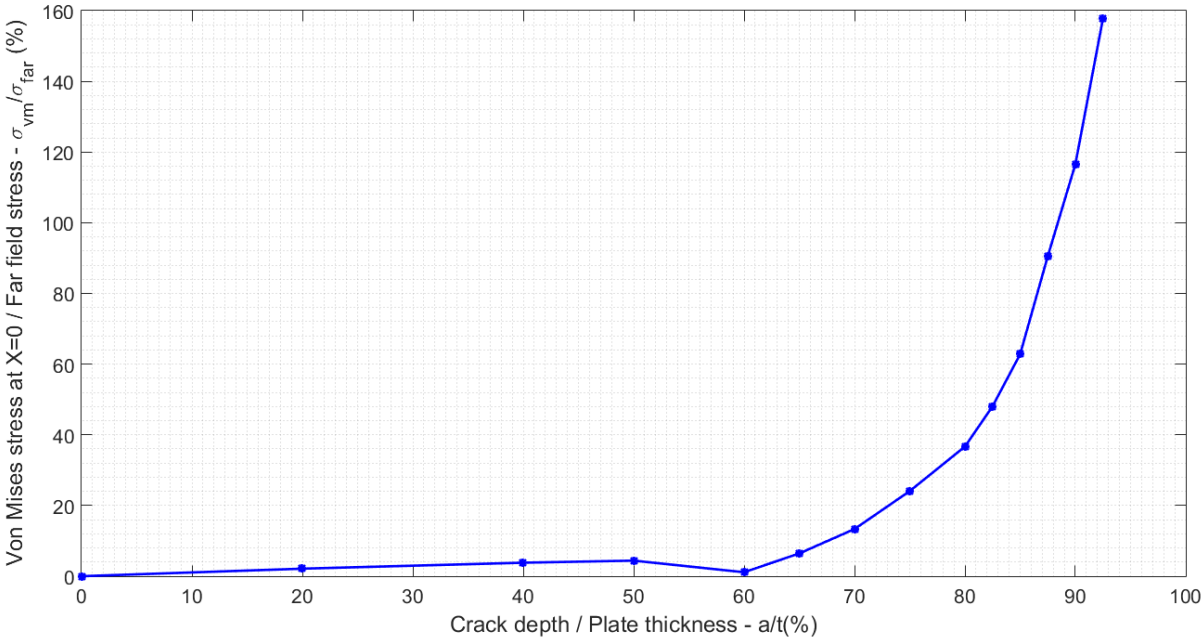

Figure 7.22: Maximum Von Mises stresses along the X-axis for various crack depths - Geometry 2 (Long crack)

7.4.1.3 Discussion

Stresses on the X-axis have been investigated for two crack geometries (i.e. 'short' and 'long' cracks). In both analyses, it has been observed that for a depth below approximatively 70-75% of thickness, the presence of a crack had a negligible effect on the back surface of the plate. For a depth greater than 70-75% of thickness, the maximum stress was observed at the deepest point (X = 0 mm) with the elastic stress field ahead of crack tip being visible in the back surface. This effect was more evident in longer crack with greater predicted Von Mises stresses. This can be seen in Figure 7.23 in which the maximum Von Mises stresses have been normalised to the applied stresses on the y-axis and crack depths normalised to component thickness on x-axis for both geometries.

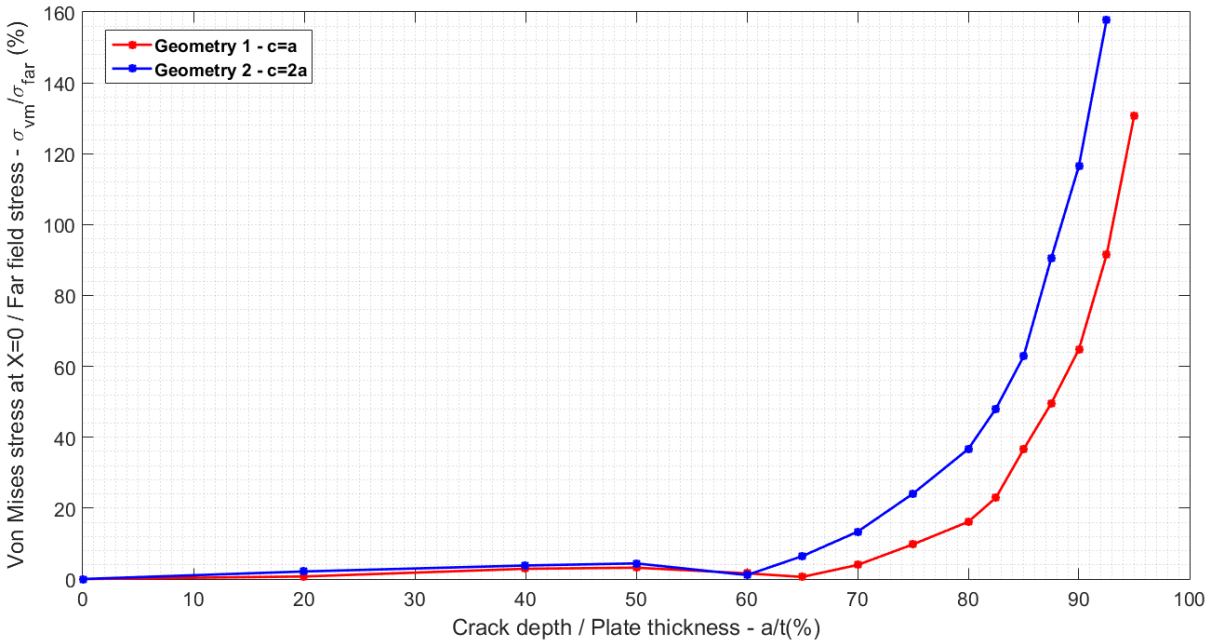

Figure 7.23: Maximum Von Mises stresses along X-axis for the different crack depths - Geometry 1 & 2

Another observation was made to examine the extend of the area affected by the increase of stress on X-axis. In contrast to Geometry 1, the effect on back surface due to the crack stress field is stretched further in Geometry 2. This presumingly was due to the spread of the cracked area on the X-axis, which is greater in the second geometry. The extend to which the stresses are varying was limited to the first 10 mm in a short crack (See Figure 7.17). On the other hand, for the second geometry, this area was increased to about 20 mm (See Figure 7.21).

7.4.2 Stress analyses along Y-axis

This section looks into the analyses of the stress evolution along the Y-axis (i.e. in the plane perpendicular to the crack - See Figure 7.2). Stress values were extracted along this axis from the deepest point at the crack tip (Y = 0 mm) to the edge of the plate (Y = 100 mm). An example of the model is given in Figure 7.24 for a crack depth equal to 80%.

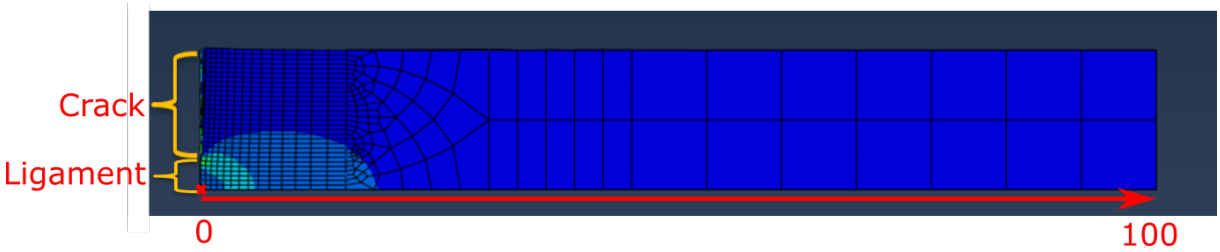

Figure 7.24: Typical mesh on the Y-axis (a/t=0.8)

7.4.2.1 Geometry 1 - Short crack with c=a

The first model considers a crack having an half-length equal to the crack depth (c=a). Figure 7.25 presents the predicted Von Mises stresses along the Y-axis for different crack depths. The horizontal axis represents the distance along the Y-axis from the deepest point on the crack tip to the edge of plate. The vertical axis shows the Von Mises stresses. A close-up of the first 10 mm is provided as it is in this region that the greatest fluctuations of stress occur.

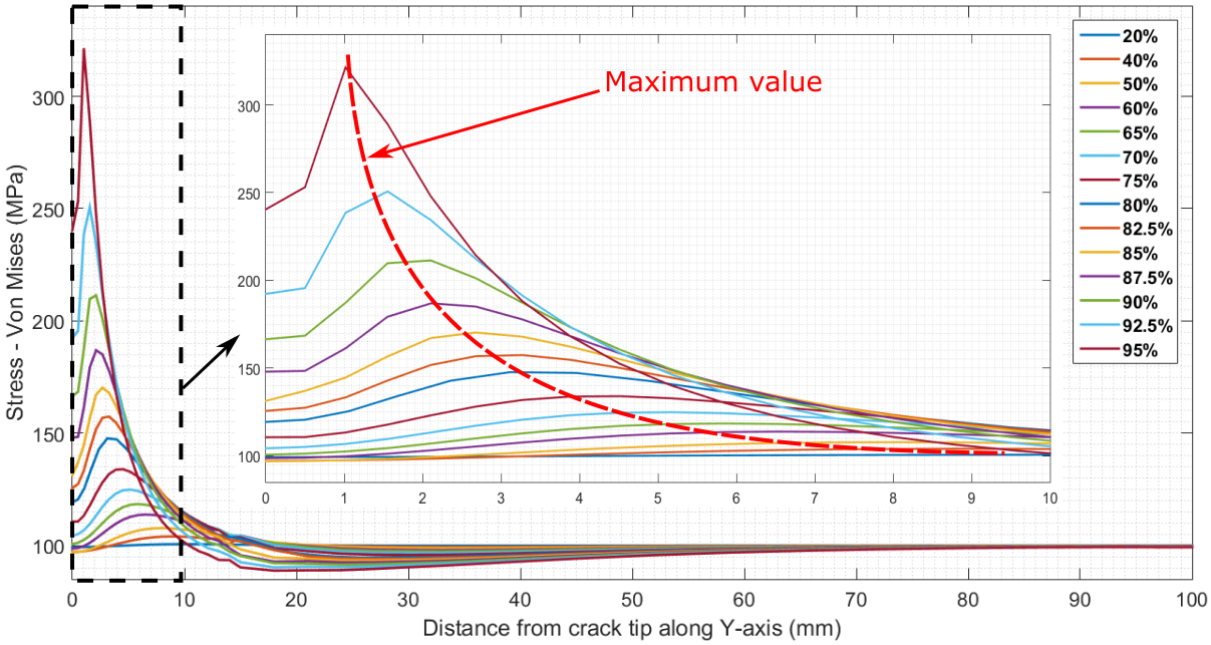

Figure 7.25: Von Mises stresses along the Y-axis for various crack depths - Geometry 1 (Short crack)

The maximum value of stress was obtained at a different position along the Y- axis compared to that along the X-axis. This peak value along with its associated position (i.e. distance from crack tip) is given in Table 7.8. Figure 7.26 presents the results in Table 7.8 on a plot to illustrate the shift of maximum value as the crack depth increases.

Table 7.8: Maximum Von Mises stresses and associated positions along Y-axis for various crack depths - Geometry 1 (Short crack)

a/t (%)	20	40	50	60	70	75	80	82.5	85	87.5	90	92.5	95
Y (mm)	10.4	8.8	8	6.5	5.2	4.5	3.1	3.3	2.7	2.1	2.1	1.6	1
Von Mises (MPa)	101	104	108	114	125	134	148	157	170	187	211	251	322

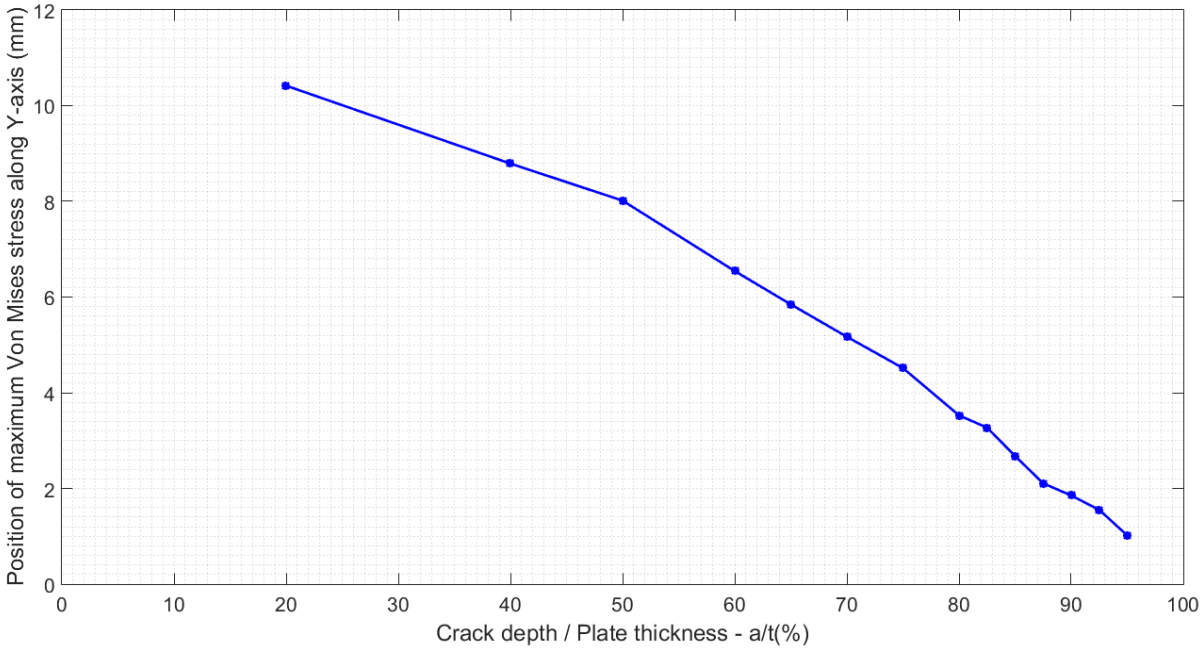

Figure 7.26: Position of maximum Von Mises stresses along Y-axis for various crack depths - Geometry 1 (Short crack)

Along the X-axis, maximum values were observed at similar positions regardless of the crack depths, at the deepest point of the crack. Along the Y-axis, when the crack is shallow, it has been observed that it has little effect on the stresses. However, along the axis perpendicular to the crack (i.e Y-axis), the maximum value has been observed at some distance away from the crack tip, even if the value is quite negligible. As the crack depth increases, the maximum value also increases and its associated position moves closer to the crack tip. Initially located about 10 mm away from the origin (i.e. Y = 0 mm), it has moved to 1 mm close to the origin when the crack depth reaches 95%.

7.4.2.2 Geometry 2 - Long crack with c≃2a

The second case considers a crack having an half-length equal to twice the crack depth (c≃2a). Figure 7.27 presents the Von Mises stresses along the Y-axis for various crack depths. The horizontal axis represents the distance along the Y-axis from the deepest point on the crack tip to the edge of the plate. The vertical axis shows the Von Mises stresses. A close-up of the first 20 mm is provided as this is the region that greatest fluctuation in stress has been observed.

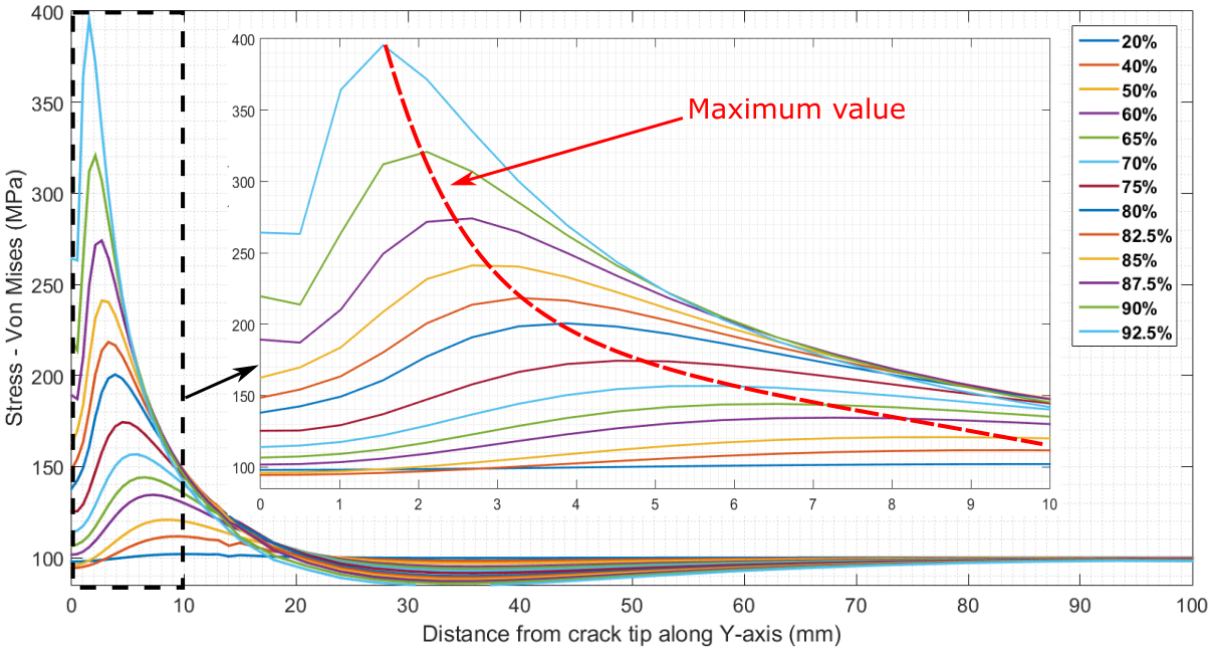

Figure 7.27: Von Mises stresses along the Y-axis for various crack depths - Geometry 2 (Long crack)

The maximum value of Von Mises stress occurs at different positions along the Y-axis. This value is given in Table 7.9 for all crack depths. The evolution of the position is given in Figure 7.28 for 50%, 75% and 90%. Figure 7.29 presents a plot of positions at which maximum Von Mises stress occurs against a/t ratios.

Table 7.9: Maximum Von Mises stresses and associated positions along Y-axis for various crack depths - Geometry 2 (Long crack)

a/t (%)	20	40	50	60	70	75	80	82.5	85	87.5	90	92.5
Y (mm)	10.4	9.6	8.8	7.3	5.8	4.5	3.9	3.3	2.7	2.7	2.1	1.6
Von Mises (MPa)	102	112	121	135	157	174	201	218	241	274	321	396

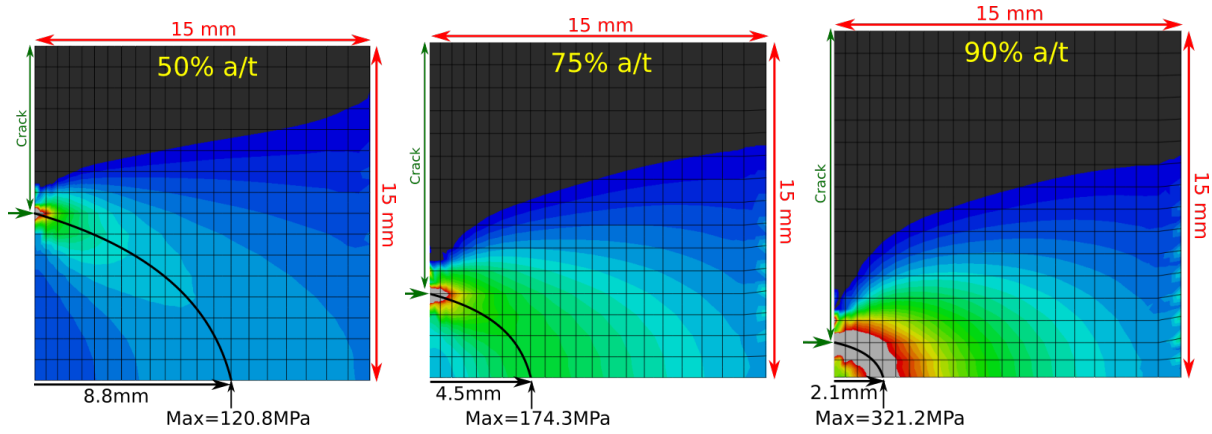

(a) Geometry 2 - 50% a/t **(b)** Geometry 2 - 75% a/t **(c)** Geometry 2 - 90% a/t

Figure 7.28: Evolution of the position of maximum stress value along Y-axis

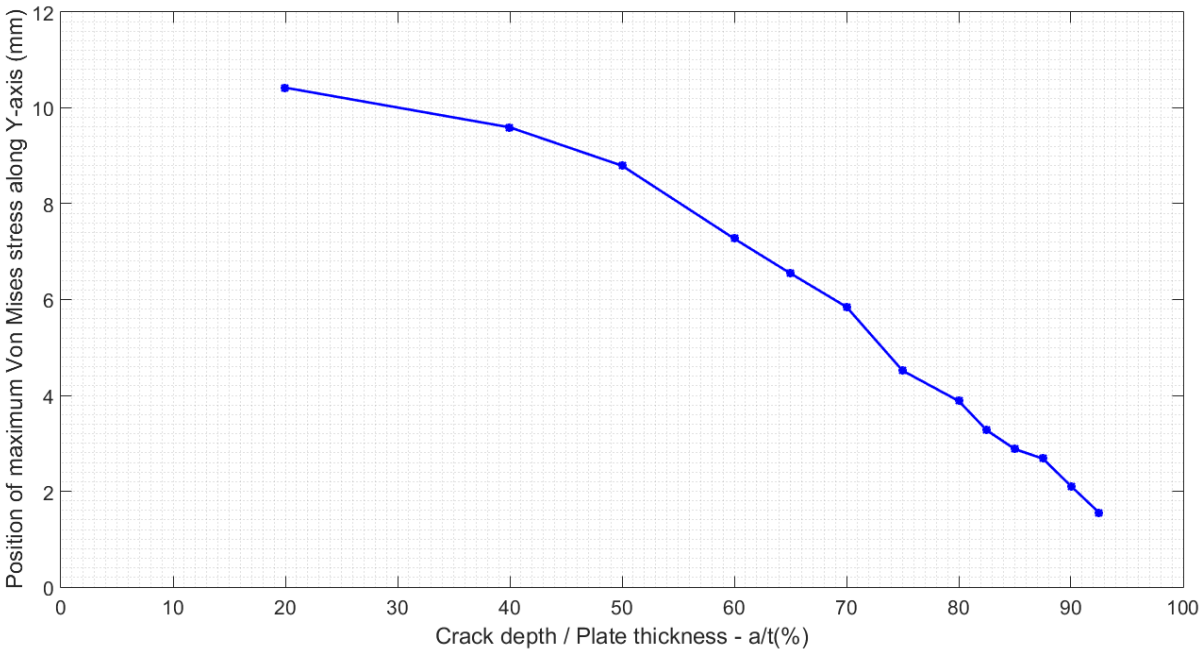

Figure 7.29: Position of maximum Von Mises stresses along Y-axis for various crack depths - Geometry 2 (Long crack)

7.4.3 Discussion

Stresses on the Y-axis have been investigated for two crack geometries. In both models, it has been observed that the presence of a crack did have an effect on the strain field on the back surface of the plate for shallow cracks. This effect was more significant for longer cracks (Geometry 2) which Von Mises stress field ahead of crack tip increased more sharply than those of shorter cracks. This can be seen in Figure 7.30 where the ratio of the maximum Von Mises stresses are normalised to the applied stresses on vertical axis and crack depth normalised to thickness on x-axis for both geometries. However the location of the maximum stresses along Y-axis was not at the origin as for X-axis.

Opposite to the observations for the X-axis, the area affected by the stress rise due to the crack on the back surface was not extended for Geometry 2. Both geometries having the same depth from the Y-axis point of view, no difference was expected. Another difference was the location of the maximum values. While they were located at (X = 0 mm) along the X-axis, they were progressing with the crack depth along Y-axis. The maximum values were observed to be at some distance from the crack tip, even if negligible (Slightly higher than far field stress). As the crack depth increased, the maximum value increased and moved closer to the crack tip. Initially located about 10 mm far from the origin ($\simeq$ 70% of the plate thickness), it moved to 1 mm when the crack depth reached 95%. Both geometries had the same trends as shown in Figure 7.31.

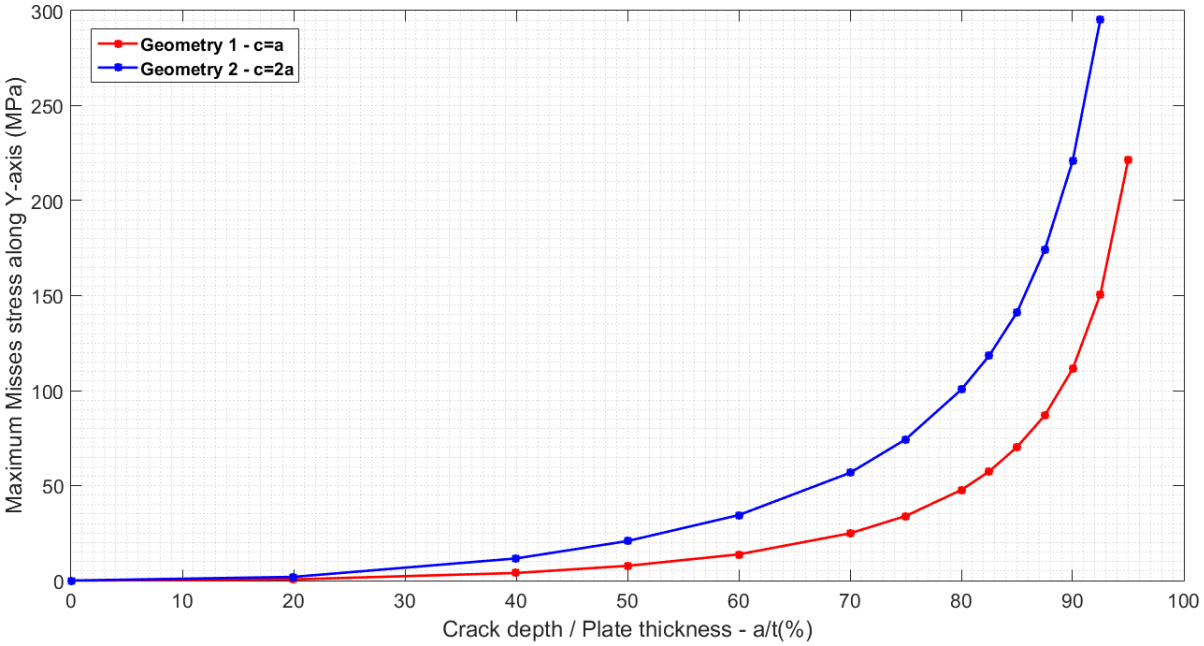

Figure 7.30: Maximum Von Mises stresses along Y-axis for various crack depths - Geometry 1 (Short crack) & 2 (Long crack)

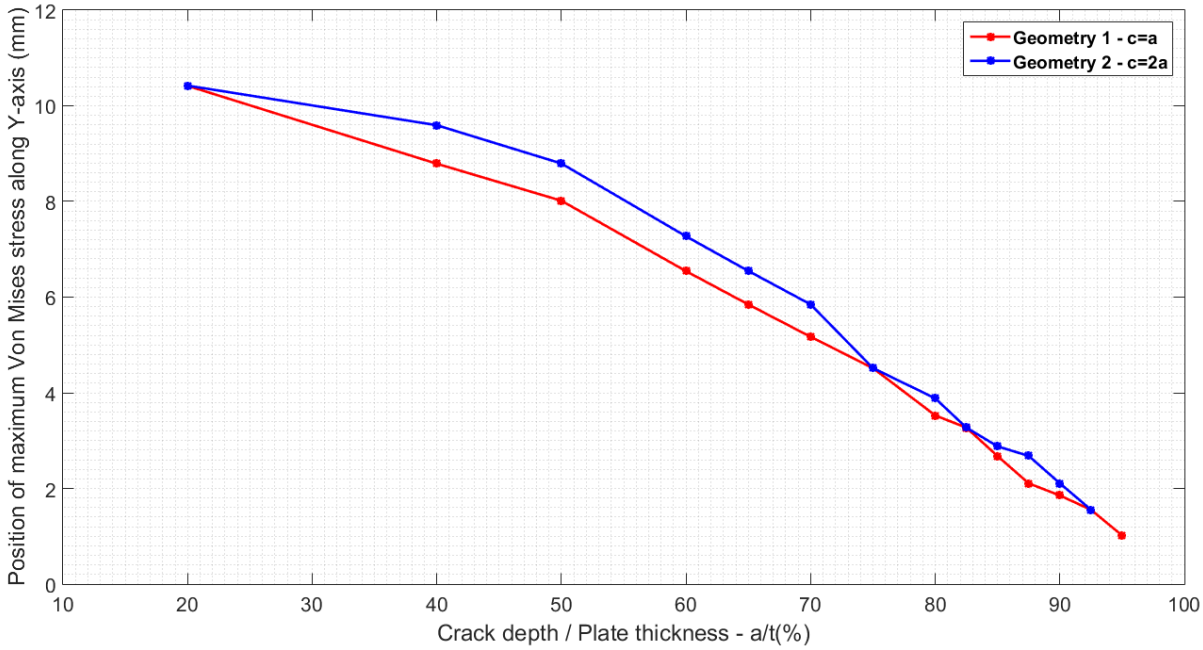

Figure 7.31: Position of maximum Von Mises stresses along Y-axis for various crack depths - Geometry 1 (Short crack) & 2 (Long crack)

7.5 Conclusions

In this chapter, different FEA models using a 0.5mm mesh with semi-elliptical cracks in a plate were used to examine the stress field developing on the back surface along two axes: (i) along the crack and (ii) perpendicular to the crack. Several observations could be drawn:

(a) While the notch radius increased, the stress field on back surface increased accordingly. In this chapter, a sharp notch model has been employed.

(b) FEA results agreed well with experimental results for both axes and geometry investigated giving confidence in the numerical models. The minor difference between FEA and experiments is due to the small discrepancy in flaw geometry.

(c) Along X-axis (Section 7.4.1), stresses on back surface were observed to be maximum at the deepest point of the crack (i.e X=0). Stresses were close to the far field stress value until for a crack depth less than 60% of the thickness. This back surface stress increased when the crack depth increased and at a greater rate in a long crack.

(d) Along Y-axis (Section 7.4.2), stresses were observed to have a maximum at a position varying with the crack depth. The maximum stresses along Y-axis came closer the origin (i.e Y=0) as the crack depth increased.

Chapter 8

Concluding remarks and future work

Contents

8.1 Introduction

The work discussed in the previous chapters presents the investigation into the leak-before-break approach. This chapter gives a summary of the study carried out in these previous chapters and key observations are addressed. Possible directions of the future research to improve upon the current work are also outlined in Section 8.4.

8.2 Summary and Conclusions

In Chapter 2, a literature study has covered different aspects of the subject. An overview of the defects that can be present at different stages of components' life ((i) during fabrication, (ii) in-service and (iii) due to third-party) was presented. The root of the damages was shown to be important with regards to the criticality assessment. Non-Destructive Testing (NDT) technologies used to help evaluate the final shape and dimensions of defects for both part-penetrating and through-wall defects were detailed. Conventional NDT or leak testing procedures were presented for the different type of defects. To assess their criticality, fracture mechanics parameters defined to characterise the stress field at proximity of the defects were shown. They provide a link between the local crack tip response (stress/strain) to the global conditions (loads, material properties, geometry). Fitness-For-Service (FFS) practices are used to evaluate the defects tolerance / acceptance either through an Engineering Critical Assessment (ECA) or other methods such that rational decisions about the remaining life, whether to repair, replace a component or reduce operating conditions could be made.

Chapter 3 covers an extensive literature review on the concept of leak-before-break. The different approaches, including basic formulations and available established procedures, their differences and limitations were elaborated for nuclear and other industries. The margin between the smallest detectable leak size and the critical crack size must be adequate and reasonable to support LBB. Reliable leak detection methods must be employed to ensure the ultimate success of the technique in order to prevent catastrophic failure. Numerous situations and types of component studied have been looked at. It has been noted that LBB is generally applied to pressurized components containing benign fluids such as water, steam and carbon dioxide. Only a few published addressed such applications in non-nuclear industries. However, LBB could be further developed in some areas of these industries. When applied to non-nuclear industries, case studies did not follow strictly the established LBB procedures such as recommended in API 579-1/ ASME FFS-1 or BS 7910. Various sources were generally used, which could lead to non-consistent results. High margins were found in screening procedures and detailed assessment procedures lacked solutions/guidance.

Chapter 4 presents a detailed comparison of LBB parameters as described in established procedures for leakage and crack stability assessment. The COA results, were provided for inner & outer surfaces or mid-thickness depending on the solution. All solutions investigated provided coherent results until half of the limit of applicability for both axial and circumferential cracks. It should be noted that BS 7910 solution were developed for flat plates and corrected for cylindrical shapes. On the other hand, API 579-1/ASME FFS-1 have been developed for cylinders by FEA. For both geometries, the stress-based solution from API 579-1/ASME FFS-1 gave greater values of COA than the pressure-based equation. For axial cracks, BS 7910 and Zahoor solutions tend to give greater values of COA at mid-thickness (similar to API 579-1/ ASME FFS-1 at the outer surface). For circumferential cracks, the handbook solutions from BS 7910 and Paris-Tada produced the lowest COA values when compared with the API 579-1/ ASME FFS-1 (for both inner and outer surfaces). BS 7910 and Zahoor models include correction factors for small-scale yielding while API 579-1/ ASME FFS-1 propose a correction factor based on the plastic collapse assessment. This results in a wider range of application for the latter. Recalling that COA solutions are used to assess the leak rate which is a critical parameter in a LBB assessment, an over-estimation of the COA can lead to non-conservative result and vice-versa an under-estimation lead to a very conservative result. Only elastic models, known to under-estimate the COA values when assessing ductile materials, were presented for comparison purpose. In terms of crack stability, different solutions provided for FAD, SIF and RS have been evaluated. Four relevant geometries for LBB assessment were chosen: (1a) through-wall axial, (1b) circumferential, (2a) part-penetrating axial and (2b) circumferential. For a given axial defect, BS 7910 tends to produce greater values in terms of reference stress for both through-thickness and surface defects. The multiplier of 1.2 introduced in the reference stress solutions, as such to achieve a certain level of conservatism partially contributed to this observation. The other factor leading to another significant difference is the correction factor employed. Validation of the reference stress solutions for axial surface defects using available experimental data show that API 579-1/ASME FFS-1 is found to successfully distinguish between leak and break cases. On the other hand, BS 7910 approach is more conservative, treating leak as failure or unacceptable result. This is also observed without the inclusion of factor 1.2. For circumferential defects, when only membrane stress loading is considered, both standards produce similar values in terms of reference stresses. However, when a bending stress loading is applied, BS 7910 solutions tend to give higher reference stresses. It is worth noting that reference stress solutions recommended in BS 7910 are mainly from local limit load solutions which are more conservative. In leak before break assessments, since that the failure mode is pre-supposed to be not dominated by brittle fracture, the criteria for break will be based mainly on the reference stress solution. Therefore, BS 7910 is likely to be significantly more conservative than API 579-1/ASME FFS-1 for its break condition.

Chapter 5 validated the solutions for through-wall cracks in plates and cylindrical components. The calculation of various solutions has been detailed for plates, with step-by-step methodologies and post-processing to generate models and results. In order to generate numerous models in a time-efficient manner, different plug-ins have been created using Python script. Cracks have been introduced into un-cracked bodies (plate or cylinder) in the assembly step, by inserting a crack-box. This permitted to generate the models changing only the desired parameters (tractable approach). FE results in this work were in good agreement with solutions available in procedures for idealized shape models. The effect of crack idealization on SIF and COA solutions has been investigated using detailed 3D elastic FE models of axial through-wall cracks in a cylindrical component under internal pressure. Idealization of a through wall crack with its largest dimension tends to be conservative when it comes to deriving SIF. However, in a LBB assessment, both crack stability and leakage have to be evaluated. Crack idealization rapidly increases COA estimation leading to an over-estimation of detectable leak rate. This implies that for a given crack size, its idealisation will be conservative in terms of SIF but the estimated resulting leak rate over-estimated. The leak detection can therefore be distorted. Models and analyses employed in this work were validated against existing solutions for SIF and COA given in BS 7910 and API 579-1/ASME FFS-1. Different reference crack lengths (inner surface) have been selected in order to cover a range of crack sizes. The observations on SIF and COA for various crack geometries can be used to carry out sensitivity studies while assessing LBB cases. The effect of non-idealized geometry on both SIF and COA could be included to assess cracks 'yet' to become idealized using the observations presented in this work. The analysis showed that a non-idealized crack at break-through (from surface to through-wall) will grow and finally evolve into an ideal shape. LBB assessment in this transition region is generally limited due to a lack of existing solutions. The effect of crack shape on SIF solutions can be used in fatigue assessment to examine cracks growing under cyclic loading. The modification on COA solutions (taking a more realistic shape into account) can improve the leak rate calculation more accurately. This is an important aspect of the assessment often overlooked, while the variation is important in the transition region. Further work to investigate more realistic crack shapes (i.e. non-straight crack front) and development of correction factors for existing solutions would be beneficial in establishing a more refined assessment of LBB.

In Chapter 6, the experimental work undertaken on surface notched plate specimens was presented. As a semi-qualitative test, fatigue testing on Perspex plate specimens with surface cracks was carried out. Different observations were made from the examination of fracture surface. If the sample was not loaded perfectly perpendicular to the applied load (non-uniform distribution of membrane stress), fatigue crack growth showed a non-symmetric growth pattern. This led to rapid extension (length-wise) of the crack size on one side. It propagated rapidly to the specimen edge and failed prematurely. Thinner

samples experienced bending during the tests (not enough remaining cross section to sustain the load). This resulted in an increase in crack length on surface and crack arrest in the thickness direction. On the other hand, thicker samples allowed the crack to grow through thickness. They achieved the expected crack shape evolution. Once the crack had broken through, a rapid crack growth in the width direction was observed until the crack shape reached an "idealised" through-wall shape. Tests were duplicated with metallic material to study the resulting stress/strain on the back surface of a deeply notched plate subject to cyclic tensile loading. Experiments consisted of four high strength steel flat plates with surface-breaking notches to a depth about 80% thickness. Two different crack geometries were examined to represent short and long cracks. Strain gauges were attached on to the back surface of the plates and strain measured during crack growth. Break-through was estimated to occur when recorded strains where between yield and ultimate strain of the material. Observations were made on different axes (i.e. parallel/perpendicular/diagonal to the crack).

Chapter 7 presented different FEA models with semi-elliptical cracks in a plate. Focus has been on the stress field developing on two axes on the back surface of the plate: (i) along the crack (X-axis) and (ii) perpendicular to the crack (Y-axis). A preliminary study has been carried out to study the effect of blunt notch radius on the back surface stress field. Results from a sharp crack were compared with those of blunt notched cracks using three different notch radii, in order to determine the effect of crack-tip / notch geometry. It has been shown that with the greater notch radii, the greater stress field on back surface. The effect of notch geometry was considered negligible. Sharp crack geometry has been used for subsequent investigations. To warrant confidence in the models used, the FE results have been validated with experimental test values. FEA results agreed well with experimental results for both axes and geometries investigated. For both geometries, various models have been generated to study the effect of the crack depth on the back surface stresses. The main observation was made on X-axis, parallel to the crack as well as Y-axis which is perpendicular to the crack. Along the X-axis, stresses on back surface were found to be maximum at the deepest point of the crack (i.e X=0). Von Mises stresses derived from FEA were close to the far field values for a crack depth less than 60%. They started to increase when the crack grew deeper and this was more rapid in a long crack (Geometry 2). Along the Y-axis, stresses exhibited a peak value at a position which varied with the crack depth. In other words, as the crack grew deeper into the section, the location at which peak stress occurred also moved closer to the origin along the Y-axis. Similar trends in the position of the maximum stresses were observed in both geometries. Same observations can be made in terms of the maximum value of the stresses as for X-axis.

In summary, it was found high margins in screening methods and a lack of solutions/guidance for detailed assessment methods in existing procedures. Depending on the procedure employed, some parameters (i.e. reference stress) provide different values. Overall, BS 7910 solutions were found more conservative, treating leak as failure or unacceptable result. The effect of non-idealized geometry should be included to assess cracks in the transition region. The effect on SIF and COA solutions can be used to improve crack stability assessment and resulting leak rate estimation. Further work to investigate more realistic crack shapes (i.e. non-straight crack front) and development of correction factors for existing solutions would be beneficial in establishing a more refined assessment of LBB. To counter over-conservatism in the estimate of LBB parameters, non-idealised flaw at breakthrough needs to be considered to take into account the evolution/transition of part-penetrating to through-thickness. It is recommended that refinement to existing LBB procedure should include the analysis of non-idealised flaw at break-through as work presented in this thesis has demonstrated that the evolution/transition of flaw from part-penetrating to through-thickness was significant. It is also beneficial to perform both experimental and numerical analysis to gain some insight of the effect of aspect ratio and to estimate the possible level of back surface stress/strain.

8.3 Main PhD Achievements Findings

The previous section presented the observations and conclusions achieved from the work carried out in for this research. A list of the main conclusions and findings is given:

- The existing solutions, available to industry, to carry out a LBB assessment were reviewed and discussed. Reference stress solutions showed important difference. BS 7910 solutions were found more conservative, treating leak as failure or unacceptable result, due to different aspects. API 579-1/ASME FFS-1 on the other hand offered more options (i.e. account of crack-face pressure or stress/pressure based solutions). Further work on parameters should focus on reference stress solutions.
- Shape idealisation for through-wall crack yet to become idealised did not always reflect the actual behaviour, especially for COA calculation. This effect should be included to assess cracks in the transition region. FEA can be used as a good predictive tool to investigate more realistic crack shapes (i.e. non-straight crack front) and develop correction factors for existing solutions. This would be beneficial in establishing a more refined assessment of LBB.
- The experiment using metallic specimens showed that high stress/strain on back surface offer an accurate monitoring mechanism to determine breakthrough and transition behaviour. Strain-mapping devices would help for a better understanding of the transition mechanisms.

8.4 Recommendations for future work

The work discussed in this thesis addressed different aspects. There are several lines of research arising from this work which should be pursued.

An extensive literature review on the concept of leak-before-break concept was drawn in Chapter 3. It was shown that the concept of LBB could be further developed in some areas of non-nuclear industries. When applied to these industries, case studies did not appear to follow established LBB procedures such as those presented in API 579-1/ ASME FFS-1 or BS 7910. A mix of different sources was generally used, which could lead to non-consistent results. A refined procedure giving more recommendation and detailed would be beneficial.A simplified procedure for screening use and a detailed procedure with guidance on the transition stage would make assessments more accessible.

In Chapter 4, the differences in the solutions related to LBB have been highlighted. It was shown difference from the comparison of the reference stress solutions, especially for pipes/cylinders containing axial flaws. The effect of different factors should be re-evaluated in order to enhance the assessment capability. Validation of the solutions against other data from industry or research papers that include leak and break analysis would be beneficial in establishing a more accurate assessment of LBB. Data presented in this thesis were limited to axial surface cracks, however data for circumferential cracks were found in the literature and other defects geometry should be evaluated. Further work to assess the effect of these difference on a full LBB case would be advantageous as well. Simplified procedures considering through-thickness crack are known to be conservative. They should be used as a screening criteria. The conservatism resulting from the safety margins employed in flaw size should be evaluated for a wide range of conditions to reduce discrepancy. Current methods to perform a detailed assessment are lacking of solutions in terms of non-idealised flaw geometry. Further numerical studies or experiments should be performed for crack propagation to assess non-idealised cracks. Two stages would be of interest: (i) close to the ideal shape to evaluate the size uncertainty and (ii) at the transition between part-penetrating to through thickness to assess the early stages. This would help to achieve a better estimate of LBB parameters. Another point worth noting is that flaw size should be designed in line with the critical flaw size determined using ECA.

The effect of idealisation on axial through-wall crack in cylindrical components has been highlighted in Chapter 5. The numerical models presented some limitations in terms of component geometry, loading and crack geometry. Further models could be developed using the techniques presented to increase the applicability range and develop a correction factor that would permit to correct the current existing solution. It is worth noting that non-idealised crack models assumed straight crack front for simplicity. More realistic crack

shape modelling based on experiment or experience would increase the accuracy of the corrections. This would affect the safety margins applied in LBB, especially on the leak side, with the calculation of crack opening area. All models were developed using elastic material properties. However it is known that elastic-plastic consideration tends to lower COA. Models with non-idealised cracks using elastic-plastic material properties would be valuable. Other factors, such as temperature gradient through the wall, are known to have an effect on the COA. Investigation of theses parameters would be valuable for a better accuracy in the developed formulations. Study on the crack idealisation in this thesis was limited to axial cracks considering internal pressure loading. Another aspect that could be investigated would be a coupled mechanical and fluidic using CFD tools. This would permit to investigate the direct effect on leak-rate from non-idealised defects.

Experimental work in Chapter 6 described the strain variation on the back surface of a cracked plate subjected to tensile loading. Transition from surface to through-thickness crack was observed with the recorded values. However due to the distance between strain gauges, only "local" evolution was analysed. Use of more sophisticated technology such as digital image correlation (DIC) for the analysis of the displacement fields could be used to improve the understanding on the back surface behaviour. This would allow to have a global understanding of the strain field variation on the back surface. The strain field presented in the thesis is for low loading to assume linear elastic behaviour. Based on similar reasoning, future research work is needed to investigate the strain field for strain hardening materials. As similar breakthrough behaviour was observed on both Perspex and metallic specimens, further study on Perspex specimens would permit to have further visual observations with live record.

Numerical simulations presented in Chapter 7 were performed to duplicate experimental geometries. Only two crack aspect ratios were considered. A wider range of crack aspect ratios would permit a mapping of its effect on back surface strain field. Higher level of loading and elastic-plastic material properties would also permit a better understanding.

Bibliography

[1] BSI. BS 7910:2013 - Guide to methods for assessing the acceptability of flaws in metallic structures . British Standards Institution, London, 2013.

[2] IAEA. Training guidelines in non-destructive testing techniques: Leak testing at level 2. Technical report, IAEA, 2012. IAEA Training Course Series No. 52, IAEA/TCS/52, ISSN 1018–5518, Vienna.

[3] G. Koch, M. Brongers, N. Thompson, Y. Virmani, and J. Payer. Corrosion costs and preventive strategies in the united states, 2002. Publication No FHWA-RD-01-156.

[4] M. Nuhi, T. Abu Seer, A.M. Al Tamimi, M. Modarres, and A. Seibi. Reliability analysis for degradation effects of pitting corrosion in carbon steel pipes. *Procedia Engineering*, 10:1930 – 1935, 2011. 11th International Conference on the Mechanical Behavior of Materials (ICM11).

[5] A. Rajabipour and R.E. Melchers. A numerical study of damage caused by combined pitting corrosion and axial stress in steel pipes. *Corrosion Science*, 76:292 – 301, 2013.

[6] J. Lee, S. Han, K. Kim, H. Kim, and U. Lee. Failure analysis of carbon steel pipes used for underground condensate pipeline in the power station. *Engineering Failure Analysis*, 34:300 – 307, 2013.

[7] G. Yang, K.B. Yoon, and Y.C. Moon. Stress corrosion cracking of stainless steel pipes for methyl-methacrylate process plants. *Engineering Failure Analysis*, 29:45 – 55, 2013.

[8] K.A. Macdonald, A. Cosham, C.R. Alexander, and P. Hopkins. Assessing mechanical damage in offshore pipelines – two case studies. *Engineering Failure Analysis*, 14(8):1667 – 1679, 2007. Papers presented at the Second International Conference on Engineering Failure Analysis (Toronto, Canada, 12–15 September 2006) Part {II}.

[9] API. API 579-1/ASME FFS-1 2007 Fitness-For-Service . American Society of Mechanical Engineers, New-York, 2007.

[10] T.L. Anderson and D.A. Osage. API 579: A comprehensive fitness-for-service guide . *International Journal of Pressure Vessels and Piping*, 77(14–15):953 – 963, 2000.

[11] M. Willcox and G. Downes. A Brief Description of NDT Techniques . Technical report, Insight NDT Equipment Ltd. Technical paper available at "http://www.insightndt.com", copyright©Insight NDT.

[12] BSI. PD 5500:2012 - Unfired fusion welded pressure vessels . British Standards Institution, London, 2012. ISBN: 9780580849756.

[13] ASME. ASME Boiler & Pressure Vessel Code, "Section V - Nondestructive Examination" . American Society of Mechanical Engineers, 2010.

[14] ASTM. E165/E165M-12 - Standard Practice for Liquid Penetrant Examination for General Industry . American Society for Testing and Materials, ASTM International, West Conshohocken, PA, 2012.

[15] ASTM. E433-71(2013) - Standard Reference Photographs for Liquid Penetrant Inspection . American Society for Testing and Materials, ASTM International, West Conshohocken, PA, 2013.

[16] ASTM. E709-14 - Standard Guide for Magnetic Particle Testing . American Society for Testing and Materials, ASTM International, West Conshohocken, PA, 2014.

[17] ASTM. E1444/E1444M-12 - Standard Practice for Magnetic Particle Testing . American Society for Testing and Materials, ASTM International, West Conshohocken, PA, 2012.

[18] ASTM. E213-14 - Standard Practice for Ultrasonic Testing of Metal Pipe and Tubing . American Society for Testing and Materials, ASTM International, West Conshohocken, PA, 2014.

[19] ASTM. E273-10 - Standard Practice for Ultrasonic Testing of the Weld Zone of Welded Pipe and Tubing . American Society for Testing and Materials, ASTM International, West Conshohocken, PA, 2010.

[20] ASTM. E94-04(2010) - Standard Guide for Radiographic Examination . American Society for Testing and Materials, ASTM International, West Conshohocken, PA, 2010.

[21] ASTM. E432-91(2011) - Standard Guide for Selection of a Leak Testing Method . American Society for Testing and Materials, ASTM International, West Conshohocken, PA, 2011.

[22] BSI. BS EN 1779:1999 - Non-destructive testing. Leak testing. Criteria for method and technique selection . British Standards Institution, London, 1999. ISBN: 0580329313.

[23] Report. Leak Detection Theory and Practise - Comparison among leak testing techniques. Technical report, VTech, 2006. VTech Report, Available at "www.vtechonline.com/pdf/vtech-leak-detection.pdf.

[24] A. Pregelj and M. Mozetic. Leak detection methods and defining the sizes of leaks . In *The 4th International Conference of Slovenian Society for Nondestructive Testing "Application of ContemporaryNondestructive Testing in Engineering"*, Ljubljana, 24 - 25 April 1997.

[25] ASTM. E1002-11 - Standard Practice for Leaks Using Ultrasonics . American Society for Testing and Materials, ASTM International, West Conshohocken, PA, 2011.

[26] ASTM. E1211/E1211M-12 - Standard Practice for Leak Detection and Location Using Surface-Mounted Acoustic Emission Sensors . American Society for Testing and Materials, ASTM International, West Conshohocken, PA, 2012.

[27] ASTM. E1139/E1139M-12 - Standard Practice for Continuous Monitoring of Acoustic Emission from Metal Pressure Boundaries . American Society for Testing and Materials, ASTM International, West Conshohocken, PA, 2012.

[28] ASTM. E569/E569M-13 - Standard Practice for Acoustic Emission Monitoring of Structures during Controlled Stimulation . American Society for Testing and Materials, ASTM International, West Conshohocken, PA, 2013.

[29] R. Rintamaa, H. Keinanen, K. Törrönen, H. Talja, A. Saarenheimo, and K. Ikonen. Fracture behaviour of large scale pressure vessels in the hydrotest. *International Journal of Pressure Vessels and Piping*, 34(1–5):265 – 291, 1988.

[30] BSI. BS EN 13184:2001 - Non-destructive testing. Leak testing. Pressure change method . British Standards Institution, London, 2001. ISBN: 0580372170.

[31] ASTM. E515-11 - Standard Practice for Leaks Using Bubble Emission Techniques . American Society for Testing and Materials, ASTM International, West Conshohocken, PA, 2011.

[32] BSI. BS EN 1593:1999 - Non-destructive testing. Leak testing. Bubble emission techniques . British Standards Institution, London, 1999. ISBN: 0580351661.

[33] ASTM. E1603/E1603M-11 - Standard Practice for Leakage Measurement Using the Mass Spectrometer Leak Detector or Residual Gas Analyzer in the Hood Mode . American Society for Testing and Materials, ASTM International, West Conshohocken, PA, 2011.

[34] ASTM. E499/E499M-11 - Standard Practice for Leaks Using the Mass Spectrometer Leak Detector in the Detector Probe Mode . American Society for Testing and Materials, ASTM International, West Conshohocken, PA, 2011.

[35] ASTM. E498/E498M-11 - Standard Practice for Leaks Using the Mass Spectrometer Leak Detector or Residual Gas Analyzer in the Tracer Probe Mode . American Society for Testing and Materials, ASTM International, West Conshohocken, PA, 2011.

[36] ASTM. E493/E493M-11 - Standard Practice for Leaks Using the Mass Spectrometer Leak Detector in the Inside-Out Testing Mode . American Society for Testing and Materials, ASTM International, West Conshohocken, PA, 2011.

[37] BSI. BS EN 13185:2001 - Non-destructive testing. Leak testing. Tracer gas method . British Standards Institution, London, 2001. ISBN: 0580372162.

[38] IAEA. Radiotracer Technology as Applied to Industry . Technical report, IAEA, 2001. IAEA-TECDOC-1262, ISSN 1011–4289, Vienna.

[39] IAEA. Leak Detection in Heat Exchangers and Underground Pipelines Using Radiotracers . Technical report, IAEA, 2009. IAEA Training Course Series No. 38, IAEA-TCS-38, ISSN 1018-5518, Vienna.

[40] C. Inglis. Stresses in a plate due to the presence of cracks and sharp corners. *Trans. Inst. Nav. Archit.*, 55:219 – 230, 1913.

[41] X.K. Zhu and J.A. Joyce. Review of fracture toughness (G, K, J, CTOD, CTOA) testing and standardization . *Engineering Fracture Mechanics*, 85:1 – 46, 2012.

[42] P. Gilles and F.W. Brust. Approximate fracture methods for pipes — part I: theory . *Nuclear Engineering and Design*, 127(1):1 – 17, 1991.

[43] A. Griffith. The phenomena of rupture and flow in solids. *Philos. Trans. R. Soc. A Math. Phys. Eng. Sci.*, 221:163–198, 1921.

[44] G.R. Irwin. Analysis of Stresses and Strains Near the End of a Crack Traversing a Plate. *Journal of Applied Mechanics*, 24:361 – 364, 1957.

[45] T. Anderson. *Fracture Mechanics: Fundamentals and Applications*. CRC Press, third edition. edition, 2005. ISBN 9780849316562.

[46] H. Westergaard. Bearing pressures and cracks . *Journal of Applied Mechanics*, 61:A49–A53, 1939.

[47] G. Irwin. Plastic zone near a crack and fracture toughness . In *7th Sagamore Conference*, 1961. Volume 4, pp 63–76.

[48] D. Dugdale. Yielding of steel sheets containing slits . *Journal of the Mechanics and Physics of Solids*, 8(2):100–104, 1960.

[49] J. Begley and J. Landes. *The J integral as a fracture criterion*. ASTM, 1972. Am. Soc. Test. Mater. Spec. Tech. Publ. ASTM STP 514, pp 1-20.

[50] J. Rice. A Path Independent Integral and the Approximate Analysis of Strain Concentration by Notches and Cracks . *Journal of Applied Mechanics*, 35:379–386, 1968.

[51] J. Rice, P. Paris, , and J. Merkle. *Some further results of J-integral analysis and estimates*. ASTM, 1973. Am. Soc. Test. Mater. Spec. Tech. Publ. ASTM STP 536, pp 231–245.

[52] J. Sumpter and C. Turner. *Method for laboratory determination of Jc*. ASTM, 1976. Am. Soc. Test. Mater. Spec. Tech. Publ. ASTM STP 601, pp 3–18.

[53] A. Wells. Application of fracture mechanics at and beyond general yielding. *British Welding Journal*, 10(5):63–70, 1963.

[54] TWI. Fracture Toughness Testing at TWI. Technical report, TWI, 2015. Internal training course notes.

[55] J. Rice and G. Rosengren. Plane strain deformation near a crack tip in a power law hardening materials. *Journal of the Mechanics and Physics of Solids*, 16(1):1–12, 1968.

[56] D. Hellmann and K.-H. Schwalbe. On the experimental determination of ctod based r-curves. In K.H. Schwalbe, editor, *The Crack Tip Opening Displacement in Elastic-Plastic Fracture Mechanics*, pages 115–132. Springer Berlin Heidelberg, 1986.

[57] C. Filiou, N. Taylor, P. Lejuste, and R. Houghton. Survey of current application and future requirements for european fitness-for-service technology. Technical report, Technical Report No. FITNET/TR2/03, 2003.

[58] R. Selva. Living with Defects:Replace/Repair or prove Fitness-For-Service (FFS)? . In *13th International Conference on Pressure Vessel and Piping Technology*, London, 20-23 May 2012. Keynote Paper – Technical Session: Replacement and Fitness For Service.

[59] M. Koçak, S. Webster, J. Janosch, R. Ainsworth, and R. Koers. FITNET Fitness-for-Service (FFS) - Procedure (Volume 1) . British Standards Institution, London, 2008. ISBN 978-3-940923-00-4, printed by GKSS Research Centre, Geesthacht.

[60] CEGB. R6 - Assessment of the integrity of structures containing defects . Central Electricity Generating Board, 2007. CEGB Document No. R/H/R6-Rev. 4.

[61] J. Shigley, C. Mischke, and R. Budynas. *Mechanical Engineering Design*. McGraw-Hill, 7th edition edition, 2004. ISBN 9780072520361.

[62] ASME. ASME Boiler & Pressure Vessel Code, "Section VIII - Rules for Construction of Pressure Vessels (Division 1 and Division 2)" . American Society of Mechanical Engineers, 2010.

[63] BSI. EN 13445-3:2014 - Unfired pressure vessels. Design" . British Standards Institution, London, 2010. ISBN: 9780580868030.

[64] European Commission. Comparative Study on Pressure Equipment Standards. Technical report, 2004. Contract No FIF.20030114.

[65] G. Irwin. Fracture of pressure vessels. *Mater. Missiles Spacecraft*, page 204–229, 1963. McGraw-Hill.

[66] G.S. Holman. Double-ended breaks in reactor primary piping. *Nuclear Engineering and Design*, 89(1):1 – 12, 1985.

[67] USNRC. Safety evaluation of Westinghouse topical reports dealing with the elimination of postulated pipe breaks in PWR primary main loop. Technical report, USNRC, 1984. (Generic Letter 84-04).

[68] USNRC. State-of-the-Art Report on Piping Fracture Mechanics. Technical report, USNRC, 1998. NUREG/CR-6540.

[69] IAEA. Applicability of the Leak-Before-Break Concept . Technical report, IAEA, 1993. IAEA-TECDOC-710, Vienna.

[70] USNRC. Standard Review Plan 3.6.3 Rev.1 - Leak-Before-Break Evaluation Procedures. Technical report, USNRC, 2007. NUREG-0800.

[71] USNRC. Report of the U.S. Nuclear Regulatory Commission Piping Review Committee - Evaluation of Potential for Pipe Breaks. Technical report, USNRC, 1984. NUREG-1061.

[72] USNRC. NRC Leak-Before-Break (LBB.NRC) Analysis Method for Circumferentially Through-Wall Cracked Pipes Under Axial Plus Bending Loads. Technical report, USNRC, 1986. NUREG/CR-4572.

[73] European Commission. European Safety Practices on the application of Leak Before Break (LBB) concept. Technical report, European Commission, 2000. Report EUR18549 EN.

[74] S. Chattopadhyay. Material Selection for a Pressure Vessel . In *Materials in Design and Manufacturing, Conference & Exposition, ASEE*, 2008.

[75] A. Blake. *Practical Fracture Mechanics in Design*. CRC Press, 1996.

[76] U. Zerbst and R. Ainsworth. Experiences with some European flaw assessment procedures . In *Proceedings of the 11th International Congress on Fracture*, 2005.

[77] B.J.L. Darlaston. Some aspects of leak before break; their quantification and application. *Nuclear Engineering and Design*, 84(2):225 – 232, 1985.

[78] D. Rieck and R. Wernicke. Experiences with fracture mechanics Leak-Before-Break evaluations within the German Integrity Concept for NPPs . In *Proceedings of the 18th European Conference on Fracture*, 2010.

[79] B.F. Beaudoin, D.F. Quiñones, and T.C. Hardin. Leak-before-break application in US light water reactor balance-of-plant piping . *International Journal of Pressure Vessels and Piping*, 43(1–3):67 – 83, 1990.

[80] L. Xie. The effect of characteristic crack sizes on the leak-before-break case of pressure vessels and piping with multiple cracks. *International Journal of Pressure Vessels & Piping*, 76(7):435 – 439, 1999.

[81] L. Xie. Multi-crack growth/coalescence simulation and its role in passive component leak-before-break concept. *Nuclear Engineering and Design*, 194(2–3):113 – 122, 1999.

[82] European Commission. 30 Years of NRWG activities towards harmonization of nuclear safety criteria and requirements. Technical report, European Commission, 2002. Report EUR20818 EN.

[83] IAEA. Guidance for the application of the Leak-Before-Break Concept . Technical report, IAEA, 1994. IAEA-TECDOC-774, Vienna.

[84] C. Faidy. Leak before break application in French PWR plants under operation . In *Proceedings of the seminar on leak before break in reactor piping and vessels*, Lyon, 1995. pp. 145–150.

[85] C. Faidy, S. Bhandari, and P. Jamet. Leak-before-break in French nuclear power plants . *International Journal of Pressure Vessels and Piping*, 43(1–3):151 – 163, 1990.

[86] R. Gerard, C. Malekian, and O. Meessen. Belgian experience in applying the 'leak-before-break' concept to the primary loop piping . In *Proceedings of the seminar on leak before break in reactor piping and vessels*, Lyon, 1995. pp. 137–144.

[87] M.L. Aggarwal, M.J. Kozluk, T.C. Lin, B.W. Manning, and D.K. Vijay. A leak-before-break strategy for CANDU primary piping systems . *International Journal of Pressure Vessels and Piping*, 25(1–4):239 – 256, 1986.

[88] J.S. Nathwani and J.D. Stebbing. Ontario hydro's leak-before-break approach to Darlington NGS heat transport system piping . *International Journal of Pressure Vessels and Piping*, 43(1–3):113 – 127, 1990.

[89] Y.W. Park and Y.K. Chung. Leak-before-break assessment of CANDU pressure tube considering leak detection capability . *Nuclear Engineering and Design*, 191(2):205 – 216, 1999.

[90] J. Chattopadhyay, B.K. Dutta, and H.S. Kushwaha. Leak-before-break qualification of primary heat transport piping of 500 MWe Tarapur atomic power plant . *International Journal of Pressure Vessels and Piping*, 76(4):221 – 243, 1999.

[91] J. Zdarek, L. Pecinka, and P. Kadecka. Leak-before-break criterion applied to VVER 440/230 unit . *Theoretical and Applied Fracture Mechanics*, 23(2):117 – 123, 1995.

[92] E. Keim and D. Lidbury. Review of assessment methods used in nuclear plant life management. Technical report, VTT, 2012. *Availableathttp* : $//www.vtt.fi/proj/nulife/nulife_d1_d2_report_master_11may2012.pdf$.

[93] USNRC. Development of Technical Basis for Leak-Before-Break Evaluation Procedures. Technical report, USNRC, 2002. NUREG/CR-6765.

[94] J. Sharples. STYLE: Comparison of Leak-Before-Break Methodologies Applied in Europe . In *Proceedings of the ASME 2012 Pressure Vessels & Piping Conference*, Toronto, 15–19 July 2012. Paper No. PVP2012-78303, pp. 763–768.

[95] Y. Takahashi. Leak-Before-Break Assessment in JSME Standard . In *Proceedings of the ASME 2011 Pressure Vessels & Piping Conference*, Baltimore, 17–21 July 2011. Paper No. PVP2011-57978, pp. 147–151.

[96] N. Drozdziel. Leak-before-break characterization and demonstration of a high-pressurant helium storage vessel . In *Proceedings of the 5th International Congress on Fracture*, 1981. pp.2145–2151.

[97] VV Knysh, AY Barvinko, YP Barvinko, and AN Yashnik. Substantiation of ≪Leak-before-Break≫ criterion for vertical cylindrical tanks for oil storage. *The Paton Welding Journal*, #9:26–29, 2012.

[98] M.R. Hackworth and J.M. Henshaw. A pressure vessel fracture mechanics study of the aluminium beverage can. *Engineering Fracture Mechanics*, 65(5):525 – 539, 2000.

[99] M. Walter and R. Lesicki. Measures taken to ensure safe operation of an ammonia storage tank. *Process Saf. Prog.*, 17(4):288–296, 1998.

[100] K.P. Kou and F.M. Burdekin. The applicability of leak-before-break on flooded member detection for offshore structures under fatigue. *Engineering Fracture Mechanics*, 75(1):31 – 40, 2008.

[101] R. Andrews, N. Millwood, S. Tiku, N. Pussegoda, M. Hoekstra, and S. Smith. Analysis and Testing of a 13Cr Pipeline to Demonstrate 'Leak Before Break . In *Proceedings of the 9th International Pipeline Conference*, 2012. pp.83–91.

[102] C. Bonn. Estimation of Crack Opening Displacement and Leak Rates Through a Through-Flaw in Aerospace Pressure Vessels. Technical report, Rensselaer Polytechnic Institute, 2008. Master Thesis.

[103] Y. Takahashi. Evaluation of leak-before-break assessment methodology for pipes with a circumferential through-wall crack. part iii: estimation of crack opening area. *International Journal of Pressure Vessels and Piping*, 79(7):525 – 536, 2002.

[104] C. Wüthrich. Crack opening areas in pressure vessels and pipes. *Engineering Fracture Mechanics*, 18(5):1049 – 1057, 1983.

[105] P. Chellapandi, R. Srinivasan, A. Biswas, S. Chetal, and S. Bhoje. Leak Before Break Investigation on Sodium Piping for Prototype Fast Breeder Reactor . In *Transactions of the 17th International Conference on Structural Mechanics in Reactor Technology (SMiRT 17)*, Prague, 17-22 August 2003. Division G10-7.

[106] P. Nagapadmaja, V. Kalyanaraman, S.R. Satish Kumar, and P. Chellapandi. Experimental study on LBB behaviour of LMFBR pipe elbows . *International Journal of Fatigue*, 30(3):574 – 584, 2008.

[107] S. Bhandari, M. Fortmann, L. Grueter, J. Heliot, P. Meyer, B. Percie Du Sert, A. Prado, and H. Zeibig. Crack propagation in a LMFBR elbow . *Nuclear Engineering and Design*, 91(2):107 – 119, 1986.

[108] N. Mani, G. Thanigaiyarasu, and P. Chellapandi. Static stress analysis of steam generator shell nozzle junction for leak before break analysis . *Int. J. Des. Manuf. Technol.*, 3(1):45–50, 2009.

[109] V. Ukadgaonker, Y. Khairnar, P. Vaidya, and P. Chellapandi. Leak-before-break analysis of shell-nozzle junction of steam generator . *Indian J. Eng. Mater. Sci.*, 9:237–249, 2002.

[110] S. Burande and Raju Sethuraman. Computational simulation of fatigue crack growth and demonstration of leak before break criterion. *International Journal of Pressure Vessels and Piping*, 76(5):331 – 338, 1999.

[111] B. Brickstad and I. Sattari-Far. Crack shape developments for LBB applications . *Engineering Fracture Mechanics*, 67(6):625 – 646, 2000.

[112] E. Roos, K.H. Herter, P. Julisch, G. Bartholomé, and G. Senski. Assessment of large scale pipe tests by fracture mechanics approximation procedures with regard to leak-before-break. *Nuclear Engineering and Design*, 112:183 – 195, 1989.

[113] R. Lukess. Predicting the Crack Response for a Pipe with a Complex Crack. Technical report, University of South Carolina, 2013. PhD Thesis.

[114] S. Yellowlees, K. Lynch, A. Warren, J. Sharples, and P. Budden. Development of Guidance for Leak-Before-Break Analysis for Complex Shaped Cracks . In *Proceedings of the ASME 2005 Pressure Vessels & Piping Conference*, Denver, 17-21 July 2005. Paper No. PVP2005-71382, pp. 361–370.

[115] S.B.M. Beck, N.M. Bagshaw, and J.R. Yates. Explicit equations for leak rates through narrow cracks. *International Journal of Pressure Vessels and Piping*, 82(7):565 – 570, 2005.

[116] D.L. Rudland, G. Wilkowski, and P. Scott. Effects of crack morphology parameters on leak-rate calculations in {LBB} evaluations. *International Journal of Pressure Vessels and Piping*, 79(2):99 – 102, 2002.

[117] T.C. Chivers. The influence of surface roughness on fluid flow through cracks. *Fatigue & Fracture of Engineering Materials & Structures*, 25(11):1095–1102, 2002.

[118] P. Gill. Investigating leak rates for 'leak-before-break' assessments. Technical report, University of Manchester, 2013. EngD Thesis.

[119] P. Gill and K. Davey. Analysis of thermo-mechanical behaviour of a crack using {XFEM} for leak-before-break assessments. *International Journal of Solids and Structures*, 51(11–12):2062 – 2072, 2014.

[120] Y. Takahashi. 7.10 - leak before break. In R.O. Ritchie B. Karihaloo, I. Milne, editor, *Comprehensive Structural Integrity*, pages 427 – 464. Pergamon, Oxford, 2003.

[121] S. Yellowlees D. Hootonand J. Sharples P. Budden and D. Dean. Crack Opening Areas During High Temperature Operation . In *Proceedings of the ASME 2002 Pressure Vessels & Piping Conference*, Vancouver, 5-9 August 2002. Paper No. PVP2002-1192, pp. 25–31.

[122] J. Sharples, C. Madew, R. Charles, and P. Budden. Further Studies to Evaluate Crack Opening Areas for Through-Wall Cracks in the Vicinity of Welded Attachments . In *Proceedings of the ASME 2010 Pressure Vessels & Piping Conference*, Bellevue, 18–22 July 2010. Paper No. PVP2010-25257, pp. 733–739.

[123] P. Dillström and W. Zang. ProLBB - A Probabilistic Approach to Leak Before Break Demonstration. Technical report, SKI, 2007. Report 2007:43.

[124] USNRC. xLPR Pilot Study Report. Technical report, USNRC, Washington, DC, and EPRI, Palo Alto, CA, 2012. NUREG-2110 and EPRI 1022860.

[125] I. Varfolomeev, D. Ivanov, D. Siegele, and G. Nagel. Probabilistic Leak-Before-Break Assessment of a Main Coolant Line . In *Proceedings of the ASME 2010 Pressure Vessels & Piping Conference*, Bellevue, 18–22 July 2010. Paper No. PVP2010-25676, pp. 371–378.

[126] D.W. Beardsmore, S.F. Yellowlees, J.K. Sharples, R.A. Ainsworth, and P.J. Budden. A Probabilistic Application of the R6 Detectable Leakage Leak-Before-Break Procedure . In *Proceedings of the ASME 2002 Pressure Vessels & Piping Conference*, Vancouver, 5-9 August 2002. Paper No. PVP2002-1180, pp. 97–104.

[127] M.P. Puls, B.J.S. Wilkins, G.L. Rigby, J.K. Mistry, and P.J. Sedran. A probabilistic method for leak-before-break analysis of CANDU reactor pressure tubes . *Nuclear Engineering and Design*, 185(2–3):241 – 248, 1998.

[128] Y.J. Oh and Y.S. Chang. Integrated probabilistic assessment for DHC initiation, growth and leak-before-break of PHWR pressure tubes . *Nuclear Engineering and Design*, 275:30 – 43, 2014.

[129] G. Wilkowski, B. Brust, T. Zhang, G. Hattery, S. Kalyanam, E. Kurth, Y. Hioe, M. Uddin, J.J. Johnson, O. R. Maslenikov, J.J. Johnson, A.P. Asfura, W. Creek, B. Sumodobila, A.A. Betervide, O. Mazzantini, and B. Aires. Robust LBB Analyses for Atucha II Nuclear Plant . In *Proceedings of the ASME 2011 Pressure Vessels & Piping Conference*, Baltimore, 17–21 July 2011. Paper No. PVP2011-57939 , pp. 107–120.

[130] T. Zhang, F. Brust, G. Wilkowski, H. Xu, A. Betervide, and O. Mazzantini. Beyond Design Basis Seismic Analysis for Atucha II Nuclear Plant . In *Proceedings of the 20th International Conference on Nuclear Engineering*, Anaheim, July 30–August 3 2012. Paper No. ICONE20-POWER2012-54241 , pp. 625–634.

[131] USNRC. International Piping Integrity Research Group (IPIRG) Program. Technical report, USNRC, 1997. NUREG/CR-6233.

[132] P. Bouchard. Practical applications of the R6 Leak-before-Break procedure . In *Proceedings of the seminar on leak before break in reactor piping and vessels*, Lyon, 1995. pp. 127–136.

[133] M.S. Mannan. The 100 Largest Losses (in the Hydrocarbon Industry) 1974-2013. Technical report, 2014. Available at `https://uk.marsh.com/Portals/18/Documents/100_Largest_Losses_23rd_Edition_2014.pdf`.

[134] A. Zahoor. Ductile fracture handbook. Technical report, EPRI, 1989. Report EPRI NP-6301-D.

[135] A.A. Willoughby and T.G. Davey. *Plastic Collapse in Part-Wall Flaws in Plates*. ASTM, 1989. Am. Soc. Test. Mater. Spec. Tech. Publ. ASTM STP 1020, pp 390-410.

[136] M.D. Rana and R.J. Selines. Structural integrity assurance of high-strength steel gas cylinders using fracture mechanics. *Engineering Fracture Mechanics*, 30(6):877 – 894, 1988.

[137] T.L. Anderson. Stress Intensity And Crack Growth Opening Area Solutions For Through-wall Cracks In Cylinders And Spheres. Technical report, WRC Bulletin 478, Welding Research Council, Inc. New York, NY, January 2003.

[138] D. Green and J. Knowles. The treatment of residual stress in fracture assessment of pressure vessels. *Pressure Vessel Technology*, 116(4):345 – 352, 1994.

[139] D. Green C.C. France and J.K. Sharples. New stress intensity factor and crack opening area solutions for through-wall cracks in pipes and cylinders. Technical report, AEA Technology Report AEAT-0643, 1996. Addendum, April, 1999.

[140] A.G. Miller. Review of limit loads of structures containing defects. *International Journal of Pressure Vessels and Piping*, 32(1):197 – 327, 1988.

[141] W. Kastner, E. Röhrich, W. Schmitt, and R. Steinbuch. Critical crack sizes in ductile piping. *International Journal of Pressure Vessels and Piping*, 9(3):197 – 219, 1981.

[142] T.L. Anderson et. al. Development of Stress Intensity Factor Solutions for Surface and Embedded Cracks in API 579 . Technical report, WRC Bulletin 471, Welding Research Council, Inc. New York, NY, May 2002.

[143] J.C. Newman and I.S. Raju. An empirical stress-intensity factor equation for the surface crack. *Engineering Fracture Mechanics*, 15(1):185 – 192, 1981.

[144] K.W. Nam, K. Ando, S. Yuzuru, and N. Ogura. Leak-before-break conditions of plates and pipes under high fatigue stresses. *Fatigue and Fracture of Engineering Materials and Structures*, 15(8):809–824, 1992.

[145] K. W. Nam, K. Ando, and N. Ogura. The effect of specimen size on the behaviour of penetrating fatigue cracks. *Fatigue and Fracture of Engineering Materials and Structures*, 16(7):767–779, 1993.

[146] Abaqus. Abaqus 6.13 documentation. Technical report, Dassault Systemes.

[147] J. Souza, F. Peres, and C. Schön. Methods for Introducing Pre-cracks in Fracture Mechanics Testing of Polymers . In *17th European Conference on Fracture*, Brno, 2 -5 September 2008. pp. 2220–2227.

[148] A. Huang, W. Yao, and F. Chen. Analysis of Fatigue Life of PMMA at Different Frequencies Based on a New Damage Mechanics Model. *Mathematical Problems in Engineering*, Volume 2014, 2014. Article ID 352676.

[149] A. Almar-Naes. Fatigue handbook - Offshore Steel Structures. TAPIR, TAPIR, Norges tekniske högskole, 7034, Trondheim-NTH, Norge, 1985.

[150] ThePlasticShop.co.uk. A guide to the technical properties and data of Perspex Sheet (cast). Technical report, 2015. Available at `http://www.theplasticshop.co.uk/plastic_technical_data_sheets/perspex_technical_properties_data_sheet.pdf`.

[151] J. C. Jr. Newman and I. S. Raju. Analysis of surface cracks in finite plates under tension or bending loads, nasa-tp-1578. Technical report, NASA Langley Research Center; Hampton, VA, United States, 1979.

[152] I.S. Raju and J.C. Newman Jr. Stress-intensity factors for a wide range of semi-elliptical surface cracks in finite-thickness plates. *Engineering Fracture Mechanics*, 11(4):817 – 829, 1979.

[153] M. Nagai, N. Miura, and M. Shiratori. Stress intensity factor solution for a surface crack with high aspect ratio subjected to an arbitrary stress distribution using the influence function method. *International Journal of Pressure Vessels and Piping*, 131:2 – 9, 2015. The 10th International Workshop on the Integrity of Nuclear Components.

[154] Z. Wu. The shape of a surface crack in a plate based on a given stress intensity factor distribution. *International Journal of Pressure Vessels and Piping*, 83(3):168 – 180, 2006.

[155] A. Hosseini and M.A. Mahmoud. Evaluation of stress intensity factor and fatigue growth of surface cracks in tension plates. *Engineering Fracture Mechanics*, 22(6):957 – 974, 1985.

[156] X.B. Lin and R.A. Smith. Finite element modelling of fatigue crack growth of surface cracked plates: Part i: The numerical technique. *Engineering Fracture Mechanics*, 63(5):503 – 522, 1999.

[157] P.P. Paris and F.F. Erdogan. A critical analysis of crack propagation laws. *ASME. J. Basic Eng.*, 85(4):528 – 533, 1963.

[158] X.B. Lin and R.A. Smith. Finite element modelling of fatigue crack growth of surface cracked plates: Part iii: Stress intensity factor and fatigue crack growth life. *Engineering Fracture Mechanics*, 63(5):541 – 556, 1999.

[159] BSI. BS EN ISO 6892-1:2009 - Metallic materials. Tensile testing. Method of test at ambient temperature . British Standards Institution, London, 2009.

[160] J.R. Yates, M. Zanganeh, and Y.H. Tai. Quantifying crack tip displacement fields with {DIC}. *Engineering Fracture Mechanics*, 77(11):2063 – 2076, 2010. International Conference on Crack Paths 2009.

[161] P. Paris and H. Tada. The application of fracture proof design methods using tearing instability theory to nuclear piping postulating circumferential throughwall cracks. Technical report, USNRC, 1983. USNRC Report, NUREG/CR-3464.

[162] E. S. Folias. An axial crack in a pressurized cylindrical shell. *International Journal of Fracture Mechanics*, 1(2):104–113, 1965.

Appendix A

Complementary photographs and plots from experiments

Contents

A.1 Fracture surface from Perspex samples

A.1.1 Series 1 (10x50x100mm)

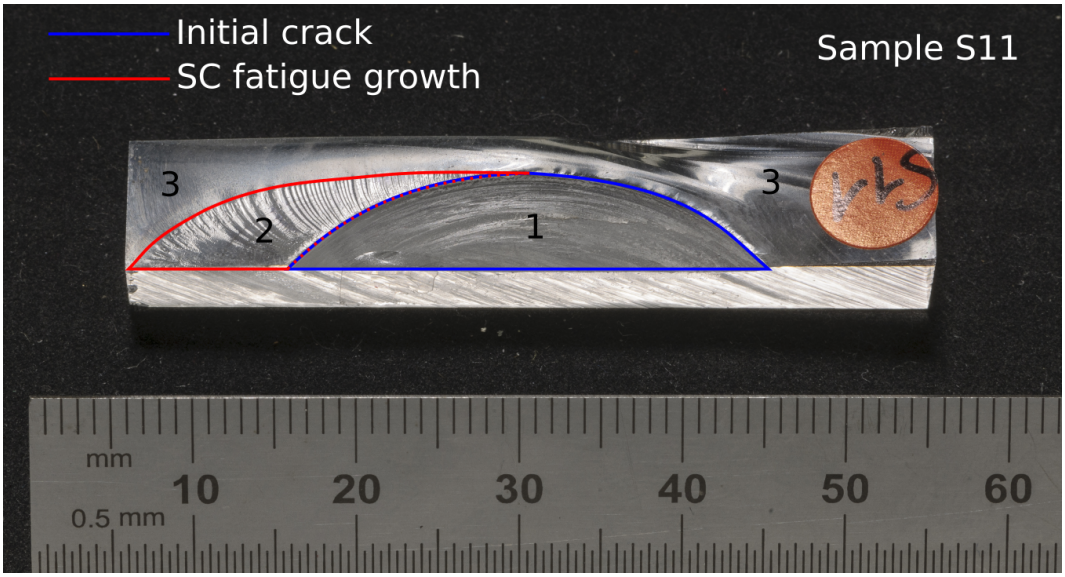

Figure A.1: Test on Perspex plate - Fracture surface - Sample S11

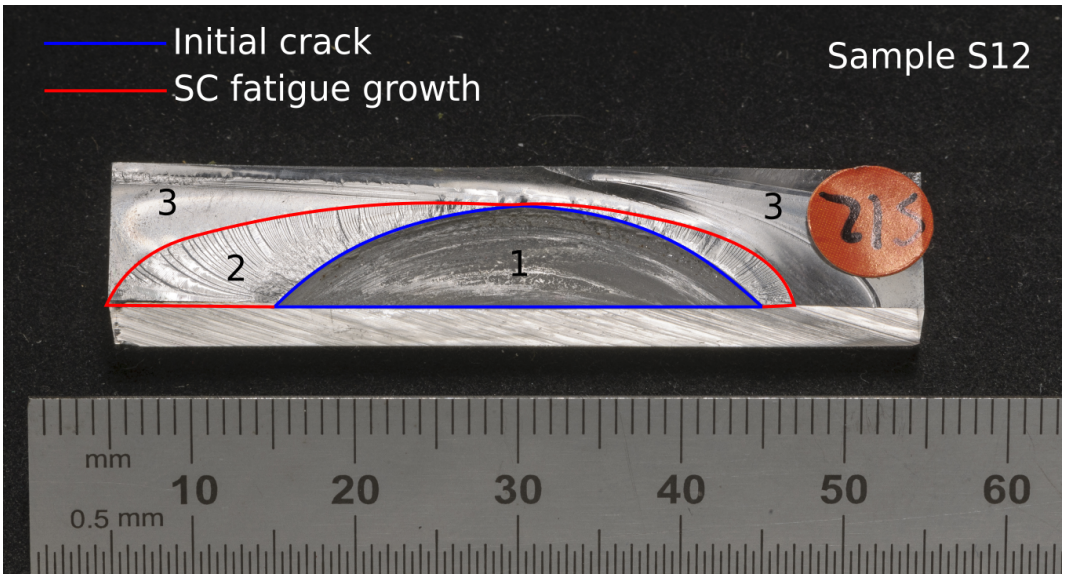

Figure A.2: Test on Perspex plate - Fracture surface - Sample S12

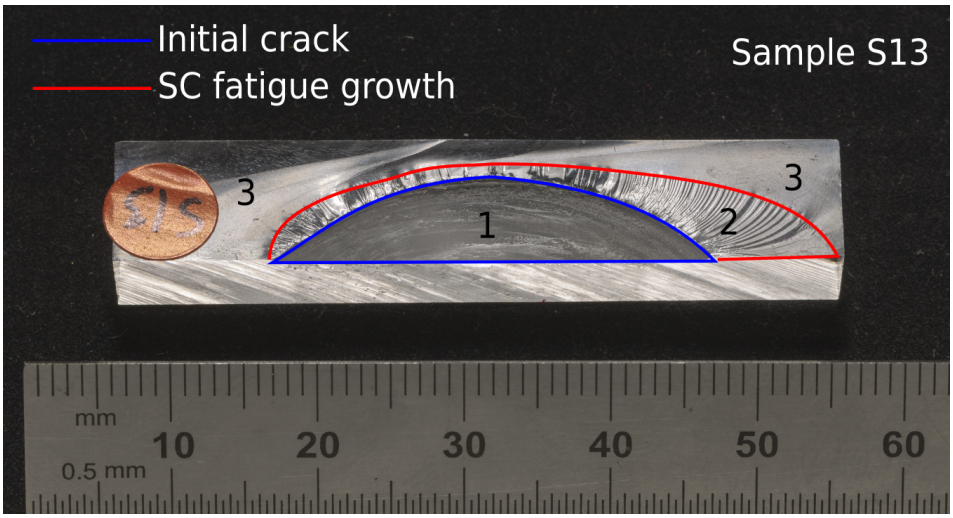

Figure A.3: Test on Perspex plate - Fracture surface - Sample S13

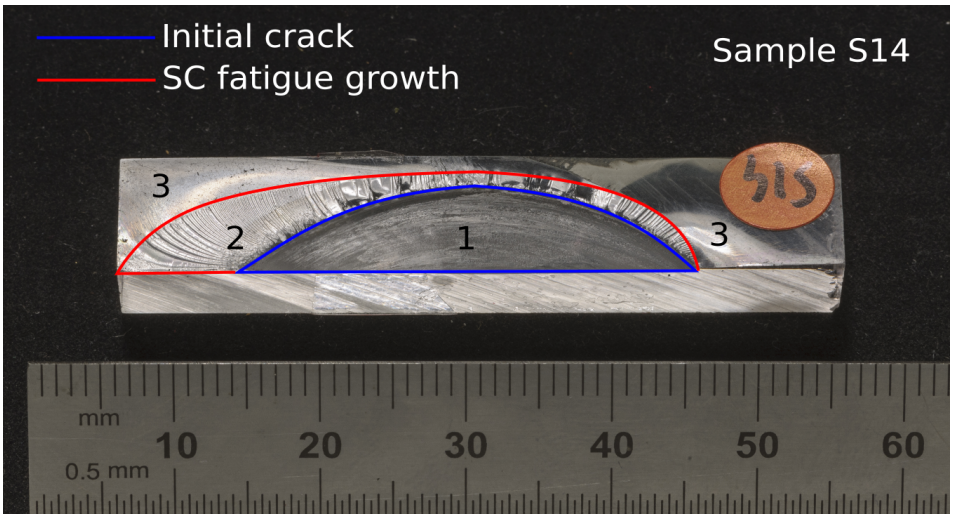

Figure A.4: Test on Perspex plate - Fracture surface - Sample S14

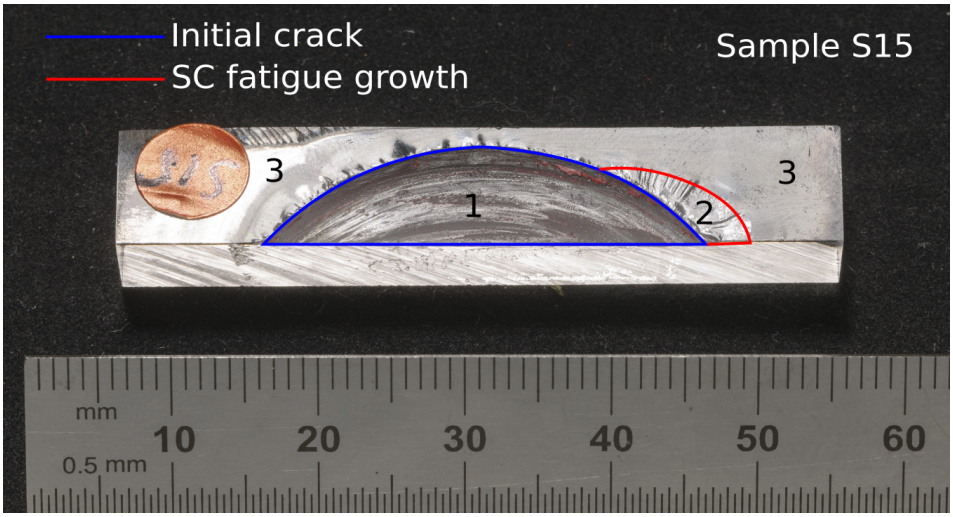

Figure A.5: Test on Perspex plate - Fracture surface - Sample S15

A.1.2 Series 2 (15x50x100mm)

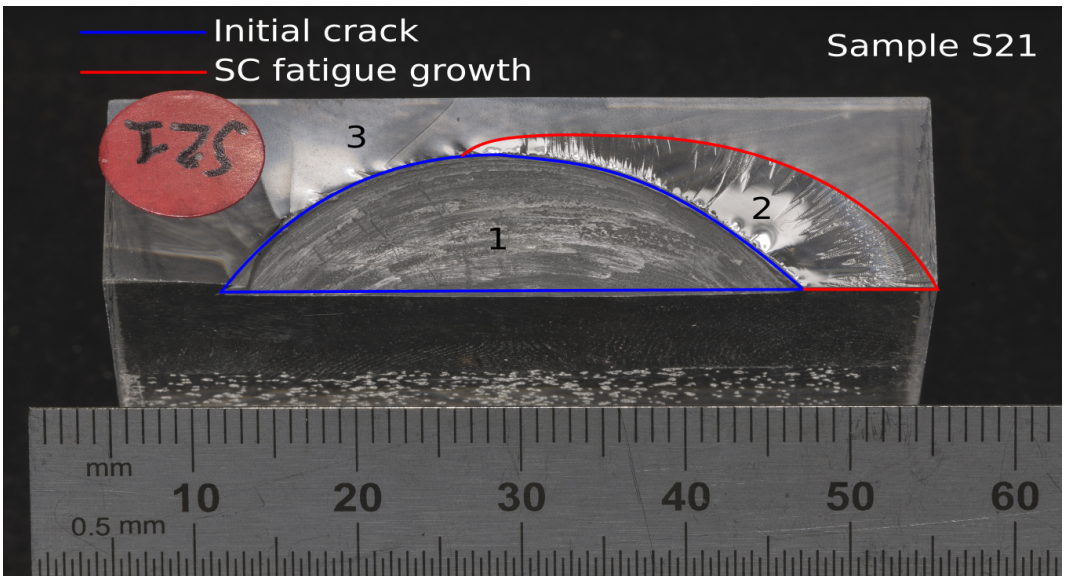

Figure A.6: Test on Perspex plate - Fracture surface - Sample S21

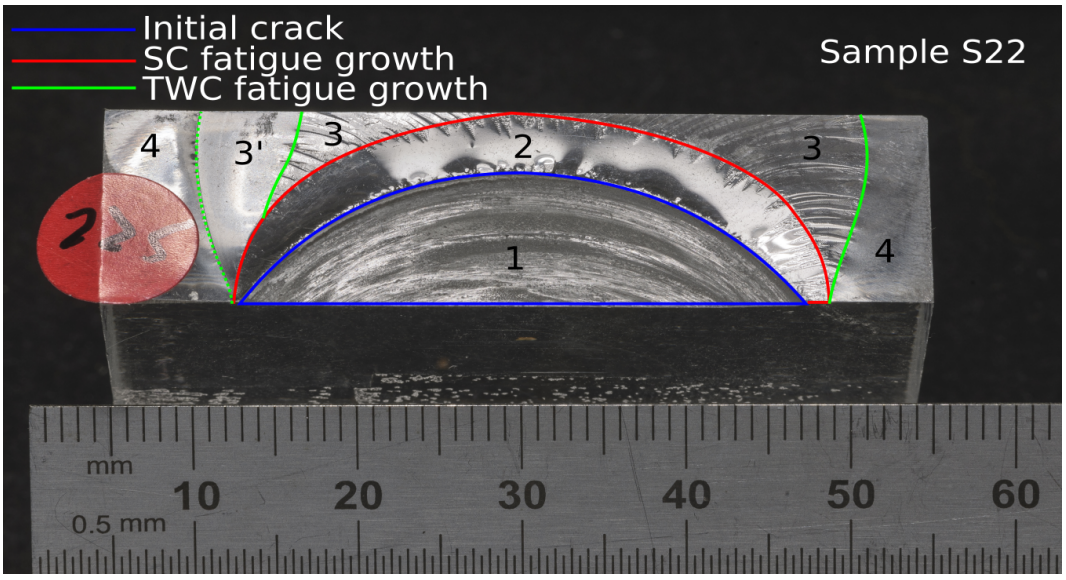

Figure A.7: Test on Perspex plate - Fracture surface - Sample S22

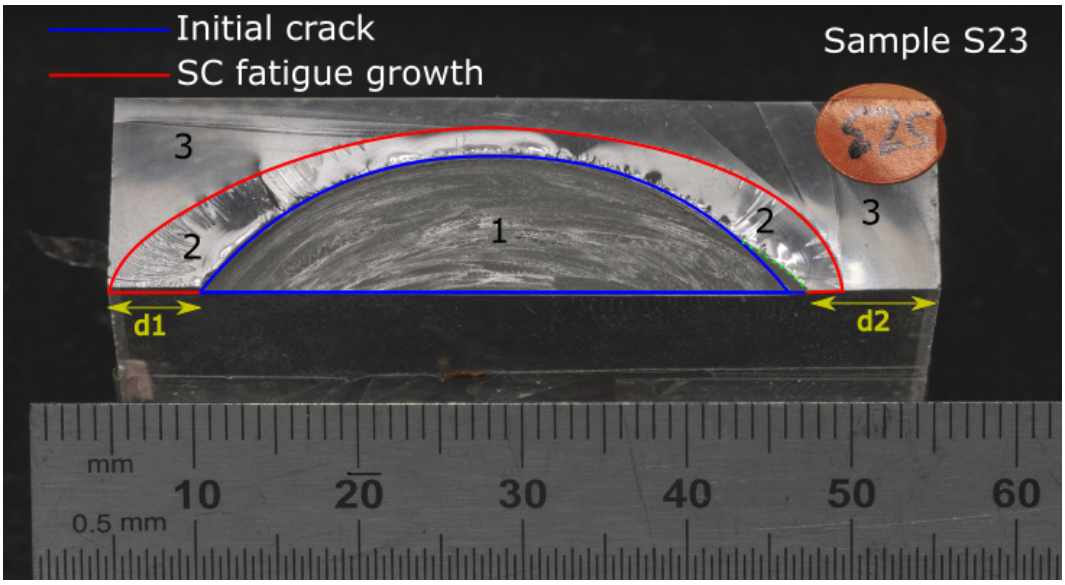

Figure A.8: Test on Perspex plate - Fracture surface - Sample S23

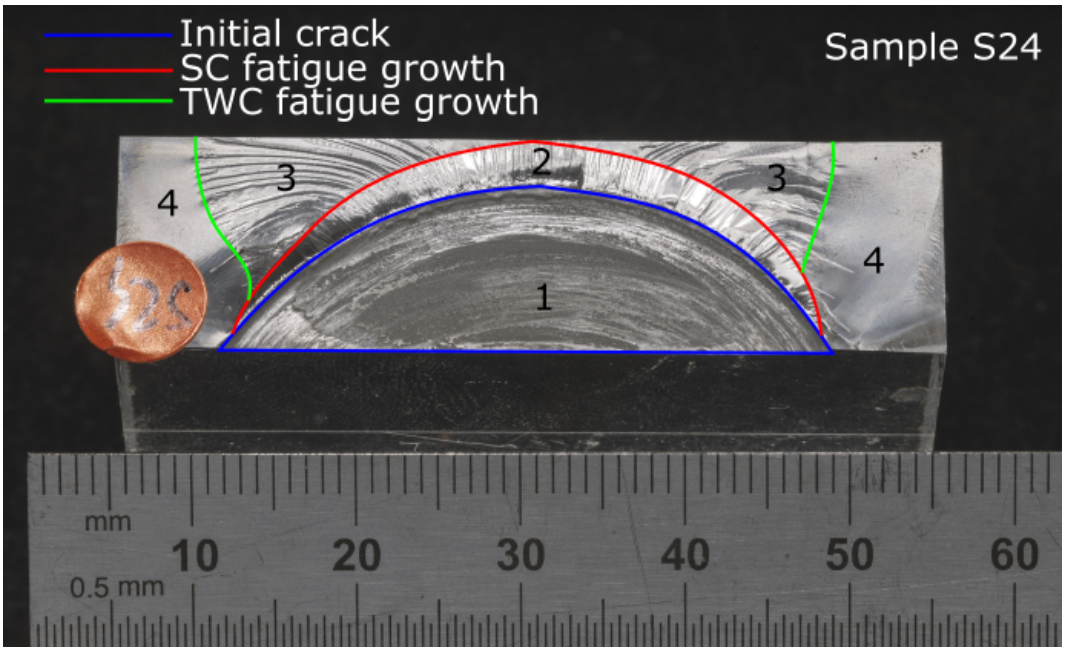

Figure A.9: Test on Perspex plate - Fracture surface - Sample S24

A.1.3 Series 3 (10x75x100mm)

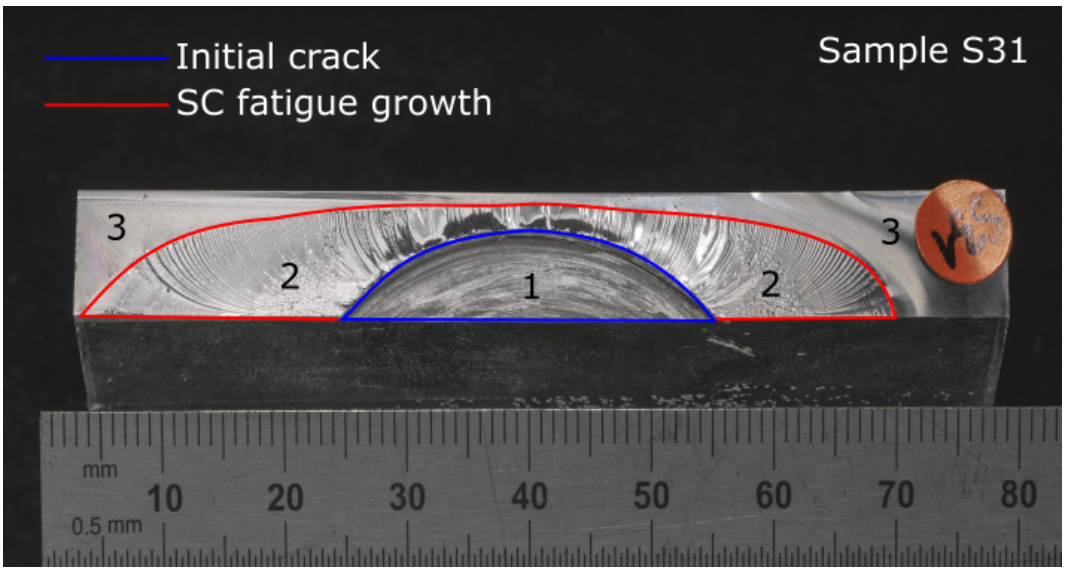

Figure A.10: Test on Perspex plate - Fracture surface - Sample S31

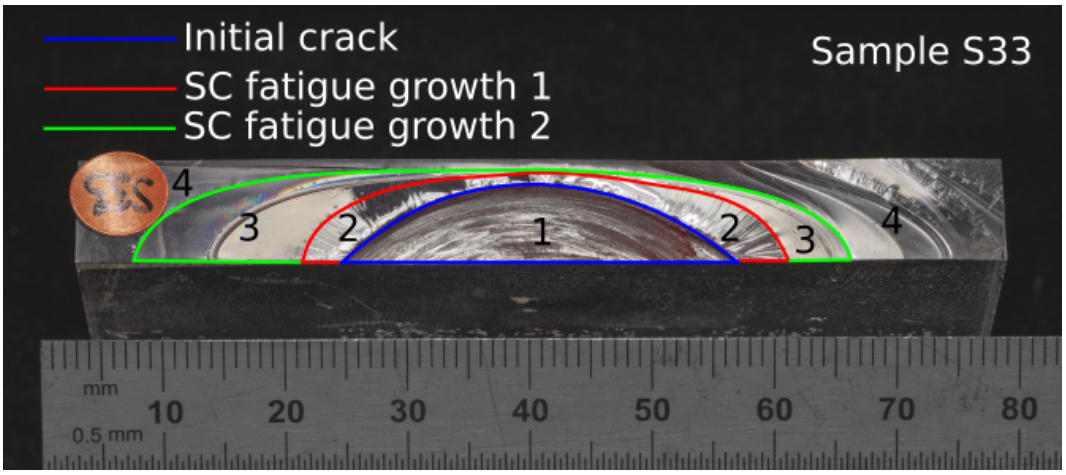

Figure A.11: Test on Perspex plate - Fracture surface - Sample S33

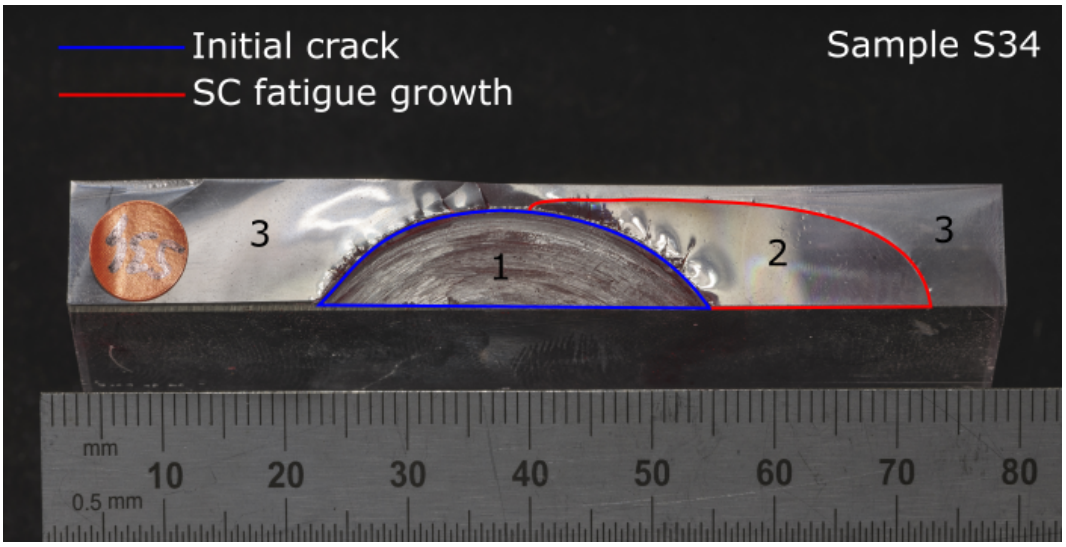

Figure A.12: Test on Perspex plate - Fracture surface - Sample S34

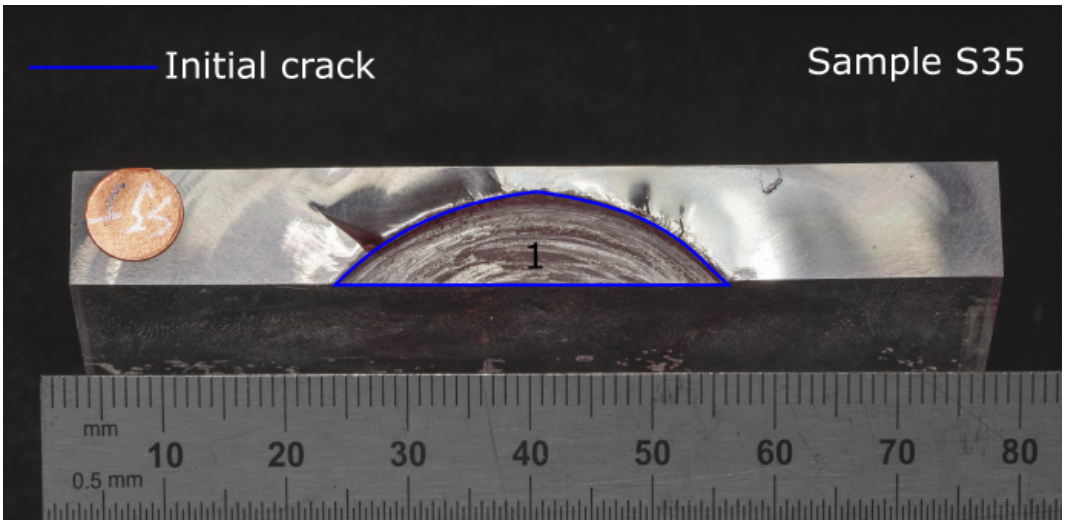

Figure A.13: Test on Perspex plate - Fracture surface - Sample S35

A.1.4 Series 4 (15x75x100mm)

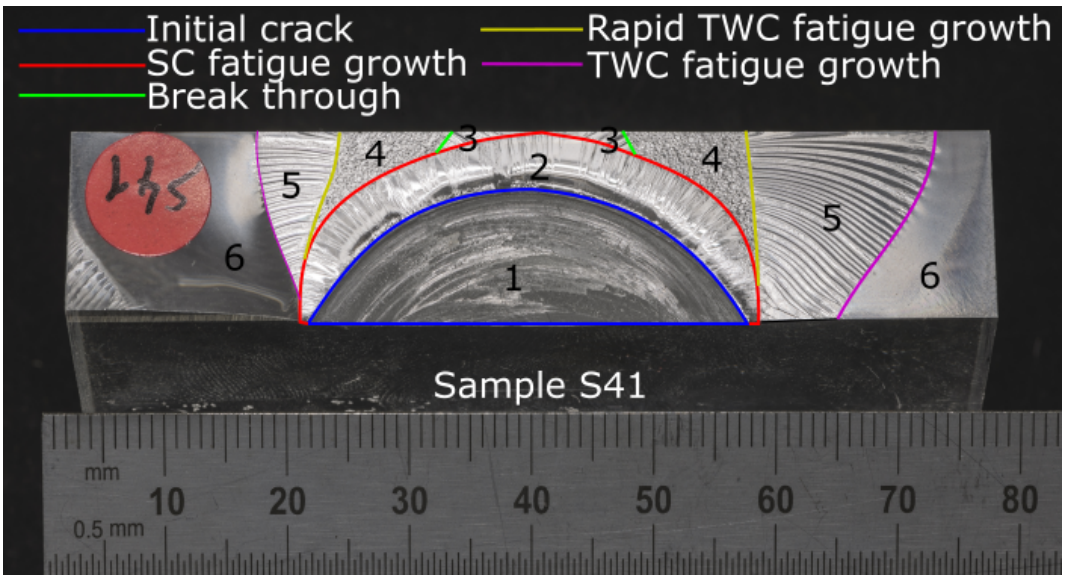

Figure A.14: Test on Perspex plate - Fracture surface - Sample S41

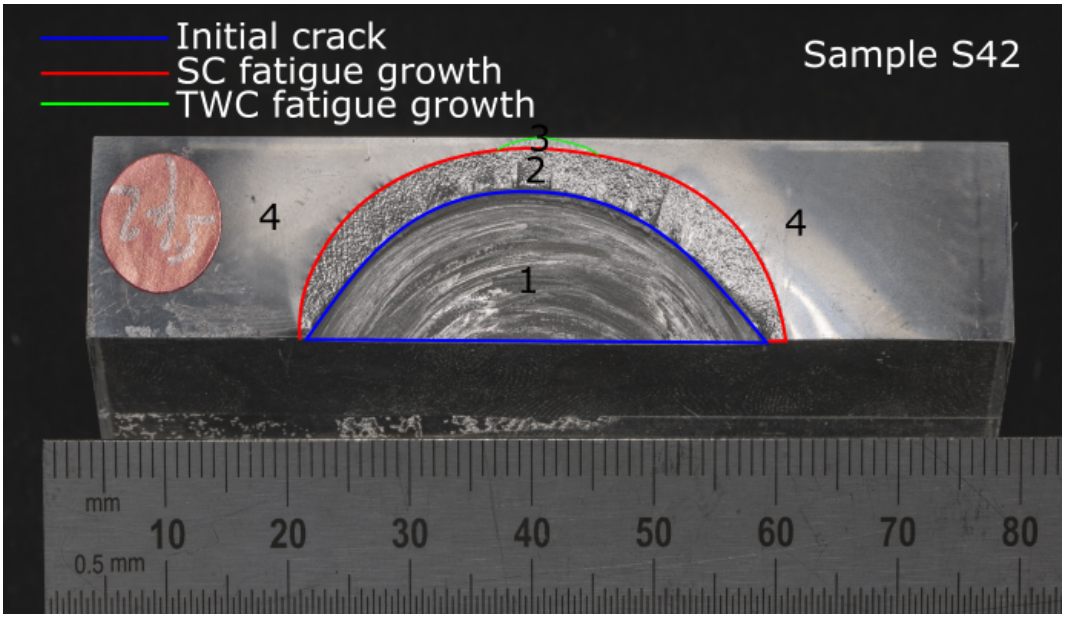

Figure A.15: Test on Perspex plate - Fracture surface - Sample S42

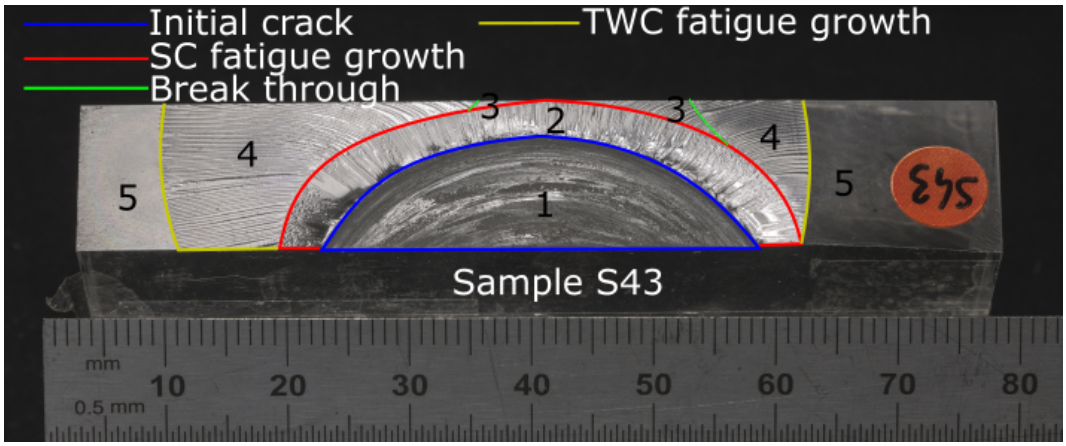

Figure A.16: Test on Perspex plate - Fracture surface - Sample S43

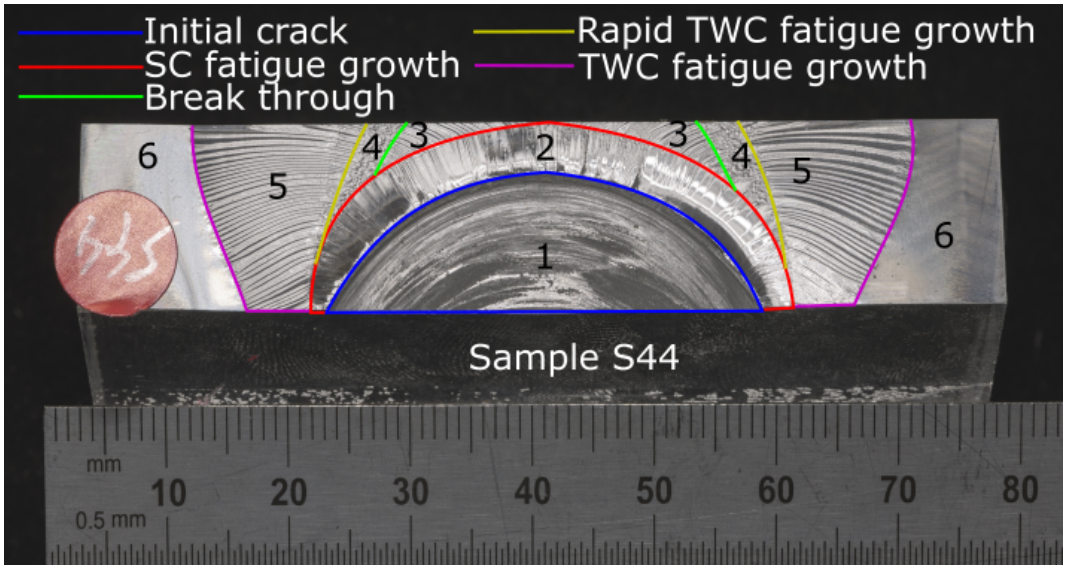

Figure A.17: Test on Perspex plate - Fracture surface - Sample S44

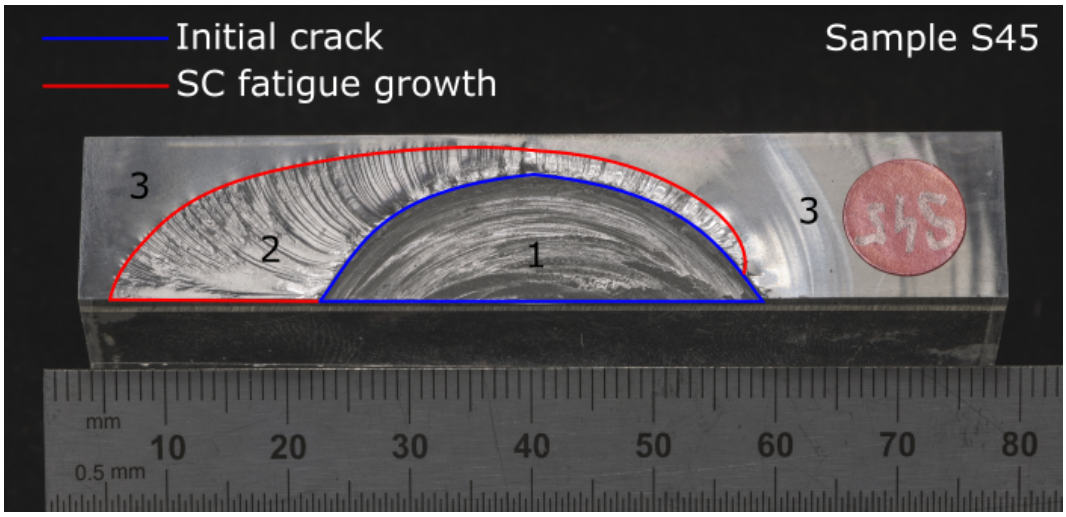

Figure A.18: Test on Perspex plate - Fracture surface - Sample S45

A.2 Recorded strain data from metallic specimens

A.2.1 Static test

Static test recorded strain data for specimens M01-01 and M01-02 were provided in Chapter6, Section6.3.4 and recorded strain data for specimens M01-01 and M01-02 are given in Figure A.19, Figure A.20 and Figure A.21.

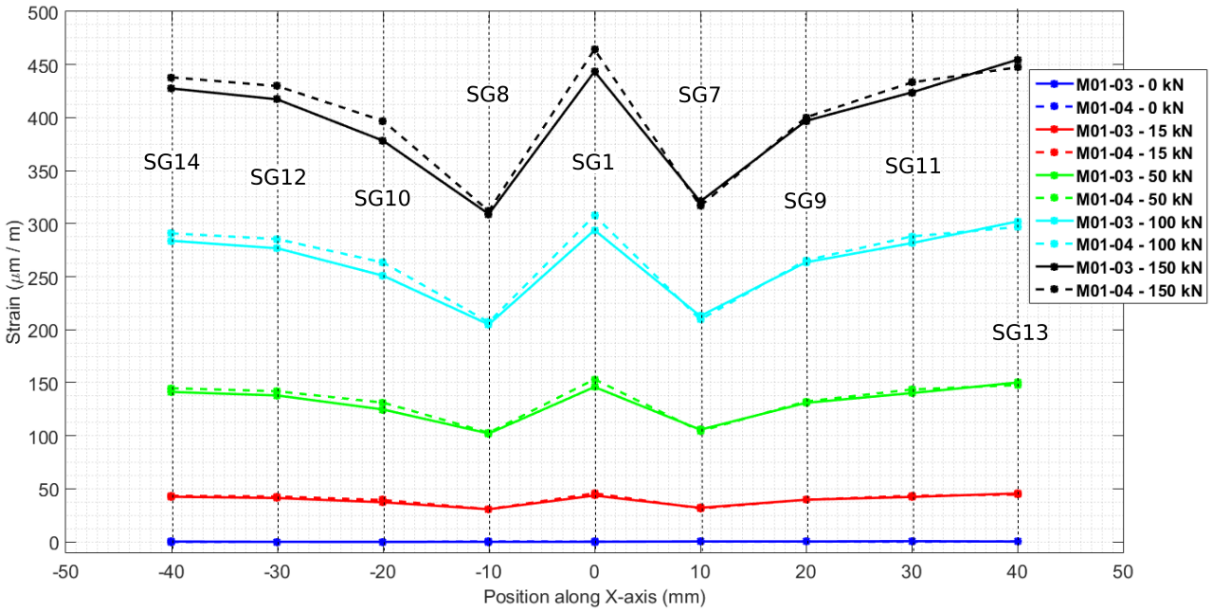

Figure A.19: Evolution of strains along X-axis under increasing static loads: 0kN, 15kN, 50kN, 100kN and 150kN for Specimens M01-03 & M01-04

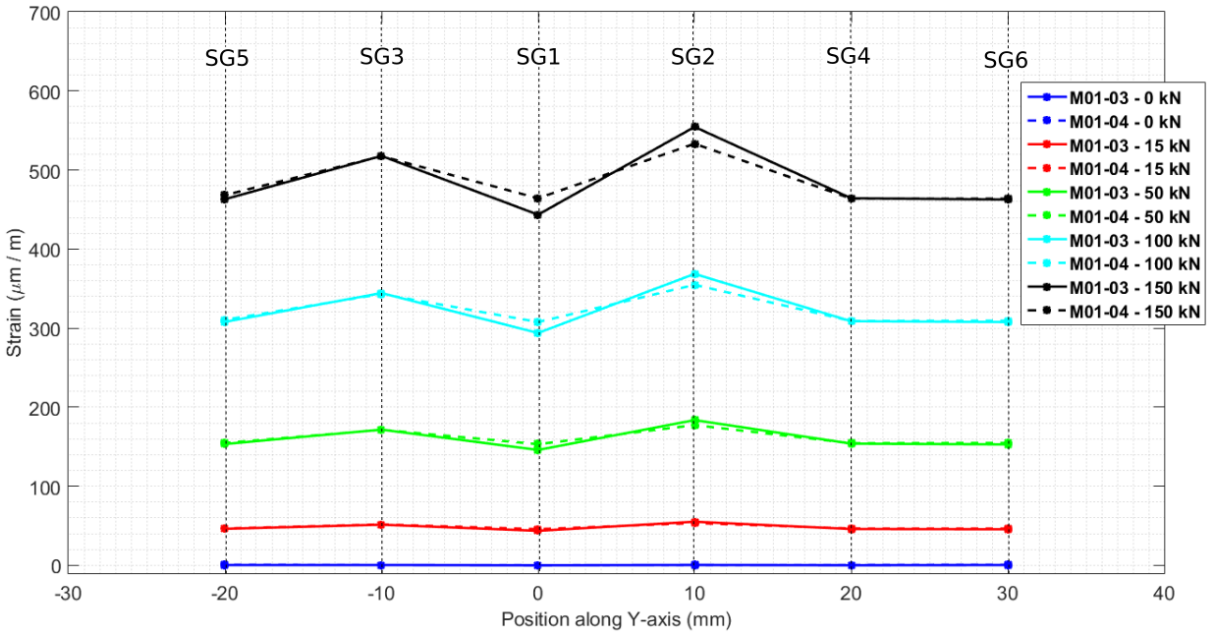

Figure A.20: Evolution of strains along Y-axis under increasing static loads: 0kN, 15kN, 50kN, 100kN and 150kN for Specimens M01-03 & M01-04

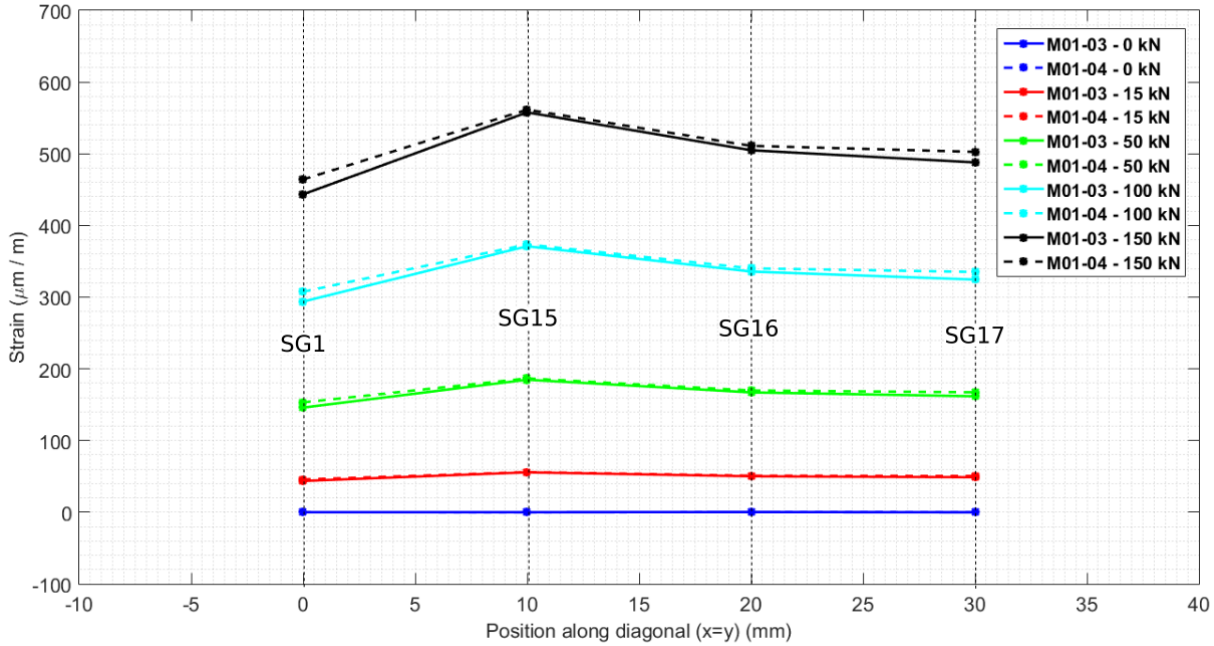

Figure A.21: Evolution of strains along the diagonal direction under increasing static loads: 0kN, 15kN, 50kN, 100kN and 150kN for Specimens M01-03 & M01-04

A.2.2 Fatigue test

The plots obtained from specimens fatigue test on M01-01 were presented in details in Chapter 6. Other specimens plots are provided in this appendix:

- M01-02
  - Figure A.22 - Strain evolution along the X-axis.
  - Figure A.23 - Strain evolution along the Y-axis.
  - Figure A.24 - Strain evolution along the diagonal axis.
- M01-03
  - Figure A.25 - Strain evolution along the X-axis.
  - Figure A.26 - Strain evolution along the Y-axis.
  - Figure A.27 - Strain evolution along the diagonal axis.
- M01-04
  - Figure A.28 - Strain evolution along the X-axis.
  - Figure A.29 - Strain evolution along the Y-axis.
  - Figure A.30 - Strain evolution along the diagonal axis.

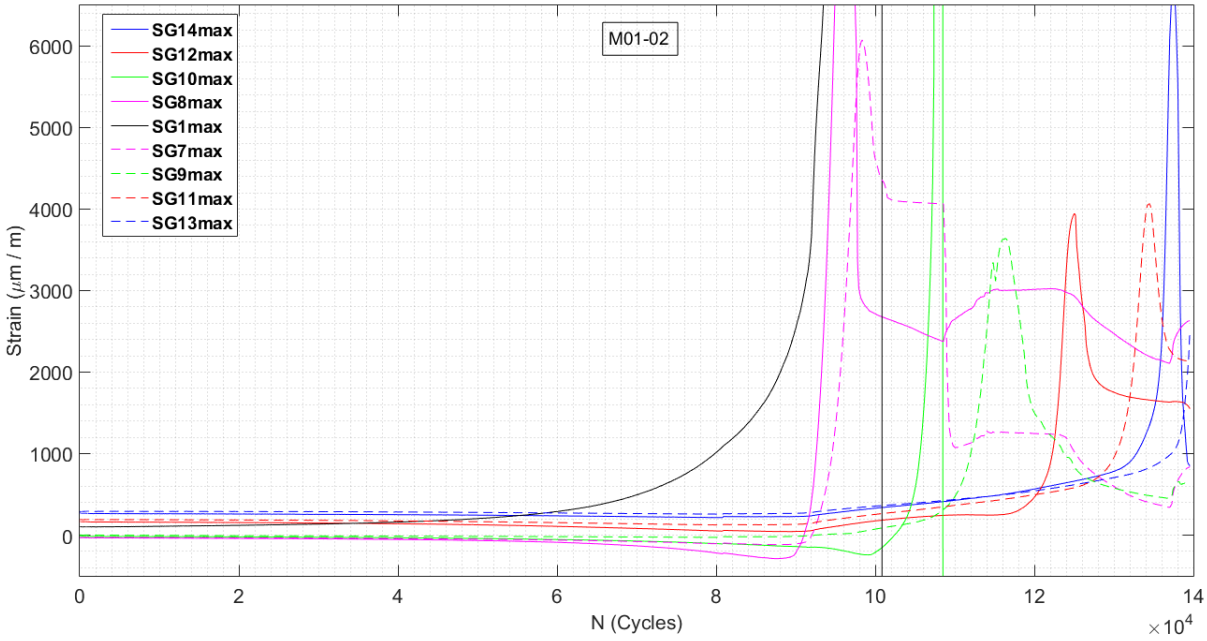

Figure A.22: Evolution of the strains along the X-axis during fatigue test - M01-02

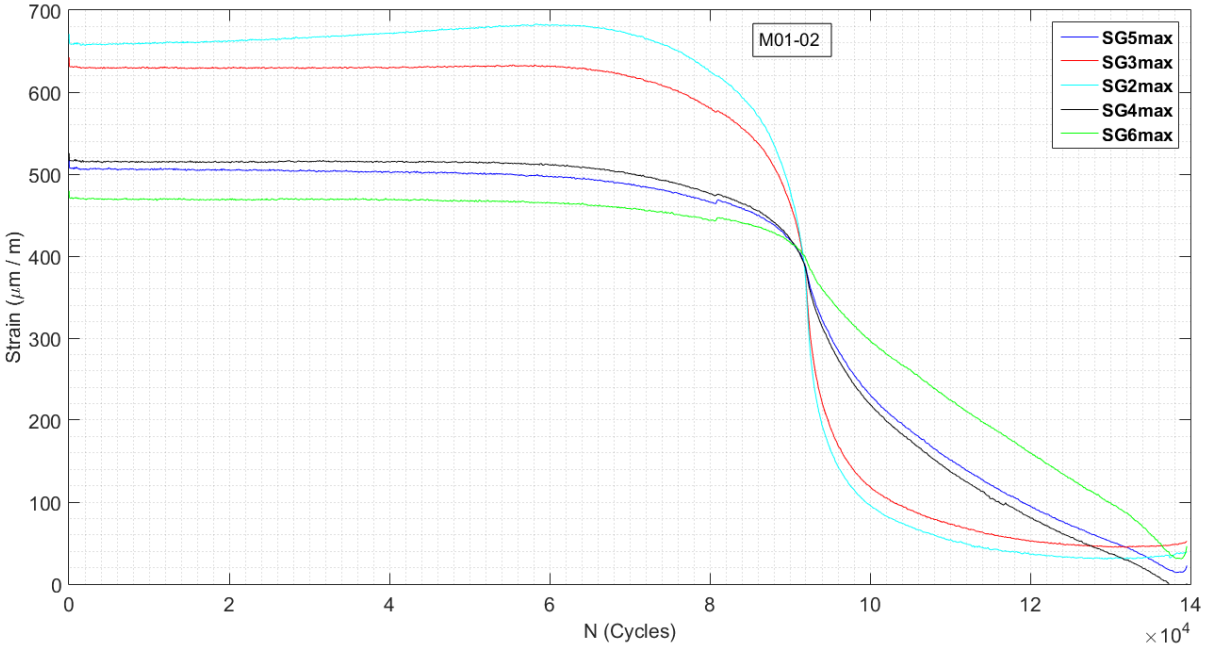

Figure A.23: Evolution of the strains along the Y-axis during fatigue test - M01-02

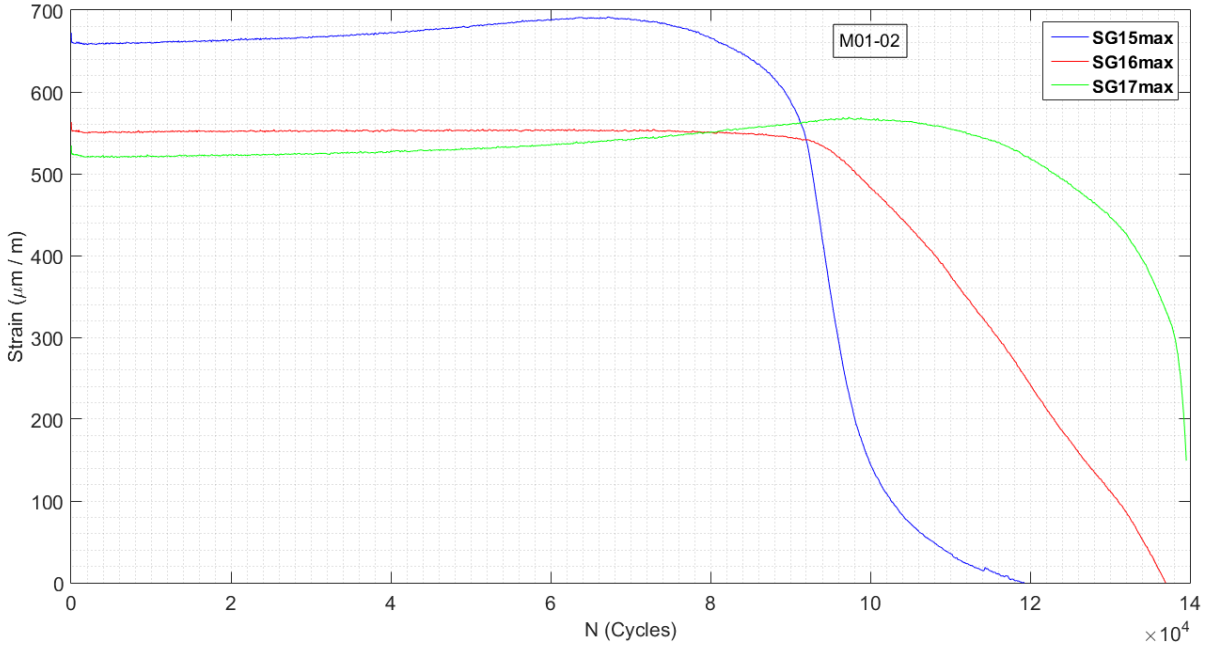

Figure A.24: Evolution of the strains for the diagonal strain gauges during fatigue test - M01-02

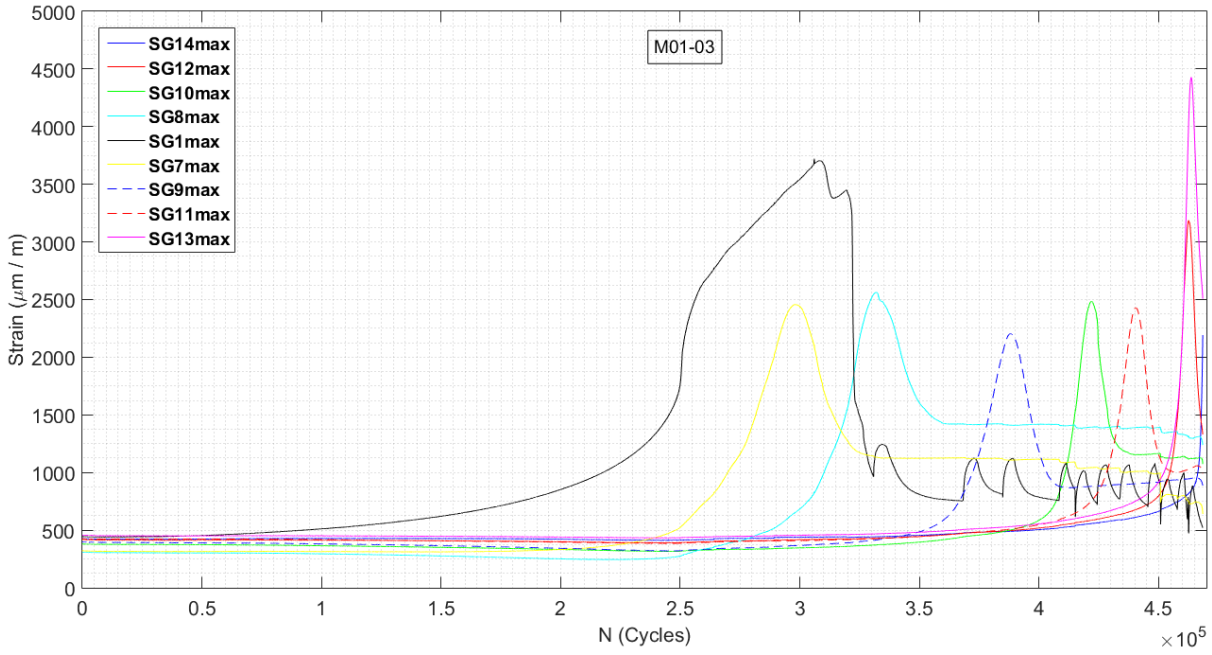

Figure A.25: Evolution of the strains along the X-axis during fatigue test - M01-03

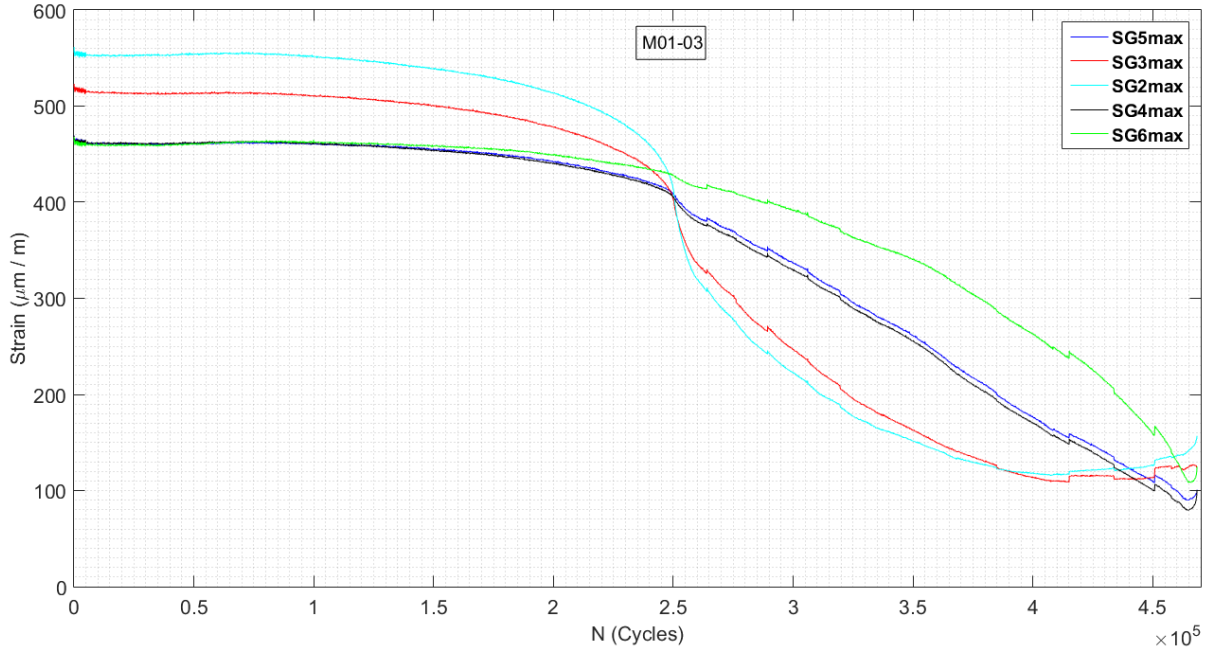

Figure A.26: Evolution of the strains along the Y-axis during fatigue test - M01-03

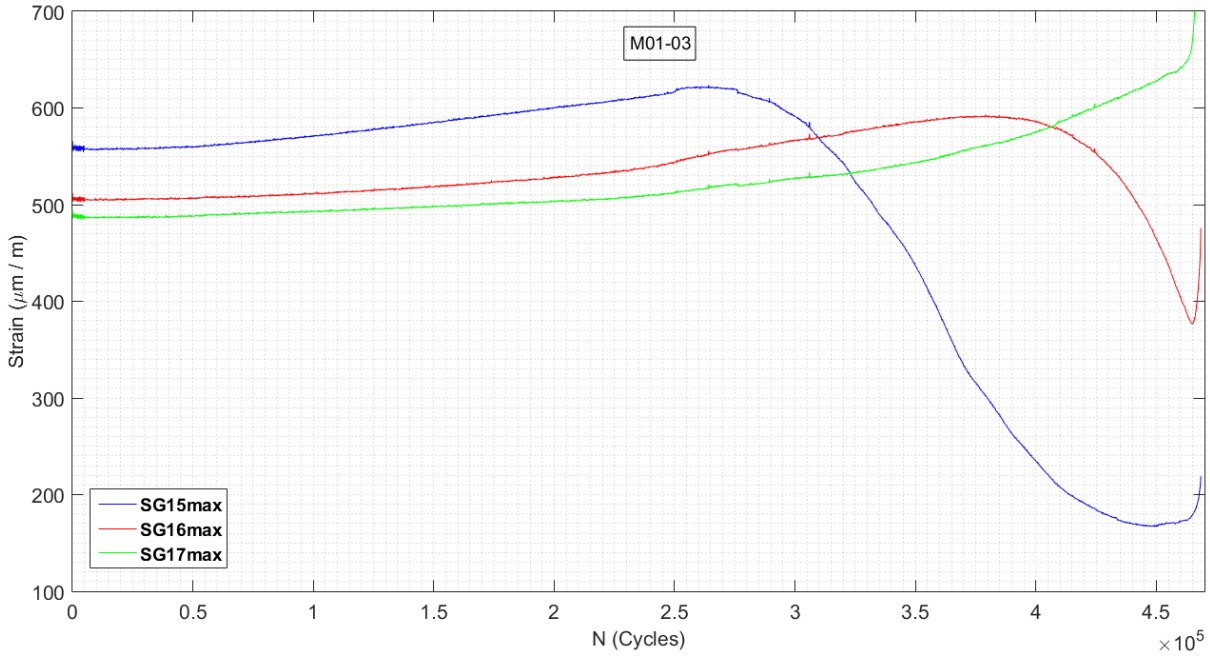

Figure A.27: Evolution of the strains for the diagonal strain gauges during fatigue test - M01-03

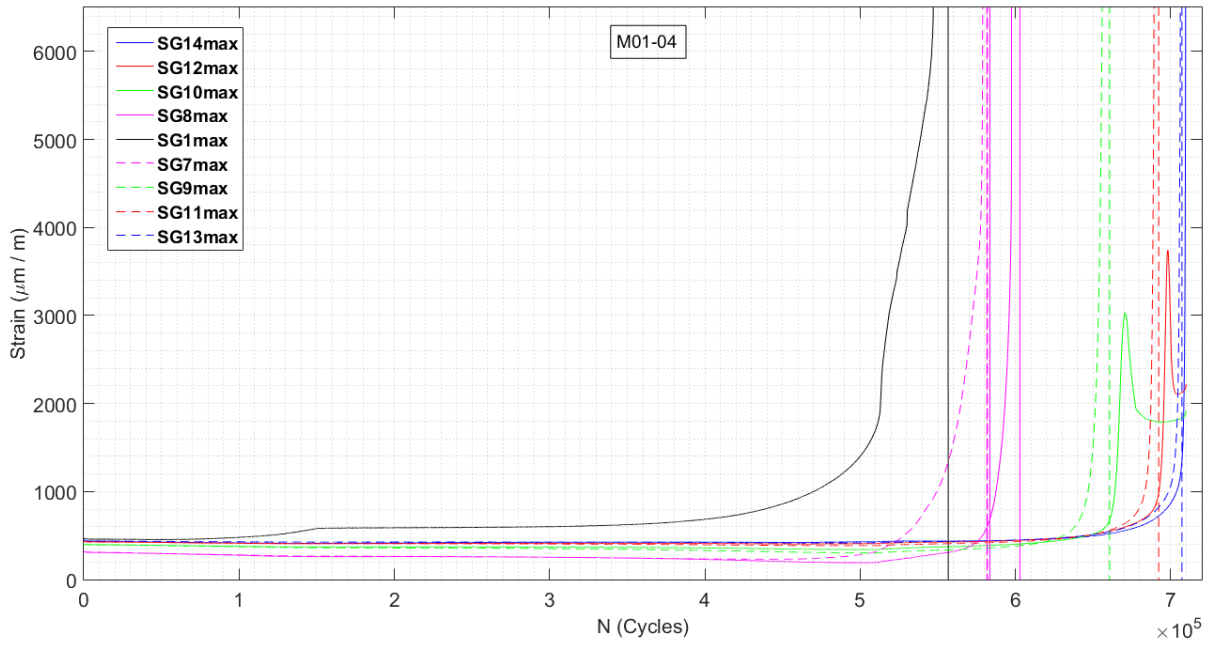

Figure A.28: Evolution of the strains along the X-axis during fatigue test - M01-04

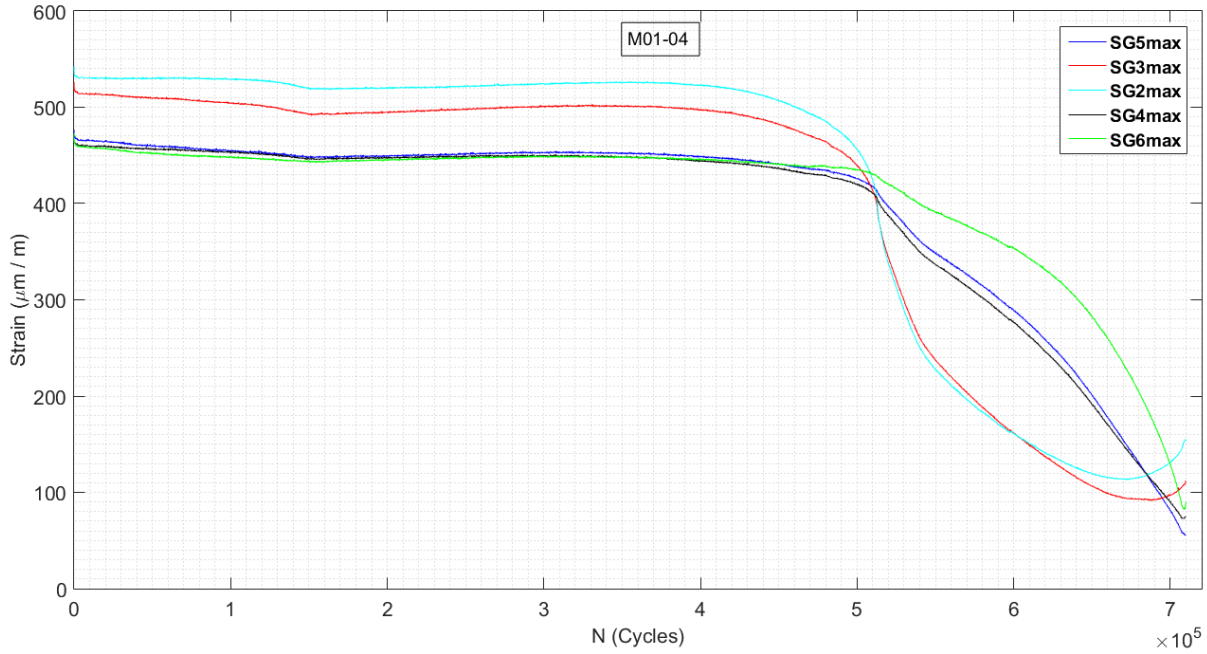

Figure A.29: Evolution of the strains along the Y-axis during fatigue test - M01-04

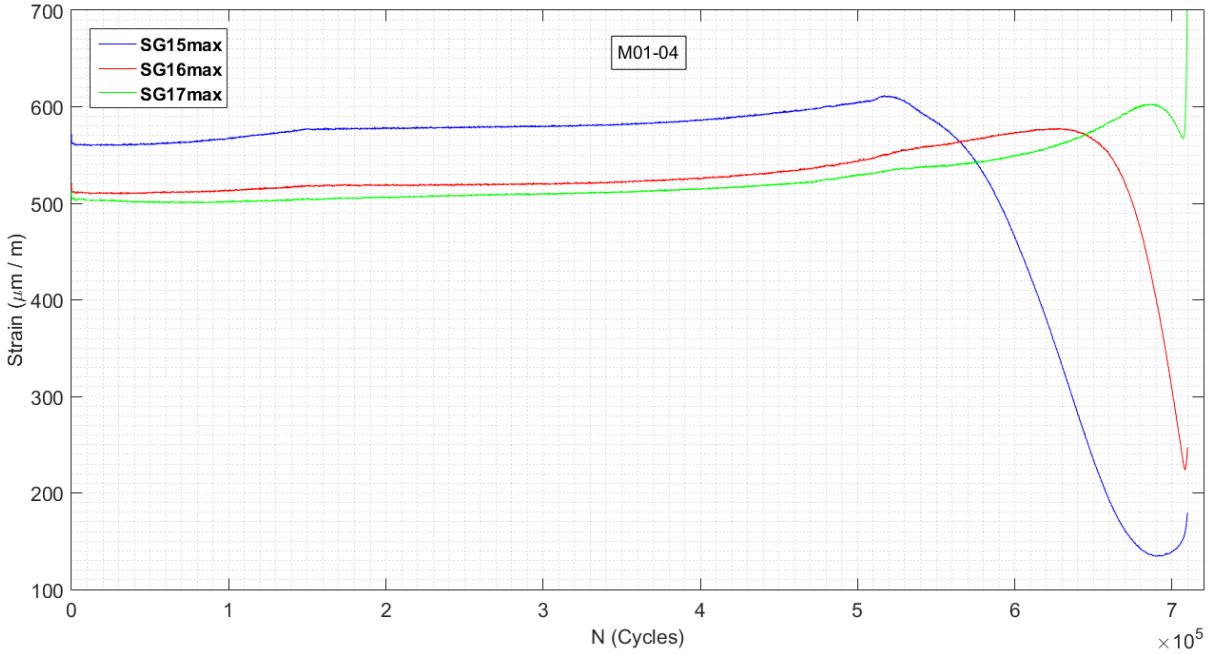

Figure A.30: Evolution of the strains for the diagonal strain gauges during fatigue test - M01-04

A.3 Photographs of high strength steel specimens

A.3.1 Fracture surface

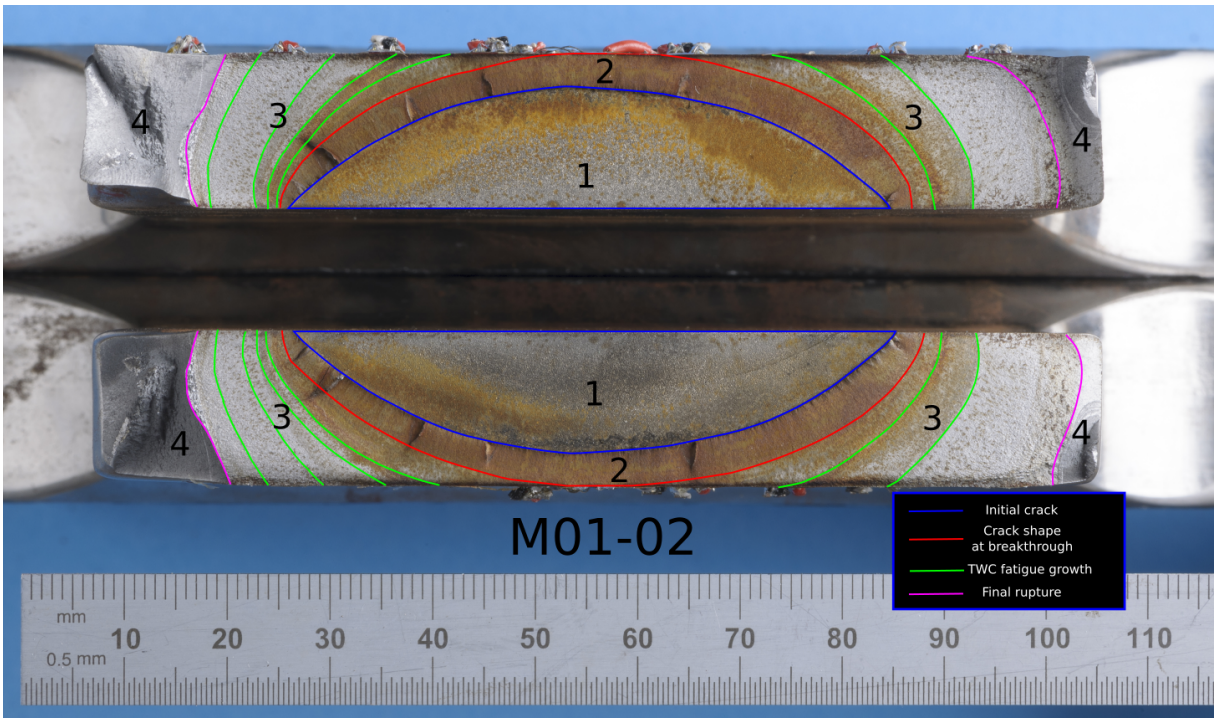

Figure A.31: Test on high strength steel plate - Fracture surface - Sample M01-02

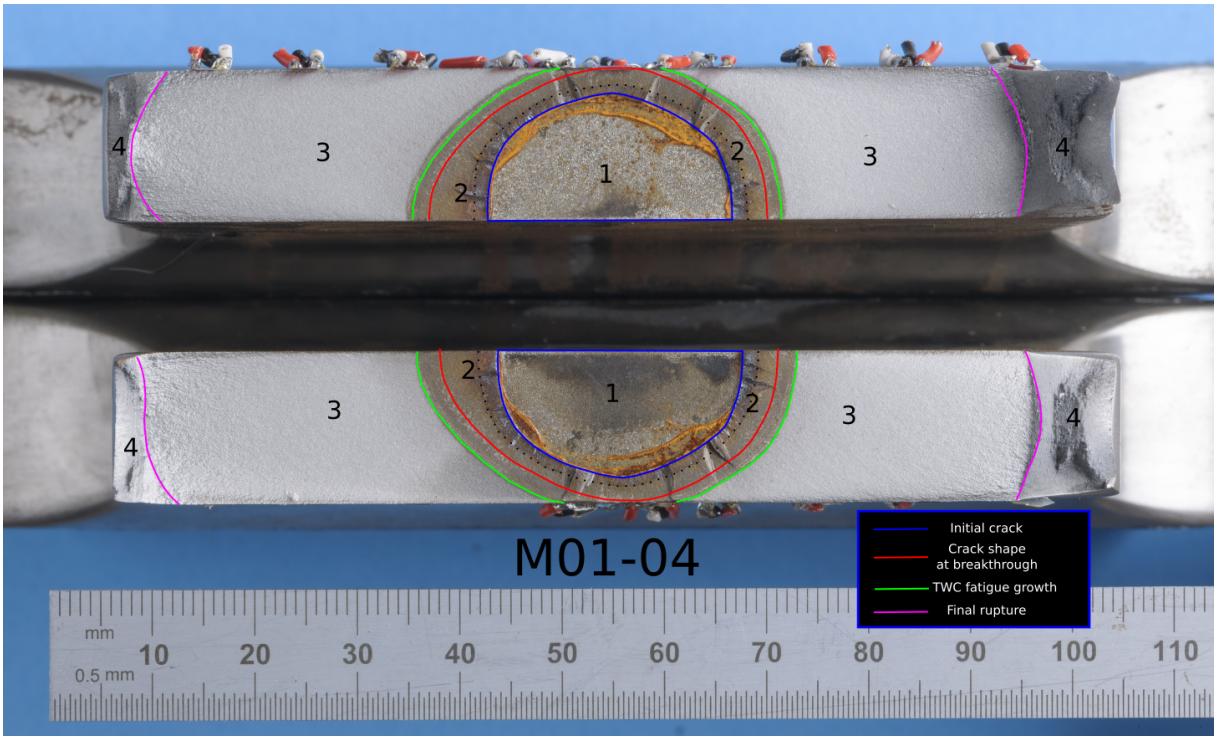

Figure A.32: Test on high strength steel plate - Fracture surface - Sample M01-04

A.3.2 Re-characterisation into through-wall crack

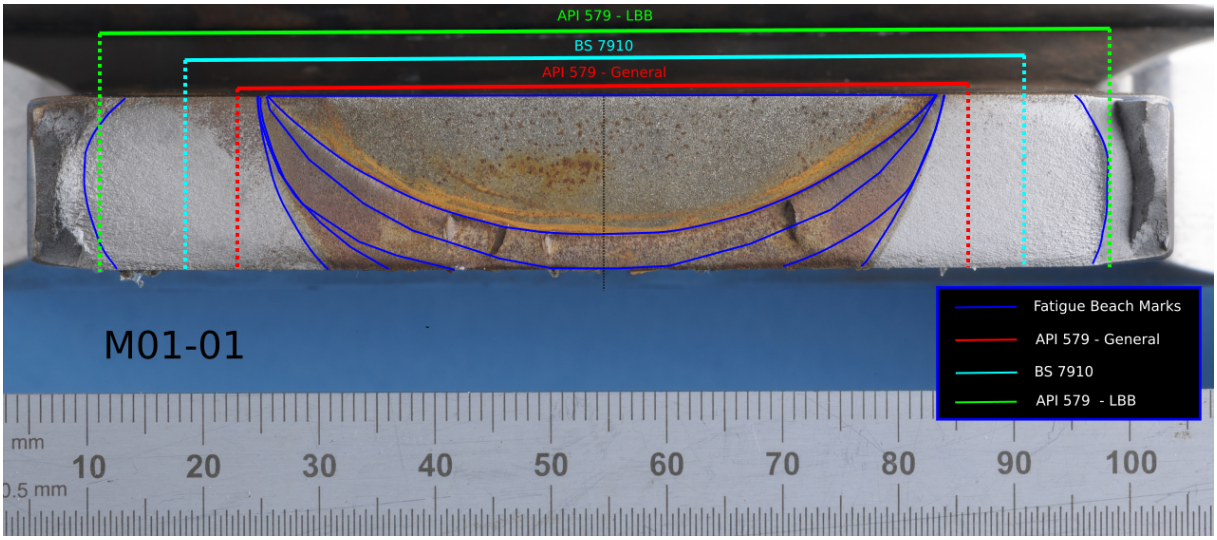

Figure A.33: Re-characterisation into through-wall crack for Specimen M01-01

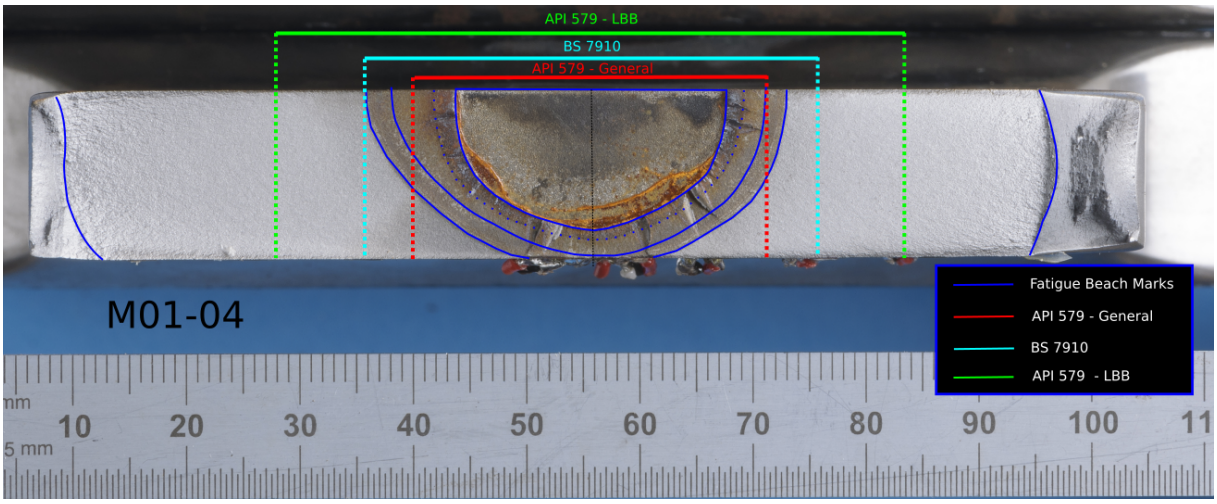

Figure A.34: Re-characterisation into through-wall crack for Specimen M01-04

Appendix B

Equations for crack opening area, stress intensity factor and reference stress

Contents

B.1 Equations of widely used COA models

B.1.1 Axial cracks

B.1.1.1 Axial Crack Opening Area Models

Zahoor's model [134]

Zahoor's model for axial crack is applicable when $\lambda \leq 5$ and $\sigma/\sigma_{ys} \leq 0.25$. This model comes from COA model of plates and has been modified to take into account the curvature of the shell on the crack length.

$$COA = \frac{2\pi P R_m a_e^2 V_0}{E' t} \tag{B.1}$$

where

$$V_0 = 1 + 0.64935\lambda^2 - 0.0089683\lambda^4 + 0.000133873\lambda^6 \tag{B.2}$$

$$\lambda = \frac{a}{\sqrt{R_m t}} \tag{B.3}$$

When small-scale yielding is taken into account λ has to be replaced by λ_e with the following definition:

$$\lambda_e = \frac{a_e}{\sqrt{R_m t}} \tag{B.4}$$

where

$$a_e = a\left(1 + \frac{F}{2}\frac{\sigma_h}{\sigma_{ys}}\right) \tag{B.5}$$

$$F = 1 + .2987\lambda^2 - 0.026905\lambda^4 + 0.00053549\lambda^6 \tag{B.6}$$

The effect of this parameter is displayed in Figure B.1. As plasticity increases, COA becomes larger. On the other hand, as the loading is far below the yield stress, the corrected expression is closer to that of the elastic model.

Using parameters presented earlier and the formulation of λ in Zahoor's solution (Eq.B.3), the limit of applicability is reached for a crack length of $2a$=454 mm.

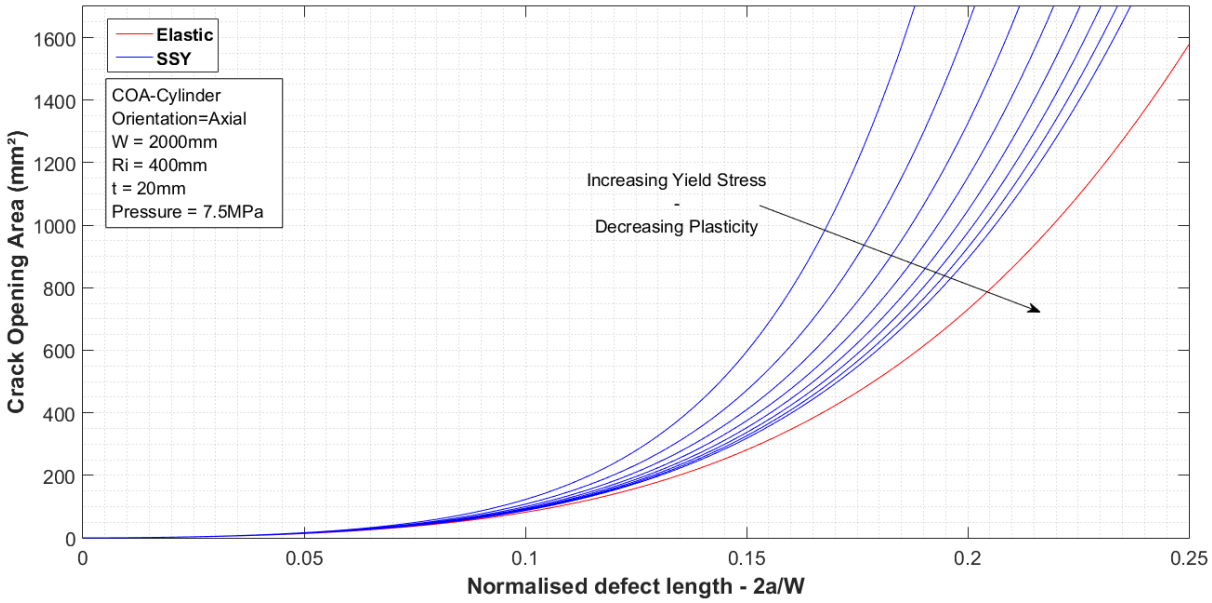

Figure B.1: Plasticity correction effect - Zahoor solution

BS 7910:2013 [1]

In BS 7910, a table is provided with different models of COA available in the literature depending on the structure and loadings. The solution presented in BS 7910 has been adopted from other codes in R6 [60] or FITNET [59]. The solution given here is originally taken from [104] which is the solution for plate corrected for cylindrical shape:

$$COA = \alpha(\lambda)\frac{2\pi\sigma_m a^2}{E'} \tag{B.7}$$

Where $\alpha(\lambda)$ is a correction factor derived using thin-wall and elasticity theories to allow for bulging in terms of the shell parameter (λ). The solution is strictly valid only when flaw lengths do not exceed the least radius of curvature of the shell. For axial cracks with $\lambda \leq 8$, $\alpha(\lambda)$ is defined as follow:

$$\alpha(\lambda) = 1 + 0.1\lambda + 0.16\lambda^2 \tag{B.8}$$

$$\lambda = \sqrt[4]{0.75(1-\nu^2)}\frac{a}{\sqrt{R_m t}} \tag{B.9}$$

When small-scale yielding is taken into account, an Irwin-type correction factor is introduced. The radius of the plastic zone is added to the physical crack size and gives a simple estimate of the influence of plastic deformation [141]. The terms in brackets represents a first-order correction for the effects of crack-tip plasticity increasing with the load level. S is the ratio of the membrane stress to the flow stress:

$$\gamma(S) = \left(1 + \frac{S^2}{2}\right)^{3/2} - \left(\frac{S^2}{2}\right)^{3/2} \tag{B.10}$$

$$S = \frac{\sigma_m}{\sigma_f} \tag{B.11}$$

Using the input parameters presented earlier, the following crack-opening area to crack length relation can be established. Remembering the formulation of λ in BS 7910, the

limit of applicability is reached for a crack half-length of a=400 mm, corresponding to a normalised length of 0.399. This model includes a small-plasticity correction factor, S. Influence of this parameter is presented in Figure B.2. As plasticity increases, COA becomes larger. However, this model is only acceptable for materials with low plasticity effects, i.e. low strain hardening.

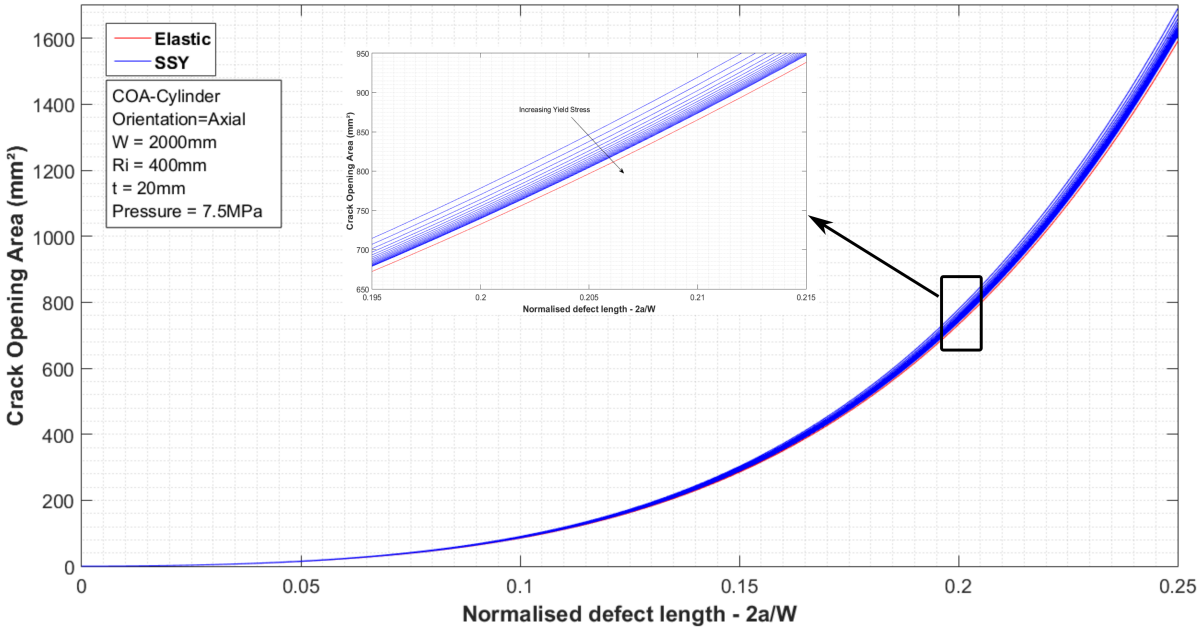

Figure B.2: Plasticity correction effect - BS 7910 solution

API 579-1/ASME-FFS-1:2007 [9]

The recommended solutions for the calculation of axial crack opening areas in API 579-1/ASME-FFS-1 are based on a wide range of linear elastic fracture mechanics FEA validation. Two solutions are provided depending on the type of loading: pressure (Eq.B.12) or stresses (Eq.B.13). They also account for the crack taper resulting from through-wall bending loads. They are evaluated using tabulated values, given for different ratios of R_i/t. Note that when compared to other solutions, the solutions are provided for both inner and outer surfaces and not at mid-thickness.

$$COA = H_p \frac{PR_o}{t} \frac{2\pi a^2}{E} \tag{B.12}$$

or

$$COA = \left(P_m H_0 + P_b \left(H_0 - 2H_1\right)\right) \frac{2\pi a^2}{E} \tag{B.13}$$

where:

$$H_p = \frac{A_0 + A_1\lambda + A_2\lambda^2 + A_3\lambda^3}{1 + A_4\lambda + A_5\lambda^2 + A_6\lambda^3 + A_7\lambda^4} \tag{B.14}$$

$$\lambda = \frac{1.818a}{\sqrt{R_i t}} \tag{B.15}$$

These elastic solutions can be corrected for elastic-plastic conditions with a plasticity correction factor computed from the load ratio as follows:

$$COA_p = \gamma_p \times COA \tag{B.16}$$

where the plasticity modifier γ_p, is determined using the following equation, valid for $0 \leq L_r \leq 1.2$:

$$\gamma_p = 1.008 - 0.33015L_r^2 + 5.53696L_r^4 - 3.96974L_r^6 + 2.00844L_r^8 \tag{B.17}$$

Influence of this parameter is displayed on Figure B.3. As plasticity increases, COA becomes larger.

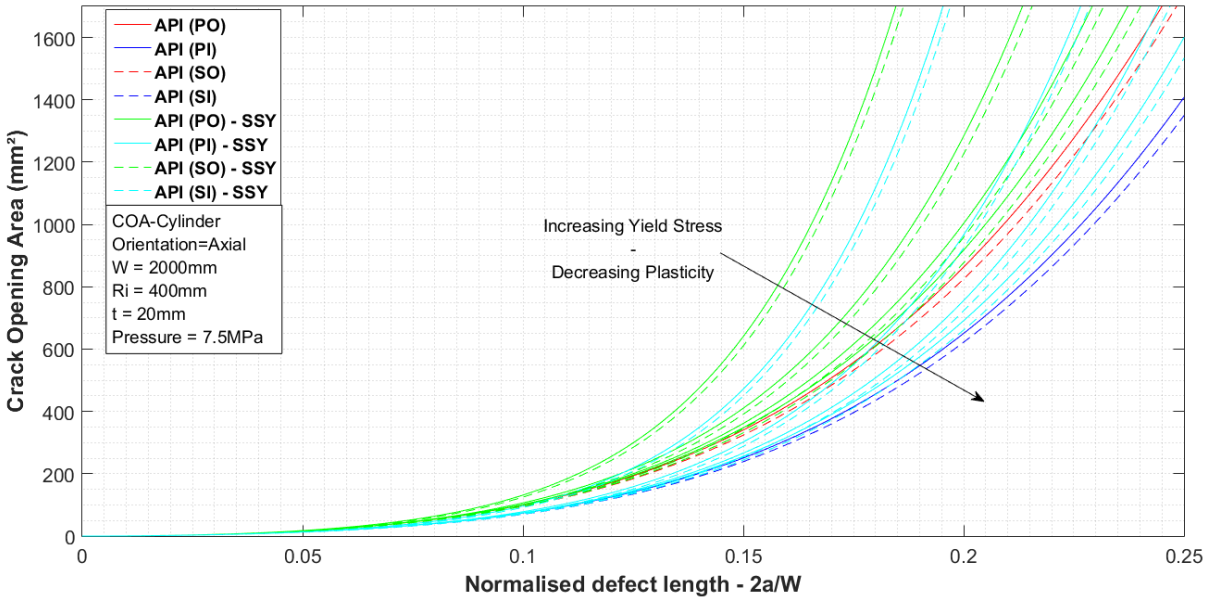

Figure B.3: Plasticity correction effect - API 579-1/ASME FFS-1 solution

B.1.2 Circumferential cracks

B.1.2.1 Circumferential Crack Opening Area Models

Paris-Tada's model [161]

Paris-Tada's model is used for a circumferential crack when $\lambda \leq 5$:

$$COA = \frac{\pi P R_m^2}{E} \times B \tag{B.18}$$

where:

$$B = \begin{cases} \lambda^2 + 0.16125\lambda^4 \text{ for } 0 < \lambda < 1 \\ 0.02 + 0.81\lambda^2 + 0.30\lambda^4 + 0.03125\lambda^4 \text{ for } 1 < \lambda < 5 \end{cases} \tag{B.19}$$

$$\lambda = \theta \times \sqrt{\frac{R_m}{t}} \tag{B.20}$$

When small-scale yielding is taken into account λ is replaced with λ_e using the following definition:

$$\lambda_e = \theta_e \times \sqrt{\frac{R_m}{t}} \tag{B.21}$$

$$\theta_e = \theta \times \left(1 + \frac{F_m^2 P^2 R_m^2}{8t^2\sigma_{ys}^2}\right) \tag{B.22}$$

$$F_m = \begin{cases} 1 + 0.1501\lambda^{1.5} \text{ for } 0 < \lambda < 1 \\ 0.8875 + 0.2625\lambda \text{ for } 1 < \lambda < 5 \end{cases} \tag{B.23}$$

BS 7910:2013 [1]

The solution used for circumferential through-wall crack is the same as that for axial through-wall crack (Eq.B.7) except for the correction factor $\alpha(\lambda)$, which is only valid for $\lambda \leq 5$:

$$COA = \alpha(\lambda)\frac{2\pi\sigma_m a^2}{E'} \tag{B.24}$$

$$\alpha(\lambda) = \sqrt{1 + 0.117\lambda^2} \tag{B.25}$$

API 579-1/ASME-FFS-1:2007 [9]

The recommended solution for crack opening areas calculation in API 579-1/ASME-FFS-1 is based on a wide range of FEA validation, with λ given in Eq.B.15.

$$COA = H_0 \frac{PR_o^2}{R_o^2 - R_i^2}\frac{2\pi a^2}{E} \tag{B.26}$$

or

$$COA = \left(P_m H_0 + P_b\left(H_0 - 2H_1\right)\right)\frac{2\pi a^2}{E} \tag{B.27}$$

where:

$$H_0 = \frac{A_0 + A_1\lambda + A_2\lambda^2}{1 + A_3\lambda + A_4\lambda^2 + A_5\lambda^3} \tag{B.28}$$

B.2 Stress Intensity Factor solutions

Stress Intensity Factor, K_I, solutions for a wide range of geometry and loading configurations are available in many handbooks or standards. Alternatively, numerical analysis methods may be used to derive solutions. This helps to establish the state of the stress at the location of a crack. A comparison of SIF solutions for various geometries can be found in Ref.[59]. For this reason, only solutions for an axial through-wall crack in a cylinder will be presented and calculations provided. Some remarks will be added to assist the understanding of the assessment method. Stress Intensity Factor solutions are functions of the applied primary stresses (P_m, P_b), the defect size ($2a$, $2c$) and the structural dimensions (t, W, R_i). Procedures as API 579-1/ASME FFS-1 or BS 7910 contain solutions for many crack geometries that are likely to occur in large range of components including pressurized components.

B.2.1 Axial through-thickness flaws

BS 7910

A general expression is provided in BS 7910 for all assessments:

$$K_I = Y\sigma\sqrt{\pi a} \tag{B.29}$$

where $Y\sigma$ is divided into two parts to take into account the contribution of primary and secondary stresses:

$$Y\sigma = (Y\sigma)_p + (Y\sigma)_s \tag{B.30}$$

These are calculated as follows, taking into account local stress concentration, misalignment or residual stresses.

$$\begin{cases} (Y\sigma)_p = Mf_w(k_{tm}M_{km}M_mP_m + k_{tb}M_{kb}M_b[P_b + (k_m - 1)P_m]) \\ (Y\sigma)_s = Q_mM_m + Q_bM_b \end{cases} \tag{B.31}$$

In a simple case of an axial through-wall crack (M,f_w=1) under internal pressure with no stress concentration factor ($k_{tm}, k_{tb}, M_{km}, M_{kb} = 1$), no misalignment ($k_m = 1$) and no residual stresses ($Q_m, Q_b = 0$) stresses, Eq.B.31 can be reduced to :

$$\begin{cases} (Y\sigma)_p = M_mP_m + M_bP_b \\ (Y\sigma)_s = 0 \end{cases} \tag{B.32}$$

The Stress Intensity Factor is therefore written in terms of membrane and bending primary stresses corrected by M_m and M_b respectively. These coefficients are given at both inner and outer surfaces from tabulated values for a range of R_m/t ratios. The stress intensity factor solution is reduced to:

$$K_I = (M_mP_m + M_bP_b)\sqrt{\pi a} \tag{B.33}$$

Note that all BS 7910 solutions exclude the effect of crack face pressure for pressurized components.

API 579-1/ASME FFS-1

Several definitions are available in API 579-1/ASME FFS-1. In terms of membrane and bending stress or polynomial stress distribution the two following equations are given:

$$K_I = \{(P_m + P_c)\,G_0 + P_b\,(G_0 - 2G_1)\}\,\sqrt{\pi a} \tag{B.34}$$

$$K_I = \{(\sigma_0 + P_c)\,G_0 + \sigma_1 G_1\}\,\sqrt{\pi a} \tag{B.35}$$

Another simplified formulation is available for internal pressure only:

$$K_I = \frac{PR_o}{t} G_p \sqrt{\pi a} \tag{B.36}$$

where:

$$G_{0,1,p} = \frac{A_0 + A_1\lambda + A_2\lambda^2 + A_3\lambda^3}{1 + A_4\lambda + A_5\lambda^2 + A_6\lambda^3} \tag{B.37}$$

$A_0 \longrightarrow A_6$ are influence coefficients given at both inner and outer surfaces from tabulated values for a range of t/R_i .

B.2.2 Circumferential through-thickness crack

BS 7910

General formulation of the stress intensity factor is used here (Eq.B.29). However primary membrane stress, P_m in the general form, should be multiplied by a factor β defined as:

$$\beta = \sqrt{\frac{2R_m}{atan\left(\frac{a}{2R_m}\right)}} \tag{B.38}$$

Other previous assumptions are also taken into account. The Stress Intensity factor can be written in terms of membrane and bending primary stress corrected by M_m and M_b respectively. These coefficients are given at both inner and outer surfaces from tabulated values for a range of R_m/t ratios. Introducing Eq.B.38 into Eq.B.33 leads to:

$$K_I = (M_m \beta P_m + M_b P_b)\sqrt{\pi a} \tag{B.39}$$

API 579-1/ASME FFS-1

Several definitions are available in API 579-1/ASME FFS-1. In terms of membrane and bending stress or polynomial stress distribution the two following equations are given:

$$K_I = \left\{(\sigma_m + P_c)\, G_0 + \sigma_b\, (G_0 - 2G_1)\right\}\sqrt{\pi a} \tag{B.40}$$

$$K_I = \left\{(\sigma_0 + P_c)\, G_0 + \sigma_1 G_1\right\}\sqrt{\pi a} \tag{B.41}$$

Another simplified formulation is available when internal pressure only is considered:

$$K_I = \frac{P R_o^2}{R_o^2 - R_i^2} G_0 \sqrt{\pi a} \tag{B.42}$$

where:

$$G_{0,1} = \frac{A_0 + A_1\lambda + A_2\lambda^2 + A_3\lambda^3}{1 + A_4\lambda + A_5\lambda^2 + A_6\lambda^3} \tag{B.43}$$

Here $A_0 \longrightarrow A_6$ are influence coefficients given for some ratio t/R_i.

B.2.3 Axial surface flaws

BS 7910

The general formulation of stress intensity factor is used here (Eq.B.29). Other previous assumptions are also taken into account. The Stress Intensity factor can be written in terms of membrane and bending primary stress corrected by M_m and M_b respectively. These coefficients are given at both inner and outer surfaces from tabulated values for a range of R_m/t ratios:

$$K_I = (M_m P_m + M_b P_b)\sqrt{\pi a} \tag{B.44}$$

API 579-1/ASME FFS-1

Several definitions are available in API 579-1/ASME FFS-1. The two following equations are given depending on the loading. For internal pressure loading, with R being the internal or external radius depending on the position of the defect:

$$K_I = \frac{PR^2}{R_o^2 - R_i^2}\left(2G_0 - 2G_1\frac{a}{R} + 3G_2\left(\frac{a}{R}\right)^2 - 4G_3\left(\frac{a}{R}\right)^3 + 5G_4\left(\frac{a}{R}\right)^4\right)\sqrt{\frac{\pi a}{Q}} \quad \text{(B.45)}$$

when Through-Wall Fourth Order Polynomial Stress Distribution is available:

$$K_I = \left(G_0(\sigma_0 + P_c) - \sigma_1 G_1\frac{a}{t} + \sigma_2 G_2\frac{a^2}{t} - \sigma_3 G_3\frac{a^3}{t} + \sigma_4 G_4\frac{a^4}{t}\right)\sqrt{\frac{\pi a}{Q}} \quad \text{(B.46)}$$

Where:

$$Q = \begin{cases} 1 + 1.464\left(\frac{a}{c}\right)^{1.65} & \text{for } a/c \leq 1 \\ 1 + 1.464\left(\frac{a}{c}\right)^{1.65} & \text{for } a/c > 1 \end{cases} \quad \text{(B.47)}$$

Here $G_0 \longrightarrow G_4$ are influence coefficients given for a wide range of ratio t/R_i. Influence coefficients are given for internal and external crack, so a different Stress Intensity Factor may be evaluated depending on the crack location.

B.2.4 Circumferential surface defect

BS 7910

The general formulae of stress intensity factor is used here (Eq.B.29). Other previous assumptions are also taken into account. The Stress Intensity factor can be written in terms of membrane and bending stress corrected by M_m and M_b given for the deepest point in the flaw and the point where the flaw intersects with the free surface from tabulated coefficients given for some ratio R_m/t.

API 579-1/ASME FFS-1

Several definitions are available in API 579-1/ASME FFS-1. The two following equations are given depending on the loading. For internal pressure and net section axial force loading, with R being the internal or external radius depending on the position of the defect:

$$K_I = \left(\frac{PR^2}{R_o^2 - R_i^2} + \frac{F}{\pi(R_o^2 - R_i^2)}\right)G_0\sqrt{\frac{\pi a}{Q}} \quad \text{(B.48)}$$

Another formulation is given based on Through-Wall Fourth Order Polynomial Stress Distribution:

$$K_I = \left(G_0(\sigma_0 + P_c) - \sigma_1 G_1\frac{a}{t} + \sigma_2 G_2\frac{a^2}{t} - \sigma_3 G_3\frac{a^3}{t} + \sigma_4 G_4\frac{a^4}{t} + \sigma_5 G_5\right)\sqrt{\frac{\pi a}{Q}} \quad \text{(B.49)}$$

Where:

$$Q = \begin{cases} 1 + 1.464\left(\frac{a}{c}\right)^{1.65} & \text{for } a/c \leq 1 \\ 1 + 1.464\left(\frac{a}{c}\right)^{1.65} & \text{for } a/c > 1 \end{cases} \quad \text{(B.50)}$$

Here $G_0 \longrightarrow G_6$ are influence coefficients given for some ratio t/R_i. Influence coefficients are given for internal and external crack, so a different Stress Intensity Factor may be evaluated depending on the crack location.

B.3 Reference Stress solutions

The reference stress, σ_{ref}, is a measure of the applied stress in the un-cracked region of a cracked component. It accounts for the loss of cross sectional area in the region containing a flaw. Reference stress solutions are functions of the applied primary stresses (P_m, P_b), the defect size ($2a$, $2c$) and the structural dimensions (t, W, R_i). API 579-1/ASME FFS-1 or BS 7910 provide reference stress solutions for many crack geometries that are likely to occur in pressurized components. As no comparison work has been previously performed for this parameter, the following section includes such discussion for the different geometries.

B.3.1 Axial through-thickness flaws

BS 7910

BS 7910 refers to both Willoughby and Davey [135] and Folias [162] solutions. The original solution from Willoughby and Davey has been developed for plates. To apply the solution to cylinder, the conversion factor developed by Folias is associated with membrane stress. A factor of 1.2, not present in the original paper [135], is also applied to the membrane stress. It is intended to produce a similar level of conservatism as that inherent in the flat plate solution.

$$\sigma_{ref} = 1.2 M_T P_m + \frac{2P_b}{3(1 - \frac{2a}{W})} \tag{B.51}$$

where

$$M_T = \sqrt{1 + 1.6\frac{a^2}{R_i t}} \tag{B.52}$$

API 579-1/ASME FFS-1

The solution for an axial through-thickness flaw in a pipe available in API 579-1/ASME FFS-1 is given as:

$$\sigma_{ref} = \frac{P_b + \sqrt{P_b^2 + 9(M_t P_m)^2}}{3} \tag{B.53}$$

where three definitions are given for M_t, reported here as M_{t1}, M_{t2} and M_{t3}:

$$M_{t1} = \sqrt{\frac{(1.02 + 0.4411\lambda^2 + 0.006124\lambda^4}{1 + 0.02642\lambda^2 + 1.533 \times 10^{-6}\lambda^4}} \tag{B.54}$$

$$M_{t2} = \begin{cases} \sqrt{1 + 0.3797\lambda^2 - 0.001234\lambda^4} \text{ for } \lambda \leq 9.1 \\ (3.3 + 0.01936\lambda)^2 \text{ for } \lambda > 9.1 \end{cases} \tag{B.55}$$

$$M_{t3} = \sqrt{1 + 0.4845\lambda^2} \tag{B.56}$$

and

$$\lambda = 1.818\frac{a}{\sqrt{R_i t}} \tag{B.57}$$

B.3.2 Circumferential through-thickness crack

BS 7910 The following solution is available in BS 7910:

$$\sigma_{ref} = \frac{\pi(P_{m,a} + P_{m,p})}{\pi - \frac{a}{R_i} - 2arcsin\left(0.5sin\left(\frac{a}{R_i}\right)\right)} + \frac{\pi P_{m,b}(R_o^4 - R_i^4)}{(4R_o R_m^2 t)\left(\pi - \frac{a}{R_i} - 2\frac{sin^2\left(\frac{a}{R_i}\right)}{\pi - \frac{a}{R_i}} - \frac{sin\left(\frac{2a}{R_i}\right)}{2}\right)} + \frac{2P_{b,l}}{3\left(1 - \frac{2a}{\pi R_i}\right)} \tag{B.58}$$

where the primary membrane stress is divided into:

- $P_{m,a}$ primary membrane stress due to global axial loads
- $P_{m,p}$ primary membrane stress due to internal pressure
- $P_{m,b}$ primary membrane stress due to global bending moments
- $P_{b,l}$ primary through-wall bending stress

API 579-1/ASME FFS-1

The following solution is available in API 579-1/ASME FFS-1:

$$\sigma_{ref} = \frac{P_b + \sqrt{P_b^2 + 9(ZP_m(1-\alpha)^2)^2}}{3(1-\alpha)^2} \tag{B.59}$$

where:

$$\theta = \frac{a}{R_m} \tag{B.60}$$

$$\alpha = \frac{a}{\pi R_m} \tag{B.61}$$

$$\tau = \frac{t}{R_o} \tag{B.62}$$

$$\phi = arcos(\frac{sin\theta}{2}) \tag{B.63}$$

$$Z = \frac{\pi(R_o^2 - R_i^2)}{(2-\tau)(R_o t(2\phi - \theta))}) \tag{B.64}$$

The reference stress solution in API 579-1/ASME FFS-1 is based on the crack angle measured on the mean radius of the pipe or cylinder shell.

B.3.3 Axial surface flaws

BS 7910

The following solution is available in BS 7910:

$$\sigma_{ref} = 1.2M_s P_m + \frac{2P_b}{3(1-\alpha'')^2} \tag{B.65}$$

where:

$$M_s = \frac{1 - \frac{a}{tM_T}}{1 - \frac{a}{t}} \text{ with } M_T \text{ from Eq.} \tag{B.66}$$

$$\alpha'' = \frac{\frac{a}{t}}{1+\frac{t}{c}} \text{ for } W \geq 2(c+t) \tag{B.67}$$

In BS 7910, the surface correction factor is based on the original Folias solution for thin walled cylinders [162]. The surface correction factor corresponds to the one called M_{s1} in API 579-1/ASME FFS-1 for a rectangular crack shape. Assuming that the crack shape is rectangular will lead to conservative results.

API 579-1/ASME FFS-1

The following solution is available in API 579-1/ASME FFS-1:

$$\sigma_{ref} = \frac{gP_b + \sqrt{(gP_b)^2 + 9(M_s P_m (1-\alpha)^2)^2}}{3(1-\alpha)^2} \tag{B.68}$$

where:

$$g = 1 - 20\alpha^3 \left(\frac{a}{2c}\right)^{0.75} \tag{B.69}$$

$$\alpha = \frac{\frac{a}{t}}{1+\frac{t}{c}} \tag{B.70}$$

Two definitions are available for the surface correction factors:

$$M_{s1} = \frac{1 - C\left(\frac{a}{tM_t}\right)}{1 - C\frac{a}{t}} \text{ where C= } \begin{cases} 1 \text{ for rectangular shape} \\ 0.67 \text{ for parabolic shape} \\ 0.85 \text{ for a best fit to the data} \end{cases} \tag{B.71}$$

$$M_{s2} = \frac{1}{1 - \frac{a}{t} + \frac{a}{t}\frac{1}{M_t(\lambda_a)}} \tag{B.72}$$

where:

$$\lambda_a = 1.818\frac{c}{\sqrt{R_i a}} \tag{B.73}$$

B.3.4 Circumferential surface defect

BS 7910

The following solution is available in BS 7910 where R represents the internal or external radius depending on the crack location:

$$\sigma_{ref} = \frac{P_m\left(\pi\left(1-\frac{a}{t}\right) + 2\frac{a}{t}sin\left(\frac{c}{R}\right)\right)}{\left(1-\frac{a}{t}\right)\left(\pi - \frac{a}{t}\frac{c}{R}\right)} + \frac{2P_b}{3(1-\alpha'')^2} \tag{B.74}$$

where

$$\alpha'' = \begin{cases} \frac{\frac{a}{t}}{1+\frac{t}{c}} \text{ for } \pi R \geq c+t \\ \frac{a}{t}\frac{c}{\pi R} \text{ for } \pi R < c+t \end{cases} \tag{B.75}$$

API 579-1/ASME FFS-1

The following solution is available in API 579-1/ASME FFS-1:

$$\sigma_{ref} = \frac{P_b + \sqrt{P_b^2 + 9(ZP_m(1-\alpha)^2)^2}}{3(1-\alpha)^2} \tag{B.76}$$

where:

$$\theta = \begin{cases} \frac{\pi c}{4R_o} \text{ for external crack} \\ \frac{\pi c}{4R_i} \text{ for internal crack} \end{cases} \tag{B.77}$$

$$x = \frac{a}{t} \tag{B.78}$$

$$\tau = \frac{t}{R_o} \tag{B.79}$$

$$A = x\left(\frac{(1-\tau)(2-2\tau+x\tau)(1-\tau+x\tau)^2}{2(1+(2-\tau)(1-\tau)}\right) \tag{B.80}$$

$$\alpha = \frac{\frac{a}{t}}{1+\frac{t}{c}} \tag{B.81}$$

$$\psi = arcos(Asin\theta) \tag{B.82}$$

$$Z = \frac{1}{\frac{2\psi}{\pi} - \frac{x\theta}{\pi}\left(\frac{2-2\tau+x\tau}{2-\tau}\right)} \tag{B.83}$$